

# Jordan Journal of Mechanical and Industrial Engineering (JJMIE)

JJMIE is a high-quality scientific journal devoted to fields of Mechanical and Industrial Engineering. It is published by Hashemite University in cooperation with the Jordanian Scientific Research and Innovation Support Fund, Ministry of Higher Education and Scientific Research.

## EDITORIAL BOARD

---

### Editor-in-Chief

Prof. Moh'd Sami Ashhab

### Assistant Editors

Dr. Ahmad AlMigdady

Dr. Mohannad Jreissat

### Editorial Board

#### **Prof. Tariq A. ALAzab**

Al Balqa Applied University

#### **Prof. Jamal Jaber**

Al- Balqa Applied University

#### **Prof. Mohamad Al-Widyan**

Jordan University of Science and Technology

#### **Prof. Mohammed Taiseer Hayajneh**

Jordan University of Science and Technology

#### **Prof. Mohammad Al-Tahat**

The University of Jordan

#### **Prof. Ali M. Jawarneh**

The Hashemite University

## THE INTERNATIONAL ADVISORY BOARD

---

#### **Abu-Qudais, Mohammad**

Jordan University of Science & Technology, Jordan

#### **Tzou, Gow-Yi**

Yung-Ta Institute of Technology and Commerce, Taiwan

#### **Abu-Mulaweh, Hosni**

Purdue University at Fort Wayne, USA

#### **Jubran, Bassam**

Ryerson University, Canada

#### **Afaneh Abdul-Hafiz**

Robert Bosch Corporation, USA

#### **Kakac, Sadik**

University of Miami, USA

#### **Afonso, Maria Dina**

Institute Superior Tecnico, Portugal

#### **Khalil, Essam-Eddin**

Cairo University, Egypt

#### **Badiru, Adedji B.**

The University of Tennessee, USA

#### **Mutoh, Yoshiharu**

Nagaoka University of Technology, Japan

#### **Bejan, Adrian**

Duke University, USA

#### **Pant, Durbin**

Iowa State University, USA

#### **Chalhoub, Nabil G.**

Wayne State University, USA

#### **Riffat, Saffa**

The University of Nottingham, U. K

#### **Cho, Kyu-Kab**

Pusan National University, South Korea

#### **Saghir, Ziad**

Ryerson University, Canada

#### **Dincer, Ibrahim**

University of Ontario Institute of Technology,  
Canada

#### **Sarkar, MD. Abdur Rashid**

Bangladesh University of Engineering &  
Technology, Bangladesh

#### **Douglas, Roy**

Queen's University, U. K

#### **Siginer, Dennis**

Wichita State University, USA

#### **El Bassam, Nasir**

International Research Center for Renewable  
Energy, Germany

#### **Sopian, Kamaruzzaman**

University Kebangsaan Malaysia, Malaysia

#### **Haik, Yousef**

United Arab Emirates University, UAE

## EDITORIAL BOARD SUPPORT TEAM

---

### Language Editor

Dr. Baker M. Bani-khair

### Publishing Layout

Eng. Ali Abu Salimeh

## SUBMISSION ADDRESS:

---

Prof. Moh'd Sami Ashhab, Editor-in-Chief  
Jordan Journal of Mechanical & Industrial Engineering,  
Hashemite University,  
PO Box 330127, Zarqa, 13133, Jordan  
E-mail: jjmie@hu.edu.jo



Hashemite Kingdom of Jordan



Hashemite University

Jordan Journal of  
Mechanical and Industrial Engineering

JJMIIE

*An International Peer-Reviewed Scientific Journal*

*Financed by Scientific Research Support Fund*

Volume 14, Number 3, September 2020

<http://jjmie.hu.edu.jo/>

ISSN 1995-6665

# Jordan Journal of Mechanical and Industrial Engineering (JJMIE)

JJMIE is a high-quality scientific journal devoted to fields of Mechanical and Industrial Engineering. It is published by Hashemite University in cooperation with the Jordanian Scientific Research and Innovation Support Fund, Ministry of Higher Education and Scientific Research.

**Introduction:** The Editorial Board is very committed to build the Journal as one of the leading international journals in mechanical and industrial engineering sciences in the next few years. With the support of the Ministry of Higher Education and Scientific Research and Jordanian Universities, it is expected that a heavy resource to be channeled into the Journal to establish its international reputation. The Journal's reputation will be enhanced from arrangements with several organizers of international conferences in publishing selected best papers of the conference proceedings.

**Aims and Scope:** *Jordan Journal of Mechanical and Industrial Engineering* (JJMIE) is a refereed international journal to be of interest and use to all those concerned with research in various fields of, or closely related to, mechanical and industrial engineering disciplines. *Jordan Journal of Mechanical and Industrial Engineering* aims to provide a highly readable and valuable addition to the literature which will serve as an indispensable reference tool for years to come. The coverage of the journal includes all new theoretical and experimental findings in the fields of mechanical and industrial engineering or any closely related fields (Materials, Manufacturing, Management, Design, Thermal, Fluid, Energy, Control, Mechatronics, and Biomedical). The journal also encourages the submission of critical review articles covering advances in recent research of such fields as well as technical notes.

## Guide for Authors

---

### **Manuscript Submission:**

High-quality submissions to this new journal are welcome now and manuscripts may be either submitted online or email.

**Online:** For online and email submission upload one copy of the full paper including graphics and all figures at the online, submission site, accessed via <http://jjmie.hu.edu.jo>. The manuscript must be written in MS Word Format. All correspondence including notification of the Editor's decision and requests for revision, takes place by e-mail and via the Author's homepage, removing the need for a hard-copy paper trail

### **Submission address and contact :**

Prof. Moh'd Sami Ashhab

Editor-in-Chief

*Jordan Journal of Mechanical & Industrial*

*Engineering*, Hashemite University

PO Box 330127, Zarqa, 13115, Jordan

E-mail: [jjmie@hu.edu.jo](mailto:jjmie@hu.edu.jo)

**Types of contributions:** Original research papers and Technical reports

**Corresponding author:** Clearly indicate who is responsible for correspondence at all stages of refereeing and publication, including post-publication. Ensure that telephone and fax numbers (with country and area code) are provided in addition to the e-mail address and the complete postal address. Full postal addresses must be given for all co-authors.

**Original material:** Submission of an article implies that the work described has not been published previously (except in the form of itstan abstract or as part of a published lecture or academic thesis), that it is not under consideration for publication elsewhere, the publication is approved by all authors and that, if accepted, it will not be published elsewhere in the same form, in English or in any other language, without the written consent of the Publisher. Authors found to be deliberately contravening the submission guidelines on originality and exclusivity shall not be considered for future publication in this journal.

**Withdrawing:** If the author chooses to withdraw his article after it has been assessed, he shall reimburse JJMIE with the cost of reviewing the paper.

### **Manuscript Preparation:**

---

**General:** Editors reserve the right to adjust style to certain standards of uniformity. Original manuscripts are discarded after publication unless the Publisher is asked to return original material after use. Please use MS Word for the text of your manuscript

**Structure:** Follow this order when typing manuscripts: Title, Authors, Authors title, Affiliations, Abstract, Keywords, Introduction, Main text, Conclusions, Acknowledgements, Appendix, References, Figure Captions, Figures and then Tables. Please supply figures imported into the text AND also separately as original graphics files. Collate acknowledgements in a separate section at the end of the article and do not include them on the title page, as a footnote to the title or otherwise.

**Text Layout:** Use 1.5 line spacing and wide (3 cm) margins. Ensure that each new paragraph is clearly indicated. Present tables and figure legends on separate pages at the end of the manuscript. If possible, consult a recent issue of the journal to become familiar with layout and conventions. All footnotes (except for table and corresponding author footnotes) should be identified with superscript Arabic numbers. To conserve space, authors are requested to mark the less important parts of the paper (such as records of experimental results) for printing in smaller type. For long papers (more than 4000 words) sections which could be deleted without destroying either the sense or the continuity of the paper should be indicated as a guide for the editor. Nomenclature should conform to that most frequently used in the scientific field concerned. Number all pages consecutively; use 12 or 10 pt font size and standard fonts.

**Corresponding author:** Clearly indicate who is responsible for correspondence at all stages of refereeing and publication, including post-publication. The corresponding author should be identified with an asterisk and footnote. Ensure that telephone and fax numbers (with country and area code) are provided in addition to the e-mail address and the complete postal address. Full postal addresses must be given for all co-authors. Please consult a recent journal paper for style if possible.

**Abstract:** A self-contained abstract outlining in a single paragraph the aims, scope and conclusions of the paper must be supplied.

**Keywords:** Immediately after the abstract, provide a maximum of six keywords (avoid, for example, 'and', 'of'). Be sparing with abbreviations: only abbreviations firmly established in the field may be eligible.

**Symbols:** All Greek letters and unusual symbols should be identified by name in the margin, the first time they are used.

**Units:** Follow internationally accepted rules and conventions: use the international system of units (SI). If other quantities are mentioned, give their equivalent quantities in SI

**Maths:** Number consecutively any equations that have to be displayed separately from the text (if referred to explicitly in the text).

**References:** All publications cited in the text should be presented in a list of references following the text of the manuscript.

*Text:* Indicate references by number(s) in square brackets in line with the text. The actual authors can be referred to, but the reference number(s) must always be given.

*List:* Number the references (numbers in square brackets) in the list in the order in which they appear in the text.

**Examples:**

**Reference to a journal publication:**

[1] M.S. Mohsen, B.A. Akash, "Evaluation of domestic solar water heating system in Jordan using analytic hierarchy process". Energy Conversion & Management, Vol. 38 (1997) No. 9, 1815-1822.

**Reference to a book:**

[2] Strunk Jr W, White EB. The elements of style. 3rd ed. New York: Macmillan; 1979.

**Reference to a conference proceeding:**

[3] B. Akash, S. Odeh, S. Nijmeh, "Modeling of solar-assisted double-tube evaporator heat pump system under local climate conditions". 5th Jordanian International Mechanical Engineering Conference, Amman, Jordan, 2004.

**Reference to a chapter in an edited book:**

[4] Mettam GR, Adams LB. How to prepare an electronic version of your article. In: Jones BS, Smith RZ, editors. Introduction to the electronic age, New York: E-Publishing Inc; 1999, p. 281-304

**Free Online Color :** If, together with your accepted article, you submit usable color and black/white figures then the journal will ensure that these figures will appear in color on the journal website electronic version.

**Tables:** Tables should be numbered consecutively and given suitable captions and each table should begin on a new page. No vertical rules should be used. Tables should not unnecessarily duplicate results presented elsewhere in the manuscript (for example, in graphs). Footnotes to tables should be typed below the table and should be referred to by superscript lowercase letters.

**Notification:** Authors will be notified of the acceptance of their paper by the editor. The Publisher will also send a notification of receipt of the paper in production.

**Copyright:** All authors must sign the Transfer of Copyright agreement before the article can be published. This transfer agreement enables Jordan Journal of Mechanical and Industrial Engineering to protect the copyrighted material for the authors, but does not relinquish the authors' proprietary rights. The copyright transfer covers the exclusive rights to reproduce and distribute the article, including reprints, photographic reproductions, microfilm or any other reproductions of similar nature and translations.

**Proof Reading:** One set of page proofs in MS Word format will be sent by e-mail to the corresponding author, to be checked for typesetting/editing. The corrections should be returned within **48 hours**. No changes in, or additions to, the accepted (and subsequently edited) manuscript will be allowed at this stage. Proofreading is solely the author's responsibility. Any queries should be answered in full. Please correct factual errors only, or errors introduced by typesetting. Please note that once your paper has been proofed we publish the identical paper online as in print.

**Author Benefits:**

*No page charges:* Publication in this journal is free of charge.

*Free offprints:* One journal issues of which the article appears will be supplied free of charge to the corresponding author and additional offprint for each co-author. Corresponding authors will be given the choice to buy extra offprints before printing of the article.



## PAGES

## PAPERS

---

271 - 277	<b>Research on the Effect of Rotation Speed on the Meshing Characteristics of Elliptical Cylindrical Gears</b> <i>Changbin Dong , Yongping Liu, Xingwen Fu, Chenchen Dou, Yuxin Yin</i>
279 - 287	<b>Systematic Approach for Selecting a Cleaning Method to Solar Panels Based on the Preference Selection Index Approach</b> <i>Mohammed Said Obeidat, Esra'a Mohammad Al Abed Alhalim, Bilal Raif Melhim</i>
289– 294	<b>The Antimicrobial Effect of UV-Activated Titanium Dioxide Material Deposited on Dental Implants</b> <i>Abdul Hai Alami, M Adel Moufti, Mohammad Hamad, Kamilia Aokal, Abdullah Abu Hawili, Rawand Naji, Mohammad Faraj</i>
295– 302	<b>Value Stream Mapping with Simulation to Optimize Stock Levels: Case Study</b> <i>Yunus Emre MIDILLI, Birol ELEVLI</i>
303– 313	<b>Analytical and Graphical Optimal Synthesis of Crank-Rocker Four Bar Mechanisms for Achieving Targeted Transmission Angle Deviations</b> <i>Sabry El-Shakery, Rokaya Ramadan, Khaled Khader</i>
315– 337	<b>Review of Experimental and Finite Element Analyses of Spot Weld Failures in Automotive Metal Joints</b> <i>Aravinthan Arumugam, Alokesh Pramanik</i>
339– 348	<b>Experimental and Numerical Study of Heat Transfer and Tensile Strength of Engineered Porous Fins to Estimate the Best Porosity</b> <i>Ali Heydari, Mehrdad Mesgarpour, Mohammad Reza Gharib</i>
349– 359	<b>Potential Utilization of Iraqi Associated Petroleum Gas as Fuel for SI Engines</b> <i>Jehad A. A. Yamin, Eiman Ali Eh Sheet</i>

---



# Research on the Effect of Rotation Speed on the Meshing Characteristics of Elliptical Cylindrical Gears

Changbin Dong<sup>\*</sup>, Yongping Liu, Xingwen Fu, Chenchen Dou, Yuxin Yin

*College of Mechanical & Electrical Engineering, Lanzhou University of Technology, Lanzhou 730050, P. R. China*

*Received October 19 2019*

*Accepted August 4 2020*

## Abstract

Aiming at the elliptical cylinder gear pair in the reversing device of the new drum pumping unit, the dynamic meshing process of tooth was simulated by LS-PREPOST software. The distribution law of effective plastic strain, effective stress, tooth surface pressure, tooth surface displacement and meshing force in the direction of tooth lines and tooth profiles under different rotational speeds were obtained. The results show that the effective plastic strain, the effective stress and the surface pressure in the tooth lines direction will decrease as the center position of the elliptical contact area of the tooth surface expands to both sides. The effective plastic strain, the effective stress and the surface pressure in the tooth profiles direction will increase with the increase of the rotational speed, and the rotational speed will affect the changing period of the tooth surface displacement and the meshing force. The research results can provide theoretical basis and certain guiding significance for the dynamic design, meshing analysis, modification and engineering application of non-cylindrical gears.

© 2020 Jordan Journal of Mechanical and Industrial Engineering. All rights reserved

*Keywords: Elliptical cylindrical gear; Tooth contact analysis; Effective plastic strain; Effective stress; Contact characteristics;*

## 1. Introduction

As one of the simplest Non-Cylindrical gears, the elliptical cylindrical gear is distinguished from the ordinary cylindrical gear by its elliptic pitch curve, which is widely used in automatic machinery, printers, hydraulic pumps, hydraulic motors and flow meters for its compact structure and variable-ratio transmission. In recent years, tooth contact analysis (TCA) technology has developed rapidly in the field of gear, but the traditional TCA technology only considers the normal engagement of gear pair under the theoretical contact condition, and does not consider the influence of load on gear engagement. In view of this situation, the loaded tooth contact analysis technology (LTCA) has attracted extensive attention, which is a bridge connecting geometric design and mechanical analysis in the field of gear research, which is more in line with the actual working conditions of gears [1-2].

The teeth of elliptical cylindrical gears are different, but each tooth can be regarded as a tooth on the equivalent cylindrical gears. The contact analysis method of cylindrical gears can be used to analyze elliptical cylindrical gears. As far as spur gears are concerned, there are already many complete analysis techniques [3-5], and a lot of research results have been accumulated in the research of tooth surface contact. References [6-7] use ANSYS LS-DYNA analysis software to study gear meshing and contact characteristics of tooth. SANCHEZ-MARIN [8] proposed

discretization and geometric adaptive refinement of the contact surface of teeth to solve the contact problem and calculate the instantaneous contact area of gear in meshing process. Wang Chen [9] proposed a method of tooth profiles modification based on tooth contact analysis technology. The modification parameters of rack cutter obtained by TCA technology can be transformed into the modification parameters of gear profile. Chen Ruibo [10], considering the contact relationship between the tooth surface, established the dynamic model of gear transmission. On this basis, the effects of meshing stage and operating conditions on the contact characteristics and dynamic characteristics of tooth are studied. Vasie Marius [1] proposed the method of generating pitch curve and tooth profiles of elliptical cylindrical gear and simulated the meshing of tooth in 2D and 3D environments respectively, and elaborated the meshing path, contact area and its change of tooth in detail. Zhang Huang [11] carried out numerical simulation of elliptical cylindrical gear transmission based on gear meshing principle and constructed a complete contact analysis method of elliptical cylindrical gear tooth profiles. Zhang Guohua [12] aimed at the high-order modified elliptical gears, and the contact stress of the tooth was obtained by simulating the meshing state of the tooth. The above research is of great significance to analyze the meshing characteristics of non-cylindrical gears, but there are few studies on the tooth surface contact in the dynamic meshing process of non-cylindrical gears. In this paper, a pair of elliptical cylindrical gears in the reversing device of

\* Corresponding author e-mail: lutdcb@126.com

a new type of drum pumping unit is taken as the research object, and an accurate finite element model is established. Based on LS-PREPOST software, the dynamic meshing process of elliptical cylindrical gears is simulated to study the distribution of stress and strain in the meshing process of gears at different rotational speeds. Figure 1 is a model of elliptical cylindrical gear reversing device.



Figure 1. Reversing device of planetary gear train with elliptical cylindrical gears

## 2. Meshing theory of elliptical cylindrical gears

The curvature radius of elliptical cylindrical gears varies everywhere on the pitch curve, and the coincidence degree varies with it in the actual meshing process and is always greater than 1, which is mainly manifested by the meshing of one or two pairs of gears. According to the engagement of involute tooth profiles, the contact characteristics can be analyzed according to the Hertz theory of two cylinders contact models [13], so the contact stress of the tooth surface is as follows:

$$\sigma_H = \sqrt{\frac{p_{ca}}{\sum \rho} \cdot \frac{1}{\pi \left( \frac{1-\mu_1^2}{E_1} + \frac{1-\mu_2^2}{E_2} \right)}} \quad (1)$$

$$p_{ca} = \frac{F_n}{B} \quad (2)$$

$$\sum \rho = \frac{\rho_1 \rho_2}{\rho_1 + \rho_2} \quad (3)$$

Where  $p_{ca}$  is the calculated load on the unit length;  $B$  is the tooth width;  $F_n$  is the normal force on the tooth surface;  $E_1, E_2$  elastic modulus of the two gears;  $\mu_1, \mu_2$  are Poisson's ratio of the two gears in contact with each other;  $\sum \rho$  is the comprehensive curvature radius at the two contact surfaces. The center distance of is  $a$ , and the extreme diameters of the pitch curve of the driving and driven wheels are  $r_1$  and  $r_2 = a - r_1$ . The input torque of the driving wheel is  $T_1(t)$ , and the output torque of the driven wheel is  $T_2(t)$ . The force diagram of the driving wheel in a pair of meshed non cylindrical gear pairs is shown in Figure 2.

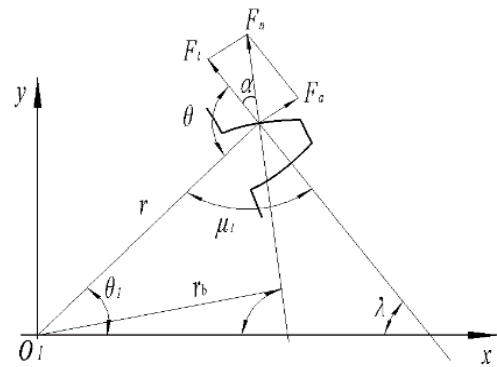


Figure 2. Stress diagram of involute profile of non-cylindrical gear

Where  $\alpha$  is the angle between the tangential force  $F_t$  and the normal force  $F_n$ ;  $F_a$  is the circumferential force;  $\theta$  is the angle between the tangential force and the radius of the pitch curve;  $\theta_i$  is the angle between the radius of the pitch curve and the x-axis, and  $\lambda$  is the angle between the tangential force and the x-axis.

The tangential force  $F_t$  and the normal force  $F_n$  of the tooth surface of non-circular involute spur gears are respectively:

$$F_t = \frac{T_1}{r_1 \sin \mu_1} \quad (4)$$

$$F_n = \frac{F_t}{\cos 20^\circ} = \frac{T_2(t) \sqrt{r_1^2 + r_1'^2}}{r_1 (a - r_1) \cos 20^\circ} \quad (5)$$

When a pair of tooth profiles engages at the pitch curve of non-circular involute spur gears, the meshing force is larger. When the gear material is the same, the nominal value of contact stress and the calculated value of surface contact stress are respectively

$$\sigma_{H0} = \sqrt{\frac{F_n E}{2\pi b (1 - \mu^2)} \left( \frac{1}{\rho_1} + \frac{1}{\rho_2} \right)} \quad (6)$$

$$\sigma_H = \sigma_{H0} \sqrt{K_S K_A K_V K_{H\beta} K_{H\alpha}} \quad (7)$$

Where  $\rho_1, \rho_2$  is the curvature radius at the two contact tooth surfaces;  $K_S$  is the meshing stiffness coefficient;  $K_A$  is the use coefficient;  $K_V$  is the dynamic load coefficient;  $K_{H\beta}$  is the load distribution coefficient of the contact stiffness calculation, and  $K_{H\alpha}$  is the load distribution coefficient of the teeth calculated by the contact stiffness.

The force acting on elliptical cylindrical gears in meshing process is complex and time-varying. The above expression can calculate the static force acting on the teeth, but some coefficients need to be selected according to experience, and it is difficult to calculate the instantaneous stress, strain and meshing force in meshing process. The LS-PREPOST software avoids the complex finite element programming and calculation and can simulate the actual meshing process completely. It can realize the load contact analysis of gears, which is more in line with the actual working conditions in the process of gear meshing, so it can be used to analyze the meshing characteristics of elliptical cylindrical gears. The parameters of elliptical cylindrical gears are shown in Table 1.

**Table 1.** Elliptical cylinder gear design parameters

Modulus $m$	3
Tooth number $Z$	47
Center distance $a$	150
Tooth top height coefficient $h_a^*$	1
Top clearance coefficient $C^*$	0.25
Tooth width $B$	30
Eccentricity $e$	0.3287
Pitch curve equation $r$	$r = \frac{64.667}{1 \pm 0.3287 \cos \varphi}$

**3. Analysis of dynamic meshing characteristics of elliptical cylindrical gears**

In the process of gear meshing, load and power are transmitted in the form of tooth surface contact. The tooth profiles and tooth lines are two important characteristics of the tooth surface, and they are also the main factors affecting the tooth surface shape, meshing characteristics and contact characteristics [14]. Rotation speed will affect the impact time in the process of gear meshing, and then affect its meshing characteristics. In order to simplify the analysis process, the dynamic meshing characteristics of elliptical cylindrical tooth are analyzed from two aspects: the direction of tooth lines and the direction of tooth profiles, respectively, without considering the manufacturing and installation errors and displacement factors.

*3.1. Load step analysis of gear tooth engagement*

In order to simulate the actual contact of tooth in meshing process, the following boundary conditions should be set: the inner ring of rigid shaft hole drives the flexible body of gear to rotate, the gear material is Solid164 flexible body, the inner ring material of shaft hole is Shell163 rigid body. The driving and driven wheels limit the degrees of freedom of movement in three directions of X, Y and Z and the degrees of freedom of rotation in X and Y. The rotational speed of the driving wheel is 600 r/min. In the process of solving gear meshing model, excessive time steps and the proportion factor of calculation time step will lead to negative volume and interrupt simulation. The generation of negative volume is mostly caused by mesh distortion, which is related to mesh quality, material and load conditions. Therefore, appropriate time step should be taken to avoid negative volume. After debugging, the time step ratio factor TSSFAC is 0.5, and the time step DT2MS is  $-2 \times 10^{-7}$ , which can completely simulate gear meshing.

According to the set boundary conditions, the finite element model of elliptical cylindrical gear is solved, and the dynamic meshing simulation of 0.1s is obtained. The elliptical contact area of the tooth at 0.0079s is shown in Figure 3. In the meshing simulation time of 0.1s, six time points are selected randomly, and the maximum contact stress in the meshing process of tooth are shown in Table 2.

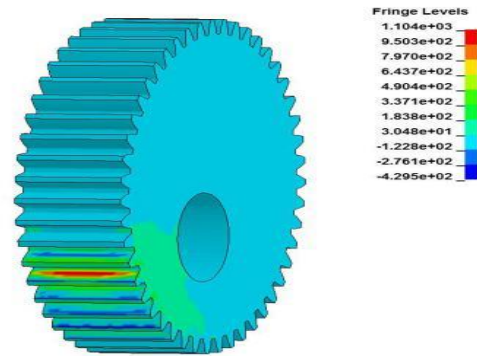


**Figure 3.** Elliptic contact area of elliptical cylindrical gear meshing

**Table 2** Maximum contact stress of gear

Time(s)	Stress( $\times 10^3$ Mpa)	Time(s)	Stress( $\times 10^3$ Mpa)
0.0079	1.104	0.029	0.9724
0.038	0.9005	0.049	0.7403
0.078	0.6217	0.083	0.6233

The data in Table 2 show that the maximum contact stress of tooth decrease with the change of meshing time. This is due to the fact that in the initial meshing stage, point contact is dominant, and the impact is large. When the contact form is changed from point contact to line contact, the meshing is stable, and the stress of tooth tends to be stable. In Figure3, the contact area of the tooth is elliptical. During meshing, the elliptical contact area will expand symmetrically from the middle section to both sides, and the maximum stress occurs at the middle section. The stress decreases gradually as the transition from the middle section to the two ends of the teeth. When the thickness of the two meshing teeth is the same, the distance between the boundary of the elliptical contact area and the end face of the gear is about 5%~10% of the thickness of the tooth. If the width of the two meshing teeth is different, the elliptical contact area of the gear with smaller width will be larger.

*3.2. Analysis of stress and strain in the direction of tooth lines at different speeds*

Literature [15] points out that the tooth profiles of a gear are generally composed of three parts: the top part, the root part and the working area. The working area of a non-cylindrical gear, represented by an elliptical cylindrical gear, is generally near the pitch curve. Therefore, in order to study the stress and strain distribution in the direction of the tooth lines, it is necessary to collect isometric data from the working area near the pitch curve of the tooth lines. The location of the data acquisition point is shown in Figure 4.

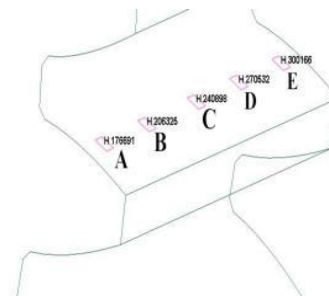


**Figure 4.** Data acquisition point of tooth surface

The increase of rotational speed will aggravate the wear and collision between teeth. In order to study the influence of rotational speed on the stress and strain distribution during meshing, the changing trends along the tooth lines under three conditions of rotational speed of 300r/min, 600r/min and 900r/min were obtained, as shown in Figure 5. The longitudinal coordinate  $\varepsilon_p$  represents the effective plastic strain,  $\sigma_c$  represents the effective stress, F represents the pressure on the tooth surface, and the abscissa represents the time.

It can be concluded from the analysis that the effective plastic strain at point C is the largest, followed by points B and D, and points A and E are the smallest under three rotating speeds. With the increase of rotational speed, the effective plastic strain and surface pressure at the center of the elliptical contact area of tooth surface are the largest,

and both decrease in varying degrees during the transition from the center position to both sides. With the increase of rotational speed, the increasing trend of C point is more obvious. At low speed, the two sides of the elliptical contact area in the direction of tooth lines are the largest, and the value of the elliptical contact area tends to decrease when it transits to the center area. When the rotational speed increases, the distribution law of the elliptical contact area in the center area is the largest and the transition area in the two sides decreases. The reason is that the meshing slip speed between the teeth is small at low speed, the stress and strain distribution in the micro contact area of the tooth surface is relatively concentrated and the numerical difference is small. At high speed, the slip velocity and wear between the teeth increase, and the stress-strain values differ greatly.

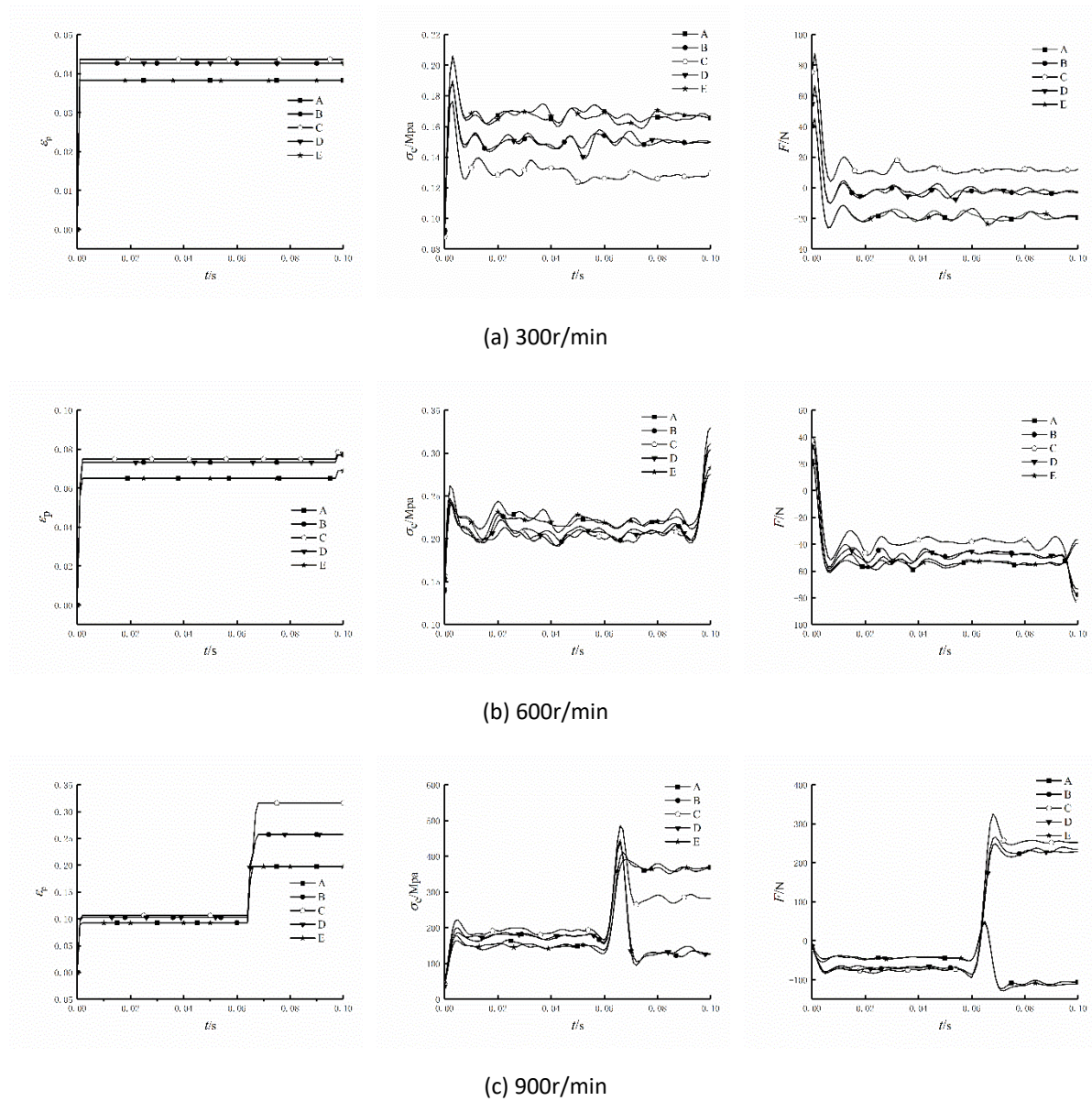
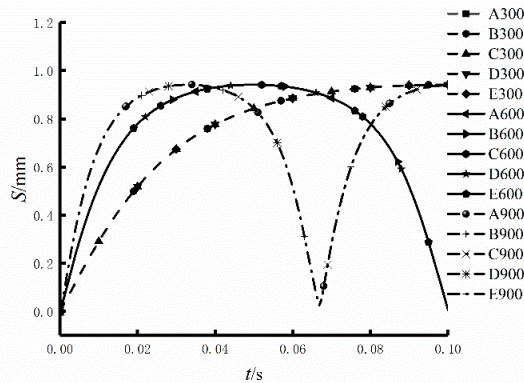


Figure 5. Comparison of stress and strain in the direction of gear line at different speeds

### 3.3. Variation of Tooth lines Directional Displacement at Different Speed

The above analysis shows that the effective plastic strain, effective stress and surface pressure will be different between data acquisition points under different rotational speeds on the same tooth surface. In order to study the displacement distribution of data acquisition points during gear meshing process, the variation trend of tooth lines direction displacement under three rotational speeds is obtained, as shown in Figure 6.



**Figure 6.** Variation trend of tooth lines displacement at different rotating speeds

In Figure 6, the displacements of five data points on the same tooth surface show the same distribution law under different rotational speeds. The maximum displacements are basically the same, but with the increase of rotational speeds, their periods change. In the meshing time of 0.2s, the driven wheels rotate 1 cycle, 2 cycle and 3 cycle respectively under three rotating speeds, so the

displacement curves in the figure 6 shows one cycle, two cycle and three cycle respectively, which indicates that the increase of rotating speed will affect the change period of tooth surface displacement, but the displacement of each point on the tooth surface will not change with the increase of rotating speed.

### 3.4. Stress and strain Analysis of Tooth profiles Direction at Different Rotational Speed

The variation trend of effective plastic strain, effective stress and surface pressure at the top of the tooth profiles, near the pitch curve and at the root of the tooth under different rotational speeds is shown in Figure 7. At 0.06s, the curves corresponding to the 900r/min rotation speed all appear sudden jump, and the effective stress and the pressure on the tooth surface near the pitch curve and the root of the tooth are impacted, which indicates that the meshing state of the tooth is not stable, and there will be noise and impact vibration. The reason is that the meshing period changes with the increase of rotational speed, and the effective plastic strain, effective stress and surface pressure of tooth increase sharply with the existence of meshing impact. But in this process, the curves are continuous and there is no interruption, which indicates that there is still a good contact characteristic between the teeth. With the increase of rotational speed, the effective plastic strain, effective stress and contact pressure at the top of the teeth, the vicinity of the pitch curve and the root of the teeth all tend to increase, which indicates that the contact condition of the gear is changing with the increase of the rotational speed. The increase of pressure and contact stress on the surface of tooth at high speed will aggravate the wear of the surface of tooth, so the plastic deformation will increase. When increases to a certain extent, the failure modes of tooth such as tooth surface gluing will occur, this is similar to that of standard cylindrical gears.

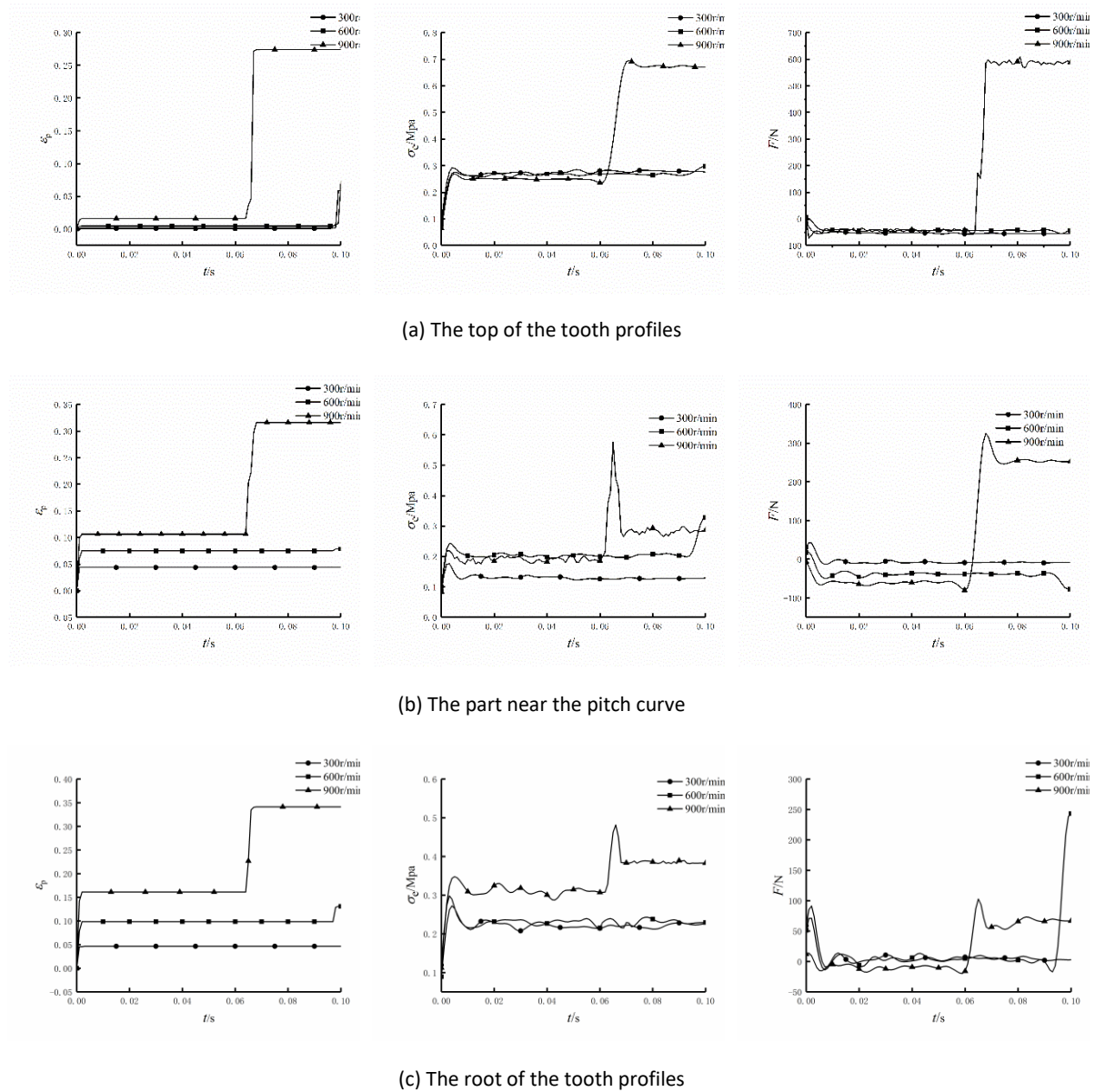


Figure 7. Stress and strain comparison of tooth profiles at different rotational speeds

3.5. Variation of meshing force of tooth at different rotational speeds

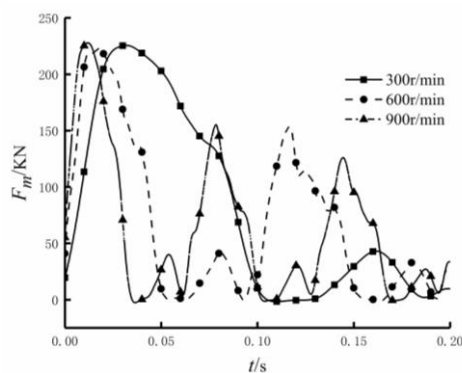


Figure 8. Trend of meshing force of tooth at different rotational speeds

Figure 8 shows that the maximum meshing force of tooth at three rotating speeds is 225.608 KN, 223.515 KN

and 226.300 KN, respectively, with little difference between them. Under three rotational speeds, the meshing force increases instantaneously due to the meshing impact between the teeth in the initial meshing stage, and then changes periodically when the meshing is stable. The meshing force curve is smooth at 300r/min. When the speed increases to 900r/min, the meshing force curve will have some impact, and the gear system will have vibration and noise. For the driven wheels rotate 1r, 2r and 3r when the speed is 300r/min, 600r/min and 900r/min, respectively. In the meshing process of 0.2s, the meshing speed of tooth is slower at low speed, the impact vibration is smaller, and the curve is smoother. In high speed, the meshing time of tooth decreases, and the instantaneous impact and the vibration increase. The meshing force curves will produce non-smooth phenomena, but the meshing force curve is always continuous and there is no interruption, which indicates that there is no separation of tooth and have a good contact characteristic.

#### 4. Conclusions

Aiming at the elliptical cylindrical gear pair, the LS-PREPOST software is used to simulate the dynamic meshing process of the tooth. The effective plastic strain, effective stress, surface pressure, displacement of the tooth lines and meshing force distribution of the tooth in the direction of tooth lines and tooth profiles at different rotational speeds are obtained.

1. The distribution of stress, strain and pressure in the direction of tooth lines will be affected by the speed of tooth. Along the direction of tooth lines, the effective plastic strain, effective stress and surface contact pressure in the center position of elliptical contact area are the largest and will decrease in varying degrees when the center position transits to both sides. The central part of elliptical contact area has the greatest wear. Therefore, the modification amount should be considered according to the meshing position, wear amount and load of the gear in the direction of tooth lines.
2. Along the tooth profiles direction of elliptical cylindrical gear, with the increase of rotational speed, the effective plastic strain, effective stress and surface contact pressure all tend to increase. The increase of rotational speed makes the meshing period of the tooth change, and the vibration and noise of the tooth will appear because of the meshing impact when the speed is large.
3. The rotation speed has a certain influence on the displacement of each data acquisition point in the tooth surface and the change period of the engagement force. The value of the engagement force will not change significantly with the increase in rotation speed. The engagement speed is slow at low speed, and the impact vibration is small. The engagement times decreases in high speed, and the wear impacts vibration between the gear surfaces increases, which will reduce the service life of gear. However, the meshing force curves of the three rotating speeds are continuous, which shows that the elliptical cylindrical gears have good contact performance under the three rotating speeds.
4. The analysis method and analysis process proposed in the article can be applied to the same type of non-cylindrical gears, which provides a new method for the subsequent study of the dynamic meshing characteristics of non-circular gears and the influence of working condition parameters on the meshing characteristics.

#### Conflicts of Interest

The authors declare that there are no conflicts of interests regarding the publication of this paper.

#### Acknowledgements

The research was supported by the National Natural Science Founding of China (No. 51765032)

#### Reference:

- [1] Vasie Marius, Andrei Laurenția. Analysis of noncircular gears meshing[J]. Mechanical testing and diagnosis, Vol.2,(2015).No.2,70-78.
- [2] Wang Yunzhi. Load contact analysis and strength calculation of spur gear.[J]. Journal of Mechanical transmission, (2016).No.3,74-77.
- [3] Chang Qinglin, Hou Li. Parallel Translating Mechanism Process-Oriented Mathematical Model and 3-D Model for Cylindrical Gears with Curvilinear Shaped Teeth.[J]. Jordan Journal of Mechanical and Industrial Engineering, Vol.10, (2016). No.3, 171-177.
- [4] Tang Qian, Jin Xiaofeng, Fan Qiulei. Parametric Coordination and Simulation Study on Nonstandard Spur Gears.[J]. Jordan Journal of Mechanical and Industrial Engineering, Vol.8, (2014). No.2, 50-55.
- [5] Ehsan Rezaei, Mehrdad Poursina, Mohsen Rezaei, Alireza Ariaei. A New Analytical Approach for Crack Modeling in Spur Gears.[J]. Jordan Journal of Mechanical and Industrial Engineering, Vol.13, (2019). No.2, 69-74.
- [6] Tang Jinyuan, Liu Xin, Dai Jin. Study on corner contact shock of gear transmission by Ansys/Ls-Dyna Software.[J]. Journal of vibration and shock, Vol.26, (2007). No.9, 40-44.
- [7] Liu Yanxue, Wang Jianjun, Zhang Tao. Dynamic meshing characteristics analysis of spur gears based on LS-DYNA.[J]. Journal of Beijing University of Aeronautics and Astronautics, Vol.42,(2016). No.10,2206-2213.
- [8] Sanchez-Marin Francisco, Iserte Jose L, Roda-Casanova Vctor. Numerical tooth contact analysis of gear transmission through the discretization and adaptive refinement of the contact surfaces[J]. Mechanism & Machine Theory, No.101, (2016). 75-94.
- [9] Wang Chen, Wang Shouren, Wang Gaoqi. A calculation method of tooth profiles modification for tooth contact analysis technology[J]. Journal of the Brazilian Society of Mechanical Sciences & Engineering, Vol. 40, (2018). No.7,340-349.
- [10] Chen Ruibo, Zhou Jianxing, Sun Wenlei. Dynamic characteristics of a planetary gear system based on contact status of the tooth surface[J]. Journal of mechanical science and technology, Vol.32, (2018). No.1, 69-80.
- [11] Zhang Huang. Digital tooth contact analysis of noncircular gear.[D]. Harbin Institute of Technology,2013.
- [12] Zhang Guohua. Analysis of meshing characteristics and carrying capacity of high order deformed elliptic gear.[D]. Hefei University of Technology, 2017.
- [13] Yao Wenxi. Non-circular Gear Design [M]. Beijing: Machinery Industry Press, 2012.
- [14] Wei Yongqiao, Ma Dengqiu, Wu Yang, et al. Study on the tooth surface and curvature characteristics of cylinder gear with variable hyperbolic arc tooth trace. Advanced Engineering Sciences, Vol49 (2017). No.6, 196-203.
- [15] Bair Bingwen. Tooth profiles generation and analysis of crowned elliptical gears[J]. Journal of mechanical design, Vol.7, (2009). No.131, 1-6.



# Systematic Approach for Selecting a Cleaning Method to Solar Panels Based on the Preference Selection Index Approach

Mohammed Said Obeidat\*, Esra'a Mohammad Al Abed Alhalim, Bilal Raif Melhim

*Department of Industrial Engineering, Jordan University of Science and Technology, PO Box 3030, Irbid 22110, Jordan*

*Received June 19 2019*

*Accepted August 8 2020*

## Abstract

Policymakers have become eager to move towards sustainability recently due to the growing costs of electricity and concerns about the environment. Environment friendly and economical energy sources, such as solar power, are being introduced at increasing rates. Photovoltaic (PV) panels are considered an important method of harnessing solar power. Although solar energy is one of the most efficient renewable and sustainable sources of energy, the accumulation of dust and debris on even one panel in a PV array reduces the efficiency of energy generation, thus highlighting the need to keep the surfaces of PV panels clean. Several methods can be used to clean PV panels, such as Heliotex technology, electrostatic cleaning, the use of self-cleaning glass, automatic cleaning and manual cleaning. The Preference Selection Index (PSI) multi-criteria decision-making approach is used in this study to compare these cleaning methods. Data were collected via a survey of solar energy experts in Jordan to enable a comparison of these cleaning methods, and several attributes were considered. After the initial PSI analysis, a follow-up sensitivity analysis was conducted that involved removing the cost attributes. The results showed that the best method was manual cleaning. The results of the sensitivity analysis confirmed that manual cleaning is the method most often preferred by experts.

© 2020 Jordan Journal of Mechanical and Industrial Engineering. All rights reserved

*Keywords: Energy; Cleaning; PV Panel; Multi-criteria Decision Making; Preference Selection Index;*

## 1. Introduction

Global demand for resources has been growing rapidly, which has created pressure on the manufacturing sector to generate new products and develop technologies. These requirements are reflected in the amount of the energy required. The world relies heavily on oil, which is expensive, and causes environmental problems, and is non-renewable. This combination of disadvantages has forced countries across the world to shift to new, alternative energy sources. Renewable sources of energy are those that are not depleted by continuous usage, do not contribute to environmental pollution in terms of greenhouse gases, and do not pose health hazards [1]. Renewable energy systems are an essential alternative energy choice and are considered the first step in the industrialized building system construction industry [2]. These energy sources, and especially solar, biomass and wind, are now playing an important role in the economics of energy production and are improving the quality of the environment [3]. Projects involving renewable energy, and especially photovoltaic (PV) systems, can result in crucial savings in terms of the energy consumed in a building [4]. Countries around the world have implemented plans to increase the share of

renewable energy sources and reduce greenhouse gas emissions [5].

Decision making and judgments are essential aspects of the average person's daily life. Human judgment has received considerable attention, both within and outside of the psychological sciences [6], [7], [8]. For some decisions, a single criterion may be the major focus of the decision makers, while other decisions are made based on multiple criteria simultaneously. Multi-criteria decision-making (MCDM) tools are used to evaluate candidate alternatives for the purpose of ranking, choosing or sorting based on a number of qualitative and/or quantitative criteria, and are associated with different measuring units [9]. Multi-criteria decision analysis can be applied to numerous types of complex decision. The Preference Selection Index (PSI) is one of the primary MCDM approaches that can help a decision maker to reach the optimal decision. Other MCDM approaches include the Analytic Network Process (ANP), Elimination and Choice Expressing Reality (ELECTRE), Technique for Order of Preference by Similarity to Ideal Solution (TOPSIS), grey theory and the Analytic Hierarchy Process (AHP).

This paper provides a systematic procedure for selecting the best cleaning method for PV panels, using an approach based on PSI. Experts in the field of solar energy were asked to voluntarily answer a survey that described the most

\* Corresponding author e-mail: msobeidat1@just.edu.jo

frequently used cleaning methods and included several attributes related to the cleaning of PV panels.

## 2. Literature Review

### 2.1 Solar Energy and the Cleaning of PV Panels

One of the largest challenges of the modern world involves how to meet the required demand for energy in a sustainable way [10]. This rise in energy demand is a result of the growing population and increases in prosperity levels [11]. Solar energy is considered one of the best alternatives of the various types of renewable energy sources which entails the conversion of the sun's rays into electrical energy. A solar or PV cell is a device that converts sunlight into electricity [12]. As the sun is the source of solar power, this form of electrical power is cleaner and less expensive than fossil fuels [13]. Solar cells are made from semiconducting materials, and to be able to absorb sunlight, these materials must have specific characteristics.

PV panels are currently the most widely used renewable energy source. There are several factors that can significantly affect the maximum efficiency of a PV installation, including the geographic location (latitude and solar insolation) and the design of the installation (tilt angle, altitude and orientation). Other factors can also significantly affect the performance (efficiency), such as the accumulation of dust and debris [14]. Mani and Pilli (2010) studied the impact of dust on PV systems; they identified various factors responsible for the settling of dust on PV panels, and suggested some solutions to reduce this accumulation [14].

There are two key cost drivers related to the use of PV cells that affect all stakeholders: the efficiency and the degradation rate [15]. The efficiency of a PV cell refers to the conversion of sunlight into electrical power, and concerns how this relationship evolves over time, while the degradation rate is a quantification of how the electrical power declines over time [15]. The latter is extremely important, as a higher degradation rate means that a lower level of power is produced, thus reducing future cash flows [16].

The conversion efficiency of a solar cell is defined as the percentage of the solar energy falling onto a PV device that is converted into electricity [17]. This efficiency is one of the main factors that can affect the selection process of a type of solar cell. Most of the sunlight that reaches a PV cell is lost rather than converted into electricity [17]. Several factors can affect the conversion efficiency, including the wavelength, recombination, temperature and reflection. These factors must be considered when designing a PV system to achieve higher efficiencies.

In any PV installation, the engineers focus on the design (tilt angle, altitude and structure) in order to harvest the maximum solar radiation. However, they may overlook the practicalities of a site, such as the deposition of dust, water, salt, or bird droppings [14]. These phenomena, when combined with losses in wires and inverters, can reduce the efficiency of a module by 10–25% [14].

Dust is defined as a solid particle with a diameter less than 500  $\mu\text{m}$ . It is generated in the atmosphere from different sources, such as wind, vehicular movement, pollution and volcanic eruption. The accumulation of dust

on PV panels is characterized by two important factors that influence each other: the properties of the dust (such as its size, weight, shape, chemical and biological properties and electrostatic properties), and the local environment (such as human activities, environmental characteristics including the orientation and height of the installation, and weather conditions) [14].

Mani and Pillai (2010) performed a study that had two phases. In phase one, they primarily studied the impacts of the characteristics of solar systems, such as the tilt angle and glazing, on dust accumulation. In phase two, they studied the effects of dust deposition via an experimental investigation. They suggested several solutions to the problem of dust on solar panels in relation to the geography of the installation; for example, dry tropical regions with temperature ranges of 20–49°C, annual precipitation greater than 150 cm and in latitude ranges of 15–25° north and south are prone to dusty desert environments and dust storms, and PV systems in these areas should be cleaned at a minimum of weekly.

Appels et al. (2013) studied the effects of dust settlement on PV modules that are installed at an optimal tilt angle with regular rainfall in Belgium. Their methodology was as follows: (i) a spectrometer was used to examine the relationship between the decrease in transmittance and the decrease in the output power of a PV module; (ii) a scanning electron microscope was used to examine dust samples; (iii) several prototype coatings were introduced to determine whether they reduced the power loss of the output; and (iv) the effects of dry residue on PV modules were studied [18]. The results showed that the accumulation of dust on PV modules in Belgium was responsible for consistent power losses in the range 3–4% after dust saturation over three or four weeks. Rainfall had a limited effect on power losses for small dust particles (2–10  $\mu\text{m}$ ), but had a better effect in terms of washing away large dust particles. A special coating was shown to be a solution for this issue, although it was not cost-effective [18]. Appels et al. (2013) also suggested regular cleaning with soft tap or demineralized water.

The use of hydrophobic coatings on photovoltaic modules is another method of cleaning them [19]. High temperatures and dust storms are the most frequent factors that reduce the maximum performance of PV modules in Middle East and North Africa [19]. These can reduce the maximum output power by 16.2% and the short-circuit current ( $I_{sc}$ ) by 6.6% [19]. In addition, dust settlement on PV modules induces a hotspot phenomenon, which increases the temperature of the PV module, thus reducing its efficiency. Fathi et al. (2017) applied a self-cleaning hydrophobic nano-coating to a PV module and measured its output performance. They found that the hydrophobic coating, which was a cost-effective method, increased light transmittance and reduced the temperature of the PV module, meaning that the output power losses were reduced [19].

Moharram et al. (2013) studied the effect of cleaning PV modules using a non-pressurized water system and a surfactant. Their objective was to remove dust from PV modules using these two methods, as they are the least costly and the most energy-efficient approaches. The experiment used a 14 kW PV system and consisted of three stages: no cleaning; cleaning with non-pressurized water;

and cleaning with anionic and cationic surfactants. They found that the accumulation of dust on PV modules (i.e. no cleaning) significantly reduced the efficiency, the non-pressurized water system was insufficiently strong to improve the efficiency of the PV modules compared to regular water, and a mixture of anion and cation surfactants was the best method of removing dust sticking to the modules [20].

A superhydrophobic and water-repellent coating offers a further method of self-cleaning for PV panels. Park et al. (2011) studied a micro-shell array that was fabricated on transparent and flexible polydimethylsiloxane (PDMS) layers. This method was compared to a non-superhydrophobic coating on PV modules. The results showed that this was an excellent water repellent, and lower dust accumulation was seen for a superhydrophobic PDMS at a contact angle that was higher than  $150^\circ$ , with a hysteresis level of less than  $20^\circ$  [21].

Chaichan et al. (2015) studied the effects of pollution and cleaning on PV modules in Baghdad, Iraq. Their experiment was conducted in outdoor conditions in order to investigate the impact of air traffic pollution on highways on the performance of PV panels. Three polycrystalline panels were installed at a tilt angle of  $30^\circ$  towards the south. Natural cleaning conditions, such as rain and wind were the main cleaning methods for the first panel, while the second panel was designed to collect pollutants such as dust, bird droppings and to preserve them by being covered during cloudy and rainy weather. The third panel was cleaned by alcohol with 99% purity before each measurement was taken. The experiment was conducted for a period of two months during the winter. The results showed that the cleaned panel had an average efficiency of 4.82%, the naturally cleaned panel 3.233%, and the polluted panel 1.749% [22]. The second phase of the study by Chaichan et al. (2015) involved evaluating the best cleaning method for PV panels. The same polycrystalline panels were tested for two further months. The first panel was cleaned with deionized distilled water, the second was cleaned with alcohol and the third with sodium surfactant. The results showed a reduction in the efficiency of the PV panels of about 0.1% for alcohol, less than 1% for sodium surfactant and about 14% for deionized distilled water. Distilled water failed to clean the PV panels due to the small particles, and especially nano-scale carbon, that were stuck to them [22].

Sayyah et al. (2015) introduced a new cleaning method to reduce soiling of a PV module using an electrodynamic screen (EDS) in an environmentally-controlled test chamber. The EDS system was composed of two stacked layers of transparent dielectric coating, which covered the PV glass. The results showed that 90% of  $I_{sc}$  was restored from its original value after several cycles, which enhanced the efficiency of the module. However, coagulations of dust were observed on some PV surfaces after using the EDS method. The authors stated that this dust coagulation was acceptable because its availability, the PV module can use the light scattered from dust particles [23].

Biris et al. (2004) studied the effect of removing dust particles from a PV module using an EDS. Their experiment involved applying an AC signal to a shield consisting of parallel wires. The electrodes were embedded into a polymer film to prevent any spark between them. A wide range of amplitudes and frequencies was applied, and it was

found that the EDS was able to remove dust particles and prevent them from re-accumulating; however, this depended on the amplitude and frequency of the voltage. The researchers concluded that increasing the amplitude of the voltage led to greater removal of dust particles, and that the 5–15 Hz frequency range was optimal [24].

## 2.2 Multi-criteria Decision Making

MCDM aims to assist decision makers in selecting the best option from many feasible alternatives [25]. MCDM approaches are designed to identify the most preferred alternative by grouping the available alternatives into a limited number of categories and ranking these alternatives in order of preference. MCDM approaches have been used in a wide range of areas according to the nature of the decisions to be made. Examples of MCDM approaches include PSI, AHP, ANP, ELECTRE, TOPSIS and grey theory. The aim of these widely used decision-making approaches is to break complex decisions down into smaller parts, which can be analyzed separately and then recombined into a weighted score [26]. The following is a brief description of the most commonly used MSDM approaches.

The ANP method is used in models with clear dependencies. It is a general class of decision-making approaches that deals with complex interdependencies among different attributes or elements [27], [28]. It provides a framework for dealing with decisions without the need for assumptions about the interdependence between elements at higher and lower levels, or between elements at the same level [29], [30]. The ANP method uses a network rather than a hierarchy of different levels [29], [30]. It has been applied to decisions in fields, such as product design, equipment replacement, and energy policy planning [31]. ANP has also been applied in the evaluation and selection of projects [32], supply chain management [33], performance management [34], environmental issues [35], strategy selection [36] and manufacturing systems [37]. If there are dependencies between the criteria, a fuzzy ANP might be a good choice [38].

ELECTRE methods (I, II, III, IV, IS, and TRI) have been chosen as the best methods by pairwise comparison of alternatives within the decision problem [9]. Examples of studies that have used ELECTRE methods include evaluating an action plan for the diffusion of renewable energy technologies at a regional scale [39], supporting decision makers with different value systems [40], solid waste management [41], choosing materials under weighting uncertainty [42] and the planning of water resources [43].

Grey theory is one of the MCDM approaches used to study the uncertainty of systems, and is a superior approach that can provide a mathematical analysis of systems with uncertain information [44], [45], [46]. In this theory, a system is referred to as 'white' if its information is known completely, 'black' if its information is unknown, and 'grey' if it is partially known [46]. Researchers have used grey theory in several fields, for example in medicine [47], economics [48], supplier selection [46], the environment [49] and airline networks [50].

AHP is an appropriate approach for decisions under conditions of certainty, where a judgment is quantified

using a systematic procedure and used as a base for making an optimal decision [51]. It is a structured technique that applies both psychology and mathematics to make complex decisions [52]. The priority levels of the decision criteria are evaluated and determined [53], and complex decisions are made by quantifying non-numeric factors related to the decision, such as the ideas, emotions, feelings, expectations, etc. of people involved in the decision [51]. A pairwise comparison matrix is constructed for all the factors considered in the decision process [54]. There are four main components of an AHP model that enable a decision to be made in a structured manner and to enhance the process of generating priorities [55]. These components are: (i) the definition of the decision problem; (ii) the construction of a decision hierarchy; (iii) the construction of pairwise comparison matrices; and (iv) the use of the priorities computed from the comparison matrices to weight the priorities of the elements [55]. Over 150 applications of the AHP approach are available, and these can be categorized into 10 areas: allocation, selection, benefit-cost, evaluation, development and planning, ranking and priority, forecasting, decision making, medicine and quality function deployment [56]. One example of the application of AHP in the solar energy sector is the research reported in [57], which investigated the connection between regional factors and the attractiveness of investing in the production of solar energy.

The TOPSIS approach is a straightforward one that generates two alternative solutions: a positive ideal solution and a negative one. In TOPSIS, the selected alternative must simultaneously have the minimum geometric distance from the positive ideal solution and the maximum geometric distance from the negative ideal solution [58], [59], [60]. A decision matrix and a normalized decision matrix are constructed using accurate scores that each alternative receives from all criteria [60]. The negative and positive ideal solutions are found by considering all attribute rates. The order of preference of the alternatives is determined by comparing the distance coefficient of each alternative. Applications of TOPSIS include financial investment decisions such as highway buses outranking [61], [62], identifying new active investment opportunities [63], operations management, for example in decision problems related to supplier selection in the manufacturing industry [64], the selection of production processes for semiconductors [65] or the selection of material for metallic bipolar plates for a polymer electrolyte fuel cell [66], water management [67] and evaluating the service quality of public transportation [68].

The PSI method is a direct decision-making method that requires fewer and simpler calculations than the other MCDM approaches [69]. This approach relies on statistical concepts without the need to weight the considered attributes [27]. The methodology consists of defining the problem goal, formulating a decision matrix of alternatives and criteria, normalizing the decision matrix, computing the preference variation value, determining the overall preference value, obtaining the preference selection index and ranking alternatives in ascending or descending order to facilitate the interpretation of results [70].

2.1.1. PSI Details

PSI is a new approach that was proposed in [70]. Unlike other MCDM methods, this technique does not require the user to give an importance between attributes. A PSI value is calculated for each alternative, where the best alternative is the one with the highest value. This method can be illustrated using the following steps [70]:

- Step I: Identification of the objective and determination of all possible criteria and the measures and alternatives to be studied.
- Step II: Formulation of the decision matrix. Let A be a set of alternatives, where  $A = \{A_i \text{ for } i = 1, 2, 3, \dots, n\}$ , C a set of decision criteria where  $C = \{C_j \text{ for } j = 1, 2, 3, \dots, m\}$  and  $X_{ij}$  the performance of alternative  $A_i$  when it is studied with criterion  $C_j$ . As a result, a decision matrix can be created as shown in Table 1.

Table 1. Decision matrix  $X_{ij}$

Alternatives ( $A_i$ )	Criteria ( $C_j$ )				
	$C_1$	$C_2$	$C_3$	...	$C_m$
$A_1$	$X_{11}$	$X_{12}$	$X_{13}$	...	$X_{1m}$
$A_2$	$X_{21}$	$X_{22}$	$X_{23}$	...	$X_{2m}$
$A_3$	$X_{31}$	$X_{32}$	$X_{33}$	...	$X_{3m}$
...	...	...	...	...	...
$A_n$	$X_{n1}$	$X_{n2}$	$X_{n3}$	...	$X_{nm}$

- Step III: Normalization of data, i.e. transforming the values in the decision matrix to the range 0–1. In the case of a positive expectancy (i.e. profit), the normalization formula will be as follows:

$$R_{ij} = \frac{X_{ij}}{X_j^{max}}, \tag{1}$$

while for a negative expectancy (i.e. cost) the normalization formula is:

$$R_{ij} = \frac{X_j^{min}}{X_{ij}}, \tag{2}$$

where  $X_{ij}$  are the attribute measures ( $i = 1, 2, 3, \dots, N$  and  $j = 1, 2, 3, \dots, M$ ) in the decision matrix.

- Step IV: Calculation of the preference variation value ( $PV_j$ ), which is determined for each attribute using the following equation:

$$PV_j = \sum_{i=1}^N [R_{ij} - \bar{R}_j]^2, \tag{3}$$

where  $\bar{R}_j$  is the mean of the normalized value of attribute  $j$  and is calculated as follows:

$$\bar{R}_j = \frac{1}{N} \sum_{i=1}^N R_{ij}. \tag{4}$$

- Step V: Computation of the deviation ( $\Phi$ ) in the preference value ( $PV_j$ ) for each attribute, using the following equation:

$$\Phi = 1 - PV_j. \tag{5}$$

- Step VI: Computation of the overall preference value ( $\Psi$ ) for each attribute as follows:

$$\Psi_j = \frac{\Phi_j}{\sum_{j=1}^M \Phi_j}. \tag{6}$$

The overall summation of the preference value of all attributes must give a value of one.

- Step VII: Computation of the preference selection index (Ii) using the following equation:

$$I_i = \sum_{j=1}^M (R_{ij} \times \Psi_j). \tag{7}$$

- Step VIII: Finally, alternatives are ranked based on the Ii value, where alternatives with the highest value are selected first.

### 3. Methodology

The main objective of this paper was to compare the most widely used methods of cleaning PV panels. The PSI MCDM approach was used to find the optimum cleaning method based on certain attributes. Five cleaning methods were compared: Heliotex technology (automatic cleaning and washing without using brushes), electrostatic cleaning, self-cleaning glass (nano-coating), automatic cleaning (by robot, dry or wet wipers and water spray) and manual cleaning (by water spray, dry or wet wipers and rotary brushes). Several relevant criteria were considered in the PSI, including the cleaning time, initial cost, running cost, efficiency, time between cleanings and safety. Data were collected via a survey that was distributed in interview format to PV experts in Jordan. The PSI method was applied twice, in two phases. In the first phase, all the abovementioned criteria were considered in a comparison of the five different cleaning methods, while in the second phase, the cost attributes were removed, and a sensitivity analysis was carried out.

### 4. Data

Data on the cleaning methods were collected using a survey of Jordanian experts in the field of solar energy. The average of the responses was considered for the PSI analysis, as shown in Table 2, which contains the decision matrix of the PSI.

### 5. Results and Discussion

In this section, the eight steps of the PSI method described in Section 2.2.1 are applied. Table 2 shows the decision matrix for selecting the most preferred cleaning method based on the PSI approach. The data in the decision matrix were normalized as shown in Table 3, following Step

III in Section 2.2.1. In this step, the cells representing the initial cost and the running cost were normalized using Equation 2, by dividing the minimum value in each column of the decision matrix by the value in each cell of the decision matrix in the corresponding column. This was not the case for the data normalization in the remaining columns of the decision matrix; each cell in these columns was divided by the maximum value in the corresponding column using Equation 1. The mean of each attribute ( $\bar{R}_j$ ) was calculated as shown in Table 3, by taking the average of all the normalized values in each column using Equation 4.

Table 4 summarizes the following quantities for each attribute: (i) the preference variation value (PVj), calculated based on Equation 3; (ii) the deviation ( $\Phi$ ) in the preference value (PVj), calculated based on Equation 5; and (iii) the overall preference value ( $\Psi$ ), calculated based on Equation 6.

**Table 2.** Responses collected from PV experts (decision matrix)

Alternatives (cleaning methods)	Attributes					
	Cleaning time	Initial cost	Running cost	Efficiency	Time between cleanings	Safety
Heliotex technology	6.33	6	5.33	5.67	5	5
Electrostatic cleaning	5.5	9	6.67	5.33	5.5	6.33
Self-cleaning glass (nano-coating)	4.5	9	4	6.67	4.5	8
Automatic cleaning (robot, dry or wet wipers and water spray)	7.33	7.67	6.67	7	5.33	6.67
Manual cleaning	8.33	4	7	7.33	5.67	5.33

**Table 3.** Normalized data

Alternatives (cleaning methods)	Attributes					
	Cleaning time	Initial cost	Running cost	Efficiency	Time between cleanings	Safety
Heliotex technology	0.7599	0.6667	0.7505	0.7735	0.8818	0.6250
Electrostatic cleaning	0.6603	0.4444	0.5997	0.7272	0.9700	0.7913
Self-cleaning glass (nano-coating)	0.5402	0.4444	1.0000	0.9099	0.7937	1.0000
Automatic cleaning (robot, dry or wet wipers and water spray)	0.8799	0.5215	0.59970015	0.9549	0.9400	0.8338
Manual cleaning	1.0000	1.0000	0.5714	1.0000	1.0000	0.6663
$\bar{R}_j$	0.7681	0.6154	0.7043	0.8731	0.9171	0.7833

**Table 4.** Values of PVj,  $\Phi$  and  $\Psi$  for each attribute

Measures	Attributes					
	Cleaning time	Initial cost	Running cost	Efficiency	Time between cleanings	Safety
PVj	0.12992	0.21781	0.12911	0.05538	0.02668	0.08833
$\Phi$	0.87009	0.78219	0.87089	0.94462	0.97332	0.91167
$\Psi_j$	0.16255	0.14613	0.16270	0.17647	0.18183	0.17032

Table 5 shows the last step in the PSI calculations in which the index ( $I_i$ ) was calculated for each alternative using Equation 7. Table 5 shows that the maximum  $I_i$  value was achieved for manual cleaning (0.40807), followed by Heliotex technology (0.34928), self-cleaning glass (nano-coating) (0.32647), automatic cleaning (0.31853) and then electrostatic cleaning (0.27412). The maximum value indicates the most preferred alternative, i.e. manual cleaning in this case.

## 6. Sensitivity Analysis

In this section, the PSI method was applied again to compare the five cleaning techniques with same attributes as used in the first PSI calculations; however, in this case, the attributes related to the cost of the cleaning method (the initial cost and the running cost) were removed to ensure that the decision was not biased. This experiment was conducted in order to compare only the techniques themselves. Table 6 shows the last step of the PSI calculation for the purposes of sensitivity analysis, in which the index ( $I_i$ ) is calculated for each alternative after removing the cost-related attributes. The maximum value of  $I_i$  is still found for manual cleaning, followed by automatic cleaning, Heliotex technology, electrostatic cleaning and then by self-cleaning glass (nano-coating).

## 7. Conclusions

In this paper, five methods of cleaning PV panels were compared, based on six attributes of these cleaning techniques. The cleaning methods were Heliotex technology, electrostatic cleaning, self-cleaning glass

(nano-coating technique), automatic cleaning (robot, dry or wet wipers and water spray) and manual cleaning. The attributes considered here were the cleaning time, initial cost, running cost, efficiency, time between cleanings and safety. The PSI MCDM technique was used as a novel tool to evaluate the cleaning methods. Solar energy experts in Jordan were asked to fill in a survey, and their judgments were used as input to the PSI approach.

The results of the PSI method indicated that the most suitable cleaning technique was manual cleaning, followed by Heliotex technology, self-cleaning glass (nano-coating), automatic cleaning and then electrostatic cleaning. A sensitivity analysis was conducted to measure the efficiency of the PSI approach when some attributes were removed. The two attributes related to the cost of the cleaning method (the initial and running costs) were removed, and the new results showed that manual cleaning remained the best cleaning method, followed by automatic cleaning, Heliotex technology, electrostatic cleaning and then by self-cleaning glass (nano-coating).

## 8. Limitations

The data used in this paper were collected from solar energy experts in Jordan. This means that the results may be influenced by conditions in Jordan, such as the weather, temperature, humidity, customs, man hour rate, technology level, etc. Hence, the criteria considered here, and the respective opinions of these experts may vary with differences in conditions related to the country, the cost of technology, and other factors. The results from this paper can therefore be applied in other countries, taking into consideration their local conditions.

**Table 5.** Computation of the preference selection index ( $I_i$ )

Alternatives (cleaning methods)	Attributes						$I_i$
	Cleaning time	Initial cost	Running cost	Efficiency	Time between cleanings	Safety	
Heliotex technology	0.1235	0.0974	0.1221	0.00175	0.00023	0.00427	<b>0.34928</b>
Electrostatic cleaning	0.1073	0.0650	0.0976	0.00376	0.00051	0.00001	<b>0.27412</b>
Self-cleaning glass (nano-coating)	0.0878	0.0650	0.1627	0.00024	0.00277	0.00800	<b>0.32647</b>
Automatic cleaning (robot, dry or wet wipers, water spray)	0.1430	0.0762	0.0976	0.00118	0.00010	0.00043	<b>0.31853</b>
Manual cleaning	0.1625	0.1461	0.0930	0.00284	0.00125	0.00233	<b>0.40807</b>

**Table 6.** PSI ( $I_i$ ) for sensitivity issues

Alternatives (cleaning methods)	Attributes				$I_i$
	Cleaning time	Efficiency	Time between cleanings	Safety	
Heliotex technology	0.1787	0.0025	0.00033	0.006171	<b>0.1877</b>
Electrostatic cleaning	0.1553	0.0054	0.00074	0.000016	<b>0.1615</b>
Self-cleaning glass (nano-coating)	0.1271	0.0005	0.00401	0.011577	<b>0.1430</b>
Automatic cleaning by (robot, dry or wet wipers and water spray)	0.2070	0.0017	0.00014	0.000628	<b>0.2094</b>
Manual cleaning	0.2352	0.0041	0.00181	0.003373	<b>0.2445</b>

## References

- [1] G. Boyle, *Renewable Energy: Power for Sustainable Future*, 3rd ed., United Kingdom: Oxford University, 2004.
- [2] B. Hassan and M. Beshara, "Using Renewable Energy Criteria for Construction Method Selection in Syrian Buildings," *Jordan Journal of Mechanical and Industrial Engineering*, vol. 13, no. 2, pp. 125-130, 2019.
- [3] A. Herzog, T. Lipman, J. Edwards and D. Kammen, "Renewable Energy: A Viable Choice," *Environment: Science and Policy for Sustainable Development*, vol. 43, no. 10, pp. 8-20, 2001.
- [4] M. Al-Widyan, I. Soliman, A. Alajlouni, O. Al Zu'bi and A. Jaradat, "Energy Performance Assessment of a Non-domestic Service Building in Jordan," *Jordan Journal of Mechanical and Industrial Engineering*, vol. 12, no. 2, pp. 69-75, 2018.
- [5] M. Bürer and R. Wüstenhagen, "Which Renewable Energy Policy is a Venture Capitalist's Best Friend? Empirical Evidence from a Survey of International Cleantech Investors," *Energy Policy*, vol. 37, no. 12, pp. 4997-5006, 2009.
- [6] N. H. Anderson, "Functional Measurement and Psychophysical Judgment," *Psychophysical Review*, vol. 77, no. 3, pp. 153-170, 1970.
- [7] R. M. Dawes, "A Case Study of Graduate Admissions: Application of Three Principles of Human," *American Psychologist*, vol. 26, no. 2, pp. 180-188, 1971.
- [8] J. Louviere, "Predicting the Evaluation of Real Stimulus Objects From Abstract Evaluation of Their Attributes: The Case of Trout Streams," *Journal of Applied Psychology*, vol. 59, no. 5, pp. 572-577, 1974.
- [9] T. Özcan, N. Çelebi and S. Esnaf, "Comparative Analysis of Multi-criteria Decision Making Methodologies and Implementation of a Warehouse Location Selection Problem," *Expert Systems with Applications*, vol. 38, pp. 9773-9779, 2011.
- [10] I. Dincer and C. Acar, "A Review on Clean Energy Solutions for Better Sustainability," *International Journal of Energy Research*, vol. 39, no. 5, pp. 585-606, 2015.
- [11] J. Lange, J. Hilgedieck and M. Kaltschmitt, "Renewable Resources of Energy for Electricity Generation-Development Trends and Necessities Within the Overall Energy System," *Jordan Journal of Mechanical and Industrial Engineering*, vol. 13, no. 3, pp. 207-220, 2019.
- [12] O. o. E. E. a. R. Energy, "Solar Photovoltaic Technology Basics," 2013. [Online]. Available: <https://energy.gov/eere/solar/articles/solar-photovoltaic-technology-basics>. [Accessed 28 January 2018].
- [13] A. Herzog, T. Lipman, J. Edwards and D. Kammen, "Renewable Energy: A Viable Choice," *Environment: Science and Policy for Sustainable Development*, vol. 43, no. 10, pp. 8-20, 2001.
- [14] M. Mani and R. Pillai, "Impact of Dust on Solar Photovoltaic (PV) Performance: Research Status, Challenges and Recommendations," *Renewable and Sustainable Energy Reviews*, vol. 14, no. 9, pp. 3124-3131, 2010.
- [15] D. Jordan and S. Kurtz, "Photovoltaic Degradation Rates: An Analytical Review," National Renewable Energy Laboratory, Golden, CO, United States, 2012.
- [16] W. Short, D. Packey and T. Holt, "A Manual for the Economic Evaluation of Energy Efficiency and Renewable Energy Technologies," National Renewable Energy Laboratory, Golden, Colorado, United States, 1995.
- [17] O. o. E. E. & R. Energy, "Solar Performance and Efficiency," 2013. [Online]. Available: <https://energy.gov/eere/solar/articles/solar-performance-and-efficiency>. [Accessed 6 2 2018].
- [18] R. Appels, B. Lefevre, B. Herteleer, H. Goverde, A. Beerten, R. Paesen, K. De Medts, J. Driesen and J. Poortmans, "Effect of Soiling on Photovoltaic Modules," *Solar Energy*, vol. 96, pp. 283-291, 2013.
- [19] M. Fathi, M. Abderrezek and M. Friedrich, "Reducing Dust Effects on Photovoltaic Panels by Hydrophobic Coating," *Clean Technologies and Environmental Policy*, vol. 19, no. 2, pp. 577-585, 2017.
- [20] K. Moharram, M. Abd-Elhady, H. Kandil and H. El-Sherif, "Influence of Cleaning Using Water and Surfactants on the Performance," *Energy Conversion and Management*, vol. 68, pp. 266-272, 2013.
- [21] Y. Park, H. Im, M. Im and Y. Choi, "Self-cleaning Effect of Highly Water-repellent Microshell Structures for Solar Cell Applications," *Journal of Materials Chemistry*, vol. 21, no. 3, pp. 633-636, 2011.
- [22] M. T. Chaichan, B. Mohammed and H. Kazem, "Effect of Pollution and Cleaning on Photovoltaic Performance Based on Experimental Study," *International Journal of Scientific and Engineering Research*, vol. 6, no. 4, pp. 594-601, 2015.
- [23] A. Sayyah, M. Horenstein and M. Mazumder, "Performance Restoration of Dusty Photovoltaic Modules Using Electrodynamic Screen," New Orleans, LA, 2015.
- [24] A. Biris, D. Saini, P. Srirama, M. Mazumder, R. Sims, C. Calle and C. Buhler, "Electrodynamic Removal of Contaminant Particles and its Applications," Seattle, Washington, 2004.
- [25] T. Erden and M. Z. Coskun, "Multi-criteria Site Selection for Fire Services: The Interaction with Analytic Hierarchy Process and Geographic Information Systems," *Natural Hazards and Earth System Sciences*, vol. 10, pp. 2127-2134, 2010.
- [26] R. Al-Aomar, "A Combined AHP-Entropy Method for Deriving Subjective and Objective Criteria Weights," *International Journal of Industrial Engineering: Theory, Applications and Practice*, vol. 17, no. 1, pp. 12-24, 2010.
- [27] R. Attri and S. Grover, "Application of Preference Selection Index Method for Decision Making Over the Design Stage of Production System Life Cycle," *Journal of King Saud University – Engineering Sciences*, vol. 27, pp. 207-216, 2015.
- [28] H. Abu Qdais and H. Alshraideh, "Selection of Management Option for Solid Waste from Olive Oil Industry Using the Analytical Hierarchy Process," *Journal of Material Cycles and Waste Management*, vol. 18, pp. 177-185, 2016.
- [29] T. Saaty, "Fundamentals of the Analytical Network Process," Kobe, Japan, 1999.
- [30] T. L. Saaty and L. G. Vargas, *Decision Making with the Analytic Network Process: Economic, Political, Social and Technological Applications with Benefits, Opportunities, Costs and Risks*, New York: Springer, 2006.

- [31] J. Sarkis, "Evaluating Environmentally Conscious Business Practices," *European Journal of Operational Research*, vol. 107, no. 1, pp. 159-174, 1998.
- [32] L. Meade and J. Sarkis, "Analyzing Organizational Project Alternatives for Agile Manufacturing Processes: An Analytical Network Approach," *International Journal of Production Research*, vol. 37, no. 2, pp. 241-261, 1999.
- [33] L. Meade and J. Sarkis, "Strategic Analysis of Logistics and Supply Chain Management Systems Using the Analytical Network Process," *Transportation Research Part E: Logistics and Transportation Review*, vol. 34, no. 2, pp. 201-215, 1998.
- [34] M. Yurdakul, "Measuring Long-term Performance of a Manufacturing Firm Using the Analytic Network Process (ANP) Approach," *International Journal of Production Research*, vol. 41, no. 11, pp. 2501-2529, 2003.
- [35] A. Güngör, "Evaluation of Connection Types in Design for Disassembly (DFD) Using Analytic Network Process," *Computers and Industrial Engineering*, vol. 50, no. 1-2, pp. 35-54, 2006.
- [36] G. Büyüközkan, C. Kahraman and D. Ruan, "A Fuzzy Multi-criteria Decision Approach for Software Development Strategy Selection," *International Journal of General Systems*, vol. 30, no. 2-3, pp. 259-280, 2004.
- [37] D. Tesfamariam and B. Lindberg, "Aggregate Analysis of Manufacturing Systems Using System Dynamics and ANP," *Computers & Industrial Engineering*, vol. 49, no. 1, pp. 98-117, 2005.
- [38] O. Yilmaz, B. Oztaysi, M. Durmusoglu and S. Oner, "Determination of Material Handling Equipment for Lean In-Plant Logistics Using Fuzzy Analytical Network Process Considering Risk Attitudes of the Experts," *International Journal of Industrial Engineering: Theory, Applications and Practice*, vol. 24, no. 1, pp. 81-122, 2017.
- [39] M. Beccali, M. Cellura and M. Mistretta, "Decision-making in Energy Planning. Application of the ELECTRE Method at Regional Level for the Diffusion of Renewable Energy Technology," *Renewable Energy*, vol. 28, no. 13, p. 2063-2087, 2003.
- [40] J. C. Lopez and E. Gonzalez, "A New Method for Group Decision Support Based on ELECTRE III Methodology," *European Journal of Operational Research*, vol. 148, pp. 14-27, 2003.
- [41] M. Rogers and M. Bruen, "A New System for Weighting Environmental Criteria For use within ELECTRE III," *European Journal of Operational Research*, vol. 107, no. 3, pp. 552-563, 1998.
- [42] A. Shaniya, A. Milanib, C. Carsona and R. Abeyaratne, "A New Application of ELECTRE III and Revised Simos' Procedure for Group Material Selection under Weighting Uncertainty," *Knowledge-Based Systems*, vol. 21, no. 7, p. 709-720, 2008.
- [43] P. A. Raj, "Multicriteria Methods in River Basin Planning: A Case Study," *Water Science and Technology*, vol. 31, no. 8, pp. 261-272, 1995.
- [44] D. Ju-Long, "Control Problems of Grey Systems," *Systems & Control Letters*, vol. 1, no. 5, pp. 288-294, 1982.
- [45] J. Deng, "Introduction to Grey System Theory," *The Journal of Grey System*, vol. 1, no. 1, pp. 1-24, 1989.
- [46] G. Li, D. Yamaguchi and N. M., "A Grey-based Decision-making Approach to the Supplier Selection Problem," *Mathematical and Computer Modelling*, vol. 46, p. 573-581, 2007.
- [47] H. Wei, .. Lin, Y. Zhang, L. Wang and Q. Chen, "Research on the Application of Grey System Theory in the Pattern Recognition for Chromatographic Fingerprints of Traditional Chinese Medicine," *Chinese Journal of Chromatography*, vol. 31, no. 2, pp. 127-132, 2013.
- [48] C. Huang, C. Lu and C. Chen, "Application of Grey Theory to the Field of Economic Forecasting," *Journal of Global Economics*, vol. 3, no. 1, 2014.
- [49] T. Pai, K. Hanaki, H. Ho and C. Hsieh, "Using Grey System Theory to Evaluate Transportation Effects on Air Quality Trends in Japan," *Transportation Research Part D: Transport and Environment*, vol. 12, no. 3, pp. 158-166, 2007.
- [50] C. Hsu and Y. Wen, "Application of Grey Theory and Multiobjective Programming Towards Airline Network Design," *European Journal of Operational Research*, vol. 127, no. 1, pp. 44-68, 2000.
- [51] H. A. Taha, *Operations Research: An Introduction*, 9th ed., New Jersey: Pearson, 2011.
- [52] K. Venkataraman, B. Vijayararnath and S. Kannappan, "Comparative Analysis of AHP and ANP Model for Lean Production System Justification," *Applied Mechanics and Materials*, vol. 591, pp. 197-201, 2014.
- [53] A. Acar, İ. Önden and K. Kara, "Evaluating the Location of Regional Return Centers in Reverse Logistics through Integration of GIS, AHP and Integer Programming," *International Journal of Industrial Engineering: Theory, Applications and Practice*, vol. 22, no. 4, pp. 399-411, 2015.
- [54] M. Obeidat, T. Qasim and A. Khanfar, "Implementing the AHP Multi-criteria Decision Approach in Buying an Apartment in Jordan," *Journal of Property Research*, vol. 35, no. 1, p. 53-71, 2018.
- [55] T. L. Saaty, "Decision Making with the Analytic Hierarchy Process," *International Journal of Services Sciences*, vol. 1, no. 1, pp. 83-98, 2008.
- [56] O. S. Vaidya and S. Kumar, "Analytic Hierarchy Process: An Overview of Applications," *European Journal of Operational Research*, vol. 169, no. 1, pp. 1-29, 2006.
- [57] N. Apostolopoulos and P. Liargovas, "Regional parameters and solar energy enterprises: Purposive sampling and group AHP approach," *International Journal of Energy Sector Management*, vol. 10, no. 1, pp. 19-37, 2016.
- [58] J. M. Benítez, J. C. Martín and C. Román, "Using Fuzzy Number for Measuring Quality of Service in the Hotel Industry," *Tourism Management*, vol. 28, no. 2, pp. 544-555, 2007.
- [59] A. Assari, T. Maheshand and E. Assari, "Role of Public Participation in Sustainability of Historical City: Usage of TOPSIS Method," *Indian Journal of Science and Technology*, vol. 5, no. 3, pp. 2289-2294, 2012.
- [60] R. Karim and C. L. Karmaker, "Machine Selection by AHP and TOPSIS Methods," *American Journal of Industrial Engineering*, vol. 4, no. 1, pp. 7-13, 2016.
- [61] C. Feng and R. Wang, "Considering the Financial Ratios on the Performance Evaluation of Highway Bus Industry," *Transport Reviews*, vol. 21, no. 4, pp. 449-467, 2001.
- [62] M. Janic, "Multicriteria Evaluation of High-speed Rail, Transrapid Maglev and Air Passenger Transport in Europe," *Transportation Planning and Technology*, vol. 26, no. 6, pp. 491-512, 2003.

- [63] G. Kim, C. Park and K. Yoon, "Identifying Investment Opportunities for Advanced Manufacturing Systems with Comparative-integrated Performance Measurement," *International Journal of Production Economics*, vol. 50, no. 1, pp. 23-33, 1997.
- [64] J. Vimal, V. Chaturvedi and A. K. Dubey, "Application of TOPSIS Method for Supplier Selection in Manufacturing Industry," *International Journal of Research in Engineering & Applied Sciences*, vol. 2, no. 5, pp. 25-35, 2012.
- [65] O. Chau and C. Parkan, "Selection of a Manufacturing Process with Multiple Attributes: A Case Study," *Journal of Engineering and Technology Management*, vol. 12, no. 3, pp. 219-237, 1995.
- [66] A. Shanian and O. Savadogo, "TOPSIS Multiple-criteria Decision Support Analysis for Material Selection of Metallic Bipolar Plates for Polymer Electrolyte Fuel Cell," *Journal of Power Sources*, vol. 159, no. 2, pp. 1095-1104, 2006.
- [67] B. Srdjevic, Y. Medeiros and A. Faria, "An Objective Multi-Criteria Evaluation of Water Management Scenarios," *Water Resources Management*, vol. 18, no. 1, p. 35-54, 2004.
- [68] A. Dehghani, "A Hierarchical TOPSIS method based on type-2 fuzzy sets to evaluate service quality of public transportation," *International Journal of Industrial Engineering: Theory, Applications and Practice*, vol. 24, no. 5, pp. 505-525, 2017.
- [69] K. Maniya and M. Bhatt, "An Alternative Multiple Attribute Decision Making Methodology for Solving Optimal Facility Layout Design Selection Problems," *Computers & Industrial Engineering*, vol. 61, no. 3, pp. 542-549, 2011.
- [70] K. Maniya and M. Bhatt, "A Selection of Material Using a Novel Type Decision-making Method: Preference Selection Index Method," *Materials & Design*, vol. 31, no. 4, pp. 1785-1789, 2010.



# The Antimicrobial Effect of UV-Activated Titanium Dioxide Material Deposited on Dental Implants

Abdul Hai Alami<sup>1,4,\*</sup>, M Adel Moufti<sup>2</sup>, Mohammad Hamad<sup>3,c</sup>, Kamilia Aokal<sup>4</sup>,  
Abdullah Abu Hawili<sup>5</sup>, Rawand Naji<sup>2</sup>, Mohammad Faraj<sup>4</sup>

<sup>1</sup>Sustainable and Renewable Energy Engineering Department, University of Sharjah, P.O.Box 27272, Sharjah, United Arab Emirates

<sup>2</sup>College of Dental Medicine, University of Sharjah, P.O.Box 27272, Sharjah, United Arab Emirates

<sup>3</sup>College of Health Sciences, University of Sharjah, P.O.Box 27272, Sharjah, United Arab Emirates

<sup>4</sup>Center for Advanced Materials Research, Research Institute of Science and Technology, University of Sharjah, P.O.Box 27272, Sharjah, United Arab Emirates

<sup>5</sup>Sharjah Research Academy, P.O.Box 60999, Sharjah, United Arab Emirates

Received December 9 2019

Accepted July 28 2020

## Abstract

This work presents a pilot study on the photoelectric effect of anatase titanium dioxide (TiO<sub>2</sub>) deposited on grade 4 titanium discs on their antimicrobial properties. The focus will be especially directed towards dental implants applications. This study details specimen preparation and microstructural characterization by scanning electron microscopy, X-ray diffraction and Raman spectroscopy to ensure a homogenous coverage of the TiO<sub>2</sub> material on the discs. The samples were further tested to highlight the photoelectric response of titanium dioxide to ultraviolet radiation in the form of electrical current within the discs. Six discs (three bare Ti, and three coated with TiO<sub>2</sub>) were seeded with a 5 µl of Escherichia coli culture. One disc of each group was subjected to the same UV light source used for the opto-electrical analysis for 0, 1 or 5 minutes. Bacteria on the discs were then harvested and incubated to examine number of viable cells. The obtained electrical properties confirmed that the surface-coating provides simultaneous oxidation-reduction driven reactions under the photoinduced catalytic activity. This activity proves the benefits of incorporating a TiO<sub>2</sub> layer in mitigating the number of active E-Coli bacteria in a microbial setup by as much as 21% after 5 minutes of UV exposure. This photoelectrical effect has a profound impact on the development of an in-situ oral disinfectant material deposited on titanium-based dental implants. It is expected that the approach will promote facile antimicrobial treatment for patients that is non-invasive and at the same time very effective.

© 2020 Jordan Journal of Mechanical and Industrial Engineering. All rights reserved

Keywords: Energy; titanium dioxide; photoelectric response; dental implants; surface modification; E-coli; anti-microbial; peri-implantitis;

## 1. Introduction

When teeth are lost, dental implants (titanium inserts) are placed into the jawbone in order to retain dental prostheses. In other words, “false teeth” are replacing missing teeth (Tagliareni and Clarkson 2015). Despite high costs associated with dental implants, the emergence and success of these implants have created a revolution in the dental profession and has greatly improved the quality of life for patients. It is estimated that *ca.* 300,000 dental implants were placed each year in the United States (Puleo and Thomas 2006). A trend of a significant and continuous increase in number of dental implant placement has been observed and is predicted. The dental industry continues to see a huge interest in the lucrative business of making titanium implants (Elani et al. 2018). Just like their natural predecessors, the integrity and survival of dental implants in the mouth is often compromised by bacteria adhering to the implant surface, secreting toxic by-products of their

metabolic processes and causing inflammation and tissue loss around the implant. This eventually leads to the loss of implant retention in the bone, and ultimately its dislodgement and detachment. This phenomenon is known as peri-implantitis, and is reported to affect up to 20% of patients during 5–10 years after implant placement (Salvi et al. 2017).

Numerous procedures have been devised to mitigate bacterial colonization upon the implant surface. These include (i) coating the implant surface with antibiotic-releasing agents such as Ag and Zn, which are known to possess anti-microbial properties and (ii) coating with materials with known photocatalytic effects that become bactericidal under ultraviolet radiation (Norowski and Bumgardner 2009). To date, no surface treatment strategy has been completely successful in providing satisfactory antibacterial effect, and thus the quest for the ideal surface modification continues.

Despite its established antimicrobial effect, UV-activated TiO<sub>2</sub> has not been utilized in clinical dentistry

\* Corresponding author e-mail: aalalami@sharjah.ac.ae

(Alami et al. 2020). This is due to two practical challenges for its use in the mouth: first, the difficulty to deliver UV to all aspects/surfaces of the implant/prosthesis (Norowski and Bumgardner 2009). These areas lie between teeth (interdental) or between the tooth and overlaying gum and already inaccessible for cleaning by the patient, and therefore may not benefit from the UV beam. Second, the very long UV exposure time required exposure duration to UV radiation to gain bactericidal effect is too long for most modern dental procedures (Norowski and Bumgardner 2009), and can cause a significant damage to DNA of the human cells.

This being said, various researchers were able to report on benefits of using TiO<sub>2</sub> material for their anti-microbial effects in the *in vitro* or *in vivo* animal settings. For example, Suketa et al. (2005) reported a substantial suppression in viability of two microbial species “*Actinobacillus actinomycetemcomitans*” and “*Fusobacterium nucleatum*” to less than 1% under UV-A illumination for 120 minutes. More recently, Pantaroto et al. (2018) examined the antimicrobial effect of titanium discs coated with different types of TiO<sub>2</sub> (anatase and rutile) and concluded that when these were subjected to UV-A for one hour. The authors found that A-TiO<sub>2</sub> (anatase) and M-TiO<sub>2</sub> (mixture of anatase and rutile) exhibited an antibacterial action by 99.9% and 99% respectively, whereas R-TiO<sub>2</sub> (rutile) did not exhibit significant bacterial reduction. The tested microorganism was a biofilm of *Streptococcus sanguinis*, *Actinomyces naeslundii* and *Fusobacterium nucleatum*. There is a consensus amongst the researchers that a minimum of one-hour exposure to UV light is required to bring significant antimicrobial effect (Norowski and Bumgardner 2009; Suketa et al. 2005; Pantaroto et al. 2018; Choi et al. 2009 and Grischke et al. 2016). This renders the application of this technique impractical in clinical dentistry as it will be too difficult to keep the patient mouth open for one hour while shining the UV on the target. In addition, there is a concern over subjecting the live tissues to UV radiation to a focussed UV beam for this period of time.

The above studies contradict with other experiments that reported significant eradication of bacterial cells in much shorter time (Pleskova et al. 2016; Joost et al. 2015; Shiraishi et al. 2009; Zaborowska et al. 2015). In fact, one of these studies argued that the 60-minute exposure to UV light was sufficient to kill the bacteria regardless of the substrate they were cultured upon by employing the effect of the UV radiation on its own (Zaborowska et al. 2015). These studies have also used UV-illuminated TiO<sub>2</sub>-coated titanium substrates and tested different stings of bacteria. Shiraishi et al. (2009) reported on the viability of suppressing of *Staphylococcus aureus* by 93% after 30 minutes of exposure to UV-A illumination. Zaborowska et al. (2015) reported elimination of 42% of *Staphylococcus aureus* after 15 minutes, while Joost et al. (2015) found a 75% reduction of the *Escherichia coli*'s viability after 5 minutes only of exposure to UV-A rays.

The varying results may be explained by the varying experimental methodology and procedures, as well as different bacterium species under investigation, not to mention the physicochemical characteristics of the anatase TiO<sub>2</sub>. For example, Singh et al. (2011) examined the effect of various TiO<sub>2</sub> microstructural characteristics (pore size, surface area, aspect ratio, ...etc.) on the bacterial cell

adhesion, and concluded that these characteristics significantly influence bacterial adhesion, with surface roughness being the major factor in enhancing this adhesion.

This study investigates the photoelectric generation of TiO<sub>2</sub>-coated titanium discs under the influence of UV-A radiation, and the associated microbicidal effect against *E. coli* microbes seeded over coated discs. The implants surface will be thoroughly cleaned and TiO<sub>2</sub> will be deposited upon it, and then subjected to UV radiation to amplify the possible photoelectric response that would be detrimental for microbial cells, thus acting as an antimicrobial agent. Titanium dioxide (TiO<sub>2</sub>), with its high chemical stability, is a widely used photocatalyst in many environmental applications. With a bandgap of 3.2 eV, the photo-induced activity of anatase TiO<sub>2</sub> under UV radiation provide it with antibacterial properties that drive a chemical reaction (photocatalysis) and allow for the production of Reactive Oxygen Species (ROS). This in turn propagates the photodegradation of organic compounds, namely bacterial (Maness et al. 1999; Carp et al. 2004). In addition to this effect, the generated current could also be beneficial for the hard-to-reach areas of teeth and thus enhance the level of dental protection achieved.

## 2. Materials and Methods

### 2.1 Specimens (disc substrate and coating):

The prepared sample consists of three sets of three grade 4 titanium discs (nine in total), 10 mm in diameter and 2.5 mm in thickness (Shaanxi Yunzhong Industry Development Co., Ltd, China, sourced through Alibaba.com). The composition of the discs was examined using X-ray fluorescence (XRF) technique and confirmed 99.7% purity of the received discs (traces of aluminium (0.26%) and iron (0.04%) are found). The TiO<sub>2</sub> coating material was obtained from a suspension of 0.5g of TiO<sub>2</sub> crystalline nano-powder particles (size 20-25 nm purchased from Sigmaaldrich.com) in a solution of 0.25g ethyl cellulose and 1.75g of terpinol dispersed in 5 ml of ethanol. The mixture was sonicated to form a homogenous slurry and then deposited on the Ti discs via spin coating (WS-650Mz-23NPPB Spin Processor) at 5000 rpm for 30 sec. The discs were annealed at 450 °C on the hotplate for 30 min.

### 2.2 Microstructural characterization:

Topographical inspection of the materials deposited on the titanium discs was done using a VEGA3 TESCAN SEM, operating at 30 kV acceleration voltage. The associated energy-dispersive X-ray spectrometer (EDS) was used for elemental analysis in two-dimensional mapping mode. Raman spectroscopy was carried out at room temperature in the back-scattering geometry using an inVia Raman microscope from Renishaw with its 514 nm laser running from 30 to 800 cm<sup>-1</sup> with an exposure time of 30s and a laser intensity of 10%. X-Ray diffraction (XRD) measurements are taken with a Bruker D8 Advance DaVinci X-ray diffractometer with Cu K $\alpha$  radiation operating at  $\lambda = 1.5406 \text{ \AA}$

### 2.3 Opto-electrical characterization:

The specimens were subjected to UV-electronic characterization, the source of which was a Mineralight Multiband handheld long-wave UV lamp operating at 6 watts (115 VAC/60 Hz) and at 365 nm wavelength. The 1 cm discs with an exposed area of 0.4 cm<sup>2</sup> were kept at a constant distance of 5 cm from the UV light source subjecting the disc to a potential input of 4.57 W/cm<sup>2</sup> for the whole duration (~10 minutes) of the experiment. This optical characterization of the TiO<sub>2</sub> on titanium discs provides evidence that the electrical effect stems from the electromagnetic excitation.

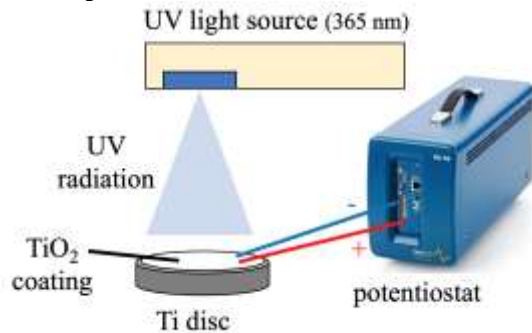


**Figure 1.** Optical characterization setup

The current was recorded with and without incident light using a Bio-Logic SP200 potentiostat in a 2-electrode setup on which two measurements have been conducted. One allowing for the control of the supplied voltage (0V) that is left constant for the duration of the experiment while the other applies a linear voltage sweep at 1mV/s from -0.1 V to 0.1 V. In the former, a 1-minute resting period is applied prior to current measurement. The experiment lasted for 10 minutes with a potential window of 50μV resolution. The latter engaged in no resting period and lasted for 200 seconds. The tests were also conducted on bare titanium discs as a reference.

### 2.4 Microbial testing:

The Gram-negative bacterium *Escherichia coli* (ATCC 25922) was selected for the current pilot study to evaluate antibacterial activity of TiO<sub>2</sub> disc in response to UV exposure. *Escherichia coli* culture was grown at 37°C to log phase in Mueller Hinton broth with shaking at 150 rpm. The culture was then washed three times with sterile phosphate-buffered saline (PBS) and adjusted to a density of 0.5 McFarland in PBS. Finally, 5 μl of 0.5 McFarland *E. coli* suspension was spotted onto 6 discs; three of which were bare Ti discs (group 1), while the other were TiO<sub>2</sub>-coated (group 2). One disc of each group was either subjected to UV ray for 5 minutes, or for 1 minute, or not subjected to UV light at all (negative control) to try to single out the best exposure time in this pilot study. The UV light (long wavelength) was the same UV light source used for the opto-electrical analysis, and was placed at a distance of 1.2 cm. Each of the 6 discs was moved into a falcon tube containing 5 ml of sterile PBS, vortexed for 30 seconds and serially diluted. 5 μl of each dilution was spotted onto Mueller Hinton Agar, allowed to dry and plates were incubated at 37°C for 24 hours. Following incubation colonies were counted to number of viable cells.

## 3. Results and discussion

### 3.1 Microstructural characterization:

The microstructural morphology of the deposited titanium dioxide film is shown in Figure 2 (a), with the energy dispersive X-ray spectroscopy (EDS) patterns shown in Figure 2(b) and (c) showing the homogenous distribution of the oxygen and the titanium. The surface of the discs shows the roughness inherent from the cutting process that was conducted to bring the discs to size. These patterns are coincidentally similar to those expected on the surface of maulers in teeth. This makes the results more relevant to the intended application.

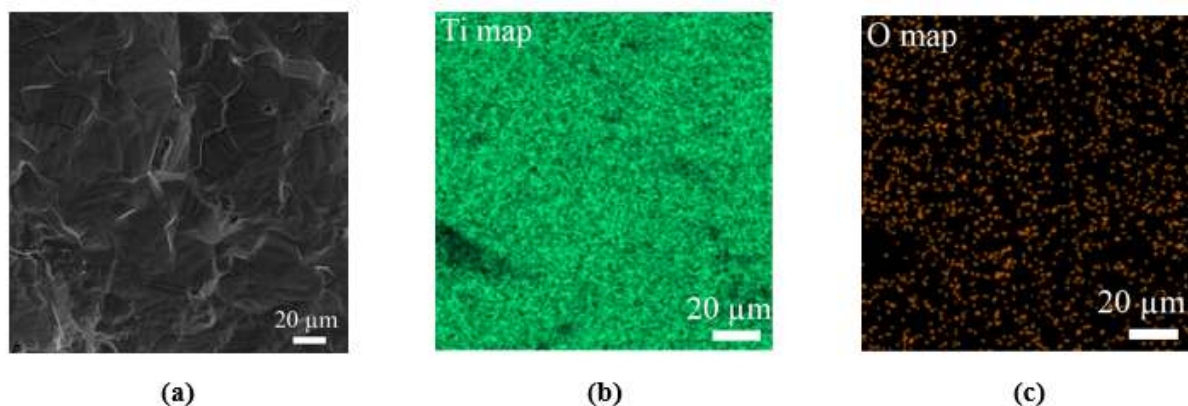


**Figure 2.** (a) SEM micrograph of the deposited titanium dioxide layer on the Ti disc with the EDS map of (b) titanium and (c) oxygen

The X-ray diffraction (XRD) patterns of the untreated discs with small traces of anatase titanium dioxide at  $38.5^\circ$  and  $74.4^\circ$ . The patterns are shown in Figure 3(a).

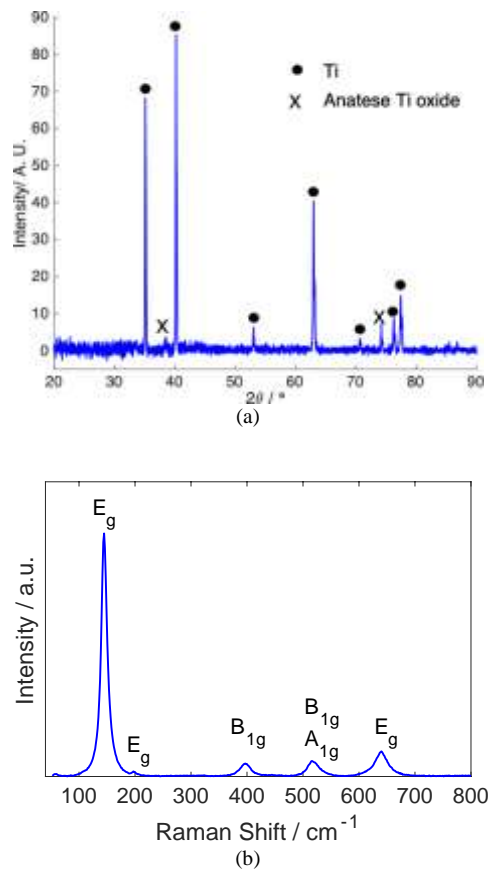


**Figure 3.** (a) X-ray diffraction patterns of bare Ti discs and (b) Raman spectra of anatase  $\text{TiO}_2$  coating

The Raman spectra shown in Figure 3(b) (Alami et al. 2020) shows six vibration modes that are characteristic of  $\text{TiO}_2$  in the anatase phase. They correspond to:  $E_g$  ( $144 \text{ cm}^{-1}$ ),  $E_g$  ( $197 \text{ cm}^{-1}$ ),  $B_{1g}$  ( $399 \text{ cm}^{-1}$ ),  $A_{1g}$  ( $513 \text{ cm}^{-1}$ ),  $B_{1g}$  ( $519 \text{ cm}^{-1}$ ), and  $E_g$  ( $639 \text{ cm}^{-1}$ ) (Ohsaka et al. 1978). The Raman test was also done for the bare discs, and no anatase  $\text{TiO}_2$  peaks were detected.

### 3.2 Opto-electrical characterization:

The specimens were exposed to UV radiation while measuring the voltage and current generated due to this electromagnetic stimulation. The addition of  $\text{TiO}_2$  is expected to generate enough charge via the interaction with UV radiation to produce the antimicrobial effects. The results show consistently low values of current readings with no externally applied excitation (either by UV radiation or voltage) shown as a black line in Figure 5 (a). Once the discs are illuminated via the UV source, the generated current, shown as a blue line in Figure 5(a), is seen to significantly increase compared with the discs in the dark up to the fifth minute (the  $\sim 320 \text{ s}$  mark), where the measured current response for the illuminated condition is seen to take a sharp dip, most likely due to the natural threshold limit of the  $\text{TiO}_2$  absorption of UV light. A cubical function curve fit was added to the data, shown as dotted blue and black lines in Figure 5(a), to assist in understanding the general trend of the photoelectric reaction to be

essentially different, and it appears to be in favour of the UV illuminated discs (the more negative the current the higher the photogeneration). The aperiodic peaks of current that appear in Figure 5(a) are due to the expected recombination that occurs once the electrons are generated and are not transported through a hole-transport material (HTM) into a counter electrode that is absent in the current setup. Similar observation can be seen in the work of (Wang et al. 2014).

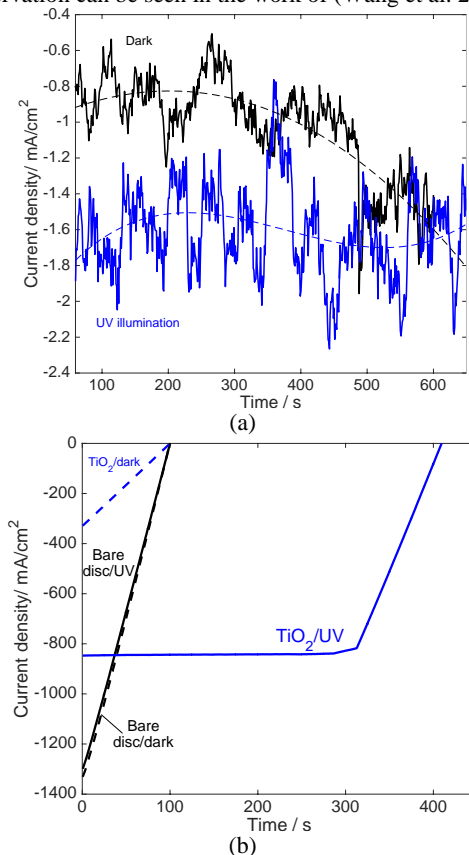


**Figure 5.** Current density vs. time over a) 0V supplied voltage and (b) a sweep voltage of -0.1 to 0.1V

On the other hand, with a linear change in voltage, a more prominent variation is seen with respect to dark and light conditions for discs with and without  $\text{TiO}_2$  deposition. The highest obtained response is recorded for the discs with  $\text{TiO}_2$  deposition are shown in Figure 5(b), where the area under the curve depicts the enhancement of the generated/stored charge within the active  $\text{TiO}_2$  material. In general, the titanium dioxide layer exhibits a significant increase in excitation with longer UV exposure (see Figure 5a), apparently due to the prolonged residence time of the radiation that allows more photocurrent to be generated.

### 3.3 The antimicrobial effect:

The results for the bacterial culture for the tested discs are shown in Figure 6 for both coated and bare samples under longwave UV illumination. It is interesting to note that the surface with titanium dioxide has shown a decrease in the number of cells by around 38% under no UV illumination. Also, the UV illumination of the discs for 1 minute is seen to provide a photo-excitation that is mild enough for bacteria to flourish, as their numbers are seen to increase. On the other hand, the opposite effect of UV radiation and  $\text{TiO}_2$  deposition is seen quite clearly for

samples that received UV soaking time of five minutes. The titanium discs that has TiO<sub>2</sub> deposits exhibit the least count of E-coli cells compared with any other disc set, and also around 20% less colonies than the bare disc set that was also exposed to UV for five minutes.

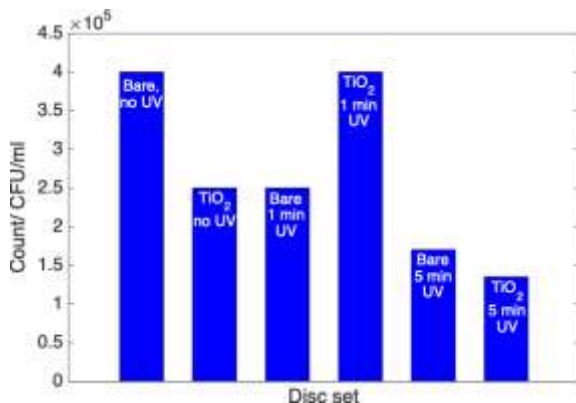


**Figure 6.** Bacterial cell count under various surface and illumination conditions

The results can be correlated with the photo-electric activity seen in Figure 5 where the reaction time of the discs covered in TiO<sub>2</sub> appear to benefit from an “activation time” that is around 5 minutes before appreciable changes to the bacterium cell count can take place. The bulge that the cubic fit exhibits (the blue dotted line of Figure 5(a)) indicates that the average current generation is increased with longer UV soak time.

#### 4. Conclusions

This paper reports on the utilization of a thin titanium dioxide coating for antibacterial effect on dental implants. These implants are usually manufactured from a special alloy of titanium metal, and thus the TiO<sub>2</sub> layer would be compatible with the implant material and also biocompatible with living tissue. The TiO<sub>2</sub> layer is known to have a photoelectric effect under ultraviolet (UV) radiation, which is an added advantage as UV light sources are available at dental clinics for various applications such as photocuring of dental cement. The results obtained highlight the benefits of the added TiO<sub>2</sub> layer in reducing the numbers of active E-Coli bacteria in a microbial setup by as much as 21% after 5 minutes of UV exposure. This photoelectrical effect has a profound impact on the development of an in-situ oral disinfectant material deposited on titanium-based dental implants. Future work will include a more comprehensive microbial study protocol that includes different UV soak time, alternate microbial species as well as structural and compositional modifications of the deposited TiO<sub>2</sub> layer.

#### References

- [1] Alami, A H et al. (2020). The Photoelectric Behavior and Antimicrobial Effect of Titanium Dioxide Deposition for Dental Implants. *Key Engineering Materials*, 865, pp.97–103.
- [2] Alami, A H et al. (2018). Assessment of Calotropis natural dye extracts on the efficiency of dye-sensitized solar cells. *Agronomy Research*, 16(4), pp.1569–1579. [online]. Available from: <https://doi.org/10.15159/AR.18.166> [Accessed April 1, 2019].
- [3] Alami, Abdul Hai et al. (2018). Assessment of Photoelectrode Material Based on (TiO<sub>2</sub>)<sub>1-x</sub> / (Al<sub>65</sub>Cu<sub>24</sub>Fe<sub>11</sub>)<sub>x</sub> in Dye-Sensitized Solar Cell Applications. *Materials Science Forum*, 928, pp.94–99. [online]. Available from: <https://www.scientific.net/MSF.928.94> [Accessed April 1, 2019].
- [4] Carp, O., Huisman, C.L. and Reller, A. (2004). Photoinduced reactivity of titanium dioxide. *Progress in Solid State Chemistry*, 32(1–2), pp.33–177. [online]. Available from: <https://www.sciencedirect.com/science/article/pii/S0079678604000123?via%3DIuh> [Accessed July 6, 2019].
- [5] Choi, J.-Y. et al. (2009). Photocatalytic Antibacterial Effect of TiO<sub>2</sub> Film of TiAg on Streptococcus mutans. *The Angle Orthodontist*, 79(3), pp.528–532.
- [6] Grischke J, Eberhard J, Stiesch M. Antimicrobial dental implant functionalization strategies -A systematic review. *Dent Mater J*. 2016;35(4):545-558. doi:10.4012/dmj.2015-314
- [7] Elani, H.W. et al. (2018). Trends in Dental Implant Use in the U.S., 1999–2016, and Projections to 2026. *Journal of Dental Research*, 97(13), pp.1424–1430.
- [8] Joost, Urmas et al. (2015). Photocatalytic antibacterial activity of nano-TiO<sub>2</sub> (anatase)-based thin films: Effects on Escherichia coli cells and fatty acids. *Journal of Photochemistry and Photobiology B: Biology*, 142, pp.178–185. [online]. Available from: <http://www.sciencedirect.com/science/article/pii/S101113441400373X>.
- [9] Maness, P.C. et al. (1999). Bactericidal activity of photocatalytic TiO<sub>2</sub> reaction: Toward an understanding of its killing mechanism. *Applied and Environmental Microbiology*.
- [10] Norowski, P.A. and Bumgardner, J.D. (2009). Biomaterial and antibiotic strategies for peri-implantitis: A review. *Journal of Biomedical Materials Research Part B: Applied Biomaterials*, 88B(2), pp.530–543.
- [11] Ohsaka, T., Izumi, F. and Fujiki, Y. (1978). Raman spectrum of anatase, TiO<sub>2</sub>. *Journal of Raman Spectroscopy*, 7(6), pp.321–324. [online]. Available from: <http://doi.wiley.com/10.1002/jrs.1250070606> [Accessed June 26, 2019].
- [12] Pantaroto, H.N. et al. (2018). Antibacterial photocatalytic activity of different crystalline TiO<sub>2</sub> phases in oral multispecies biofilm. *Dental Materials*.
- [13] Pleskova, S.N., Golubeva, I.S. and Verevkin, Y.K. (2016). Bactericidal activity of titanium dioxide ultraviolet-induced films. *Materials Science and Engineering: C*, 59, pp.807–817. [online]. Available from: <https://linkinghub.elsevier.com/retrieve/pii/S0928493115304537>.
- [14] Puleo, D.A. and Thomas, M. V. (2006). Implant Surfaces. *Dental Clinics of North America*, 50, pp.323–338.
- [15] Salvi, G.E., Cosgarea, R. and Sculean, A. (2017). Prevalence and Mechanisms of Peri-implant Diseases. *Journal of Dental Research*, 96(1), pp.31–37.
- [16] Shiraishi, K. et al. (2009). Antibacterial metal implant with a TiO<sub>2</sub>-conferred photocatalytic bactericidal effect against Staphylococcus aureus. *Surface and Interface Analysis*.
- [17] Singh, A.V. et al. (2011). Quantitative characterization of the influence of the nanoscale morphology of nanostructured surfaces on bacterial adhesion and biofilm formation. *PLoS ONE*.
- [18] Suketa, N. et al. (2005). An Antibacterial Surface on Dental Implants, Based on the Photocatalytic Bactericidal Effect. *Clinical Implant Dentistry and Related Research*, 7(2), pp.105–111.
- [19] Tagliareni, J.M. and Clarkson, E. (2015). Basic Concepts and Techniques of Dental Implants. *Dental Clinics of North America*, 59, pp.255–264.

- [20] Wang, Y. et al. (2014). A novel self-cleaning, non-enzymatic glucose sensor working under a very low applied potential based on a Pt nanoparticle-decorated TiO<sub>2</sub> nanotube array electrode. *Electrochimica Acta*, 115, pp.269–276.
- [21] Zaborowska, M. et al. (2015). Bacteria-material surface interactions: methodological development for the assessment of implant surface induced antibacterial effects. *Journal of Biomedical Materials Research Part B: Applied Biomaterials*, 103(1), pp.179–187. [online]. Available from: <http://doi.wiley.com/10.1002/jbm.b.33179>.
- [22] Zhang, D. et al. (2018). Efficiency and high-temperature response of dye-sensitized solar cells using natural dyes extracted from Calotropis. In *5th International Conference on Renewable Energy: Generation and Application, ICREGA 2018*.

# Value Stream Mapping with Simulation to Optimize Stock Levels: Case Study

Yunus Emre MIDILLI, Birol ELEVLI

Riga Technical University, Information Technology Dept., LV-1658 RIGA/LATVIA  
Ondokuz Mayıs Üniversitesi, Industrial Engineering Dpt., 55139 Atakum-SAMSUN/TURKEY

Received December 2 2019

Accepted July 6 2020

## Abstract

Value stream mapping (VSM) is a simple tool used to identify the waste present within the processes by mapping the current state. The future state is suggested to eliminate the waste. However, transition from current state to future state has always been a challenge in real life applications. One of the biggest challenge is to determine where to establish continuous flow and controlled stock levels due to numerous reasons, such as probabilistic characteristics of demand, unexpected behaviors, complexity etc. In this context, simulation is used to assess lean improvements, to analyze the system under scenarios based on suggested improvements and to optimize an objective, subject to constraints or requirements. In this paper, a simulation-based optimization approach is proposed to determine optimum stock levels in lean manufacturing, and a case study was carried out for a filter manufacturing department of a tobacco company. The results showed that stock level could be reduced by 50% while reducing the number of machines.

© 2020 Jordan Journal of Mechanical and Industrial Engineering. All rights reserved

Keywords: VSM ; Simulation ; Optimization ; Lean ; Stock level;

## 1. Introduction

Lean concepts have gained a lot of attention in order to identify, eliminate, and optimize non-value added (NVA) activities within business processes (Porter, 1985; Govindarajan, 2008). In this context, there are various lean methodologies, such as Just-in-Time (JIT), total productive maintenance (TPM), single-minute exchange of dies (SMED), 5S etc. that have been used widely [3, 4]. Value stream mapping (VSM) has been used as a tool to identify current state and to design the future state of the processes based on lean methodologies. However, transition from current state map to future state map has been a challenge due to lack of verification. To overcome this challenge, simulation models are used. Besides reducing the risk of failure, simulation models enable researchers to design the future states in an optimum way even for the complex systems. In general, simulation models can be used for the purposes of validation, decision making and optimization. In this study, simulation modeling is used to optimize controlled stock levels with the objective of building continuous flow. To the best of our knowledge, there is no stepwise guideline where practitioners can design future state maps via simulation-based optimization technique to determine controlled stock levels. In this context, contribution of this study can be listed as follows:

- A stepwise approach from current state map to future state map in VSMS to optimize the controlled stock levels via simulation-based optimization method and

- A case study in filter manufacturing department of a tobacco production company.

The rest of the paper is arranged as follows: In Section 2, literature where simulation is being used together with VSM in different types of industrial areas. In Section 3, proposed stepwise approach is explained. In Section 4, a case study is demonstrated to design a future state in filter manufacturing department of a tobacco production company. Finally, the conclusion from this study is given in Section 5.

## 2. Literature Review

Value chain was first described by [1], and it is a set of activities that a company performs in order to deliver valuable products. (Govindarajan, 2008) define that the value chain is the interconnected set of all activities that create value, from a basic source of raw materials, through component suppliers, until handing over the final product to consumers. Value stream mapping (VSM) is a value chain tool to illustrate, analyze and improve the activities in production in a way to categorize them value added (VA) or non-value-added (NVA) from customer perspective. In the book titled "Learning to See" [5], transition from current state map to future state map has been described in a stepwise approach for a factory. The book titled "Creating Leveled Pull System" introduced the implementation of pull system in an automotive part supplier thanks to VSM. In addition, it benefits the steps of book "Creating Material

\* Corresponding author e-mail: birol.elevli@omu.edu.tr

Flow" [7] in order to provide transfer system of materials, Kanban cards and trays.

Practices revealed that transition from current state to future state needs to be validated before implementation. In this context, researchers attempted to use simulation techniques to enhance VSM approach. There are case studies where simulation models are applied with VSM in various industries such as food [9], furniture [10], automotive [11], painting [12], glass [13], construction [14] etc. Authors of [15] presented about inputs and outputs that could be used for the simulation model and future state map. Simulation is considered as an assessment tool for different future state designs before implementation [16]. Researchers of [17] suggested three different configurations of independent variables, such as setup time, changeover time, routine checks, worker allocations etc. Based on these variables, process performance metrics such as process scrap rate, motion waste, average lead time, work-in-progress (WIP) stocks etc. are compared within the simulation environment. Authors of [18] used multivariate factorial analysis to design future state with objective of minimizing the average lead time and WIP stocks via production leveling (heijunka) in microelectronics assembly line. ANOVA is applied based on simulation outputs for the different configurations of number of pitch times and arrangement of orders in pitch times. Similarly, [19] have used full factorial analysis to identify the best future state design for the minimization of throughput rate in an assembly line of a construction and mining equipment manufacturer. Researchers of [20] designed future state map with lean methodologies, such as total preventive maintenance, setup time reduction, switching from push system to pull system within steel production factory. They have analyzed single and interaction effects of these improvements via ANOVA. They have emphasized that focusing on only the lean methodologies that have significant effect has also increased the management team's commitment. In the study of [21], design of experiments have been used for the production unit, pacemaker process, production sequence and number of the batches in fishing net manufacturing. According to each scenario, simulation-based optimization tool is used to find the best supermarket sizes. Based on selected supermarket sizes, response values of service level and WIP inventory level is noted for each scenario. Optimum results are obtained via Taguchi method.

### 3. Methodology

This study presents a stepwise methodology to design future map via using simulation-based optimization. After current state map is completed, following steps should be applied to design a future state with continuous flow in production environment:

- a) Calculate takt time – is calculated by dividing total available working time in a day to daily customer demand. It represents the frequency of demand arrival.
- b) Estimate cycle time – is estimated for each process according to product proportions. Cycle times should be compelling with takt time. Understanding of cycle time and takt time concepts are very essential to increase the efficiency in future state designs [22].

- c) Identify and schedule pacemaker process– If full continuous flow is not possible in the system, a supermarket or FIFO line should be established between last process of system and customer arrival. Based on the type of this flow, pacemaker process that will be scheduled according to pitch levels should be defined.
- d) Identify controlled stocks–First aim is to build full continuous flow but most of the time, it is very difficult to build full continuous flow due to various constraints in the system. Therefore, controlled stock areas such as FIFO lines or supermarkets can be used. Optimizing the level of these stock units is the main objective of this paper.
- e) Identify process metrics and assumptions of simulation model – Process metrics that have effect on objective function or constraints of the optimization problem should be identified. To simplify simulation model, some assumptions can be considered.
- f) Build simulation model – Input analysis should be applied for the demand arrival and machine breakdown and maintenance activities of the processes. For input analysis, Minitab [23] and Easy Fit [24] are used. AnyLogic [25] simulation software is used to build simulation model. Any Logic is based on Java programming language which capable to model even complex systems via using the benefits of object-oriented programming. After simulation model is built, it should be executed to identify the steady-state point. There are broadly four methods for dealing with the initial transient [26]: (i) The model is run-in for a warm-up period until it reaches a steady-state and the data from the warm-up period are deleted. (ii) The initial conditions of the model are set in such that the model is in steady-state from the beginning of the run. (iii) The model is run for a very long time, making the bias effect negligible. (iv) The steady-state parameters are estimated from a short transient simulation run [27].
- g) Build optimization model – This process consists of repetitive simulations of a model under different configurations of parameters [28]. AnyLogic's optimization model uses with OptQuest [29] optimization engine. Using grid search algorithms, the OptQuest Engine varies controllable parameters from simulation to simulation to find the optimal parameters for solving a problem [29]. To optimize a simulation model following items should be defined:
  - I. Decision variables – Initial levels of controlled stock units,  $x_i^0$ , are decision variables of optimization model.
  - II. Objective function – Let  $x_i^t$  denote the total number of stock levels in controlled stock unit  $i$  during the simulation time  $t$  after steady-state point, then the goal of the optimization model is to minimize the average controlled stock units in the system.
 
$$\min z = (\sum_t \sum_i x_i^t) / T \text{ where } t = \{0, 1, \dots, T\} \quad (1)$$
  - III. Constraints and requirements – Let  $d^t$  denote the service level to customer during the simulation time  $t$ , then minimum service level requirement  $r^t$  should be satisfied:
 
$$d^t \leq r^t, \forall t = \{0, 1, \dots, T\} \quad (2)$$

### 4. Application

A tobacco manufacturing company’s filter manufacturing department is considered to apply proposed methodology. The company has a manufacturing facility located in Turkey. Due to legal reasons, name of the company is mentioned as ABCTobacco in this paper. Product and process information is presented with converted values. In the company, production planning department is responsible for scheduling. 30-60-90 days of demand forecasts are received via e-mail. Weekly schedule is prepared in an ERP system. Daily orders are sent to the departments based on weekly schedule. Facility works every weekday. The company works two shifts and each shift is 8 hours. There are breaks in the shifts but during breaks, production is going on with replaced workers.

The facility consists of three departments known as Primary Manufacturing Department (PMD), Filter Manufacturing Department (FMD) and Cigarette Manufacturing Department (CMD). PMD and FMD provide semi-finished products to the CMD that produces finished good. CMD is considered as internal customer of FMD and PMD. In FMD, there are two types of machines: filter maker machines (FMM) and combiner machines (CM). FMM makes base rod filters and CM combines few base rod filters based on some proportions. Raw material of base rod filter is called a stow. There are other materials used in filter production, such as tracetine, charcoal, adhesive, plug wrap etc. however, illustrating one raw material is enough to express current state for simplification. There are two types of filter base rods produced in FMD: mono and charcoal. These products are known as MN2 and CH1 respectively. The combined filter of these two base rods is known as MNCH1. MNCH1 has

446 million stick demand in last 100 days. This amount is %80 percent of total demand.

#### 4.1. Current State Map

In machine FM35, product MNCH1 is combined from two base rods: MN2 and CH1. MN2 is produced in machine FM80. CH1 is produced in both machine FM70 and machine FM90. Both combined filters use material named Tow2. Base rods are carried in the trays that contain 4500 filter sticks. There are 28 base rod trays in each base rod pallet. There are 32 trays in each combined filter pallet. Daily demand of MNCH1 is 993 trays. In one tray of MNCH1, there are 1/3 trays of CH1 and 1/3 trays of MN2. In one tray of CH1 there is 2.7 kg Tow2 and in one tray of MN2 there is 3.5 kg of Tow2. According to these proportions, it can be calculated that in one MNCH1 tray, there is 2.1 kg of Tow2. Stock levels are observed while current state map is drawn. These levels are just a snapshot of corresponding day. Figure presents current state map of MNCH1. All stock levels are converted to time unit. This conversion is done based on Little’s law [30], which asserts that waiting time in the queue (stock area) is calculated by dividing the inventory amount to daily requirement. Daily requirements should be calculated based on product proportions of MNCH1 as stated in **Table 1**.

**Table 1:** Conversion of Stock Levels to Time Unit

Material/Product	Stock Level	Daily Requirement	Waiting Time (minute)
MNCH1	3359 tray	993 tray	4871.1
CH1	1600 tray	331 tray	6960.7
MN2	530 tray	331 tray	2305.7
Tow2	95000 kg	2085.3 kg	65602.1

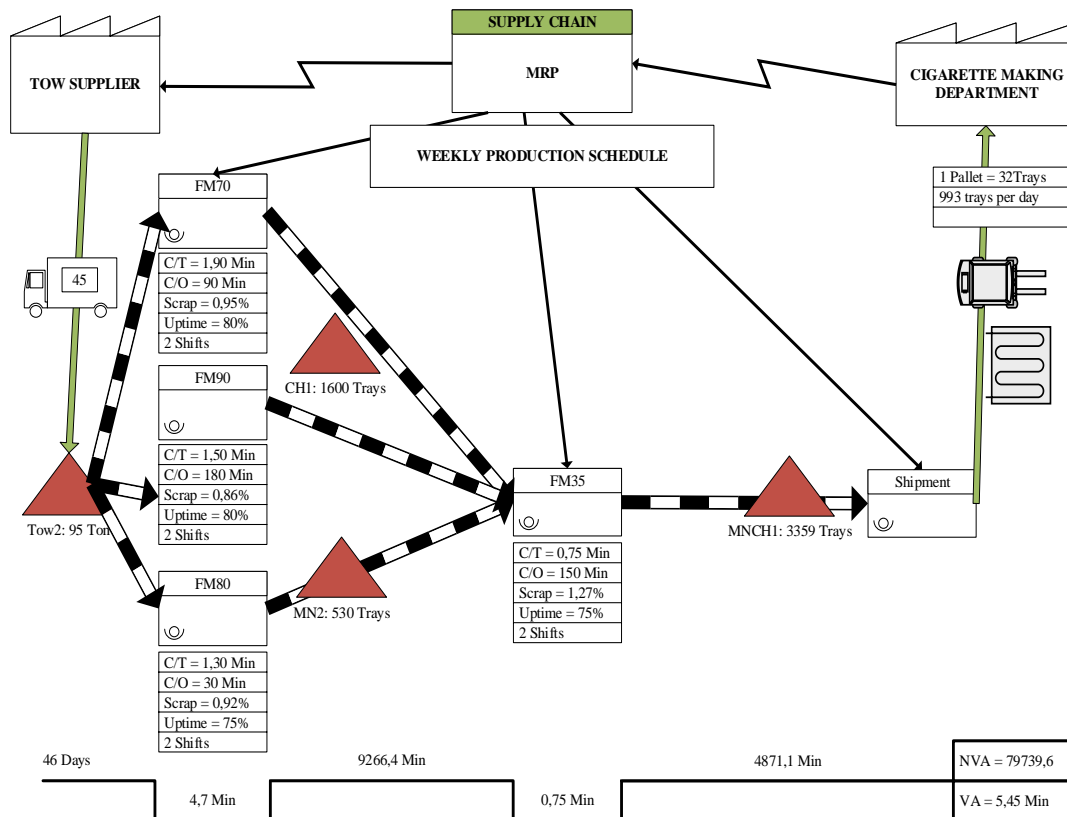


**Figure 1:** Current State Map of MNCH1

Total non-value added activities for MNCH1 is 79739.6 minutes (apprx. 46 days). Total value added activities take only 5.45 minutes for a tray. The efficiency of the process is percentage of VA activities in whole activities:

$$\text{Efficiency} = \frac{5.45}{79739.6+5.45} \times 100 = 0.007\% \quad (3)$$

#### 4.1. Future State Map

Future state map is a design that contains suggested improvements to eliminate wastes in current state map. To draw a future state map, proposed stepwise approach is used:

##### a) Calculate takt time

Takt time shows the frequency of demand arrivals from customer. Takt time for MNCH1 is:

$$\text{Takt time} = \frac{\text{Total available working time(second)}}{\text{Daily demand(tray)}} = \frac{16 \times 60 \times 60}{993} = 58 \text{ (second/tray)} \quad (4)$$

Customer demands one tray of MNCH1 in each 58 seconds. FMD should work based on this time frame to satisfy customer demand.

##### b) Estimate cycle time

Cycle times are estimated based on product proportions (Table 2). It demonstrates that cycle times are below the takt time. Since both FM70 and FM90 machines work below takt time, only one machine (FM90) can be assigned for charcoal filter production.

Table 2: Estimated Cycle Times

Work Center	C/T (second/tray)	Proportion in Combined Filter	Estimated C/T (second/tray)
FM70	114	1/3	37.62
FM90	90	1/3	29.70
FM80	78	1/3	25.74
FM35	45	1	45.00

##### c) Identify and schedule pacemaker process

Pacemaker process that manages the tempo of the system, should be closest process to the customer. FM35 is pacemaker process of FMD. There should be controlled WIP stock area between machine FM35 and shipping department, and FIFO rule should be applied there.

Ideally, FM35 should produce each tray at once. This is called as every part every interval (EPEI). When customer demands one tray, the tray should be produced immediately in that interval. This is very difficult due to facts, such as expected and unexpected stops, demand variation, rejects, changeovers, scraps etc. In this study, unit of product is tray and unit of container is pallet. Each pallet should be produced in each interval. Pallet size is decreased from 32 trays to 16 trays in order to work with smaller lot sizes. The leveled time intervals that FM35 should produce is called as pitch (required time to produce one pallet). Pitch of pacemaker process is calculated as:

$$\text{Pitch} = \text{Takt Time} \times \text{Pallet Size} = 58 \times 16 =$$

$$928 \text{ sec} \cong 15 \text{ mins} \quad (5)$$

FM35 should produce 16 trays in every 15 minutes. The pitch interval is calculated by using the equation:

$$\text{Pitch Interval} = \text{Available Time in a Shift} \div \text{Pitch} = (8 \times 60) \div 15 = 32 \text{ intervals} \quad (6)$$

In a shift, there should be 32 production orders for FM35 to produce to FIFO line. In order to visualize the production orders, visual management tools such as Heijunka boxes can be used.

##### d) Identify controlled stocks

Supermarkets should be established between pacemaker process and upstream processes. Supermarkets should be set for each type of product or material. There will be one supermarket for each CH1 and MN2. In FMD, supermarkets are located next to the pacemaker process (FM35). Base rod machine operators and supervisors can track the stock levels instantly thanks to manufacturing execution system.

Raw materials should be stored in controlled stock areas. Since tow suppliers are located different countries, batch orders should be applied. After pull Kanbans are collected reach to reorder point, supply chain department will order new batches from tow suppliers.

##### e) Identify process metrics and assumptions of simulation model

Objective function of optimization is based following process metrics:

- Average stock level – is the average of inventory levels of Tow2, MN2, CH1 and MNCH1 in whole system during simulation run.
- Average service level – is calculated by dividing total satisfied customer demands into total demand.

To simplify the simulation model following assumptions are stated:

- Tow supplier is capable to deliver an order once in 10 days.
- Arrival time of produced tray from base rod machine to supermarket is 1 minute.
- Kanban signals for production order go to the upstream processes immediately with a manufacturing execution system.
- When a material is demanded from supermarket or FIFO area, it arrives to work station with no variation.

##### f) Build simulation model

Input analysis is conducted to build the simulation model for the period of 100 days. Daily demand of MNCH1 is noted based on tray amount. Input analysis of demand arrival reveals that demand fits with Poisson distribution ( $p = 0.840$ ,  $\alpha = 0.05$ ,  $\lambda = 993$ ). Distributions and parameters of machine breaks and repairs are given in Table 3 based on historical maintenance logs of machines.

Table 3: Distribution of Maintenance Data

Work Center	Breaks Int. Arr. (hour)	Repair Duration (min)
FM70	Triangular(4,5,6)	Triangular(50,60,70)
FM80	Triangular(4,5,6)	Triangular(20,30,40)
FM90	Triangular(4,5,6)	Triangular(20,30,40)
FM35	Triangular(4,5,6)	Triangular(10,15,20)

Any Logic discrete event simulation blocks are used for modeling (Figure2). In the model, WIP\_MN2, WIP\_CH1, WIP\_MNCH1 and WIP\_Tow2 represent the decision variables. Warm-up and simulation run length is identified to discover steady-state of the model.

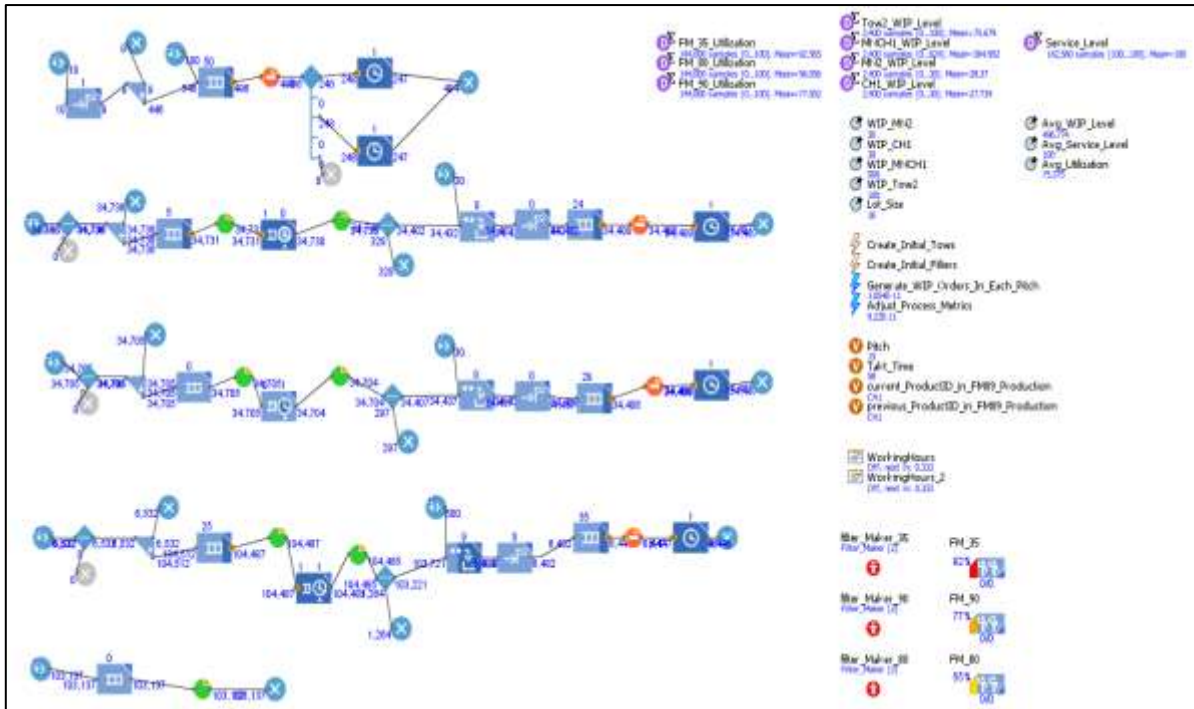


Figure2: Simulation Model for Future State Design

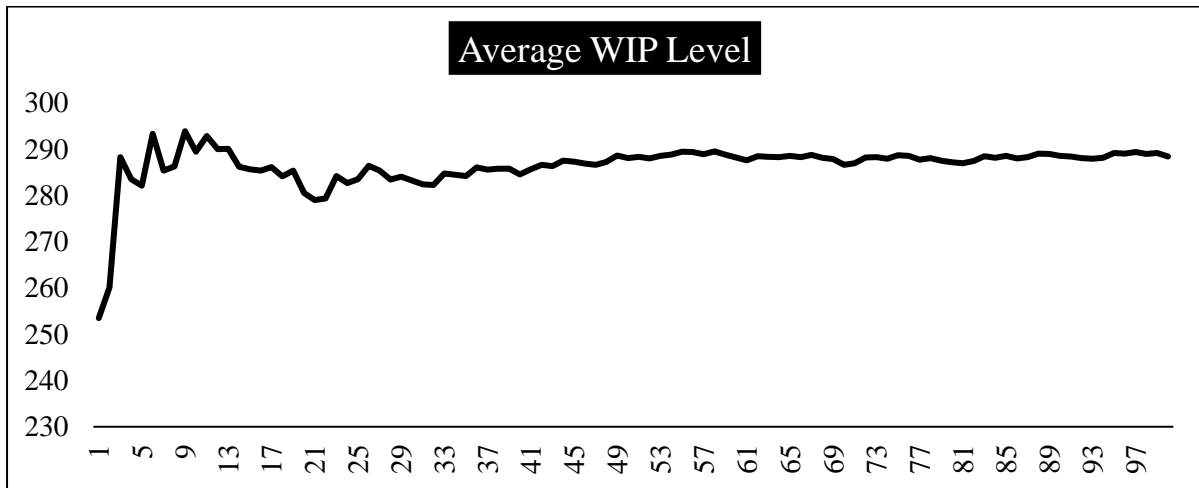


Figure 3: Result of Simulation Run

When simulation run is executed, steady-state for average WIP level is identified as 50<sup>th</sup> day(Figure 3). Data for input analysis is collected for 100 days, therefore it is enough to have 100 days of output result after steady-state. Since first 50-day period is warm-up period, simulation run length should be 150 days and data should be collected after 50th day after the simulation model reaches to steady-state.

g) Build optimization model

There are 864 iterations that represent different configurations of grid vectors for each controlled stock unit (Table 4). Objective function is minimization of the average stock level in the system. Service level constraint is to provide at least 99 percent service level to customer. Optimization model is executed for 150 days (including 50 day warm-up period)with 864 iterations. Data is collected

after simulation model reaches to steady state point (50<sup>th</sup> day).

Table 4: Grid Vectors of Optimization Model

Controlled Stock Unit	Min	Max	Step	Grid Vector
MN2	10	15	1	[10, 11, 12, 13, 14, 15]
CH1	10	15	1	[10, 11, 12, 13, 14, 15]
MNCH1	300	370	10	[300, 310, 320, 330, 340, 350, 360, 370]
Tow2	40	50	5	[40, 45, 50]

When the model is run with a computer featured with 4 GB RAM, 64 bit, it took 15 minutes in real time to find optimum solution. Optimum solution indicates that there should be 50 units of Tow2, 10 units of MN2, 15 units of CH1 and 360 units of MNCH1 in the controlled stock areas where 273.16 unit of average WIP stock level in the system. The future state map is drawn based on this solution (Figure 4). Future state map reveals that VA time increases from 3.55 min to 5.45 min, NVA time decreased from 79739.6 min to 17910.8 min. Efficiency in future state map (0.02%) is 2.8 times better than current state map (%0.007). Output analysis for the performance metrics of the system is shown (Table 5). Results depict that there is significant improvement in future state not only on inventory levels but also on machine utilizations and service level. Additionally, future state results less variation than current state.

Table 5: Output Analysis of Optimal Solution

Process Metric	Current State		Future State	
	Mean	SD	Mean	SD
<b>Tow2 Avg. Inventory Level</b>	200.1	20.11	25.77	14.35
<b>MN2 Avg. Inventory Level</b>	1000.9	198.15	8.65	2.14
<b>CH1 Avg. Inventory Level</b>	1499.1	201.66	12.79	3.25
<b>MNCH1 Avg. Inventory Level</b>	3500.0	120.43	236.41	118.43
<b>FM80 Avg. Utilization</b>	54.6	0.13	56.19	0.07
<b>FM90 Avg. Utilization</b>	55.5	0.80	77.61	0.10
<b>FM35 Avg. Utilization</b>	92.6	0.20	94.36	0.13
<b>Avg. Service Level</b>	95.0	13.10	99.11	9.40

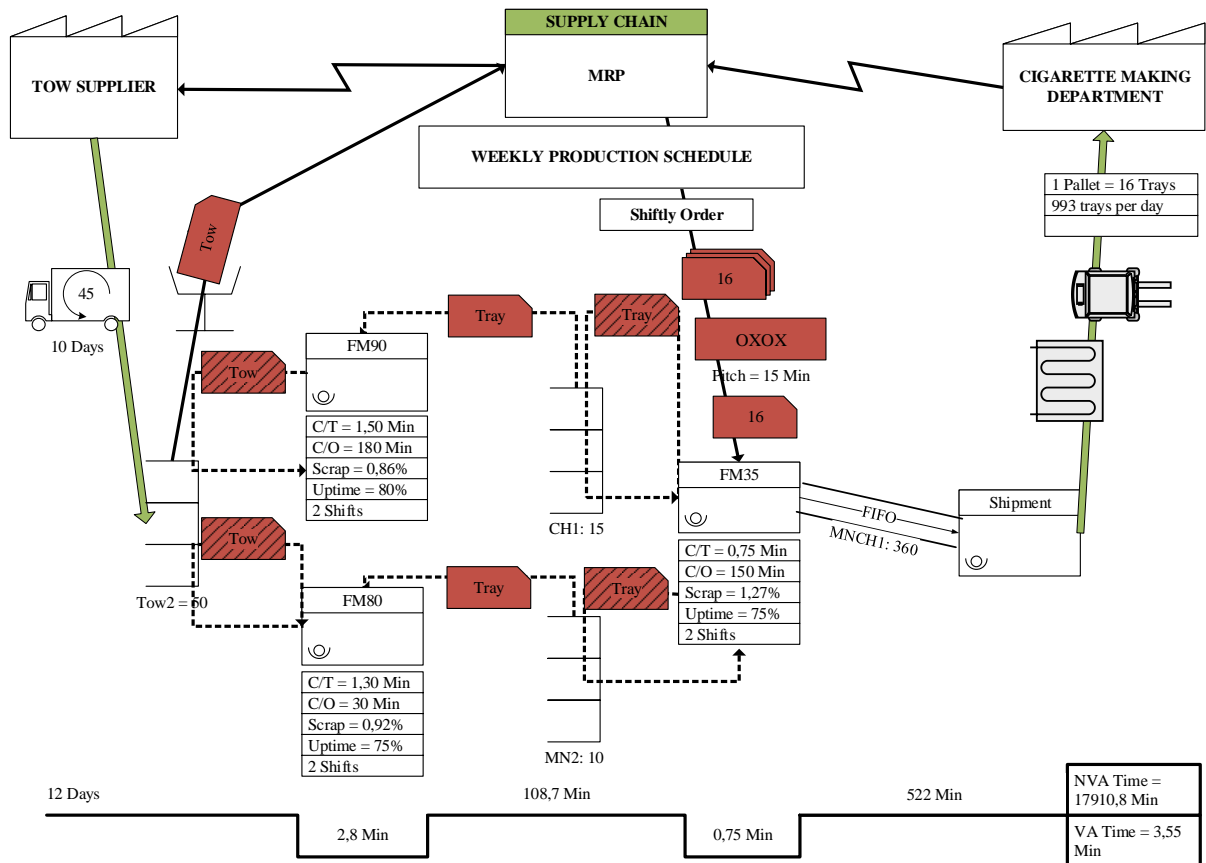


Figure 4: Future State Map of MNCH1

## 5. Conclusion

In this paper, transition from current state to future state in value stream mapping, has been taken into consideration. After current state map is drawn, stepwise approach is presented to design future state via using simulation-based optimization approach. In this context, filter manufacturing department of a tobacco production company is considered as case study. In the case study, controlled stock areas instead of batch production have been proposed to provide continuous flow within the organization. Levels of controlled stock areas have been determined with simulation-based optimization model. After optimum results of future state design is implemented to simulation model, outputs show that there is significant improvement for inventory levels, machine utilization and service level. Additionally, deviation of current state process metrics is higher than future state process metrics. This demonstrates that future state is working in more stable manner. To sum up these improvements, number of machines assigned to production has been decreased 25%, lot size in the production has been decreased 50%. As a result, efficiency of the system has been improved 2.8 times.

## 6. Acknowledgements

The authors gratefully acknowledge the in-depth comments and constructive suggestions of referees, which improved the presentation of our paper scientifically. The authors thank to the anonymous company for providing data for the case study.

## References

- [1] M. E. Porter, *The Competitive Advantage: Creating and Sustaining Superior Performance*, New York: Free Press, 1985.
- [2] S. Govindarajan, *Strategic Cost Management: The New Tool for Competitive Advantage*, New York: Free Press, 2008.
- [3] J. Sisson and A. Elshennawy, "Achieving success with Lean," *International Journal of Lean Six Sigma*, vol. 6, no. 3, pp. 263-280, 2015.
- [4] A. Camuffo, *Lean Transformations for Small and Medium Enterprises: Lessons Learned from Italian Businesses*, Productivity Press, 2017.
- [5] M. Rother and J. Shook, *Learning to See*, Michigan: Lean Enterprise Institute, 1998.
- [6] A. Smalley, *Creating Leveled Pull System*, Huntington Beach: Lean Enterprise Institute, 2004.
- [7] R. Harris, C. Harris and E. Wilson, *Creating Material Flow*, Georgetown: Lean Enterprise Institute, 2003.
- [8] J. H. Marvel and C. R. Standridge, "A simulation-enhanced lean design process," *Journal of Industrial Engineering and Management*, vol. 2, no. 1, pp. 90-113, 2009.
- [9] N. S. Suhadak, N. Amit and M. N. Ali, "Facility Layout for SME Food Industry via Value Stream Mapping and Simulation," *Procedia Economics and Finance*, no. 31, pp. 797-802, 2015.
- [10] H. G. Goren, "Value stream mapping and simulation for lean manufacturing: A case study in furniture industry," *Pamukkale University Journal of Engineering Sciences*, vol. 23, no. 4, pp. 462-469, 2016.
- [11] P. Andrade, V. G. Pereira and E. G. Del Conte, "Value Stream Mapping and Lean Simulation: A Case Study in Automotive Company," *International Journal of Advanced Manufacturing Technology*, pp. 547-55, 2016.
- [12] J. M. Rohani and S. M. Zahraee, "Production line analysis via value stream mapping: a lean manufacturing process of color industry," in *2nd International Materials, Industrial, and Manufacturing Engineering Conference*, Bali, Indonesia, 2015.
- [13] A. M. Atieh, H. Kaylani, A. Almuhtady and O. At-Tamimi, "A Value Stream Mapping and Simulation Hybrid Approach: Application to Glass Industry," *International Journal of Advanced Manufacturing Technologies*, pp. 1573-1586, 2016.
- [14] M. Goh and Y. M. Goh, "Lean production theory-based simulation of modular construction processes," *Automation in Construction*, vol. 101, pp. 227-244, 2019.
- [15] D. Antonelli and D. Stadnicka, "Combining factory simulation with value stream mapping: a critical discussion," in *11th CIRP Conference on Intelligent Computation in Manufacturing Engineering*, Ischia, 2018.
- [16] G. G. Sastry and R. Garg, "Analysis of Single Flow Line Multi Stage Multi-Product Pull Control Systems," *Journal of Scientific & Industrial Research*, no. 76, pp. 289-293, May 2017.
- [17] O. Omogbai and K. Salonitis, "Manufacturing system lean improvement design using discrete event simulation," *Procedia CIRP*, no. 57, pp. 195-200, 2016.
- [18] P. Korytkowski, T. Wisniewski and S. Rymaszewski, "Multivariate simulation analysis of production leveling (heijunka) - a case study," in *7th IFAC Conference on Manufacturing Modelling, Management, and Control*, Saint Petersburg, 2013.
- [19] M. Nagi, F. F. Chen and H.-D. Wan, "Throughput Rate Improvement in a Multiproduct Assembly Line Using Lean and Simulation Modeling and Analysis," in *27th International Conference on Flexible Automation and Intelligent Manufacturing*, Modena, Italy, 2017.
- [20] A. A. Fawaz and J. Rajgopal, "Analyzing the benefits of lean manufacturing and value stream mapping via simulation: A process sector case study," *International Journal of Economics*, pp. 223-236, 2007.
- [21] T. Yang, Y. Kuo, C.-T. Su and C.-L. Hou, "Lean production system design for fishing net manufacturing using lean principles and simulation optimization," *Journal of Manufacturing Systems*, no. 34, pp. 66-73, 2015.
- [22] M. Shakoor, M. R. Qureshi and S. Jaber, "Applying Management Principles of Lean Manufacturing for Enhancing Efficiency and Effectiveness of Emergency Department Rooms," *Jordan Journal of Mechanical and Industrial Engineering*, vol. 13, no. 4, pp. 291-299, 2019.
- [23] I. Minitab, "Minitab," 2014. [Online].
- [24] EasyFit, "EasyFit Website," EasyFit, 2017. [Online]. Available: <http://www.mathwave.com/easyfit-distribution-fitting.html>. [Accessed 3 August 2019].
- [25] Anylogic, "Anylogic 8.4 Website," Anylogic, February 2019. [Online]. Available:

- <https://www.anylogic.com/features/>. [Accessed 3 August 2019].
- [26] S. Robinson and A. Ioannou, "The Problem of the Initial Transient: Techniques for Estimating the Warm-up Period for Discrete-Event Simulation Models," 2004.
- [27] V. PA, H. J and W. TR, "Estimating the Steady State Mean from Short Transient Simulations," in *Proceedings of the 1996 Winter Simulation Conference*, Piscataway, 1996.
- [28] P. D. D. Ivanov, Operations and Supply Chain Simulation with Anylogic 7.2, Berlin: Berlin School of Economics and Law (preprint), 2016.
- [29] I. OptTek Systems, "OptQuest The world's leading simulation optimization engine," OptTek Systems, Inc., 2020. [Online]. Available: <https://www.opttek.com/products/optquest/#:~:text=OptQuest%20is%20our%20proprietary%20simulation,search%2C%20to%20name%20a%20few..> [Accessed 21 June 2020].
- [30] J. D. Little, "A Proof of the Queuing Formula," *Operations Researches*, vol. 9, no. 3, pp. 383-387, 1961.

### Data Availability Statement

All data underlying the results are available as part of the article and no additional source data are required.

### Consent

There is no written participant data or information in the article.

### Competing Interests

No competing interests were disclosed

### Grant Information

The author(s) declared that no grants were involved in supporting this work.

# Analytical and Graphical Optimal Synthesis of Crank-Rocker Four Bar Mechanisms for Achieving Targeted Transmission Angle Deviations

Sabry El-Shakery, Rokaya Ramadan, Khaled Khader\*

Production Engineering and Mechanical Design Department, Faculty of Engineering, Menoufia University, Egypt

Received February 28 2020

Accepted August 27 2020

## Abstract

This paper presents a detailed methodology to optimally synthesize links' lengths of planar Crank-Rocker (C-R) mechanism to achieve a targeted design with definite transmission angle deviation. Analytical and graphical proposed methodologies are applied to three different case studies; each satisfies a definite case (task). The analytical methodology is based on deducing six design equations with equality constraints, which represent relations between the desired case conditions and the mechanism's lengths. Meanwhile, deflection and transmission angles; the time ratio limits or output angular stroke can be easily obtained. Furthermore, optimal synthesized results can fulfil any definite case requirements which can be represented using the corresponding six deduced equations. The optimal charts are presented to quickly obtain the optimal (C-R) mechanism's lengths, which are achieving the targeted transmission angles deviations. Consequently, the designers can easily select optimal synthesized crank-rocker mechanisms' lengths, instead of time consuming of optimization calculations. Also, this paper presented a fast-graphical methodology to directly obtain an optimal synthesized (C-R) mechanism's lengths. This methodology requires only identifying the design case related to the chosen mechanism class and the desired transmission angle deviations through giving the minimum and maximum transmission angles ( $\gamma_{min}$  and  $\gamma_{max}$ ). Moreover, a direct relation between the mini-max transmission angle deviations, the (C-R) mechanisms classes and the performance parameters can be presented. Hence, this facilitates the specialists' mission in designing (C-R) mechanisms for special uses as driving conveying, screening and shaking mechanisms.

© 2020 Jordan Journal of Mechanical and Industrial Engineering. All rights reserved

Keywords: Synthesis, Optimization, Crank-rocker mechanism, Transmission angle, Mechanism Design;

## Nomenclatures

C-R	Crank-Rocker mechanism
$J$	Jacobian of the system
$l$	The longest link of the mechanism
$R_1$	The fixed link of the mechanism
$R_2$	The crank link of the mechanism
$R_3$	The coupler link of the mechanism
$R_4$	The rocker link of the mechanism
$s$	The shortest link of the mechanism
$TR$	Time ratio
$p$	Link is not the shortest or longest links
$q$	Link is not the shortest or longest links
$x_n$	The design variables
$\epsilon$	A certain tolerance
$\delta$	Deflection angle
$\gamma$	The transmission angle
$\gamma_{min}$	The minimum transmission angle
$\gamma_{max}$	The maximum transmission angle
$\gamma_i$	Angle $\gamma$ at initial position of $R_4$
$\gamma_f$	Angle $\gamma$ at final position of $R_4$
$\theta_1$	The angular position of the fixed link
$\theta_2$	The crank angular position

$\theta_3$	The coupler angular position
$\theta_4$	The rocker angular position
$\theta_{3i}$	Angular position of $R_3$ at initial position
$\theta_{3f}$	Angular position of $R_3$ at final position
$\theta_{3n}$	Angular position of $R_3$ at 1 <sup>st</sup> extreme position
$\theta_{3x}$	Angular position of $R_3$ at 2 <sup>nd</sup> extreme position
$\theta_{4i}$	Initial angular position of $R_4$
$\theta_{4f}$	Final angular position of $R_4$
$\Delta_1$	Deviation of $\gamma_{min}$
$\Delta_2$	Deviation of $\gamma_{max}$
$\Delta_{cr}$	Deviation of critical values of $\gamma$
$\Delta_l$	Certain deviation of links

## 1. Introduction

The four-bar mechanism is commonly employed in different mechanical engineering applications. The main components of these planar mechanisms are links, joints, or pairs that satisfy the requirements of many practical engineering applications. Four bar Crank-Rocker (C-R) mechanism is the most applied type of planar mechanisms in mechanical systems and devices. Furthermore, one of the

\* Corresponding author e-mail: khkhm62@hotmail.com

main effective design criteria of the planar mechanism is the transmission angle. The planar four bar mechanism's transmission angle is the one between the output and the coupler links. The optimal values of this angle variation are around  $90^\circ$ . Generally, synthesis of the crank rocker four bar mechanisms has been discussed through the last decades. In earlier studies, the problem of optimizing the transmission angle of the crank-rocker mechanism is investigated in [1], which deals with a least square solution. In addition, a theoretical procedure for synthesizing four bar function generation with keeping the transmission angle in a specified range is proposed by Gupta in [2]. While graphical and analytical synthesizes of the crank rocker four bar mechanisms are introduced in [3], where the results are depending on maximizing the minimum of the transmission angle. Moreover, a synthesis procedure which satisfies a prescribed time ratio and rocker's angular swinging amplitude is presented in [4], which optimizes the required definite objective function. Also, synthesis equations are developed in [5] dealing with position, path, function generation and transmission angle constraints of four bar mechanisms to denote an approximation of the design region.

An analytical method for synthesizing the crank rocker mechanism with good quality motion and unit time ratio is proposed in [6], which introduces the synthesized results as a design chart. Furthermore, the transmission quality of planar and spherical linkages is discussed considering the zero mean linkages definition in [7]. While, a graphical method for designing the optimal links lengths of crank rocker mechanism is introduced in [8]. This method presents the synthesized mechanism's lengths depending on initial crank angle, minimum transmission angle, rocker link's amplitude and the two crank angles of the dead center positions of the rocker link. A synthesis algorithm for the planar four-bar mechanism with a single degree of freedom is investigated in [9]. This algorithm is dealing with the synthesized maximum deviation of transmission angle which is less than a certain specified bound. The graphical and analytical approaches of synthesizing (C-R) mechanisms considering the design parameters, such as rocker's swing angle, transmission angle and time ratio are developed in [10] associated with design charts via some specified parameters. The transmission angle's influence on the different parameters of a mechanism (for example; friction, mechanical advantage, pressure angle, transmission force, velocity, acceleration, input crank angle, tolerance and the performance sensitivity) is discussed in [11]. Furthermore, various mechanism's defects, such as branching, order, circuit and poor transmission angle are introduced in [12], in addition to present the rectification solution for successful synthesis. Synthesizing methodology of the planar four bar mechanism lengths for generating a certain motion is explained in [13], which depends on minimizing the maximum deviation of transmission angle. Furthermore, an analytical optimization of (C-R) mechanism through maximizing the minimum transmission angle is presented in [14]. Moreover, design nomograms for directly synthesizing the crank rocker mechanism links' ratios with a definite synthesized transmission angle range are given in [15]. Also, an approach dealing with the mechanism's lengths and transmission angle deviations is presented in [16]. On the

other hand, a force transmissivity index is proposed for the planar mechanisms in [17], this index is based on the concepts of static force analysis, transmission angle deviation and power flow. Likewise, the influence of joint's clearance on path generation considering the transmission angle of four bar mechanism is investigated in [18]. Many published researches have been devoted to the optimal synthesis of (C-R) mechanism using suitable design optimization techniques. Some of these techniques are dealing with a specified path generation [19-26] and motion generation in addition to the design for finitely separated positions [27-30] considering the transmission angle as a design constraint.

In this paper, the transmission angle deviation is adopted as the desired task. Consequently, this paper presents a detailed methodology to optimally synthesize links' lengths of planar crank-rocker mechanism to achieve the targeted designs with definite transmission angle deviations. This suggested that the analytical methodology is based on deriving a set of nonlinear equations. The Newton-Raphson's iterative numerical technique can be employed using the MATLAB software in order to simultaneously solve these nonlinear equations. Three different case studies are discussed in this paper. The first case considers the deviations of minimum and maximum transmission angles, which are equal around  $90^\circ$  as mentioned in [15, 16]. While the second case exists when the total value of the minimum transmission angle's deviation from  $90^\circ$  can be increased more than the total value of the maximum transmission angle's deviation from  $90^\circ$  that is kept at a constant small value. Conversely, the reverse of the second case study represents the third case condition. This third case exists when the total value of the maximum transmission angle's deviation from  $90^\circ$  can be increased more than the total value of deviation of the minimum transmission angle from  $90^\circ$ . Moreover, six design equality constraints equations can be deduced using some mathematical manipulation for each mechanism's desired condition. Also, these constraints clarify a direct relation between the mini-max transmission angle deviations, the (C-R) mechanisms classes and their performance.

Fortunately, if at least one of these deduced equations can be verified, the remaining conditions or equations can be also verified. This reveals the effectiveness of the proposed methodology. This methodology could be used directly to construct the required optimal (C-R) mechanism's lengths. Likewise, each case's optimal numerical solution can be compared with those of the other corresponding deduced equations of some approaches in the published literature. Finally, an effective simple graphical methodology is introduced in order to directly construct such optimal mechanisms through fast and simple steps.

## 2. Methodology

The methodology is organized in four steps. The first step is the identification of an initial feasible design domain, while the second one is selecting the main required parameters to synthesize the (C-R) mechanism's lengths satisfying a definite condition of transmission angle deviations. The third one is deducing six design equations as equality constraints for achieving the optimal (C-R) mechanism lengths. Finally, in the fourth step either the

Newton-Raphson's iterative numerical technique can be used for obtaining the optimal mechanism lengths or the graphical method to quickly obtain the optimal lengths.

2.1. Initial feasible design domain (F.D.D)

Crank-Rocker mechanism is shown in Fig. 1. This (C-R) mechanism contains an input link having a full rotation that is called a crank ( $R_2$ ) and an output link that is called rocker ( $R_4$ ) which oscillates between two dead-center positions as shown in Fig. 2. Also, links ( $R_2$ ) and ( $R_4$ ) are connected to the fixed link ( $R_1$ ) by kinematics pairs  $O_2$  and  $O_4$ , respectively. Coupler link ( $R_3$ ) connects ( $R_2$ ) with ( $R_4$ ).

Clearly, the Newton-Raphson's iterative numerical method needs effective initial values for solving the deduced nonlinear equations. These initial values must be assumed within the following suitable feasible design domain.

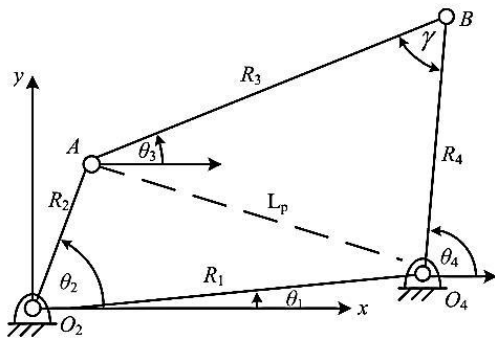


Figure 1: The crank-rocker mechanism

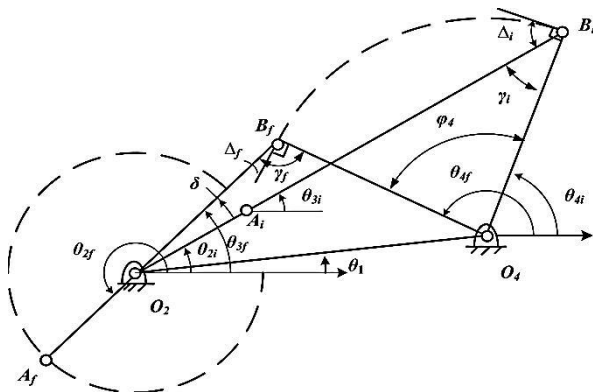


Figure 2: The two extreme positions of (C-R) mechanism

2.1.1. Mechanism Links' Lengths Domain

Planar kinematic chains have three inversions, as shown in Fig. 3. These three inversions of such planar kinematic chains can construct two different crank-rocker mechanisms when the Grashof's criterion is valid as stated in [12] and [30], as;  $s+l < p+q$ .

Where, ( $s$ ) denotes the shortest link of the mechanism, ( $l$ ) denotes the longest link and ( $p, q$ ) denote the lengths of the other two links. In addition, ( $s$ ) is the input link of length ( $R_2$ ), while the fixed link of length ( $R_1$ ) is any link besides the input link ( $R_2$ ). Furthermore, suggested limitations of these links ( $s, p, q$  and  $l$ ), are;

$$0.2 \leq s_{min} \leq s \leq s_{max}, s \leq p \leq p_{max}, p \leq q \leq q_{max} \text{ and } q \leq l \leq l_{max} \leq 1.1m$$

Where, the maximum value of any link's length equals to its minimum value plus a suggested certain deviation

which equals to ( $\Delta l$ ). The numerical solution is presented for the inversions of the three different kinematic chain of links ( $s, p, q$  and  $l$ ) arrangements, which realize six possible (C-R) lengths domain considering  $\Delta l = 0.04m$  as shown in Table 1. Generally, each mechanism can be represented as follows:

- M1<sub>1</sub>:  $R_2 < R_3 < R_4 < R_1$ ; M1<sub>2</sub>:  $R_2 < R_1 < R_4 < R_3$
- M2<sub>1</sub>:  $R_2 < R_4 < R_1 < R_3$ ; M2<sub>2</sub>:  $R_2 < R_4 < R_3 < R_1$
- M3<sub>1</sub>:  $R_2 < R_1 < R_3 < R_4$ ; M3<sub>2</sub>:  $R_2 < R_3 < R_1 < R_4$

In addition, the mechanism lengths must verify the following inequality constraints as;

$$G_f = ((p + q) / (s + l)) - 1 > 0 \tag{1}$$

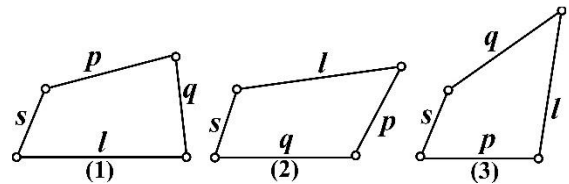


Figure 3: Three kinematic planar chains

Table 1. Six possible crank-rocker mechanisms lengths

$R_i$	Kinematic chain (1)		Kinematic chain (2)		Kinematic chain (3)	
	M1 <sub>1</sub>	M1 <sub>2</sub>	M2 <sub>1</sub>	M2 <sub>2</sub>	M3 <sub>1</sub>	M3 <sub>2</sub>
$R_1$	l	p	q	l	p	q
$R_2$	s	s	s	s	s	s
$R_3$	p	l	l	q	q	p
$R_4$	q	q	p	p	l	l

2.1.2. Prescribed Timing Domain

The frame ( $R_1$ ) has a fixed angular position ( $\theta_1 \geq 0$ ). In order to grantee a full mobility rotation of the input link ( $R_2$ ) with avoiding order and branch defects, the following inequalities should be achieved as stated in [12] as follows;

$$0 \leq \theta_2 \leq 360^\circ, \theta_2^{i-1} \leq \theta_2^i \leq \theta_2^{i+1} \text{ and } \sin \gamma > 0 \tag{2}$$

Where, ( $\theta_2$ ) describes the crank angular position and ( $i$ ) denotes angular position number. Also, ( $\gamma$ ) denotes the transmission angle, which is shown in Fig. 1. The transmission angle is given by the following equation;

$$\gamma = \theta_4 - \theta_3, 40^\circ \leq \gamma \leq 140^\circ, \text{ as presented in [11]} \tag{3}$$

Where,  $\theta_3$  and  $\theta_4$  are the coupler and rocker angular positions. If the obtained values of the mechanism synthesis are outside the prescribed domain, the selection of the initial values must be repeated using other modified values until the obtained results fall within the prescribed feasible domain. One or two of the six mechanisms tabulated in Table 1 represent the feasible design domain which can be considered for constructing the required optimal (C-R) mechanism.

2.2. The Optimal Synthesis of (C-R) Mechanism

The proposed technique for synthesizing the (C-R) mechanism is dealing with finding the optimal mechanism's lengths. These mechanism's lengths are synthesized to verify the definite minimum and maximum transmission angle deviations. Whereas, the optimum value of transmission angle ( $\gamma$ ) is close to  $90^\circ$  as much as possible with a recommended maximum tolerance about  $\pm 50^\circ$  as mentioned in [11] and [30] for achieving smooth operation without jerky movements and maintaining a good quality of

force transmission. Transmission angle ( $\gamma$ ) can be obtained as stated in [1, 2] and [11] as follows;

$$\cos \gamma = \frac{R_3^2 + R_4^2 - R_1^2 - R_2^2 + 2R_1R_2 \cos(\theta_2 - \theta_1)}{2R_3R_4} \quad (4)$$

The minimum and maximum transmission angles ( $\gamma_{min}$ ,  $\gamma_{max}$ ) are shown in Fig. 4. The values of angles ( $\gamma_{min}$ ,  $\gamma_{max}$ ) can be formulated using the first derivative of Eq. (4) with respect to  $\theta_2$  which equals to zero at  $(\theta_2 - \theta_1) = 0$  and  $(\theta_2 - \theta_1) = 180^\circ$ . Hence,  $\gamma_{min}$  and  $\gamma_{max}$  can be obtained as presented in [6] using the following equations;

$$\cos \gamma_{min} = \frac{R_3^2 + R_4^2 - (R_1 - R_2)^2}{2R_3R_4} \quad (5)$$

$$\cos \gamma_{max} = \frac{R_3^2 + R_4^2 - (R_1 + R_2)^2}{2R_3R_4} \quad (6)$$

The deviations  $\Delta_1$ ,  $\Delta_2$  and  $\Delta_{cr}$  of the minimum, maximum and critical values of the transmission angles from  $90^\circ$  are respectively presented in [1] as follows;

$$\Delta_1 = 90^\circ - \gamma_{min}, \Delta_2 = \gamma_{max} - 90^\circ \text{ and } \Delta_{cr} = \text{Max}[\Delta_1, \Delta_2] \quad (7)$$

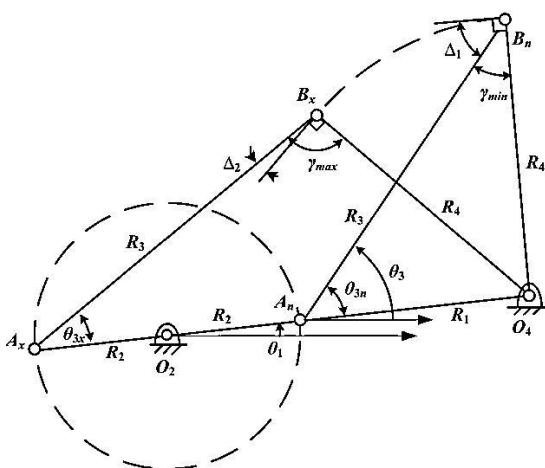


Figure 4: Minimum and maximum transmission angles of (C-R) mechanism

In addition, ( $\gamma_i$ ) and ( $\gamma_f$ ) are the transmission angles at the initial and final angular positions of the rocker link as shown in Fig. 2, both ( $\gamma_i$ ) and ( $\gamma_f$ ) can be respectively computed using Eq. (8) and Eq. (9) as follows;

$$\gamma_i = \cos^{-1} \left( \frac{R_4^2 + (R_3 + R_2)^2 - R_1^2}{2R_4(R_3 + R_2)} \right) \quad (8)$$

$$\gamma_f = \cos^{-1} \left( \frac{R_4^2 + (R_3 - R_2)^2 - R_1^2}{2R_4(R_3 - R_2)} \right) \quad (9)$$

Where  $\Delta_i$  and  $\Delta_f$  which are shown in Fig. 2 can be computed as follows;

$$\Delta_i = (90^\circ - \gamma_i) < \Delta_1 \quad \text{and} \quad \Delta_f = (\gamma_f - 90^\circ) < \Delta_2 \quad (10)$$

Applying sine and cosine law for two triangles ( $A_nB_nO_4$  and  $A_xB_xO_4$ ), which are shown in Fig. 4, the following equations can be obtained as follows;

$$\frac{R_1 - R_2}{\sin \gamma_{min}} = \frac{R_4}{\sin \theta_{3n}} \quad (11)$$

$$\frac{R_4}{\sin \theta_{3n}} = \frac{R_3}{\sin(180^\circ - \theta_{3n} - \gamma_{min})} \quad (12)$$

$$\frac{R_1 + R_2}{\sin \gamma_{max}} = \frac{R_4}{\sin \theta_{3x}} \quad (13)$$

$$\frac{R_4}{\sin \theta_{3x}} = \frac{R_3}{\sin(180^\circ - \theta_{3x} - \gamma_{max})} \quad (14)$$

$$\cos \theta_{3n} = \frac{(R_1 - R_2)^2 + R_3^2 - R_4^2}{2R_3(R_1 - R_2)} \quad (15)$$

$$\cos \theta_{3x} = \frac{(R_1 + R_2)^2 + R_3^2 - R_4^2}{2R_3(R_1 + R_2)} \quad (16)$$

Where  $\theta_{3n} = \theta_3 - \theta_1$  at  $(\theta_2 = \theta_1)$  and  $\theta_{3x} = \theta_3 - \theta_1$  at  $(\theta_2 = 180^\circ + \theta_1)$ .

Thus, the synthesis can be performed by deriving six nonlinear equations in six desired mechanism's parameters;  $R_1$ ,  $R_2$ ,  $R_3$  and  $R_4$ , in addition to coupler link positions ( $\theta_{3n}$ ,  $\theta_{3x}$ ) as unknowns.

The six nonlinear equations are derived as functions of ( $\Delta_1$ ,  $\Delta_2$ ) which can be solved using the Newton-Raphson iterative numerical method [30, 31].

The Eqs. (5-7) in addition to Eqs. (11-14) can be rewritten in the form of  $[f_n(x_n)] = [0]$  using mathematical manipulation as follows;

$$[f_n(x_n)] = \begin{bmatrix} f_1 \\ f_2 \\ f_3 \\ f_4 \\ f_5 \\ f_6 \end{bmatrix} = \begin{bmatrix} R_3^2 + R_4^2 - (R_1 - R_2)^2 - 2R_3R_4 \sin \Delta_1 \\ R_3^2 + R_4^2 - (R_1 + R_2)^2 + 2R_3R_4 \sin \Delta_2 \\ (R_1 - R_2) \sin \theta_{3n} - R_4 \cos \Delta_1 \\ R_4 \cos(\theta_{3n} - \Delta_1) - R_3 \sin \theta_{3n} \\ (R_1 + R_2) \sin \theta_{3x} - R_4 \cos \Delta_2 \\ R_4 \cos(\theta_{3x} + \Delta_2) - R_3 \sin \theta_{3x} \end{bmatrix} = [0] \quad (17)$$

The design variables ( $x_n$ ) are;

$$[x_n] = [R_1 \ R_2 \ R_3 \ R_4 \ \theta_{3n} \ \theta_{3x}]^T \quad (18)$$

Furthermore, Jacobian ( $J$ ) of the system is defined as;  $J = [\partial f_n / \partial x_n]_{6 \times 6}$ . Also, the iterative formula is expressed as  $[\Delta x_n] = -[J]^{-1} \cdot [f(x_n)]$ , thus, the determinate of the Jacobian matrix should not equal to zero ( $\det[J] \neq 0$ ).

The successive approximations for a solution can be obtained using the following form  $x_n^{i+1} = x_n^i + \Delta x_n^i$ , the first guess for the solution ( $x_n^i$ ), which lies inside the initial values of the feasible design domain. Consequently, the Newton-Raphson's process takes less number of iterations and less computation time for obtaining the results. A convergence criterion of such system's solution could be achieved when the magnitude of the vector  $f(x_n)$  is smaller than a certain tolerance ( $\epsilon$ ). Where  $|f(x_n)| < \epsilon$  and  $\epsilon = 10^{-5}$ .

The obtained mechanism's lengths  $R_i$  ( $R_1$ ,  $R_2$ ,  $R_3$  and  $R_4$ ) using this solving technique are considered as the optimal mechanism's lengths. If one of these obtained results falls outside the prescribed range (F.D.D), the initial mechanism's lengths should be changed in order to repeat the solving procedure until the optimal mechanism lengths fall within the feasible design domain.

Consequently, these obtained mechanism's lengths are not unique, but these fall within the optimal design domain ( $M1_1$  or  $M2_2$ ).

### 2.2.1. Rocker Swing Angle of the (C-R) Mechanism

Figure 2 shows the swing angle ( $\varphi_4$ ) of the output link ( $R_4$ ) as an angle of oscillation between its angular position's limitations, which depends upon the mechanism's application. The rocker swing angle ( $\varphi_4$ ) can be obtained as presented in [6] as follows;

$$\varphi_4 = \theta_{4f} - \theta_{4i} \quad (19)$$

Where  $\theta_{4i}$  and  $\theta_{4f}$  are the initial and final angular positions of output rocker link ( $R_4$ ). Values of  $\theta_{4i}$  and  $\theta_{4f}$  can be computed as follows;

$$\theta_{4i} = 180^\circ + \theta_1 - \cos^{-1} \left( \frac{R_1^2 + R_4^2 - (R_3 + R_2)^2}{2R_1R_4} \right) \quad (20)$$

$$\theta_{4f} = 180^\circ + \theta_1 - \cos^{-1} \left( \frac{R_1^2 + R_4^2 - (R_3 - R_2)^2}{2R_1R_4} \right) \quad (21)$$

### 2.2.2. Time Ratio of the (C-R) Mechanism

The time ratio ( $TR$ ) between the forward and return angular strokes of the rocker link depends on the mechanism's lengths and the rotation's direction of the crank as shown in Fig. 2.

Time ratio becomes greater than one ( $TR > 1$ ), if the direction of the working (forward) stroke is the same as the rotation direction of the input link; where the value of deflection angle ( $\delta$ ) is positive. Otherwise, ( $TR < 1$ ) and ( $\delta < 0$ ) if these directions are not the same as mentioned in [1, 6, 7]. The time ratio can be formulated as follows;

$$TR = (180^\circ + \delta) / (180^\circ - \delta) \quad (22)$$

Where, ( $\delta$ ) is called the deflection angle which can be formulated as follows;

$$\delta = \theta_{3f} - \theta_{3i} \quad (23)$$

Where, ( $\theta_{3i}$ ) and ( $\theta_{3f}$ ) are the angular positions of the coupler link at initial and final positions as shown in Fig. 2. These angular positions ( $\theta_{3i}$ ) and ( $\theta_{3f}$ ) can be formulated as follows;

$$\theta_{3i} = \cos^{-1} \left( \frac{R_1^2 - R_4^2 + (R_3 + R_2)^2}{2R_1(R_3 + R_2)} \right) + \theta_1 \quad (24)$$

$$\theta_{3f} = \cos^{-1} \left( \frac{R_1^2 - R_4^2 + (R_3 - R_2)^2}{2R_1(R_3 - R_2)} \right) + \theta_1 \quad (25)$$

### 2.3. Design Equality Constraints of the Synthesized (C-R) Mechanism Lengths

Using the previous analysis and some mathematical manipulation, the general constraint equations can be deduced as follows;

$$TR = \frac{180^\circ + (\varphi_4 - (\gamma_f - \gamma_i))}{180^\circ - (\varphi_4 - (\gamma_f - \gamma_i))} \quad (26)$$

$$\varphi_4 = \gamma_f - \gamma_i + \delta \quad (27)$$

$$\gamma_{\min} + \gamma_{\max} = 180^\circ - \lambda_d \quad (28)$$

$$\gamma_i + \gamma_f = 180^\circ - \lambda_{if} \quad (29)$$

$$S_s = \frac{2R_1R_2}{R_3R_4} \quad (30)$$

$$S_d = \frac{R_3^2 + R_4^2 - R_1^2 - R_2^2}{R_3R_4} \quad (31)$$

The previous six deduced equality equations may be called the mechanism's characteristics, where;

$$S_s = \sin \Delta_1 + \sin \Delta_2 = 2 \sin (0.5\lambda_s) \cdot \cos (0.5\lambda_d)$$

$$S_d = \sin \Delta_1 - \sin \Delta_2 = 2 \cos (0.5\lambda_s) \cdot \sin (0.5\lambda_d)$$

$$\lambda_d = \Delta_1 - \Delta_2, \lambda_s = \Delta_1 + \Delta_2, \lambda_{if} = \Delta_i - \Delta_f, \theta_1 = 0$$

Equations (24) and (25) can be rewritten using some mathematical manipulation as follows;

$$\theta_{3i} = \cos^{-1} \left( \frac{2(R_3 + R_2) - R_4 S_d}{2R_1 + R_4 S_s} \right) = \cos^{-1}(c + c_i) \quad (32)$$

$$\theta_{3f} = \cos^{-1} \left( \frac{2(R_3 - R_2) - R_4 S_d}{2R_1 - R_4 S_s} \right) = \cos^{-1}(c + c_f) \quad (33)$$

$$\text{Where; } c = \frac{R_3}{R_1}, c_i = \left( \frac{R_1^2 - R_4^2}{2R_1(R_3 + R_2)} \right) - \left( \frac{R_3 - R_2}{2R_1} \right)$$

$$\text{and } c_f = \left( \frac{R_1^2 - R_4^2}{2R_1(R_3 - R_2)} \right) - \left( \frac{R_3 + R_2}{2R_1} \right)$$

$$\text{So; } \theta_{4i} = \gamma_i + \theta_{3i}, \theta_{4f} = \gamma_f + \theta_{3f} \quad (34)$$

The previous six deduced Eqs. (26-31) can be used as general equations for any case study or task of transmission angles deviations as follow;

#### 2.3.1. The First Case Study: ( $\Delta_1 = \Delta_2 = \Delta$ )

For the first case, the previous six deduced Eqs. (26-31) can be rewritten after substituting the deviations  $\Delta_1 = \Delta_2 = \Delta$  as follows;

$$TR = 1, \text{ as in [1, 3, 5, 6]} \quad (35)$$

$$\varphi_4 = 2(90^\circ - \gamma_i) = \gamma_f - \gamma_i \quad (36)$$

$$\gamma_{\min} + \gamma_{\max} = 180^\circ, \text{ as in [3, 6, 23]} \quad (37)$$

$$\gamma_i + \gamma_f = 180^\circ \quad (38)$$

$$\sin \Delta = \frac{R_1R_2}{R_3R_4}, \text{ i.e. } \cos \gamma_{\min} = \pm \frac{R_1R_2}{R_3R_4}, \text{ as in [3]} \quad (39)$$

$$R_3^2 + R_4^2 - R_1^2 - R_2^2 = 0, \text{ as in [1-3] and [7, 23]} \quad (40)$$

Hence, these pervious equations imply the following necessary and sufficient conditions that must be verified as follows;

$$\theta_{3i} = \theta_{3f} = \cos^{-1}(R_3 / R_1) = \cos^{-1}(c) \quad (41)$$

Where; ( $\Delta_i = \Delta_f$ ) and ( $\lambda_d, \lambda_{if}, S_d, c_f, c_i, \delta$ ) are zeros values.

#### 2.3.2. The Second Case Study: ( $\Delta_1 > \Delta_2$ )

For the second case, the six deduced Eqs. (26-31) can be rewritten after substituting the deviations  $\Delta_1 = \Delta$  and  $\Delta_1 > \Delta_2$  as follows;

$$TR = \frac{180^\circ + \varphi_4 - \Delta_f - \Delta_i}{180^\circ - \varphi_4 + \Delta_f + \Delta_i}, \text{ where, } (TR > 1) \quad (42)$$

$$\varphi_4 = (\gamma_f - \gamma_i + \delta) > \gamma_f - \gamma_i \quad (43)$$

$$\gamma_{\min} + \gamma_{\max} = (180^\circ - \lambda_d) < 180^\circ \quad (44)$$

$$\gamma_i + \gamma_f = (180^\circ - \lambda_{if}) < 180^\circ \quad (45)$$

$$\cos \gamma_{\min} - \cos \gamma_{\max} = \frac{2R_1R_2}{R_3R_4} \quad (46)$$

$$R_3^2 + R_4^2 - R_1^2 - R_2^2 = (R_3R_4) \cdot (\cos \gamma_{\min} + \cos \gamma_{\max}) \quad (47)$$

The conditions  $(R_3^2 + R_4^2 - R_1^2 - R_2^2) > 0$  and  $(TR > 1)$  are mentioned in [1] and [14]. Hence, these pervious equations imply the following necessary and sufficient conditions that must be verified as follows;

$$\theta_{3i} = \cos^{-1}(c + c_i), \theta_{3f} = \cos^{-1}(c + c_f) \quad (48)$$

Where;  $\Delta_i > \Delta_f, c_f < c_i, \theta_{3f} > \theta_{3i}$  and ( $\lambda_d, \lambda_{if}, S_d, \delta$ ) are positive definite values.

#### 2.3.3. The Third Case Study: ( $\Delta_1 < \Delta_2$ )

For the third case, the six deduced Eqs. (26-31) can be rewritten after substituting the deviations  $\Delta_2 = \Delta$  and  $\Delta_1 < \Delta_2$  as follows;

$$TR = \frac{180^\circ + \varphi_4 - \Delta_f - \Delta_i}{180^\circ - \varphi_4 + \Delta_f + \Delta_i}, \text{ where, } (TR < 1) \quad (49)$$

$$\varphi_4 = (\gamma_f - \gamma_i + \delta) < \gamma_f - \gamma_i \quad (50)$$

$$\gamma_{\min} + \gamma_{\max} = (180^\circ - \lambda_d) > 180^\circ \quad (51)$$

$$\gamma_i + \gamma_f = (180^\circ - \lambda_{if}) > 180^\circ \quad (52)$$

The conditions ( $TR < 1$ ) and  $(R_3^2 + R_4^2 - R_1^2 - R_2^2) < 0$  are mentioned in [1] and [14]. Hence, these previous equations imply the following necessary and sufficient conditions that must be verified Eqs. (46-48).

Where;  $\Delta_i < \Delta_f$ ,  $c_f > c_i$ ,  $\theta_{3f} < \theta_{3i}$  and  $(\lambda_d, \lambda_{if}, S_d, \delta)$  are negative definite values.

## 2.4. Graphical Synthesis Methodology

The graphical methods have been widely adopted in several fields such as mechanisms design and control for their simplicity and competency [32-34]. In this paper, the suggested graphical methodology can be easily and rapidly conducted according to six sequential steps as follows;

The first step is the identification of the synthesis case study (task) either by identifying the class of (C-R) mechanism or the desired transmission angle deviations through giving the desired values of  $\Delta_1$  and  $\Delta_2$ . Hence, the minimum and maximum transmission angles ( $\gamma_{min}$  and  $\gamma_{max}$ ) can be directly calculated.

The second step is assuming the initial angular position ( $\theta_{3i}$ ) of the coupler link ( $R_3$ ), where ( $\theta_{3i}$ ) can be proportionally assumed within the values ( $30^\circ, 30.8^\circ, 34^\circ$  and  $37.5^\circ$ ), which are respectively corresponding to the values ( $85^\circ, 75^\circ, 60^\circ$  and  $45^\circ$ ) of ( $\gamma_{min}$ ) for the first case ( $\Delta_1 = \Delta_2$ ). Also, ( $\theta_{3i}$ ) can be assumed within the values ( $30^\circ, 32.8^\circ, 35.8^\circ$  and  $37.4^\circ$ ), which are corresponding to the same previous values of ( $\gamma_{min}$ ) for the second case ( $\Delta_1 > \Delta_2$ ). Moreover, ( $\theta_{3i}$ ) can be proportionally assumed within the values ( $29^\circ, 28^\circ, 27.7^\circ$  and  $37.5^\circ$ ), which are corresponding to the values ( $100^\circ, 105^\circ, 120^\circ$  and  $135^\circ$ ) of ( $\gamma_{max}$ ) for the third case ( $\Delta_1 < \Delta_2$ ).

Assuming a value of ( $\lambda_{in}$ ) is the third step. Where, ( $\lambda_{in}$ ) is the difference between initial and minimum transmission angles ( $\gamma_i, \gamma_{min}$ ), hence ( $\gamma_i$ ) can be computed. Value of ( $\lambda_{in}$ ) can be assumed like the previous step using the values ( $0.7^\circ, 2.2^\circ, 5.5^\circ$  and  $10.9^\circ$ ), ( $0.6^\circ, 1.6^\circ, 3.6^\circ$  and  $6.3^\circ$ ) and ( $0.9^\circ, 1.2^\circ, 1.9^\circ$  and  $4.7^\circ$ ) for the three cases, respectively.

The fourth step is assuming a value of ( $\lambda_{if}$ ), where ( $\lambda_{if}$ ) is the difference between final and maximum transmission angles ( $\gamma_f, \gamma_{max}$ ), hence ( $\gamma_f$ ) can be calculated. Value of ( $\lambda_{if}$ ) can be assumed like the second step using the values ( $0.7^\circ, 2.2^\circ, 5.5^\circ$  and  $10.9^\circ$ ), ( $0.6^\circ, 1.7^\circ, 4.1^\circ$  and  $8.5^\circ$ ) and ( $0.9^\circ, 1.1^\circ, 1.7^\circ$  and  $3.4^\circ$ ) for the three cases, respectively.

The fifth step is drawing the Cartesian coordinate  $XO_2Y$ . Thus, the  $xO_2y$  axis can be drawn by rotating  $XO_2Y$  with the angle ( $\theta_1$ ), as shown in Fig. 5. Locate the point ( $O_4$ ) on the line ( $O_2x$ ), where ( $O_2O_4$ ) is a unit length represents the mechanism fixed link. Hence, the first or initial construction line "ICL" ( $ICL = O_2A_iB_i$ ) can be drawn from point ( $O_2$ ) with an inclination angle ( $\theta_{3i}$ ) with respect to the direction of the line ( $O_2O_4$ ). Also, the line ( $O_4B_i$ ) can be drawn from point ( $O_4$ ) with an inclination angle ( $\theta_{3i} + \gamma_i$ ) with respect to the direction of the line ( $O_2x$ ) to intersect the direction of the line (ICL) in the point ( $B_i$ ). Therefore, the length of ( $O_4B_i$ ) represents ( $r_4$ ). Also, the length of ( $O_2B_i$ ) represents ( $r_3 + r_2$ ). Where, the mechanism links proportions ( $r_2, r_3$  and  $r_4$ ) are based on the length of  $R_1$  as;  $r_2 = R_2/R_1$ ,  $r_3 = R_3/R_1$  and  $r_4 = R_4/R_1$ .

The last step is the drawing of an arc with a radius ( $O_4B_i$ ) from the center ( $O_4$ ). Hence, two lines ( $O_4B_f$ ) and ( $B_f O_2$ ) can be drawn using the arc points with keeping the angle between these two lines equals to ( $\gamma_f$ ).

Where, the line ( $O_2B_f$ ) can be considered as the final construction line (FCL). Therefore, the length of ( $O_2B_f$ ) represents ( $r_3 - r_2$ ).

Finally, ( $r_3$ ) equals to half of ( $O_2B_i + O_2B_f$ ). Also, ( $r_2$ ) equals to ( $O_2B_i - r_3$ ). Hence, the desired given data ( $\Delta_1$  and  $\Delta_2$ ) can be checked via the obtained mechanism's ratios ( $r_2, r_3$  and  $r_4$ ).

If these mechanism's ratios satisfy both the desired  $\Delta_1$  and  $\Delta_2$ , the six design constraint equations of the mechanism can be validated. Also, the position of the point ( $B_f$ ) related to the line ICL can denote to the mechanism class number. Where, point ( $B_f$ ) lies on ICL for the first case study of mechanism synthesis which can be named by class I, i.e.; inline or unit time ratio optimal mechanisms. While, the point ( $B_f$ ) lies over ICL for the second case study of mechanism synthesis (class II mechanisms), while ( $B_f$ ) lies down ICL for the third case study (class III mechanisms).

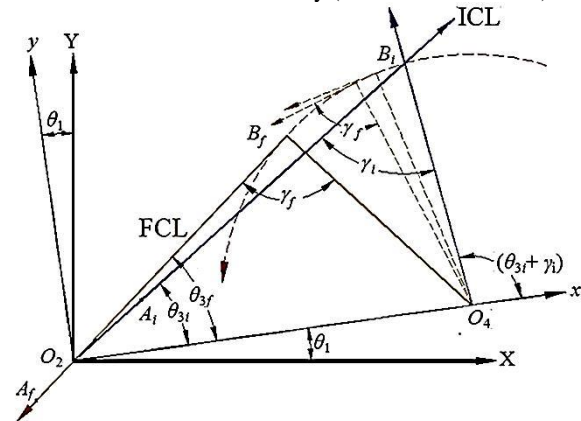


Figure 5: Graphical synthesis methodology

## 3. Results and Discussions

The presented analytical methodology can be used for achieving the targeted transmission angle deviations via the corresponding optimal mechanism links' lengths. These optimal links' lengths can be presented as lengths' proportions ( $r_2, r_3$  and  $r_4$ ) to facilitate the selection process for the proper mechanisms, which depends on a working area of various applications.

The optimal synthesized results concerned with the presented three case studies in the following sections.

### 3.1. Results of the First Case Study: ( $\Delta_1 = \Delta_2 = \Delta$ )

The optimal synthesized (C-R) mechanism's proportions in addition to the other important parameters of this case study are illustrated in Fig. 6 and Fig. 7. These are dealing with the equality deviations ( $\Delta_1 = \Delta_2 = \Delta$ ) which increase from  $5^\circ$  to  $60^\circ$ .

The obtained results reveal the following significant observations;

Optimal mechanism's proportions  $r_2, r_4$  of the type M22:  $r_2 < r_4 < r_3 < 1$  increase as shown in Fig. 6 and the tabulated results in Table 2.

Obviously, the sum of the values ( $\gamma_{min} + \gamma_{max}$ ) equals to ( $180^\circ$ ) and ( $\gamma_i + \gamma_f$ ) equals to ( $180^\circ$ ). Also,  $\Delta_i = \Delta_f$  where  $\Delta_i$  increases from  $4.3^\circ$  to  $45^\circ$ .

Moreover, the deflection angle ( $\delta$ ) is zero i.e.  $\theta_{3f} = \theta_{3i} = \theta_{2i}$  where  $\theta_{3f}$  increases from  $30^\circ$  till  $35.4^\circ$ . These results indicate that  $c_f = c_i = 0$  and  $c = r_3$  for any mechanism's proportions in addition to  $\theta_{3f} = \theta_{3i} = \theta_{2i} = \cos^{-1}(c)$  that verify the Eq. (41), hence,  $TR = 1$ .

Also, the output angular stroke ( $\varphi_4 = \gamma_f - \gamma_i$ ) increases from  $8.6^\circ$  till  $89.9^\circ$  and the difference ( $\lambda_{in}$ ) increases from  $0.67^\circ$  till  $11.75^\circ$  as ( $\Delta$ ) increases from  $5^\circ$  to  $50^\circ$ .

All these obtained results of the first case study concur with the six deduced design equality constraints in Eqs. (35-40), which may fall inside the required feasible design domain (F.D.D). Otherwise, other results that may appear through increasing ( $\Delta$ ) greater than  $50^\circ$  lies within the unfeasible design domain (U.F.D.D). This is due to the jamming and/or locking problems.

All the optimal synthesized results of (C-R) mechanism satisfying the conditions of this case study can be denoted by mechanisms of class I. Many of the previous literature as [1-3] and [7] are dealing with this kind of mechanisms which can be called zero deflection angles, zero mean, central, inline and unit time ratio.

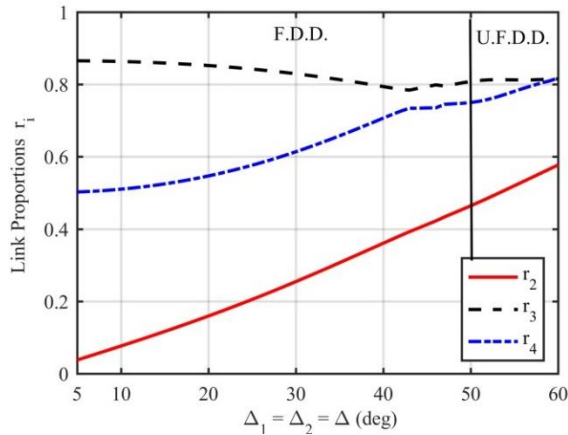


Figure 6: Optimal results of (C-R) mechanism's proportions of the first case study

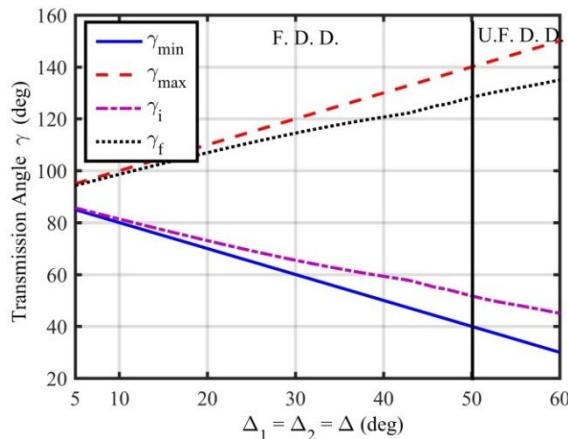


Figure 7: Transmission angles of optimal (C-R) mechanism of the first case study

3.2. Results of the Second Case Study: ( $\Delta_1 > \Delta_2, \Delta_1 = \Delta$ )

The results of the optimal synthesized mechanism's proportions, in addition to the other important parameters of this case study are illustrated in Figs. 8 in addition to Fig. 9. These are dealing with the first deviation ( $\Delta_1 = \Delta$ ) which increases from  $6^\circ$  to  $60^\circ$  while the second deviation ( $\Delta_2$ ) is kept at a fixed value of  $5^\circ$ .

The obtained results reveal the following important notes;

The optimal mechanism's proportions increase as shown in Fig. 8 in addition to the tabulated results in Table 3.

Clearly, the sum of both values ( $\gamma_{min} + \gamma_{max}$ ) and ( $\gamma_i + \gamma_f$ ) are less than  $(180^\circ)$ . Furthermore, the value of ( $\Delta_i$ ) is greater than the value of ( $\Delta_f$ ) where  $\Delta_i$  increases from  $(5.2^\circ)$  to  $(49.3^\circ)$  and  $\Delta_f$  decreases from  $(4.2^\circ)$  to  $(-13.5^\circ)$ .

Furthermore, the value of the deflection angle ( $\delta$ ) increases from  $0.05^\circ$  to  $31.6^\circ$ , i.e.  $\theta_{3f} > \theta_{3i}$  where  $\theta_{3f}$  increases from  $30.4^\circ$  till  $70.9^\circ$ . Also,  $\theta_{3i}$  increases from  $30.35^\circ$  till  $39.32^\circ$ . These results indicate that  $c_f < c_i$  and  $c = r_3$  in addition to  $\theta_{3f} = \cos^{-1}(c + c_f)$  as well as  $\theta_{3i} = \cos^{-1}(c + c_i)$  which verifies the Eq. (48) for any mechanism's proportions. Besides, the output angular stroke  $\varphi_4 = \gamma_f - \gamma_i + \delta$  increases from  $9.5^\circ$  till  $67.36^\circ$  and the time ratio range is  $1 < TR \leq 1.42$ .

The obtained results of this case study concur with the six deduced design equality constraints in Eqs. (42-47) of M2:  $r_2 < r_4 < r_3 < 1$  and may be to lie inside the required feasible design domain (F.D.D).

The optimal synthesized results of (C-R) mechanism satisfying this case's conditions can be named by mechanisms of class II. Some of the published literature are concerned with these kinds of mechanisms, which can be called positive off-central, positive off-line, more than unity time ratio and positive deflection angle mechanisms.

Table 2. Calculated results of the first case study

Mech. No.	$\Delta^\circ$	$\gamma_{min}^\circ$	$\gamma_{max}^\circ$	$r_2$	$r_3$	$r_4$	$G_f$	$\theta_{3f}^\circ$
1	5	85	95	0.0379	0.8654	0.5025	0.318	30.072
2	15	75	105	0.1167	0.8591	0.5249	0.239	30.783
3	30	60	120	0.2546	0.8295	0.6138	0.150	33.951
4	45	45	135	0.4125	0.7937	0.7350	0.082	37.469
5	60	30	150	0.5773	0.8154	0.8176	0.035	35.377
Mech. No.	$\theta_{3i}^\circ$	$\delta^\circ$	TR	$\varphi_4^\circ$	$\gamma_i^\circ$	$\gamma_f^\circ$	$\Delta_i^\circ$	$\Delta_f^\circ$
1	30.072	0.0	1.0	8.651	85.674	94.326	4.326	4.326
2	30.783	0.0	1.0	25.695	77.153	102.848	12.847	12.847
3	33.951	0.0	1.0	49.008	65.496	114.504	24.504	24.504
4	37.469	0.0	1.0	68.281	55.860	124.140	34.140	34.140
5	35.377	0.0	1.0	89.840	45.080	134.920	44.920	44.920

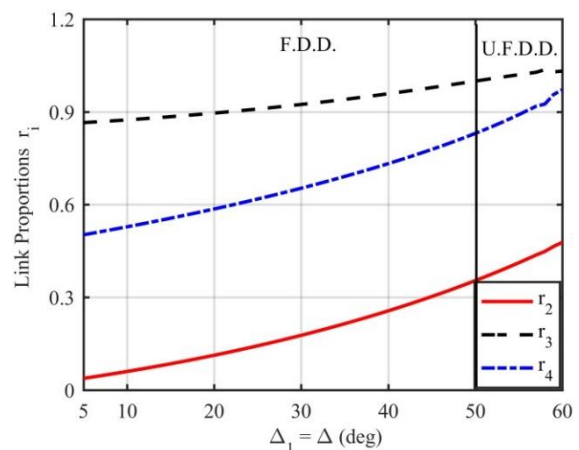


Figure 8: Optimal results of (C-R) mechanism's proportions of the second case study

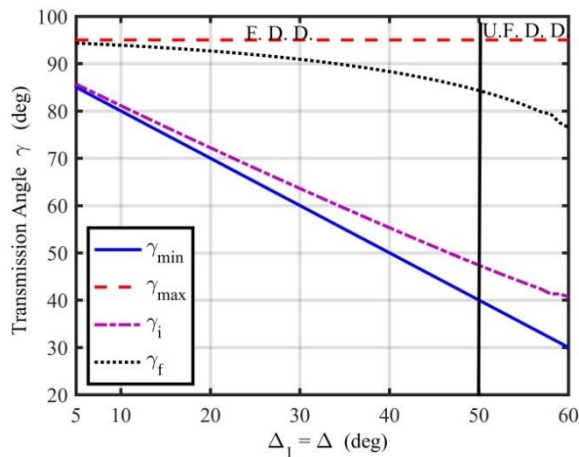


Figure 9: Transmission angles of optimal (C-R) mechanism of the second case study

Table 3. Calculated results of the second case study

Mech. No.	$\Delta^\circ$	$\gamma_{\min}^\circ$	$\gamma_{\max}^\circ$	$r_2$	$r_3$	$r_4$	$G_f$	$\theta_{3f}^\circ$
1	10	80	95	0.0602	0.8743	0.5284	0.323	31.813
2	15	75	95	0.0851	0.8846	0.5561	0.328	33.721
3	30	60	95	0.1772	0.9241	0.6532	0.340	40.773
4	45	45	95	0.3026	0.9786	0.7786	0.349	51.007
5	60	30	95	0.4781	1.0322	0.9718	0.306	70.898
Mech. No.	$\theta_{3i}^\circ$	$\delta^\circ$	$TR$	$\phi_4^\circ$	$\gamma_i^\circ$	$\gamma_f^\circ$	$\Delta_i^\circ$	$\Delta_f^\circ$
1	31.467	0.346	1.004	13.106	81.114	93.874	8.886	3.874
2	32.753	0.969	1.011	17.671	76.626	93.328	13.374	3.328
3	35.808	4.965	1.057	32.268	63.609	90.911	26.392	0.911
4	37.413	13.593	1.163	48.861	51.288	86.555	38.712	-3.455
5	39.327	31.571	1.425	67.366	40.703	76.498	49.297	-13.50

3.3. Results of the Third Case Study: ( $\Delta_1 < \Delta_2$ ,  $\Delta_2 = \Delta$ )

The optimal results of synthesized mechanism's proportions in addition to the other essential parameters of this case study are illustrated in Fig. 10 in addition to Fig. 11. These results are dealing with the second deviation ( $\Delta_2 = \Delta$ ) which increases from  $6^\circ$  to  $60^\circ$  while the first deviation ( $\Delta_1$ ) is kept at a fixed value of  $5^\circ$ .

The obtained results reveal the following significant observations;

The optimal results of mechanism's proportions concerning with the mechanism's type M2<sub>2</sub>:  $r_2 < r_4 < r_3 < 1$  and type M1<sub>1</sub>:  $r_2 < r_3 < r_4 < 1$  are shown in Fig. 10 and the tabulated results in Table 4.

Obviously, the sum of both values ( $\gamma_{\min} + \gamma_{\max}$ ) and ( $\gamma_i + \gamma_f$ ) are greater than ( $180^\circ$ ). Moreover, the value of ( $\Delta_i$ ) less than the value ( $\Delta_f$ ), where  $\Delta_i$  decreases from ( $4.27^\circ$ ) to ( $-2.5^\circ$ ) and  $\Delta_f$  increases from ( $5.7^\circ$ ) till ( $55.99^\circ$ ).

Furthermore, the value of the deflection angle ( $\delta$ ) changes from ( $-0.05^\circ$ ) to ( $-20.9^\circ$ ), i.e.  $\theta_{3f} < \theta_{3i}$ . These results indicate that  $c_f > c_i$  and  $c = r_3$  in addition to  $\theta_{3f} = \cos^{-1}(c + c_f)$  as well as  $\theta_{3i} = \cos^{-1}(c + c_i)$  which verifies Eq. (55) for any mechanism's proportions. Moreover, the output angular stroke ( $\phi_4 = \gamma_f - \gamma_i + \delta$ ) increases from ( $9.5^\circ$ ) till ( $32.52^\circ$ ) and the time ratio relation is  $1 > TR > 0.79$ .

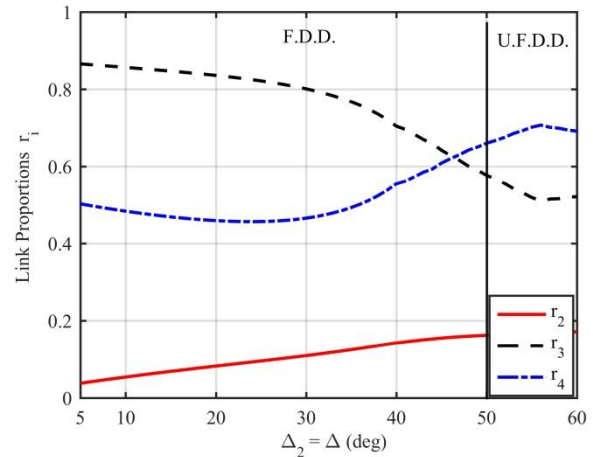


Figure 10: Optimal results of (C-R) mechanism's proportions of the third case study

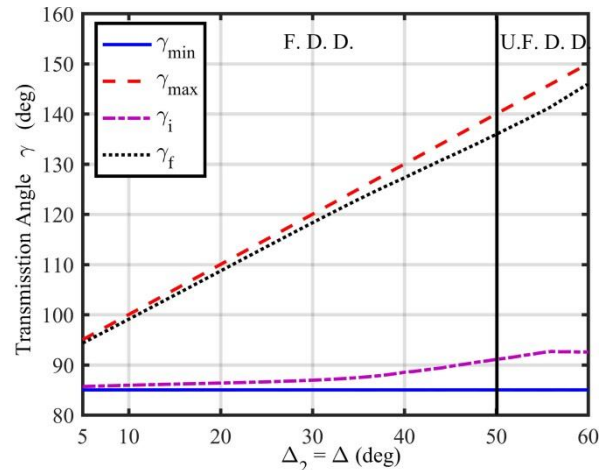


Figure 11: Transmission angles of optimal (C-R) mechanism of the third case study

All of these obtained optimal results of (C-R) mechanism concur with the six deduced design equality constraints in Eqs. (46-47) in addition to Eqs. (49-52), through considering the mechanism's proportions of M2<sub>2</sub> and M1<sub>1</sub>, which are recommended to lie inside the required feasible design domain (F.D.D)

Mechanisms satisfying this case's conditions can be called mechanisms of class III. Some of previous literature are concerned with these kinds of mechanisms, which can be called negative off-central, negative off-line, less than unity time ratio and negative deflection angle mechanisms.

**Table 4.** Calculated results of the third case study

Mech. No.	$\Delta^\circ$	$\gamma_{min}^\circ$	$\gamma_{max}^\circ$	$r_2$	$r_3$	$r_4$	$G_f$	$\theta_{3f}^\circ$
1	10	85	100	0.0540	0.8562	0.4837	0.271	28.531
2	15	85	105	0.0687	0.8466	0.4689	0.231	27.079
3	30	85	120	0.1095	0.8008	0.4656	0.142	24.202
4	45	85	135	0.1551	0.6417	0.6084	0.082	27.076
5	60	85	150	0.1716	0.5212	0.6909	0.035	22.729
Mech. No.	$\theta_{3i}^\circ$	$\delta^\circ$	TR	$\phi_4^\circ$	$\gamma_i^\circ$	$\gamma_f^\circ$	$\Delta_i^\circ$	$\Delta_f^\circ$
1	28.847	-0.316	0.966	12.834	85.930	99.080	4.070	9.080
2	27.894	-0.816	0.991	16.907	86.155	103.878	3.845	13.878
3	27.708	-3.506	0.962	27.867	86.934	118.307	3.066	28.307
4	37.476	-10.40	0.891	31.472	89.703	131.574	0.297	41.574
5	43.648	-20.92	0.792	32.525	92.555	145.999	-2.555	55.999

The obtained results of each case concerning with the time ratio ( $T_r$ ) are shown in Fig. 12. On the other hand, the results of each case dealing with the swing angle ( $\phi_4$ ) of rocker link are illustrated in Fig. 13. Clearly, the swing angle ( $\phi_4$ ) has the highest increasing rate with the first case study which falls inside the required feasible design domain (F.D.D) compared with other cases, where  $\phi_4$  increases till 76.4° for the first case, 55° for the second one and till 30.9° for the third one.

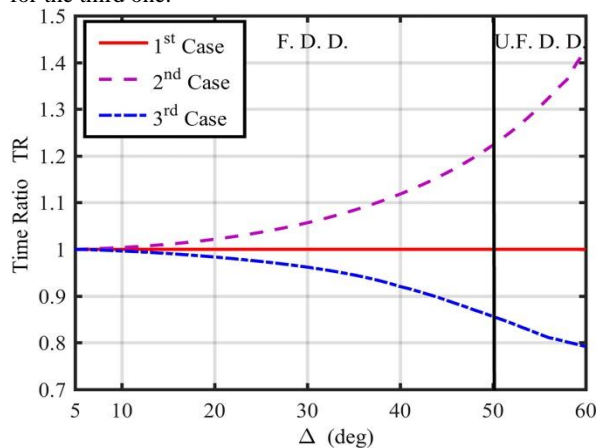


**Figure 12:** Time ratio of optimal (C-R) mechanism for three cases

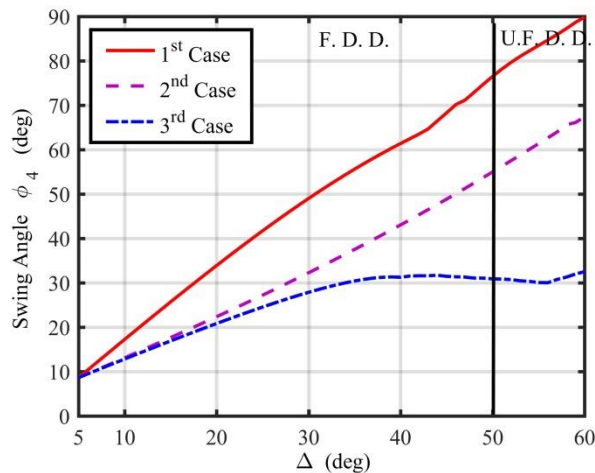


**Figure 13:** Rocker swing angle of optimal (C-R) mechanism of the three cases.

**4. Validating the Optimal Results**

Clearly, the obtained results facilitate the designer's work through selecting the appropriate mechanism's proportions for achieving the design requirements. It is very important to validate the calculated optimal synthesized (C-R) mechanism's proportions which satisfy the six design constraint equations. The optimal results are validated through comparisons with those of some earlier researches as [1, 2, 3, 6] and [14-16] which are tabulated in Table 5.

**Table 5.** Results validation through comparisons with earlier researches

Conditions	The Three Cases		
	$\Delta_1=\Delta_2$	$\Delta_1>\Delta_2$	$\Delta_1<\Delta_2$
$\gamma_{min} + \gamma_{max} = \pi - \lambda_d$	= $\pi$ , as [3], [6], [15], [16]	< $\pi$	> $\pi$
$\gamma_i + \gamma_f = \pi - \lambda_{if}$	= $\pi$	< $\pi$	> $\pi$
$S_5 = (2R_1R_2) / (R_3R_4)$	[16]		
$R_3^2 + R_4^2 - R_1^2 - R_2^2 = (R_3R_4)S_d$	[1], [2], [3], [15], [16]	[1], [14]	[1], [14]
$TR = (\pi + \delta) / (\pi - \delta)$	=1, as [1], [3], [6], [15], [16]	>1, as [1], [14]	<1, as [1], [14]

**4.1 Solved Examples Using Graphical Synthesis Methodology**

First example is dealing with given data; ( $\Delta_1 = \Delta_2 = \Delta = 30^\circ$ , i.e.,  $\gamma_{min} = 60^\circ$  and  $\gamma_{max} = 120^\circ$ ) of the first class I mechanism. This graphical synthesis methodology can be used to construct (C-R) mechanism's lengths via these given data through applying the sequential graphical steps. The second step is assuming the initial angular position ( $\theta_{3i} = 34^\circ$ ) of the link ( $R_3$ ) related to the value of ( $\gamma_{min}$ ). Also, the third and fourth steps are assuming values of ( $\lambda_{in} = \lambda_{if} = 5.5^\circ$ ) which are similar to the second step. The fifth step is drawing  $xO_2y$  axis which coincides with  $XO_2Y$  axis where ( $\theta_1 = 0^\circ$ ), as shown in Fig. 14.

Locate the point ( $O_4$ ) on the line ( $O_2x$ ), where ( $O_2O_4$ ) is a unit length. Hence, the first line ( $O_2A_iB_i$ ) can be drawn from point ( $O_2$ ) with inclination angle ( $\theta_{3i} = 34^\circ$ ) with respect to the direction of the line ( $O_2O_4$ ). Also, the line ( $O_4B_i$ ) can be drawn from point ( $O_4$ ) with inclination angle ( $\theta_{3i} + \gamma_i = 99.5^\circ$ ) with respect to direction of line ( $O_2x$ ) to intersect the direction of ( $O_2B_i$ ) in ( $B_i$ ). Therefore, the length of ( $O_4B_i = 0.615$ ) represents ( $r_4$ ). Also, the length of ( $O_2B_i$ ) represents ( $r_3 + r_2 = 1.082$ ).

Obtained optimal (C-R) mechanism's links ratios using the pervious steps are;  $r_2 = 0.254$ ,  $r_3 = 0.829$  and  $r_4 = 0.615$  which, satisfy the six deduced design constraint equations. The mechanism's characteristics are approximately equal to:  $\gamma_{min} = 60^\circ$ ,  $\gamma_{max} = 119.9^\circ$ ,  $\gamma_i = 65.5^\circ$ ,  $\gamma_f = 114.5^\circ$ ,  $\phi_4 = 48.9^\circ$  and  $TR \approx 1.0$ , which satisfy the desired design requirements.

Also, a second example dealing with the class II of mechanism synthesis can obtain mechanism's links ratios via this graphical method using given data; ( $\Delta_1=\Delta=25^\circ$ , i.e.,  $\gamma_{min}=65^\circ$  and  $\gamma_{max}=95^\circ$ ) as shown in Fig. 15. Hence,  $\theta_{3i}$ ,  $\lambda_{in}$  and  $\lambda_{if}$  can be proportionally assumed as; ( $\theta_{3i}=34.9^\circ$ ,  $\lambda_{in}=3^\circ$  and  $\lambda_{if}=3.4^\circ$ ).

The mechanism's ratios using these data are;  $r_2=0.144$ ,  $r_3=0.907$  and  $r_4=0.614$ . The mechanism's characteristics are approximately equal to:  $\gamma_{min}=65.2^\circ$ ,  $\gamma_{max}=95.7^\circ$ ,  $\gamma_i=68^\circ$ ,  $\gamma_f=91.6^\circ$ ,  $\phi_4=27.5^\circ$  and  $TR \approx 1.02$ , which satisfy the desired design requirements.

Moreover, this method can be used as a third example for synthesizing the mechanism of the third class III using given data; ( $\Delta_2=\Delta=25^\circ$ , i.e.,  $\gamma_{min}=85^\circ$  and  $\gamma_{max}=115^\circ$ ) as shown in Fig. 16. Hence,  $\theta_{3i}$ ,  $\lambda_{in}$  and  $\lambda_{if}$  can be proportionally assumed as; ( $\theta_{3i}=27.7^\circ$ ,  $\lambda_{in}=1.7^\circ$  and  $\lambda_{if}=1.5^\circ$ ).

The mechanism's ratios using these data are;  $r_2=0.1$ ,  $r_3=0.818$  and  $r_4=0.463$ . The mechanism's characteristics are approximately equal to:  $\gamma_{min}=84.4^\circ$ ,  $\gamma_{max}=115.6^\circ$ ,  $\gamma_i=86.7^\circ$ ,  $\gamma_f=113.5^\circ$ ,  $\phi_4=25.3^\circ$  and  $TR \approx 0.93$ , which satisfy the desired design requirements.

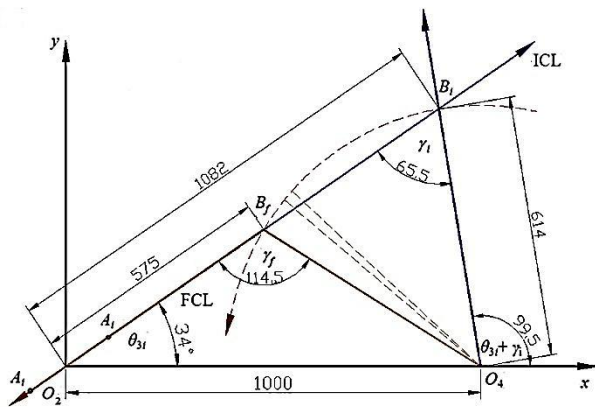


Figure 14: Graphical synthesis methodology for first case

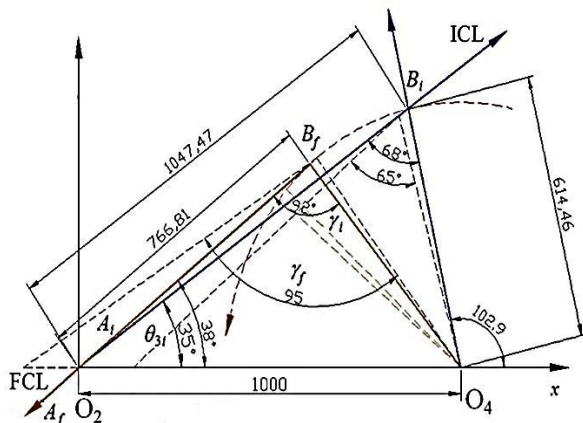


Figure 15: Graphical synthesis methodology for second case

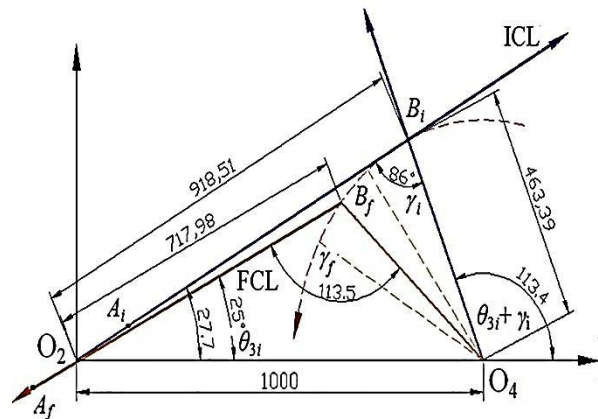


Figure 16: Graphical synthesis methodology for third case

### 5. Conclusion

This work proposed a detailed analytical methodology in addition to a fast-graphical methodology to optimally synthesize lengths' proportions of planar crank-rocker mechanism in order to accomplish targeted design with a definite transmission angle deviation. The analytical methodology deals with deducing six design equality constraint equations that satisfy three case studies. The discussion of the presented results reveals that the optimal synthesized (C-R) mechanisms are classified into three classes according to the three case studies for achieving targeted definite transmission angle deviations. The direct relation between the mini-max transmission angle deviations and the (C-R) mechanisms classes in addition to their six performance parameters are presented.

If and only if the (C-R) mechanism's lengths verify the desired case conditions, the six deduced design constraint equality equations can be verified. The obtained optimal results using the presented methodology are concurring with those introduced in the previous literature using different approaches.

On the other hand, the suggested graphical synthesis methodology can be carried out to directly construct such optimal (C-R) mechanism's lengths. This graphical method is based on only choosing the design case related to the selected class of (C-R) mechanism beside the desired transmission angle deviations through giving the minimum and the maximum transmission angles in order to achieve an optimal synthesized crank-rocker mechanism's lengths.

The optimal charts are introduced to directly obtain the optimal (C-R) mechanism's lengths, which are achieving the targeted transmission angles deviations. Therefore, the designer can easily select optimal synthesized crank-rocker mechanisms' lengths which can be employed in several industrial applications. These applications may include using (C-R) mechanisms associated with a desired equal deviation of mini-max transmission angle for achieving vibrating motions in sieve conveyors. Also, these kinds of mechanisms with time ratio greater than one can be used for generating a required quick-return motion for shaper machines and the mechanisms with time ratio less than one can be used for generating a positive sliding stage of a

conveyed mechanism and increasing the conveying capacity.

## References

- [1] K.C. Gupta, A note on the optimum design of four bar crank-rocker mechanisms, *Mech. Mach. Theory.* 12 (1977) 247–254.
- [2] K.C. Gupta, A general theory for synthesizing crank-type four-bar function generators with transmission angle control, *J. Appl. Mech.* 45 (1978) 415–421.
- [3] A.K. Khare, R.K. Dave, Optimizing 4-bar crank-rocker mechanism, *Mech. Mach. Theory.* 14 (1979) 319–325.
- [4] W.L. Cleghorn, R.G. Fenton, Optimum synthesis of an angular function generating mechanism with prescribed time ratio and rocker angular swing amplitude, *Mech. Mach. Theory.* 19 (1984) 319–324.
- [5] K.C. Gupta, Synthesis of position, path and rotatable generating 4-bar mechanisms with completely rotatable driving links, *Mech. Mach. Theory.* 15 (1980) 93–101.
- [6] R.J. Brodell, A.H. Soni, Design of the crank-rocker mechanism with unit time ratio, *J. Mech.* 5 (1970) 1–4.
- [7] C. Gosselin, J. Angeles, Optimization of planar and spherical function generators as minimum-defect linkages, *Mech. Mach. Theory.* 24 (1989) 293–307.
- [8] P.W. Jensen, Motion and force transmission in linkages, in: *Class. Mod. Mech. Eng. Invent.*, Marcel Dekker, New York, 1991: pp. 11–27.
- [9] R. Soylu, Analytical synthesis of mechanisms-Part 1 transmission angle synthesis, *Mech. Mach. Theory.* 28 (1993) 825–833.
- [10] M. Lun, Y. Leu, Design of crank-rocker mechanisms with optimum transmission angle over working stroke, *Mech. Mach. Theory.* 31 (1996) 501–511.
- [11] S.S. Balli, S. Chand, Transmission angle in mechanisms (Triangle in mech), *Mech. Mach. Theory.* 37 (2002) 175–195.
- [12] S.S. Balli, S. Chand, Defects in link mechanisms and solution rectification, *Mech. Mach. Theory.* 37 (2002) 851–876.
- [13] S.G. Sarganachari, V.B. Math, R.A. Mehabubsubahani, B.K. Belleri, S.J. Sanjay, Optimal synthesis of planar four-bar mechanism for motion generation, *Int. J. Appl. Eng. Res.* 5 (2010) 2411–2424.
- [14] S. Jian, Analysis and optimization of the transmission angle of crank rocker mechanism, in: *2015 Int. Conf. Mechatronics, Electron. Ind. Control Eng.*, 2015: pp. 155–158.
- [15] K.M. Khader, Nomograms for synthesizing crank rocker mechanism with a desired optimum range of transmission angle, *Int. J. Mining, Metall. Mech. Eng.* 3 (2015) 155–160.
- [16] S.A. El-Shakery, K.M. Khader, R. Ramadan, Optimal synthesis of crank-rocker mechanism with unit time ratio and desired equal deviation of minimax transmission angle, *Int. J. Adv. Eng. Glob. Technol.* 3 (2015) 1159–1164.
- [17] C. Lin, W. Chang, The force transmissivity index of planar linkage mechanisms, *Mech. Mach. Theory.* 37 (2002) 1465–1485.
- [18] S. Erkaya, I. Uzmay, Determining link parameters using genetic algorithm in mechanisms with joint clearance, *Mech. Mach. Theory.* 44 (2009) 222–234.
- [19] S.B. Matekar, G.R. Gogate, Optimum synthesis of path generating four-bar mechanisms using differential evolution and a modified error function, *Mech. Mach. Theory.* 52 (2012) 158–179.
- [20] M. Khorshidi, M. Soheilypour, M. Peyro, A. Atai, M.S. Panahi, Optimal design of four-bar mechanisms using a hybrid multi-objective GA with adaptive local search, *Mech. Mach. Theory.* 46 (2011) 1453–1465.
- [21] A. Smaili, N. Diab, Optimum synthesis of hybrid-task mechanisms using ant-gradient search method, *Mech. Mach. Theory.* 42 (2007) 115–130.
- [22] H. Zhou, E.H.M. Cheung, Optimal synthesis of crank-rocker linkages for path generation using the orientation structural error of the fixed link, *Mech. Mach. Theory.* 36 (2001) 973–982.
- [23] G. Galán-Marín, F.J. Alonso, J.M. Del Castillo, Shape optimization for path synthesis of crank-rocker mechanisms using a wavelet-based neural network, *Mech. Mach. Theory.* 44 (2009) 1132–1143.
- [24] N. Nariman-Zadeh, M. Felezi, A. Jamali, M. Ganji, Pareto optimal synthesis of four-bar mechanisms for path generation, *Mech. Mach. Theory.* 44 (2009) 180–191.
- [25] R. Singh, H. Chaudhary, A.K. Singh, Defect-free optimal synthesis of crank-rocker linkage using nature-inspired optimization algorithms, *Mech. Mach. Theory.* 116 (2017) 105–122.
- [26] R. Mishra, T. Kanti Naskar, S. Acharya, Optimum Design of Elastic and Flexible Linkages for Motion and Path Generation, *Mater. Today Proc.* 5 (2018) 4629–4636.
- [27] P.J. Martin, K. Russell, R.S. Sodhi, On mechanism design optimization for motion generation, *Mech. Mach. Theory.* 42 (2007) 1251–1263.
- [28] Q. Shen, Y.M. Al-smadi, P.J. Martin, K. Russell, R.S. Sodhi, An extension of mechanism design optimization for motion generation, *Mech. Mach. Theory.* 44 (2009) 1759–1767.
- [29] E. Pennestri, *Engineering Kinematics: Mechanisms Design for Finitely Separated Positions*, Second ed, Independently Published, 2020.
- [30] R.L. Norton, *Kinematics and Dynamics of Machinery*, Second ed, McGraw-Hill Higher Education, New York, 2013.
- [31] S.C. Chapra, *Iterative Methods*, in: *Appl. Numer. Methods with MATLAB® Eng. Sci.*, McGraw-Hill, 2012: pp. 284–300.
- [32] H. Darina, F. Peter, B. Gabriel, Kinematical analysis of crank slider mechanism with graphical method and by computer simulation, *American Journal of Mechanical Engineering*, 4 (2016), 329–343.
- [33] T. Norton, A. Midha, L. Howell, Graphical synthesis for limit positions of a four-bar mechanism using the triangle inequality concept, 1994.
- [34] Z. Masoud, and M. Daqaq, A graphical design of an input-shaping controller for quay-side container cranes with large hoisting: theory and experiments, *Mech. and Ind. Eng. (JMMIE)*, 1(1), (2007) 57–67.



# Review of Experimental and Finite Element Analyses of Spot Weld Failures in Automotive Metal Joints

Aravinthan Arumugam\*, Alokesh Pramanik

*School of Civil and Mechanical Engineering, Curtin University, Kent.St, WA 6102, Australia*

*Received April 25 2020*

*Accepted August 30 2020*

## Abstract

The spot weld failure analysis using experimental and numerical finite element analysis methods has been reviewed. The spot weld strength is governed by the welding parameters, sheet metal thicknesses and the loading conditions. Spot weld fails either by pull-out failure (PF) mode or interfacial failure (IF) mode. The spot weld failure modes depend on the diameter of weld and the loading types. Most reported experimental spot weld failure analyses were based on industrial standard test samples under quasi static loading. Limited work on combined loading on dissimilar metal joints with different thicknesses was found in the review. The review further observed that weld bonded joints have better fatigue life compared to spot welded joints. Extensive work has been proposed in this review on this type of hybrid joints as current research showed limited investigation in this area. In the finite element analysis of spot weld failures, current researches mostly investigated single spot weld failures using the standard tests under quasi static loading. The review proposed further study of spot weld failure of multiple spot welds under fatigue loading for dissimilar joints and hybrid joints. Finally, a hybrid system has been proposed to relate the experimental and computational weld failure analyses for spot weld optimization.

© 2020 Jordan Journal of Mechanical and Industrial Engineering. All rights reserved

*Keywords: spot weld; failure mode; diameter; strength; weld joint; lap-shear; coach -peel; cross-tension; FEA; quasi-static; fatigue;*

## 1. Introduction

The typical joining method used for joining automotive metals together is the welding process. Different types of welding processes have been employed in the automotive manufacturing, such as resistance spot welding (RSW), resistance seam welding (RSEW), friction welding (FW), laser beam welding (LBW) and arc welding. However, the welding process that is widely used in the Body in White (BIW) fabrication and still dominates the automotive industry is the resistance spot welding (RSW). Popularly known as the spot welding, the welding process gained its popularity because of being a cost-effective process, easily automated, and has a rapid production rate, low component distortion as well as its simplicity and versatility. Automotive BIW has about 2000-5000 spot welds used to join the different types and shapes of metal sheets together. Numerous studies have been carried out in the use of the spot-welding process to join similar and dissimilar metals, such as Advanced High-Speed Steels (AHSS), aluminium and magnesium, a design strategy known as multi-materials lightweight (MML) design.<sup>[1-7]</sup> With a large number of spot welds involved in the forming of automotive BIW, the spot welding process has close relationship with the structural integrity and performance of the BIW. The spot welds function as the elements responsible in load bearing and load transfer during automotive crash and impact. The

strength of the individual spot weld plays a role in ensuring that it can sustain the impact load without failing and maintaining the structural strength of the BIW while providing safety of passengers.

However, as the trend of automotive metals is going towards lighter metals yet stronger metals with lesser thicknesses, the control of the spot weld strength has become a challenge for the automotive manufacturers. The strength of a spot weld depends on various factors, such as material weldability, sheet thickness, spot weld positions, welding parameters, material coating, joint and loading types.<sup>[8-13]</sup> Due to the inherent uncertainty on an individual spot weld's strength, automotive industries tend to add significant number of redundant spot welds to ensure the structural integrity of the BIW is achieved.<sup>[14]</sup> These redundant spot welds obviously increase the overall spot weld manufacturing cost and could be eliminated if the spot weld failures under different loading conditions can be predicted earlier during design stage. The optimization of the number of spot welds and the positions for spot welds are crucial in reducing the RSW related manufacturing cost. With the advancement in computer technology and the field of finite element analysis (FEA), such prediction is now possible.

There are numerous researches in this area and many results are reported. However, those are not well organised and properly linked. In fact, it is not easy to have a complete understanding in this area though it is essential for

\* Corresponding author e-mail: aravinthan.arumugam@curtin.edu.au

improving the efficiency and effectiveness of spot-welding testing. To address this issue, this paper critically reviews and scientifically links the information available in the recent works related to spot weld failure on different automotive metals, the spot weld failure modes as a result of different loading conditions and finally the use of experimental and numerical FEA in spot weld failure analysis and prediction. The paper also aims to propose future work in the area of experimental and computational spot weld failure analyses and development of a hybrid system for failure analyses.

## 2. Spot welding

The spot-welding process consists of two water cooled copper electrodes, connected electrically to a welding transformer. The electrodes are usually actuated through an upwards and downward motion by means of pneumatic or servo motor-based actuation system. The metal sheets to be welded are placed in between the copper electrodes and the area to be welded is brought into intimate contact by the force applied by the clamped electrodes during squeeze cycle. In the weld cycle, the welding current is then supplied through the upper electrode which flows to the lower electrode through the metal sheets and the sheet interface. As the resistance to current flow is greater at the sheets interface compared to the bulk material of the sheet metals, the copper electrodes and the electrode and sheet interface, localised heating and melting will occur at the sheets interface. The melting area is related to the diameter of both the copper electrodes which are compressing the metal sheets together. After a pre-set weld time, during hold cycle, the current is turned off, but the electrode force is maintained while the weld solidifies and joins both metal sheets together via a spot weld. Figure 1 gives the schematic of the spot-welding process.

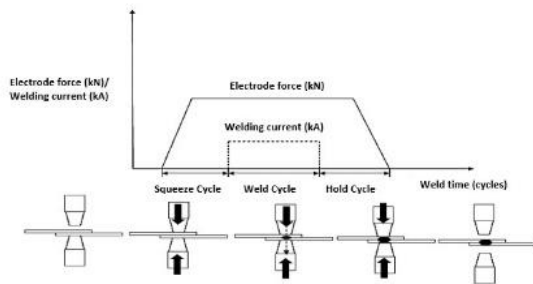


Figure 1. Spot welding process

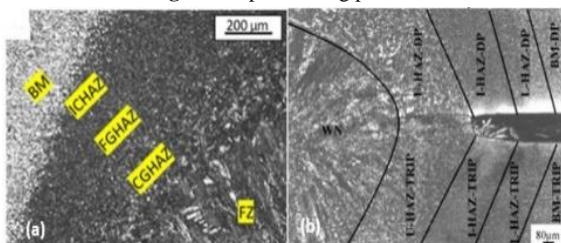


Figure 2. Microstructural zones in (a) Galvannealed DP600/bare DP600<sup>[42]</sup> and (b) DP1000/TRIP 980<sup>[43]</sup> weld joints

The heat generated during the spot-welding process can be represented by the Equation (1)

$$Q = \int_{T_1}^{T_2} I(t)^2 R(t) dt \quad (1)$$

where the  $Q$  is the heat generated during the welding process,  $I(t)$  is the supplied current,  $R(t)$  is the dynamic resistance of the sheet metals,  $T_1$  and  $T_2$  are the time limits of the process respectively.

## 3. Welding parameters and weld strength

The spot-welding process mainly has three important parameters based on the Equation 1, which controls the heat generation during welding for spot weld formation and directly impacts the weld strength. The process parameters are weld current, electrode force and weld time. Increase in the spot weld current with weld time and electrode force maintained constant or the increase in weld time with both welding current and electrode force maintained constant during the welding of two metal sheets, has been reported to increase the heat generation during spot welding process. The increased heat generation in turn increased the size of the spot weld diameter as well as the weld strength.[10, 15-21] Taguchi method has been used by various authors to analyse the contribution of both the welding current and weld time in the heat generation for spot weld formation. Welding current has been shown to have major contribution in heat generation and spot weld development during the welding process with ANOVA results giving an average of 60.9% for welding current and 20.6% for weld time. [15, 18, 22-25] However, the increase in welding current and weld time are limited to a certain range, after which further increase in either parameter, will cause expulsion during welding. Expulsion is referred to as the ejection of molten metal from the weld zone due to overheating. Presence of expulsion was found to cause excessive electrode indentation, shrinkage void and solidification cracks in spot weld, leading to deterioration of spot weld strength. Expulsion was found to occur at the electrode/sheet metal interface and sheet metal/sheet metal interface. [26, 27]

The third weld parameter, that contributes to the heat generation in the welding process and relates closely to the dynamic resistance in Equation 1 is the electrode force.[28] Unlike welding current and weld time, decreasing electrode force while maintaining welding current and weld time, increased the heat generation during spot welding process. Lower electrode force will increase the resistance to current flow at the sheets' interface due to high number of surface asperities and lower sheet-to-sheet surface contact. This leads to increase in the current density and in turn increase the heat generation at the interface for weld development. Higher electrode force will cause these surface asperities to collapse creating increased sheet-to-sheet surface contact. Current density will therefore decrease leading to reduction in heat generation. However, extremely low electrode force will cause expulsion mainly due to overheating and very high electrode force will lead to development of undersized weld due to low heat generation.[29, 30]

Traditionally, welding current has been the only control parameter in spot welding to control the development of spot weld and in turn the achieved weld strength. Welding current was easy to measure with the use of current probes or transducers and the amperage that is supplied to the weld joint can be controlled by controlling the individual firing angles of the two silicon-controlled rectifiers (SCRs) in a single-phase AC resistance spot welding machine. The

control strategy which is known as the constant current control (CCC) has been discussed by Zhou.[31, 32] As most of these welding machines were based on pneumatically actuated electrode system, force was not used as a control parameter due to the inability to control the electrode force at a faster rate with the use of the mechanical system. This is due to the inherent mechanical inertia in the pneumatic system. However, when the electronically controlled electrodes by servo drives were introduced, this created an opportunity for electrode force to be included as a control parameter apart from welding current. The advantages of servo actuated electrodes are that the electrodes' position, speed and applied force (electrode force) can be precisely controlled.[33] As spot welding process is naturally a non-linear process involving different variables (current, time, electrode force, sheet thickness, electrode diameter, mechanical and electrical characteristics of machine used etc) and interaction between electrical, thermal, mechanical and metallurgical changes at the sheets interface, the application of more than one control parameter to control the weld nugget development and weld strength was widely investigated. Also, with the automotive industries increasingly use different types of sheet metals with various thickness to fabricate the BIW, in-process real time control of welding parameters was studied to achieve stringent quality control of spot welds. The use of force and current profiles i.e step control of welding current and servo system driven electrode force to control both parameters in real-time during welding and the improvements that were achieved in terms of the weld strength, expulsion reduction and ability to weld joints with different materials and thicknesses have been reported by different studies. [34-38]

Even though weld current, time and electrode force are the basic parameters in the spot-welding process to produce spot welds, the melting of metal at the sheets interface and development of weld nugget is influenced by the dynamic contact resistance. The dynamic contact resistance accounts for the combined effect of the interfacial resistance and bulk material resistance.[39] Shome and Chatterjee[39] concluded from their study that dynamic contact resistance which determines the energy input and control spot weld formation is dependent on the coating type, thickness, surface roughness, bulk material resistance and external factors, such as temperature and pressure. From the previous factors, thickness and bulk material resistance relate closely to the problem that is faced by the automotive industries, joining dissimilar materials. Automotive structure design involves dissimilar metals with different thicknesses. Formation of a sound spot weld between two different metals requires an efficient heat balance in both metals considering the different material properties of the metals. This results in the formation of a weld nugget of approximately the same thickness on each side of the sheets interface.[40] Numerous works have been researched in the weldability of materials of dissimilar metals to form spot weld joint.

The weldability and failure of spot weld between two dual phase steels; DP600 and DP1000 with 0.8 mm thickness and galvanized and bare DP600 with 1.3 mm thickness were studied by Aydin[41] and Kishore et al.[42] respectively. Weld nugget size and weld strength were found to increase by increase in welding current. These studies also found that weld formed by both the DP steels

has three distinct microstructural zones; base metal (BM), fusion zone (FZ) and heat affected zone (HAZ). In the heat affected zones, there are further transition zones; outer heat affected zone (OHAZ), centre heat affected zone (CHAZ) and inner heat affected zone (IHAZ)[41] or inter critical heat affected zone (ICHAZ), fine grain heat affected zone (FGHAZ) and coarse grain in heat affected zone (CCHAZ).[42] As for failure mode, pull out failure was obtained for the range of current investigated. From the lowest current to the intermediate current, failure occurred at the CHAZ on the DP1000 side and above the intermediate current till the highest current, failure occurred at the CHAZ on the DP600 side.[41] Mousavi et al.[16] studied the optimization of process parameters to join dissimilar metals; DP600 and AISI304 stainless steel with thickness of 1 mm. The study revealed that the microstructure of the DP steel's HAZ is martensitic and the AISI304 steel's HAZ is austenitic. Also, the microstructure of the FZ is fully martensitic with the FZ chemical composition influenced by the chemical compositions of both the AISI304 steel and DP steel. Weld failure test carried out with tensile lap-shear test also showed at optimum parameters, weld pull-out failure is obtained with the failure occurring at the AISI304 stainless BM. The weldability of similar and dissimilar joints between 1.36 mm thick DP1000 steel and 1.56 mm thick transformation induced plasticity (TRIP980) steel was studied by Wei et al.[43] Similar to Aydin and Kishore's work[41, 42], the microstructural study between DP/DP, TRIP/TRIP and DP/TRIP showed three distinct microstructural zones; base metal (BM), fusion zone (FZ) and heat affected zone (HAZ). For the DP/TRIP weld joint, the heat affected zone is further divided into; upper heat affected zone (UHAZ), intermediate heat affected zone (IHAZ) and lower heat affected zone (LHAZ). The weld nugget diameter and weld strength for similar joints (DP/DP and TRIP/TRIP) and dissimilar joints (DP/TRIP) increased with increase in current till a certain current limit after which due to expulsion both properties of the spot weld reduced at higher current. The study also showed the FZ of all joints exhibit fully martensite microstructure and the spot weld failure in pull out mode increased in the order of DP/DP, TRIP/TRIP and DP/TRIP. Figures 2(a) and 2(b) show the different microstructural zones in the galvanized and bare DP600 and DP1000/TRIP980

Liu et al.[44] studied the weldability of similar and dissimilar spot welds made from lightweight magnesium alloy (Mg) and high strength low alloy (HSLA) steel. The thickness of Mg strip is 1.5 mm and the HSLA steel thickness is 0.77 mm. Interestingly unlike in Mg/Mg joint, in Mg/steel joint, FZ representing weld nugget, was only noticed on the Mg side while Mg and steel was bonded by three different regions; weld brazing, solid-state joining and soldering as in Figure 3. The hardness test on the Mg/steel joint showed that the hardness on the steel side of the joint is almost twice the hardness of the Mg side. As for weld failure in this study, fatigue test was carried out and the test showed initiation of crack at the Mg/steel interface. The crack propagates further at higher rate into the Mg base metal until failure occurred. However, at the steel side, a slower crack propagation rate was noticed along the Mg and steel interface into the weld nugget. Manladan et al.[45] studied the spot welding of Mg alloy and austenitic stainless steel under two joints; dissimilar spot welded joint (RSW)

and dissimilar spot weld-bonded joint (RSWB) using epoxy structural adhesive. Lap-shear test was carried out to analyse weld failure on these joints. The results showed that for a range of welding currents (6 kA to 18 kA), RSWB joints have higher bonding diameters, peak loads and energy absorption prior to failure compared to RSW joints. The failure analysis observed that in RSW spot weld failure, failure occurred through the Mg nugget/stainless steel interface and weld zone formed through welding brazing mode as reported by Liu[44].

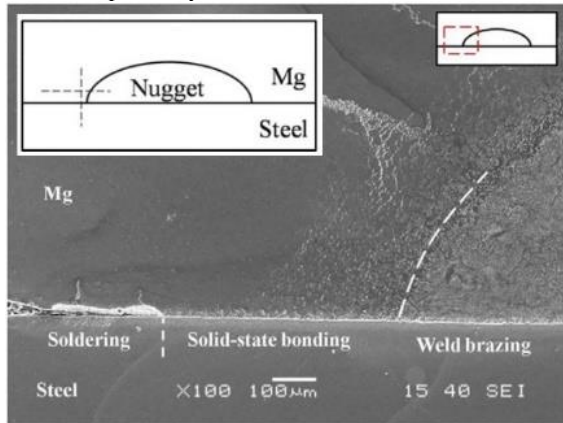


Figure 3. Microstructure of Mg/HSLA weld joint<sup>[44]</sup>

The weldability of aluminium alloy with steel was investigated by Miyamoto et al.[46] The study investigated joining of steel with aluminium alloy; galvanized steel (GA) with 600 series aluminium alloy (Al) plate with 0.55 mm and 1 mm thicknesses respectively. The GA are coated by layer of FeZn8 ( $\delta$  phase). Two types of samples were created; resistance spot welded sample by welding both metals together and seal spot welded sample by having a sealant in between both metals. For both samples, nugget diameter was found to increase with increase in time with welding current maintained at 30 kA for resistance spot weld sample and 27.5 kA for seal spot weld sample. The nugget diameter in the steel side and the formation of Al-Fe intermetallic compound (IMC) layer at the joint interface is shown in Figure 4[5]. The study also reported that seal spot welded joints can inhibit electrolytic corrosion while electrolytic corrosion occurred at the joint interface of resistance spot welded joint. To analyse the weld strength, cross tension test was carried out. Weld pull-out failures were observed for both samples with failure occurring at the aluminium alloy and the circular spot weld remaining on the steel. The decrease in aluminium sheet thickness during welding was deduced as the reason for failure on the aluminium sheet. Strength comparison between resistance spot welded joint and seal spot welded joint also showed that for the same welding condition, cross tension strength of seal spot weld joints is approximately half that of the resistance spot welded joints. The difference in strength between samples was related to the difference between the degrees of decrease in the sheet thickness of the aluminium alloy in the resistance spot weld joints and seal spot weld joints. The reduction in sheet thickness in the Al side and its influence to weld strength have also been reported by Sakiyama et al.[47].

The weldability of spot weld joints of AA5052 aluminium alloy with dissimilar thickness was investigated by Mat Din et al.[48] One sheet had a constant thickness of

2 mm and the other sheet thickness was varied from 1.2 to 3.2 mm (7 different sheet thicknesses). Peel test was carried out to analyse the spot weld failure due to different thicknesses. Increasing the sheet thickness increased nugget diameter and weld time. Failure strength to achieve pull out failure also initially increased till thickness combination of 2 mm - 2.3 mm after which there was a drop in strength till the last combination of 2 mm - 3.2 mm. Hence from the reviews in this section, it can be concluded that in order to obtain spot welds with strengths required to maintain the structural integrity of the of the automotive structure. Attention must be focused on the welding current and electrode force used during spot welding. The correct combination of welding current and electrode will generate the heat required for spot weld nugget initiation and development. Also, another important consideration is due to the increase use of dissimilar metal and sheet thicknesses in automotive structures, fundamental knowledge in metallurgical transformation in dissimilar metals and heat balance for both dissimilar metals and dissimilar thicknesses are required for welding parameters selection to produce spot welds that are well developed on both the metal sheets creating a strong joint at the sheets interface.

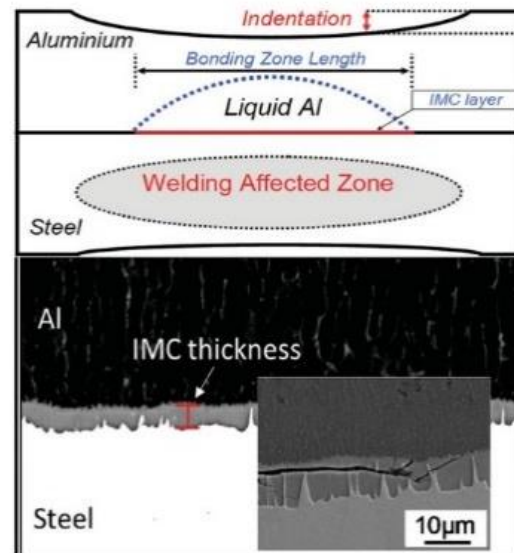
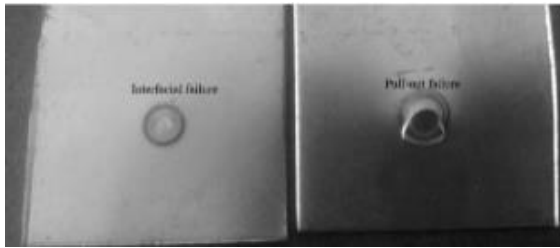


Figure 4. The microstructure in the Al/steel joint with the IMC layer at sheets interface<sup>[5]</sup>

#### 4. Experimental weld failure analysis

As seen in previous section, spot weld strength is influenced by the selection of the welding parameters as well as the metallurgical transformation and heat balance in the sheets to be welded. Weld failure modes are of two types; pull-out failure (PF) (failure due to weld pulled out from one sheet) and interfacial failure (IF) (failure due to crack propagation through the fusion zone) as seen in Figure 5. [49-51] Other authors have also further divided the failure modes into an intermediate failure mode called the partial interfacial failure (PIF) or partial pull-out failure (PPF).[49, 52, 53] Automotive industries require spot welds to fail by pull-out failure mode rather than interfacial failure mode as the former has higher failure load and absorb more energy prior to failure compared to the latter.[54]



**Figure 5.** Interfacial failure (IF) and pull out failure (PF) of spot weld joints

The weld diameter and loading conditions influence the tendency of the spot weld to fail by either failure modes. Spot welds fail by PF mode above the critical weld diameter and IF mode below the critical diameter.[55, 56] Critical diameter is defined as the minimum weld diameter required to achieve pull-out failure. Abadi[57] has also defined critical weld diameter as the weld diameter between the maximum weld diameter which will produce IF mode and the minimum weld diameter which will produce the PF mode. Pouranvari[56] developed a relationship to calculate the critical diameter ( $d_{cr}$ ) based on the relationship between the ultimate tensile stress of pull-out failure location ( $(\sigma_{UTS})_{FL}$ ) and the shear strength at the fusion zone ( $\tau_{FZ}$ ) as given in Equation (2).

$$d_{cr} = 4t \frac{(\sigma_{UTS})_{FL}}{\tau_{FZ}} \tag{2}$$

Similarly Zhao et.al[58] suggested Equation (3) as the critical nugget diameter to achieve PF mode for DP600 joints. This relationship was also developed considering the tensile stress at the HAZ and shear stress at FZ.

$$d_{cr} = 3.51t \tag{3}$$

where  $t$  is the sheet thickness in mm for both equations.

These equations are, however, based on the lap-shear test which will be discussed later. The standard used by the automotive industries states that to achieve PF mode, the average weld diameter is equal to  $4\sqrt{t}$  where,  $t$  is the sheet thickness[49]. This standard is, however, based on tensile-shear static loading to produce spot weld failure. Spot welds in real conditions for instance in automotive crashes, experience mixed loading such as shear force ( $f_s$ ), normal force ( $f_n$ ), bending moment ( $m_b$ ) and in-plane torsion ( $m_t$ ) as shown on Figure 6.[59]

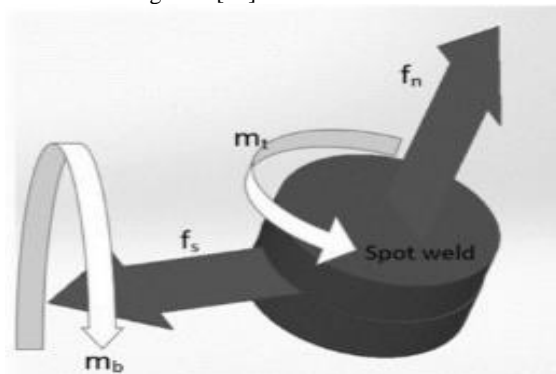


**Figure 6.** Loadings on spot weld

Failure of spot welds are due to two loading conditions; quasi static loading i.e load is applied slowly with low strain rate to deform a structure with inertia effects neglected and dynamic loading i.e will cause the structure to vibrate and the inertia force needs to be considered. Spot weld performance is based on its static and dynamic strength.[60] Hence it is important for the automotive design engineers to understand the mechanical behaviours of joints subjected to both static and dynamic loading conditions and incorporate the static strength, impact and fatigue strength in the early design stage. As a single, standard experiment is not available to evaluate the effect of all the forces to spot weld failure modes, experimental analyses have used three different test samples to separately analyse spot weld failure due to shear force, normal force and bending moment. The test samples are as shown in Figure 7. Test sample A is used to analyse spot weld failure due to bending moment and the test is named as the coach peel test. Test samples B and C are used in lap-shear and KSII tests, respectively. Sample B is used to evaluate the tensile and shear load on spot weld and sample C is used to test the normal load (90o) that will fracture the spot weld.

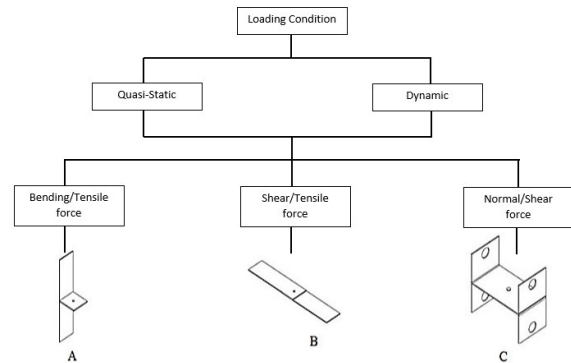


**Figure 7.** Spot weld loading conditions and test samples

Various works have been reported on the test samples used to analyse spot weld failures. Lap-shear test is the common test that has been widely used by many researchers in their spot weld failure experiments. Pouranvari[56] analysed weld failure with lap shear test for weld joints made from high strength low alloy (HSLA) 420 steel. The study showed the relationship between welding current, weld diameter or fusion zone size and the interfacial and pull-out failure modes as shown in Figure 8. The study reported that the driving force for IF mode in lap shear test is the shear stress at the sheet/sheet interface. Meanwhile the driving force for PF mode is the tensile stress at the nugget circumference. An equation was also suggested as in Equation (3) to calculate the PF load in tensile shear test.

$$PPF = \pi dt(\sigma_{UTS})_{FL} \tag{3}$$

where  $d$ - weld diameter,  $t$  – sheet thickness and  $(\sigma_{UTS})_{FL}$  – ultimate tensile strength at failure location which is the weld nugget.

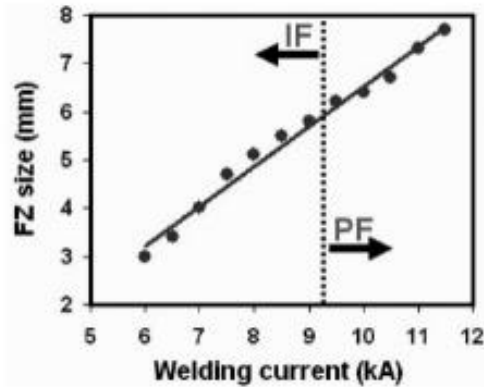


**Figure 8.** Spot weld failure modes at different currents and weld diameters.<sup>[56]</sup>

The spot weld strength and failure modes of Quenching and Partitioning (Q&P) 980 similar steels joints in single pulse RSW and double pulse RSW was studied by Liu et.al[61]. Lap-shear test (and cross tension test which will be discussed later) was used to test the weld samples. This investigation showed that applying a higher secondary current, for instance 7 kA-7.5 kA compared to a constant current of 7 kA, improved the tensile shear strength and failure mode. The weld with constant current of 7 kA, failed with IF due to a small weld developed during welding and crack propagation through the weld and along the sheets interface during lap-shear test. However, with the use of a secondary current within the range of 4.5 kA to 7.5 kA, weld strength increased during the lap shear test and failure mode changed from IF to partial thickness-partial pull-out (PT-PF). Crack propagation during lap-shear test was noticed to penetrate around the circumference of the weld as well as along the partial melting zone (PMZ) and later progressing through the sheet thickness. Zhang et.al[49] used lap-shear test to analyse the spot weld failure on the weld joints made from 1.2 mm DP780 and 1.5 mm DP600 steel sheets. This study reported that during tensile shear test, weld joints first experience shear stress which is parallel to the force direction. The nugget will later rotate in order to realign with the applied force direction. This will lead to a bending moment which in turn creates a tensile stress that is perpendicular to the weld nugget. Even in this study, shear stress was reported to be the driving force for IF and tensile stress being the driving force for PF. However unlike in Pouranvari's work[56], since this study used dissimilar steels, pull-out failure was observed with failure being initiated from the stronger base metal; DP780 in this case. The higher stress concentration on the DP780 side due to the formation of a sharp notch at the sheets interface during lap-shear test initiates crack on the DP780 side which will

later propagate through the base metal to create BM fracture on the D780 side and weld remain intact on the DP600 side.

Duric and Markovic[62] used lap-shear test for 1 and 2 mm thick aluminium and 1 mm thick stainless steel weld joints. This study showed that for dissimilar metals with same thickness, the spot weld failure is dominantly PF while for different thicknesses (aluminium 2mm and steel 1 mm), the spot weld failure is dominantly IF. As in this study, the upper electrode is 5 mm in diameter and the lower electrode is a flat faced back up electrode, which metal is in contact with the upper electrode need additional consideration. The study showed tensile strength is higher for joints with steel in direct contact with the upper electrode compared to joints with aluminium in contact with the upper electrode. Boriwal[63] studied spot weld failure in 0.8 mm thick galvanized steel joints using lap-shear test. This study concluded that welding current and nugget diameters are the main factor for the transition zone of both the IF and PF failure modes similar to the analysis by Pouranvari.[56] The spot weld failure mode transition from IF to PF on 1.7 mm thickness DP600 steel joints for range of welding current, weld time and electrode force as shown in Figure 9 was investigated by Wan et al.[3] This study also used lap-shear test to analyse spot weld failures. A crucial information obtained from this study states that IF of spot weld is usually accompanied by low penetration rate and small size nugget. When the penetration reaches rate of 75% or more, majority failure falls in PF mode. Mousavi et.al[16] used lap shear test to determine the optimum welding parameters to join dissimilar joint of DP600 steel and AISI304 stainless steel. The optimum welding schedule of current 8 kA, 16 cycles weld time and 5 kN electrode force produced PF mode with crack initiation and necking in the thickness direction on the softer base metal i.e. AISI304 stainless steel. To investigate the effect of intermetallic compound (IMC) thickness, nugget diameter and sheet thickness to spot weld failure for joints made from 1.2 mm thick aluminium and 2 mm thick low carbon steel, lap shear test was carried out and the failure modes for different welding schedules were analysed by Chen et al.[64] Three different failure modes were observed in this study. The first failure is a PF with Al button left on the steel surface. The second failure is known as the thickness failure which resembles the IF in similar weld joints, with fracture occurring at the faying surface and the third is a unique failure for Al/steel welds with failure along the IMC layer. The study also concludes when the IMC layer thickness is less than 3  $\mu\text{m}$ , the failure mode is either PF or thickness failure. When the IMC layer thickness is more than 3  $\mu\text{m}$ , the failure will occur with the IMC layer. The study further suggested, to produce a strong and ductile Al/steel weld joint, it is crucial to maintain the thickness of the IMC layer within 3  $\mu\text{m}$  in a lap-shear test.

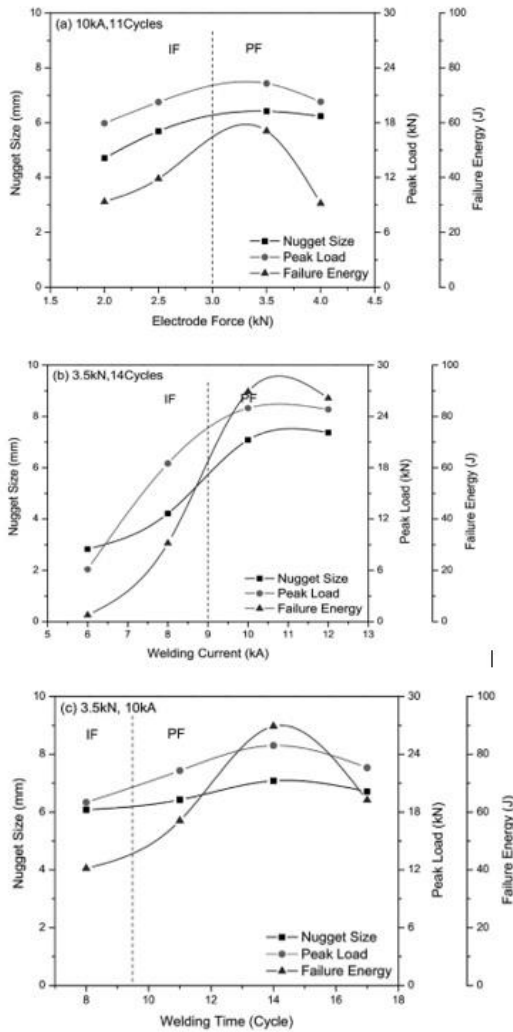


**Figure 9.** Effect of welding parameters to weld failure modes (IF and PF) [3]

To analyse the effect of boron content and welding current to weld joint failure load and mechanism, lap shear test was used by Kong et al.[65] The test samples are made from 1.2 mm thick cold rolled complex steel (CP) sheets containing different amount of boron (B). The lap-shear test showed that for a current range from 5 kA to 10 kA, below 6.4 kA, IF mode was observed regardless of the B content and the variation range of the tensile shear load was narrow. Above 7.4 kA, PF mode was observed, and the tensile shear load increased with increase in current and B content. Also, the study indicated, for weld diameters that failed with IF mode, the change in tensile shear load due to B content is negligible. However, for nugget diameters which failed with PF mode, tensile shear load increased with increase in weld diameter and for the same diameter, load increased with the B content. Kang et.al[66] also contributed in the study of the weldability of dissimilar metals and have used

lap-shear test for strength and weld failure analysis. This work investigated the weldability of aluminium alloy, 1.2 mm AA6022-T4 with 2.0 mm AA6022-T4 and 1.2 mm AA6022-T4 with 2.0 mm interstitial-free (IF) steel. In both joints, welds failed in IF mode during the lap-shear test. The study showed AA6022-T4-IF steel weld joints produced greater weld diameters and higher lap-shear strength as compared to the AA6022-T4- AA6022-T4 weld joints. Tavasolizadeh et.al[67]’s study was different from all the other study discussed above. Unlike other work that used lap-shear test to analyse weld joints made from two metals sheets, this work investigated the use of lap-shear test to analyse weld failure in weld joints made from 3 similar metal sheets. The metal sheet is 1.25 mm thick uncoated load carbon steel and the weld joint is made from 3 sheets stacked together and was identified as the top sheet, middle sheet, and bottom sheet. This study discussed that in a triple sheet stack, weld diameter along the sheet/sheet interface is lower than that of along the geometrical centre of the joint. This type of joint has a high tendency to fail via IF mode during lap-shear test.

The next weld failure test that is quite common especially in the automotive industry is the coach peel test and PF mode is the common failure mode for this test.[68] The continuous bending of the sheet metals in coach-peel test, due to the applied force develops a notch tip closer to the weld, initiating a crack near HAZ. The crack will propagate along sheet thickness causing sheet tearing around weld circumference at a lower load. The stress intensity factor in coach peel to produce a pull-out failure can be divided into stress factor due to bending moment and stress factor due to tensile (axial) force at weld as shown in Equation (4).[69]

$$KI = K_{axial} + K_{moment} = \frac{F}{d\sqrt{\pi d/2}} + \frac{6M}{d^2\sqrt{\pi d/2}} \quad (4)$$

Pouranvari and Marashi[70] concluded the difference in PF mode mechanism for lap-shear and coach-peel tests. In lap-shear test, the PF mode is due to thickness necking while the coach peel test PF mode is due to initiation and propagation of the crack created at the notch tip. This work also presented some crucial information regarding weld strength between both these tests. Firstly, the failure load of spot weld tested with coach peel test was significantly lower than the failure load of the spot weld tested with lap-shear test, for the same weld diameter as shown in Figure 10(a). This attributed to the crack initiation and propagation that was observed in coach peel test. Secondly the displacement of sample prior to failure in the load-displacement graph for coach-peel test is greater than the displacement of sample prior to failure in the load-displacement graph for lap-shear test as in Figure 10(b). This is due to the large sample deformation that was observed in the coach peel test before weld failure occurred. Thirdly, the energy absorption capability of spot welds in coach peel is lower than the same spot welds in lap shear test.

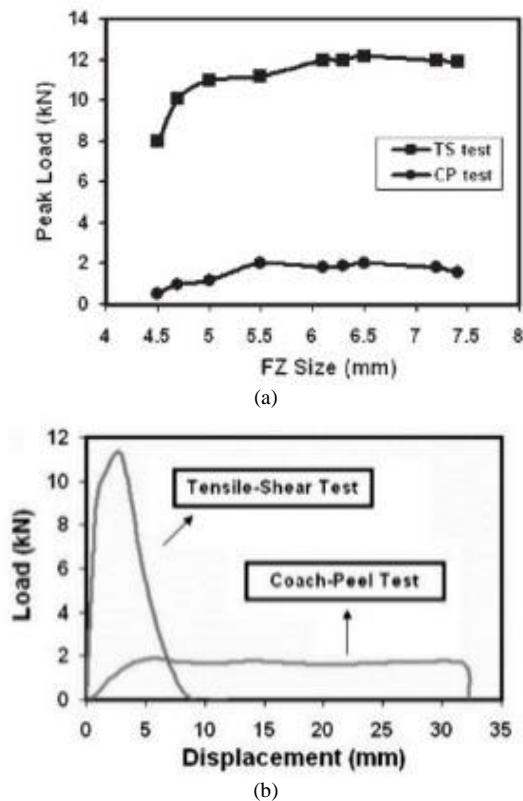


**Figure 10.** (a) Load-displacement curves for lap-shear and coach-peel tests and (b) weld diameters (FZ) and peak loads for lap-shear and coach-peel tests.<sup>[70]</sup>

A comparison study between coach peel test and cross tension test for aluminium and steel joints was discussed in Chen et al.[71] Cross tension test will be discussed in the next section. Similar to Pouranvari and Marashi[70], this work also reported the crack initiation and propagation mechanism prior to spot weld failure during coach peel test. The work further divided the mechanism into 3 stages; a) initial stage; the crack propagates into the Al FZ adjacent to the Al/steel interface and further progressing through the Al sheet top surface resulting in button initiation b) tearing stage; crack propagates circumferentially on both sides of the weld nugget to form button pull out on the steel and finally c) breaking stage; high tensile stress fractured partial Al/steel faying interface and rapidly propagated within the Al sheet until fracture of weld. In a comparison study with the lap-shear test that was carried out by the same authors, Chen et al.[64], lap shear test for Al/steel weld joint showed three fracture modes while for the same Al/steel weld joint, in coach-peel test only one fracture mode was observed i.e partial button pull-out fracture. This work also supported the work of Pouranvari and Marashi [70] indicating that welds, tested with coach peel test had lower peak load compared to the same welds tested with lap shear test. However unlike in Pouranvari and Marashi's work[70], this work reported the welds tested with coach peel test had larger energy absorption capability compared to welds tested with lap-shear test. This difference might possibly be due to the different metals tested by both authors. Yang et.al[72] also investigated the failure modes of spot welds under both cross tension and coach peel test for aluminium alloy (6061-T6 aluminium and 5754-O aluminium) joints

with different thicknesses (1mm, 1.5mm and 2 mm). The peel test samples were made from three sheets of aluminium alloy with two different joint configurations. The IF and PF failure modes were observed for joint configurations with IF failure occurred at the interior of weld nugget and PF mode occurred at the heat affected zone (HAZ) which is referred as the partially melted zone (PMZ) in this work. This work also confirmed that the driving force for IF mode is the tensile stress at the sheets interface and the driving force for PF mode is the shear stress at the weld nugget circumference. Expressions for failure load at IF and PF mode for coach peel test with three sheet thickness were also given as in Equations (5) and (6) respectively

$$F_{IF}^{CP} = P \frac{\pi(\beta d_{IN})^2}{4} \sigma_{FZ} \quad (5)$$

where P – porosity constant (0.9 in this case),  $\beta$  – coefficient =1,  $d_{IN}$  – weld nugget diameter at the interface for a 3-stack joint and  $\sigma_{FZ}$  – tensile strength of the fusion zone.

$$F_{PF}^{CP} \sin\theta = \frac{\pi d_{IN} t \tau_{PFL}}{2} \quad (6)$$

where t = sheet thickness and  $\tau_{PFL}$  – shear strength of the PF location.

Another comparison study between spot weld strength under coach peel test, lap shear test and cross tension test which is yet to be discussed was carried out by Han et.al[73]. Aluminium alloy sheets were used to produce 27 different joint stack-ups (two to four different sheet thicknesses) with differing process parameters. Important information was concluded by this study with regards to the comparison with lap -shear test and coach peel test for the different joint stack-ups with governing metal thickness (GMT); which is the thinnest sheet to be joined in the stack up. The study showed that in the case of the lap-shear test, there is a linear relationship between weld strength and weld diameter with the best fit line having a coefficient of determination (R<sup>2</sup>) of 0.9135. However, in the case of coach-peel test, increase in weld diameter did not lead to significant increase in weld strength with the R<sup>2</sup> for a best fit line being only between -0.13 to 0.1 as the data fall in discrete bands according to the GMT value. Hence this study concluded, unlike in lap shear test, where the shear load is primarily sustained by the weld, in coach-peel, the GMT is a dominant factor governing weld strength. This observation was also supported by the work reported by Yang et al.[72] The effect of weld process variations such as electrode length, current level, sheet metal gap and sheet angle (misalignment) on spot welds made from aluminium steel combination was studied by Chen et al.[74] Coach-peel and lap-shear test were also used to analyse spot weld strength due to these variations. Coach peel samples were found to be insensitive to change in current of about  $\pm 500$  A, however, in lap shear test samples, weld strength increased with increase in current. Both test samples showed sensitivity towards gaps between metal sheets. However, lap shear specimens showed increase in weld strength with introduction of gap between sheets and coach peel specimens showed reduction in weld strength due to introduction of gap between sheets. Misalignment of sheet metals during welding (off normal) was found to affect drastically spot welds in lap-shear test with increase in angle reducing tensile shear strength. However, in coach peel test, the reduction in weld strength due to increase in angle was

not significant. The study also finally concluded at the combination for sheet metal gap and sheet angle was significant for lap-shear test while combination of welding current and sheet angle was significant for coach-peel test.

The final test to analyse spot weld failure is the cross-tension test. Pouranvari[75] and Aghajani and Pouranvari[76] studied the failure modes in similar and dissimilar spot weld joints made from DP600 steel and low carbon steel and joints made from martensitic stainless steels with and without nickel interlayer respectively; using both cross tension test and lap-shear test. The minimum weld diameter required for PF mode during cross tension was observed to be lower than the minimum weld diameter for PF during lap shear test. The reason for this was the difference in stresses the welds will be subjected to during both tests. During cross tension test, the weld circumference will be subjected to shear stress while during lap-shear test, the weld circumference will be subjected to tensile stress. Shear stress and tensile stress in ductile materials can be related either by using von Mises failure criterion or Tresca failure criterion as in Equations (7) and (8):- [77]

$$P_f^{cross\ tension} = 0.735 P_f^{lap\ shear} \quad \text{von Mises} \quad (7)$$

$$P_f^{cross\ tension} = 0.64 P_f^{lap\ shear} \quad \text{Tresca} \quad (8)$$

Hence welds that failed during lap shear tests were found to have a higher strength than weld produced at the same condition but tested under cross tension test. An equation was also suggested as in Equation (9) to calculate the pullout failure load in cross tension test.[78]

$$PPF = \pi dt(\tau)HZ \quad (9)$$

where d- weld diameter, t – sheet thickness and  $(\tau)HAZ$  – shear stress at HAZ.

In Chen et al's work[71], the coach peel test for aluminium and steel weld joints had been discussed in the coach peel section and the cross tension test will be reviewed now. For cross tension test, three different fracture modes were observed while for coach peel test, only one mode was observed as mentioned earlier. The three modes are interfacial fracture mode (IF) where fracture occurred within the IMC layer; partial thickness fracture mode (PTF) where the failure occurred at the Al FZ due to crack initiation and propagation at Al FZ and finally partial button pull-out fracture (PBF or PF in general) where fracture initiated in IMC layer, later propagates towards Al thickness resulting in a small Al button on the steel side. This work also compared the peak load for failure between all three tests discussed, with lap-shear test having the highest peak load or weld strength followed by weld strength from cross tension test and lastly weld strength from coach peel test. This surely supports observation from Pouranvari[75] that stated lap shear test gave a higher weld strength compared to cross tension test.

Yang et.al[72]'s work was earlier discussed in the coach peel section as they have investigated the failure modes of spot welds under both cross tension and coach peel test for aluminium alloy joints with different thicknesses. In the case of cross tension, just as the coach peel test, samples were made from three sheets of aluminium alloy with two joint configurations. As in the case of coach-peel test, in the cross-tension test also, IF and PF were observed in both joint configurations. The IF mode was observed in the interior of the weld nugget mainly due to the formation of

voids in the weld nugget. During cross tension test, crack propagated along the voids and led to IF in spot welds. In Pouranvari's study[75], the IF failure was reported to be controlled by the fracture toughness of the weld or FZ. As fracture toughness in metallurgy refers to the ability of a material containing a crack to resist further fracture, existence of voids in the weld nugget will introduce formation of cracks and reduction the fracture toughness of the weld. In the case of PF of weld, weld fracture was initiated by a tensile stress leading to crack formation along weld circumference. However, the final weld fracture was mainly contributed by the shear stress due to crack propagation along the sheet thickness as reported by Pouranvari[75] and Chen et al.[71]

Expressions for failure load at IF and PF mode for cross tension test with three sheet thickness were also given as in Equations (10) and (11) respectively

$$F_{IF}^{CT} = P \frac{\pi(\alpha d_{IN})^2}{4} \sigma_{FZ} \quad (10)$$

where P – porosity constant (0.9 in this case),  $\alpha$  – coefficient = >1,  $d_{IN}$  – weld nugget diameter at the interface for a 3-stack joint and  $\sigma_{FZ}$  – tensile strength of the fusion zone.

$$F_{PF}^{CT} = \pi d_{IN} t \tau PFL \quad (11)$$

where t = sheet thickness and  $\tau PFL$  – shear strength of the PF location. Equation (10) is the same as Equation (5).

Han et.al[73], whose work on lap shear test and coach peel test for aluminium weld joints of different thicknesses with a GMT was discussed earlier. The same work has also investigated the effect of weld joints made from different joint stack ups to the failure load during cross tension test. The study observed that like the coach peel test, GMT is a dominant factor governing weld strength in cross tension test. However, the load carrying capacity of a spot weld tested in cross tension is twice that for the equivalent spot weld tested with coach peel test. Also, as in the case of the coach peel, the data for relationship between weld diameter to weld strength fall in discrete bands according to the GMT value. But the R2 for a best fit line was between 0.364 to 0.471 which is higher than coach peel test that indicates a certain degree of linear relationship between weld diameter to weld strength in cross tension test. The weldability of 1.1 mm thick Quenching and Partitioning (Q&P) steel with 1.5 mm thick Transformation Induced Plasticity (TRIP) steel was investigated in Spena et al[79]'s work. This work used lap-shear test and cross tension test to analysis spot weld strength and failure in these dissimilar steel joints. Interestingly, this work also reported the same results as Han et.al[73] when analysing the relationship between weld strength and weld diameter for spot welds made from samples of different thickness and tests with lap-shear test and cross tension test. Considering the samples that were tested with the lap shear test, there was a linear relationship between weld diameter and tensile shear strength of weld with coefficient of determination (R2) of 0.82. However, in the case of cross tension test samples, the linear relationship between weld diameter and shear strength fall into three different groups based on the value of the ratio normalised to the spot weld size,  $\alpha$  (kN/mm<sup>2</sup>). The value of  $\alpha$  is calculated considering the minimum thickness of the steel. The work also showed that spot welds with the same diameter fail with a higher tensile strength compared to the shear strength with failure occurring

mainly at the HAZ of the Q&P steel due to its lower thickness and minimum HAZ hardness compared to TRIP steel.

Subramanian et al.[80] who investigated the effect of constant current and step current/pulse current on weld strength, also used lap-shear test and cross tension test in their analysis. The study reported improvement in spot weld strength in lap shear test and cross tension test by using pulse current compared to the achieved weld strengths for both tests using constant current. Furthermore, the study also showed that for the 5 different welding schedules experimented (one welding schedule with constant current of 12 kA and the remaining four with different current steps with starting current of 12 kA), lap-shear test produced higher spot weld strength compared to the strength measured during cross tension test for a given welding schedule. In addition to that, the failure energy that was calculated from the load -displacement curve also showed that for a given welding schedule; weld failure energy in lap shear test being higher than the weld failure energy in cross tension test.

The weld failure of boron and phosphorous containing steels were investigated using coach-peel test and cross tension test by Amirthalingan et al.[81] The study used three types of steels to form similar spot weld joints; Steel-CP (contains carbon 0.07 wt% and phosphorus 0.08 wt%), Steel-2CP (contains carbon, C 0.14 wt% and phosphorous, P 0.08 wt%) and Steel-CPB (contains carbon, C 0.07 wt%, phosphorous, P 0.08 wt% and boron, B 0.0027 wt%). The thickness of the steels is 1.5 mm. The FZ for all steels had martensite microstructure and Vickers hardness test on the FZ showed that Steel-2CP's FZ have the highest hardness followed by FZs of Steel-CPB and finally Steel-CP. The highest hardness was related to the highest carbon content of Steel-2CP. The coach peel test showed that due to the highest hardness, brittle failure or IF mode was observed in joints made from Steel-2CP. Steel-CP joint showed PPF and joints made from Steel-CPB gave predominantly PF mode. The presence of boron gave better tensile behaviour to the spot weld and Steel-CPB joints had the highest weld strength followed by joints from Steel-CP and Steel-2CP respectively. In the case of cross tension test, Steel-2CP joint again failed by IF while both Steel-CP and Steel-CPB joints failed by PPF. The weld strengths obtained from the cross-tension test also indicated joints of Steel-CPB having the highest strength compared to the Steel-CP and Steel-2CP respectively. A comparison between weld strengths between coach-peel test and cross tension test showed that as with results obtained by Chen et al.[71] and Yang et al.[72], for joints made from either steels, cross tension weld strength was higher than coach peel weld strength.

Cross-tension test was also used by Park et al.[82] to analyse weld failure in medium-Mn TRIP (MT) similar steel joints and MT/DP dissimilar steels joints. The MT similar steel joints were also welded with and without pre-pulse current. The cross-section test showed that for MT similar steels joint with and without pre-pulse current, even though there was a 59% increase in weld diameter with pre-pulse current, the peak loads for failure for both steel joints were very close to each other. This indicated that the increase in weld diameter with the use of pre-pulse current does not give significant effect on the failure load. Also, MT/MT similar joint failed by IF and MT/DP dissimilar joint failed

by PF with failure occurring at MT's HAZ. The difference in fracture path for both joints were observed to be due to the dilution in the FZ.

Based on the above reviews, the driving forces for IF and PF modes in all the three tests discussed are given in Table 1.

**Table 1.** IF and PF driving forces in spot weld for different test samples

Test sample	Driving force	
	IF	PF
Lap-shear	Shear stress at sheet/sheet interface (Mode II)	Tensile stress at weld circumference
Coach peel	Tensile stress at sheet/sheet interface (Mode III)	Bending stress
Cross tension	Opening mode stress intensity (Mode I)	Shear stress at weld circumference.

## 5. Static and dynamic loading

All the tests discussed in the previous section were conducted in the quasi-static loading condition. However since, in real situations, welds commonly fail by means of fatigue fracture, dynamic loading on spot welds required additional consideration. The static and dynamic tensile tests on seven different types of DP and TRIP steels with differences in chemical compositions and thickness were investigated by Ujil et al.[83] The tests were carried out using lap-shear and peel test samples. The static tests were carried out with displacement rate of 10 mm/min. The dynamic tests used an impact-tensile test configuration. Results from this investigation showed that the standard deviation for failure load for static lap-shear test is generally smaller than the failure load standard deviation for dynamic lap-shear test. The same results were also obtained for static and dynamic peel tests. Also, the joints subjected to dynamic loading for both tensile-shear and coach-peel showed higher strength than the joints subjected to static loading. The difference in standard deviation between the failure load of static and dynamic tests was reported to be partly due to the strain rate dependency of the materials. It was also reported in the lap shear tests (static and dynamic), welds predominantly failed in IF mode and peel tests (static and dynamic) predominantly failed in PF mode. The study also showed when the failure load results of static and dynamic loading are combined either for the lap-shear configuration or the peel test configuration, within the grades of steels tested, weld strength of welded joints increased with increase in sheet thickness. Increase in sheet thicknesses was also reported as in Mat Din's study [48], to increase the weld diameters which in turn increases the performance of the welded joints.

Static and dynamic loading of spot weld joints made from DP590 steel was investigated in Song and Huh's study.[59] To create a combined loading condition with an applied failure load that can be decomposed into axial load and shear load, special testing fixtures were used. The fixtures produce different loading angles on the spot welds; 0o, 15o, 30o, 45o, 60o and 75o. Additionally, a pure shear test was also performed by applying the load 90o to the spot weld joints. A quasi static test on all the loading angles were

carried out on a material tensile testing machine with a tensile speed of  $1 \times 10^{-5}$  m/s. Dynamic loading on all the loading angles were carried out on the same machine with three different tensile speeds; 0.01 m/s, 0.1 m/s and 1.2 m/s. Results from this study showed that for a given tensile speed either in quasi static or dynamic condition, maximum failure loads obtained from the load-displacement curves decreased as the loading angles increased till angle of 30°. Further on, the failure loads increased with increase in angle from 45° to 90°. Also, for a particular angle, as the imposed strain rate increased, the maximum failure load from a load-displacement curve increased with increase in tensile speed. Hence dynamic loading will produce higher load compared to quasi static load. The results are the same as the results reported by Ujil et al. [83] when comparing failure loads between quasi static and dynamic loading. In term of the failure mode, loading angle of 0° create pull-out failure with shearing occurring at the circumferential boundary of the nugget. For other angles, the combined axial and shear loading, failure was initiated with the localised necking at the interface between the HAZ and the base metal. The study further showed that when the effect of tensile speeds on the axial load and shear load components were analysed using a logarithmic scale, it was noticed that axial and shear failure loads increase with increase in tensile speed.

The spot weld failure under static loading and cyclic loading (fatigue failure) was investigated by Pizzorni et.al[84]. Two types of lap-shear test samples were prepared; a spot welded (RSW) sample and a hybrid spot weld-epoxy-polyurethane adhesion bonded (RSW-EPUR) sample. DP1000 steel was used as the sheet metals to be joined. The quasi static tensile shear test was conducted with speed of 5 mm/min. Meanwhile the fatigue test was carried out on the same machine using three base load levels (high, medium, low) at a frequency of 10 Hz with sinusoidal variation and constant amplitude. Fatigue test failure criterion: either complete separation of samples or  $1 \times 10^6$  cycles limit, was set for test to stop. Quasi static test results showed that the failure loads for RSW-EPUR samples to be higher than the failure loads for RSW samples. The addition of adhesive to a spot-welded joint was found to increase the resistance to initial shearing of the weld joint hence making the hybrid joint stiffer than the spot welded joint. The overall displacement before failure in the load-displacement curves, however, was the same for both samples and both samples failed by means of PF. In the fatigue tests, RSW-EPUR joints were found to have better resistance to fatigue failure and longer fatigue life compared to RSW joints. Both samples also showed increase in fatigue life with decrease in amplitude of the load cycles. The increase in fatigue life in the hybrid joints compared to welded joints at the same loading condition was due the slow propagation of crack in the adhesive layer. The investigation by Xiao et.al[85] which was similar as the investigation by Pizzorni et.al[84] gave a contradicting result in the case of quasi static experiment. This work used stainless steel and epoxy resin adhesive to form two joint samples; spot welded joint and weld-bonded joint. Unlike in Pizzorni's work[84], the quasi static tensile shear test with the speed of 5 mm/min showed that spot welded joints have higher shear strength than the weld-bonded joints. The adhesive layer in between the stainless-steel sheets were found to raise the contact resistance causing expulsion during welding, hence leading

to reduction in weld strength. The failure mode for the spot-welded joints were base metal tearing/base metal failure while the weld-bonded joints failed by PF. The results in the fatigue test where the no.of cycles before test stops was limited to  $2 \times 10^6$  cycles, however was the same as in Pizzorni's report [84] with the weld-bonded joints have better fatigue performance than the spot welded joints. The other work that supports observation by Pizzorni et.al[84] and Xiao et.al[85] was reported by Fujii et.al.[86] The difference in this work compared to the other two was that the joints were made from three stack of sheets of mild steel and ultra-high strength steel. This work also reported that is the quasi static tensile shear test, the weld-bonded samples for both steels to have higher failure loads compared to the steels spot welded samples. In the fatigue test, just in the case of the previous work, the inclusion of adhesive layer was found to delay the fatigue crack initiation and propagation in the weld-bonded samples hence weld-bonded samples of both steels have longer fatigue life compared to the spot-welded samples.

A comparison study on quasi static lap-shear test, quasi static coach peel test and fatigue test on spot weld joints made from dissimilar metals (1.2 mm thick AA6022-T4 with 2 mm thick IF steel) and similar metals (1.2 mm thick AA6022-T4 with 2 mm thick AA6022-T4) was carried out by Rao et al.[87] The quasi static lap-shear test and coach peel test were performed with speed of 2 mm/min. The fatigue tests were conducted with a constant frequency of 40 Hz for lap-shear and 20 Hz for coach-peel. In both lap-shear test and coach peel test, the dissimilar joint configuration of AA6022-T4-IF produced high fracture load compared to the similar joint configuration of AA6022-T4- AA6022-T4. The reason for this was referred to the weld diameters with dissimilar joints produced bigger welds than similar joints. The results also showed that coach peel tests for both joints produced lower failure loads than the joints tested with lap-shear tests. Referring to the fracture modes, lap-shear tests for the similar and dissimilar joints produced IF and coach-peel tests for both joints produced PF with the weld button on the 1.2 mm AA6022-T4 aluminium sheet. The work also reported that the lap-shear tests were dominated by shear forces and coach-peel tests dominated by bending force. In the case of fatigue test, overall lap-shear joints showed greater fatigue strength compared to coach-peel joints as shown in Figure 11. The fatigue failure was dominated by crack initiation at the notch root opening close to the HAZ which will later propagate through the sheet thickness. The superior fatigue performance in the dissimilar weld joints were deduced to a combination of factors such as weld diameter, HAZ properties and weld nugget hardness.

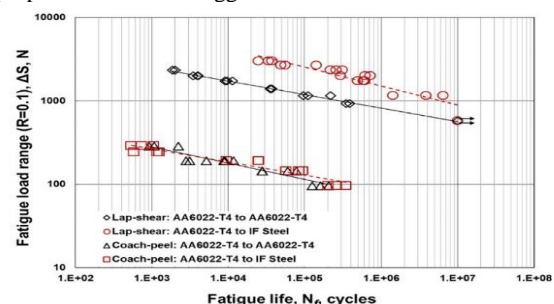


Figure 11. Fatigue life of similar and dissimilar weld joints tested with lap-shear and coach peel [87]

Similar results to Rao et al. [87] was also obtained by Tanegashima et al.[88] where quasi static lap-shear tests produced higher failure strength compared to quasi static coach-peel tests. Lap-shear samples were also reported to have better fatigue strength compared to coach-peel samples. This study also reported fatigue failure occurred due to crack initiation mainly at the notch root opening and further propagated in the thickness direction. The relationship between weld diameters and fatigue life of welds was investigated by Heewon.et.al[89]. The study used two different electrode tip diameters (8 mm and 10 mm) to produce two different weld diameters (5.1 mm and 5.7 mm respectively). Weld joints were made using 1.2 mm thick TRIP steels. The bigger weld diameter was noticed to have a better fatigue strength as in Figure 12. The reason deduced that increase in weld diameter, led to increases joint area. Three different failure modes were observed in this study which depended on the crack initiation and propagation during testing. As reported in Tanegashima et al. work[88], crack initiation was observed at the notch root. However, the way the crack propagated led to three different failure modes. Crack propagation around the nugget gave the PF mode. Crack propagation in the HAZ region, slightly further from the nugget produced the plug failure and finally crack propagation along the sheet thickness produce HAZ failure.

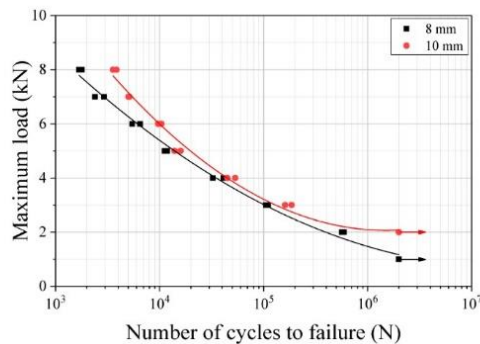


Figure 12. Fatigue life of different weld diameters<sup>[89]</sup>

## 6. Simulation of spot-welding failure

The weld quality and failure analyses reviewed in the previous section are referred to as destructive testing. Destructive testing to measure the spot weld diameter, to determine the weld failure load, process parameter optimization or to analyse the weld failure criterion involved destroying the samples in the testing process. Destructive testing of weld samples usually conducted in a laboratory experimental setup is expensive and time consuming. Also, each test only represents a single loading condition and analyses the effect of combined loading conditions as in the case of the automotive crashes which is not experimentally possible. Advancement in computer technology and knowledge in Finite Element Analysis (FEA) has made many researchers to investigate the use Computer Aided Engineering (CAE) to simulate and analyse spot weld development and failure as a cheaper option to destructive testing and better potential to create complex simulations of weld failure in a crash situation.

Spot welding FEA can be divided into electro-thermal analysis and mechanical-thermal analysis. Figure 13 shows

the RSW FEA procedure. The failure analysis on the spot welds requires an accurate and reliable simulation of the spot welds based on the welding parameters, sheet types and thicknesses as well other process variations such as current shunting, electrode deformation and gap between sheets. Initially, work that have concentrated in the FEA of spot weld development will be reviewed. Two-dimension (2D) axisymmetric models and three dimensional (3D) models have been developed to simulate spot weld formation in DP steels, stainless steels and aluminium steels joints by Vigneshkumar et.al, Baskoro et al, Wan et.al, Jagadeesha, et.al, Lee et.al and Zhao et.al. [90-95] All simulation investigated the spot weld growth in different welding currents and weld time and reported that weld diameter increased with increase in current and weld time with an average error percentage between experimental and simulation of less than 10% indicating good agreement between both results. Figure 14 shows an example of temperature distribution plots for different welding currents, with the distribution of the highest temperature represents the spot weld size (diameter and height).

The simulations of the contact pressure between electrode-sheet interface and sheet-sheet interface during squeeze cycle were investigated by Zhao et.al and Wan et.al.[95, 96] The contact pressure in the workpiece/electrode and workpiece/workpiece interfaces was analysed during the weld cycle and hold cycle. The contact pressure at both interfaces was noticed to increase during weld cycle due to thermal expansion and later decrease due to plastic deformation at the weld centre and eventually changes back to the initial state similar to during squeeze cycle. Concentration of contact pressure at the edge of the contact interfaces was formed after nugget formation which was expected to be beneficial in expulsion prevention. Higher contact pressure at the edge of the electrode was also observed which will lead to electrode plastic deformation.

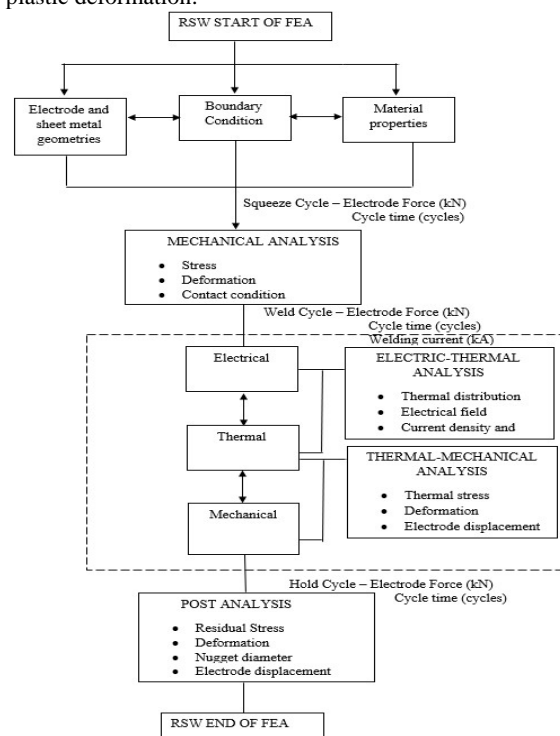
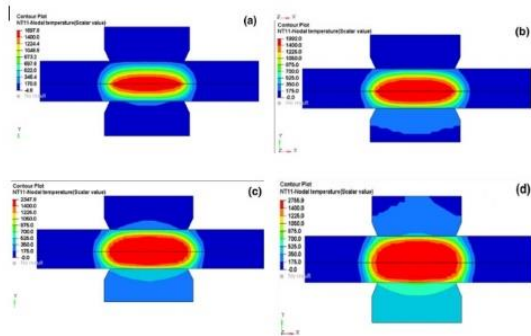


Figure 13. Flowchart of RSW FEA procedure



**Figure 14.** Temperature distribution plots for different welding currents at constant weld time

Numerous works on modelling spot weld joints made of more than two stacks and dissimilar metals have also been carried out. The FEA on nugget growth with three different steels and thickness was analysed by Zhao et al. [97] The study intended to analyse the effect of epoxy adhesive on nugget formation during spot welding. Measurement of the dynamic resistance during spot welding process and weld bonding process showed that existence of adhesive in between sheets increased the contact resistance and initiated nugget formation earlier compared to the spot-welding process which does not have adhesives. The simulations also showed for the same welding parameters, weld-bonding process generated more heat during welding and produced a bigger weld compared to the spot-welding process. The FEA on the spot welding of LITECOR, a hybrid material with a polymer core (0.3 – 1.0 mm thick) between two steel face sheets (each 0.2 – 0.3 mm thick) was developed by Tanco et.al[98]. The modelling of dissimilar joints with aluminium and steel had been studied by Wang et.al, Wan et.al and Du et.al. [99-101] These models concentrated in modelling the IMC thickness at the Al-steel interface and the partial melting zone (PMZ) that is observed in aluminium spot welding which involved unequal thickness. Formation of the PMZ, due to its low thermal conductivity, was observed to function as a heat barrier for molten nugget development. Important information such as the mechanical analysis on sheet deformation and stress/strain rate showed that after welding, the lower electrode which was in contact with the steel showed significant plastic strain compared to the upper electrode that was in contact with aluminium. This indicates the steel side electrode wears out faster than the aluminium side electrode. Further, the analysis on thermal analysis, showed that during welding, steel generated almost 75% of heat while aluminium only generated 4.4% of the total heat used for nugget development and growth in this welding process. All these models agreed well with the experimental results

Sedighi et al.[102] developed a finite element model (FEM) to analyse the effect of sheet thickness on residual stress that exist once the weld nugget has been formed. Aluminium 6061-T6 sheets with four different thicknesses were used in this analysis to form spot weld joints with similar sheet thicknesses. Simulation of residual stress showed that maximum residual stress occurs at the centre of the nugget and diminishes moving towards the edges. Microstructure and thermal gradient were pointed out as the reason for the high residual stress at the weld centre. The analysis also showed that the increase in sheet thickness also

increases the residual stress. This is because when sheet thickness increases, larger nugget diameters are required to create proper weld joint. The larger welds contribute to increase in residual stress due to the increase in tensile residual stress in the nugget during solidification, the more the increase in the compressive residual stress in the adjacent regions. The residual stress on spot weld investigation conducted in Moharrami and Hemmati's work[103] gave a contradictory result compared to Sedighi et al.[102] , yet an accurate representation in term of distribution of residual stress in spot welds after welding. The model analysis showed that the maximum tensile residual stress was located near the edge of the weld nugget. As in Sedighi's report[102], this work also reported that tensile residual stress decreased along the thickness of the sheet. A simulation on the mechanical loading post spot weld also showed plastic deformation along weld nugget due to high stress concentration. The loading analysed with a lap shear test simulation also showed the stress distribution was altered along the direction of loading with tensile stress on one side of the weld and compressive stress on the other side of the weld due to sheet bending.

The effect of electrode tip deformation, current shunting and poor fit on weld nugget development were numerically analysed for using 2D FEMs by Wang et.al, Bi et.al, Yang et.al, Podrzaj et.al.[104-107] The electrode deformations considered in this study were electrode pitting (EP) and electrode tip diameter enlargement (ETDE). Simulation showed that electrodes that had undergone changes in tip morphology either EP or ETDE, produce deterioration in weld strength in comparison to the weld strength achieved by using the normal electrode tip. Both Bi et.al and Yang et.al[105, 106] reported that current shunting is severe when welds are closer to each other hence affecting development of the successive welds. Increasing the weld spacing between the welds reduced the effect of current shunting. The recommended practical weld spacing was 20 mm to 25 mm. Bi also suggested that welds which are closer for instance 16 mm apart may increase the welding current for the second weld, which were found to solve the shunting problem. Even though current shunting to the first weld occurred, the increased current density due to increase in welding current, was found to be able to produce a second weld within the required weld diameters. The concept of increasing welding current was also discussed by Yang who increased the welding current for the third weld when weld spacing between the three welds was 20 mm. Yang also reported that in spot welding, for two spot welds arranged in a line, the current shunting depends only on weld spacing. However, for three spot welds arranged in a triangular pattern, shunting in the third weld depends on the weld spacing and the weld size of prior welds. These models were also validated with experimentation and showed good agreements with experimental results.

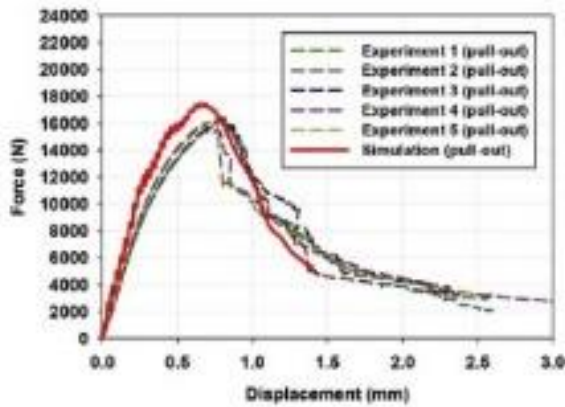
The simulation of spot weld failures involved development of force-displacement curves based on different failure criterion for static loading and dynamic loading and S-N curve for fatigue loading. The FEA on spot weld failure using lap-shear test and U-shape test (cross tension test) was conduct in the work by Chung et.al[108]. The weld failure of similar sheet metal joints in three different types of steels; 1.2 mm thick TRIP980, 1.6 mm thick DP980 and 1.2 mm thick low carbon steel GMW2,

were analysed using both test samples. The analysis considered the hardening deterioration that occurred after ultimate tensile strength (UTS) due to the transformation of micro-voids into macro-cracks especially in ductile sheets. Therefore, stress triaxiality dependent fracture strain and numerical inverse method was used to accurately characterise the failure criterion and hardening behaviour past UTS, which in usual practise would just be extrapolating the hardening behaviour obtained up to the UTS to cover the range beyond UTS. In this study, the simulated force displacement curves corresponded well with the experimental curves for both lap-shear test and U-shape cross tension test. The failure strength and failure modes with both numerical and experimental also agreed well to each other. The averaged errors of the load at the peak between simulation and experiment were 5.92% for lap-shear and 13.5% for U-shape test. However, a larger displacement at fracture error was noticed for both tests with averaged error of 13.2% for lap-shear and 29.8% for U-shape tension test. All experimental tests were conducted under quasi-static loading condition. Noh et al.[109] have also analysed dissimilar steel weld joints DP980-TRIP980 and GMW2-TRIP98 with the same sheet metal thicknesses, failure criterion and test samples as discussed by Chung[108]. This work also showed good agreement between the simulated and experimental load-displacement curves for both lap-shear and U-shaped test samples. The investigation also concluded that the failure in the test coupon was the result of competition between high strength/low ductility zone and low strength/high ductility zone. Figures 15(a) and 15(b) give examples of simulated force-displacement curves for lap-shear test and cross tension test for TRIP980 at 6 kA welding current respectively. Figures 16(a) and 16(b) showed the simulated and experimental failure modes for TRIP980 at 6 kA for lap-shear test and cross tension test, respectively.

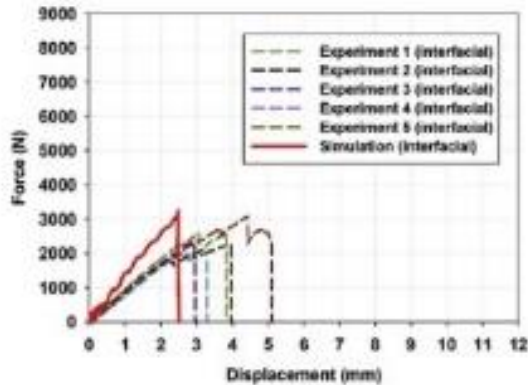
Paveebunvipak and Uthaisangasuk [110] also developed FEMs to simulate the lap-shear and cross-tests for similar and dissimilar steel joints of high strength steel grade 1000 and press hardened (PH) 22MnB5 steel. The study developed the fracture loci for different weld zones, such as base metal (BM), fusion zone (FZ), transition of heat affected zone, and base metal (HAZ/BM) and transition of heat affected zone and fusion zone (HAZ/FZ) by using physical simulation, 2D representative volume element (RVE) and fracture modelling methods. The simulated force-displacement curves and fracture modes which used the developed fracture loci agreed well with the experimental force displacement curves and fracture modes for 1000-1000, PH-PH and 1000-PH steel joints. The effect of the IMC layer's morphology and location to spot weld failure was numerically analysed using FEA by Chen.et.al[111]. This study developed a micro scale model to study the IMC layer's strength in relation to its thickness and location for Al-steel spot welds. A macro model was also developed to analyse the Al-steel spot weld strength using coach peel, lap shear and cross tension test samples. Both models were validated by experimental results. Shear failure model was used to approximate the weld failure. The micro scale model showed that under tensile and shear loading, thin IMC layer ( $<10\mu\text{m}$ ) produced higher failure load compared to thick IMC layer as the crack propagation was obstructed by the large metal remnants in the thin layer.

The stress-displacement curves also showed IMC layer has higher strength in tensile loading compared to shear loading. Also, the highest weld strength in both loading conditions were found to be at the nugget edge rather than the nugget centre as the IMC thickness is relatively thin at the edge. The results of the IMC tensile and shear strengths from the micro-scale model were used to predict the fracture modes in the macro-scale model under coach-peel, lap-shear and cross-tension testing conditions. The load-displacement curves and different fracture modes under lap-shear, coach peel and cross tension agreed to the experimental observation. As reported by other experimental work [75-77,84] with quasi-static loading condition, lap shear test produced the highest spot weld strength, followed the weld strength from cross-tension and finally spot weld from coach-peel test.

The spot weld failure modes using lap-shear, coach peel and cross tension were also studied using FEA by Nguyen et.al.[112] This study used EWK rupture model; a strain damage model for weld failure prediction. Similar to Chen.et.al[111], the spot welds that joined the high strength steels failed either by IF or PF when simulated under the three tests. The load-displacement curves produced by the simulations in this study as well as fracture modes under lap-shear, coach peel and cross tension agreed to the experimental observation. The failure of multiple spot welds during vehicle crash was modelled by Wang et.al[113] using the resultant based failure criterion. The force and moment values for the failure criterion were obtained experimentally via unidirectional loading of single spot weld joints using KSII, coach-peel and torsion tests. The failure criterion was later used in the modelling of a multiple weld joints components subjected to crush test. The peak loads in the load-displacement curves from the crash simulation and experimental crush test results had a relative error of 5%. The simulation however was not able to simulate the local plastic deformation in the sheet that occurred after the peak load hence a difference was observed in the final displacements after the peak loads in both the simulation and experimental load-displacement curves. The use of J-integral fracture criterion to simulate spot weld failure and to calculate the joint's maximum force was investigated by Dorribo et.al.[114] The study concentrated on spot welds in martensite boron steels and considered multiple sheet thickness combinations (0.8 mm, 1.5 mm and 2.0 mm), loading angles (0o-shear loading, 90o-normal loading and 45o- mixed loading) and weld diameters. The failure criterion was able to predict the maximum load for failure in lap shear test and mixed loading test with small relative error percentage compared to experimental maximum load values. However, in the case of the normal test, there was an obvious difference between the simulated and experimental maximum loads and huge error percentage. The results also showed that for a given combination of sheet thicknesses and weld diameter, the peak load for shear test was greater followed by mix-mode and finally normal test as given in Figure 17. The results of mixed mode tests are closer to shear tests, due to the higher relevance of the shear component.

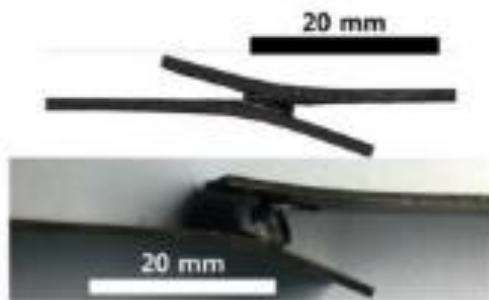


(a)

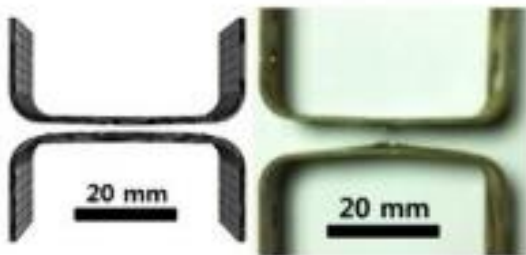


(b)

**Figure 15.** (a) Simulation and experimentation force-displacement curves for lap-shear test and (b) simulation and experimentation force-displacement curves for cross-tension test (TRIP980 6 kA) [108]



(a)



(b)

**Figure 16.** (a) Simulation and experimentation failure modes (PF) for lap-shear test and (b) simulation and experimentation failure modes (IF) for cross-tension test (TRIP980 6 kA) [108]

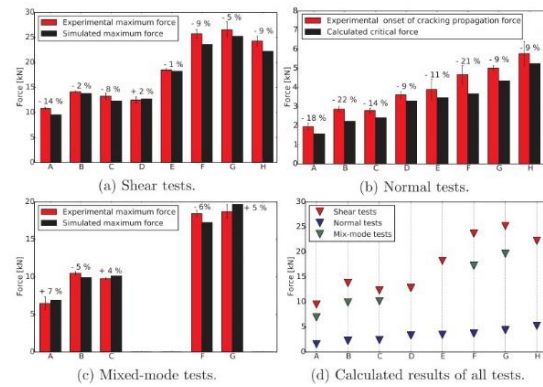


**Figure 17.** Simulation and experimental peak loads for shear test, normal test and mixed mode test [114]

The FEM of hybrid joints of spot weld and epoxy based adhesive was studied by Weiland et.al[115]. KSII cross tension test samples made from 1.4 mm HCT600X DP steel sheets were used in this work. The fracture mode of three different joints; spot weld, adhesive bonded and spot weld-adhesive bonded were modelled by applying tensile (Mode I) and shear (Mode II) loading. A programmed optimization routine based on 10 step calculation schemes was used to simulate the joint fracture and minimize the difference between the mean experimental force-displacement curve and the numerically simulated force-displacement curve. The work reported that the simulated load-displacement curves for all joint types under shear loading agreed well with the experimental data with a percentage error of 9%. However, the simulated load-displacement curves for all joints under tensile loading had a significant error difference of 16% which was attributed to the inability to accurately model the KSII sample deformation at the point of fracture. Another similar work on hybrid joints was also reported by Souza et al.[116] In this work, the numerical models of spot welded joint and spot weld-epoxy adhesive bond joint were tested under lap-shear test. The lap-shear samples were produced using 0.75 mm interstitial free (IF) steel sheets. This work also found good agreement between the simulated load-displacement curves for both joint types with their respective experimental curves. Even though this work did not indicate the fracture model used to simulate the fracture, similar to Weiland et.al's work[115], it also reported higher stiffness and greater failure load in hybrid joints compared to spot welded joints. All the simulations and experimentations reviewed in this section so far were conducted under quasi-static condition.

Researches on FEA of spot weld failure in dynamic loading condition have also been presented. The J-integral fracture criterion, which is associated to crack initiation and propagation was also used by Long et.al[117] to estimate the fatigue life of spot welds of dissimilar metals and unequal thickness joints of DP590 and low carbon steel DC01. Lap-shear test samples were used in this investigation. The study showed that stress intensity factor KI was significantly affected by crack shape and crack length. The developed FEA model in this study was able to estimate closely the fatigue life of lap-shear weld joints to the experimental results at longer life cycle but at lower life cycles, the numerical estimate was twice higher than the experimental results. Chung et al.[108] and Noh et al.[109] also worked on the simulation models to analyse the effect of dynamic loading on spot weld failure.[118] Similar weld

joints of TRIP980 and GMW2 and dissimilar weld joint of TRIP980/GMW2 were analysed using the failure criterion and hardening behaviour discussed in their previous work. Lap-shear and coach-peel test samples were used in this work and dynamic loading speeds of 500 mm/s and 3000 mm/s were applied to these test samples. TRIP980 similar weld joint failed at the FZ via IF for both lap-shear and coach peel tests and the simulation and experimental force-displacement curves and failure modes had a good agreement to each other. The results also showed that the peak load increases with increase in the speed of dynamic loading. GMW2 similar weld joints failed via PF due to the low strength of the BM. However, for GMW2, there was a disagreement in the peak load between simulation and experimentation for both lap-shear and coach peel tests. A variable strain rate-sensitivity model was later used for more accurate prediction of peak load. The dissimilar weld of TRIP980-GMW2 showed only PF for both coupon tests with fracture triggered at the BM of GMW2. As in the case of the GMW2 similar weld joint, variable rate-sensitivity model had to be used to observe better agreement between the simulation and experimental results. The results also showed that the peak load increased with increase in the speed of dynamic loading.

The fatigue life of DP780GI spot weld joints was experimentally and numerically analysed in Wu et.al's work[119]. Lap-shear test and coach peel tests were used in the investigation. Experimental results of weld joint fatigue life in lap-shear and coach peel were similar to results presented in Figure 11. The crack propagation model based on the stress intensity factor (SIF) and Paris Law was used to simulate the crack development in lap-shear and coach-peel tests. In the lap-shear joint, the crack that was initiated at the weld edge and later propagated through the sheet thickness and across the width of the sheet was modelled as a semi oval surface crack. The crack in the coach-peel test, was a combination of interfacial crack and followed by kinked crack. The calculated fatigue life agreed well with the experimental fatigue life for both test samples. Kang et.al[120] developed FEMs to analyse the fatigue life of joints made from spot weld and adhesive and joint made from just adhesive by itself. Lap-shear, coach-peel and cross-tension test samples were used in the finite element modelling. Structural stress equation was used in the development of the S-N curves from the experimental fatigue data for similar steel joints made from DP600 and HSLA340 with lap-shear and coach peel tests. The model was later used to predict the fatigue life of various steel joints made from spot weld and adhesive and joint made from just adhesive only, tested with cross tension test. The simulation showed that there was good agreement between experimental and simulation in the shorter-life region, but difference was observed in the longer-life region. The reasons for this was concluded due to the shortcoming in the model that was developed using lap-shear and coach-peel test samples as well as the inability of the failure criterion to accurately predict the fatigue characteristics of adhesive joints.

## 7. Future work

Review of spot weld failure analyses both, experimentally using test samples as well as numerically

with computational finite element analysis method was carried out. The test samples that are commonly used in experimental analyses were able to analyse spot weld failure in unidirectional loading condition. However, spot weld failure in crash condition is due to combined loading. Patil et.al's [121] FEA model on B-pillar which was subjected to impact loading and Rosch et.al's[122] FEA model on vehicle tow bar subjected to fatigue loading have confirmed that the spot welds are subjected to loads that have components of stresses from the lap-shear, coach-peel and cross tension tests. Figure 18 shows the welds on a B-pillar and the stress components in each weld.

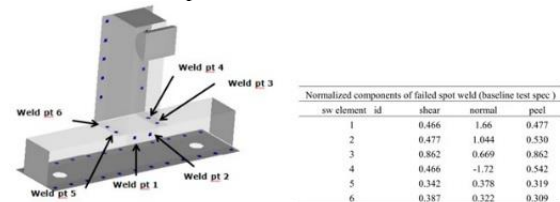
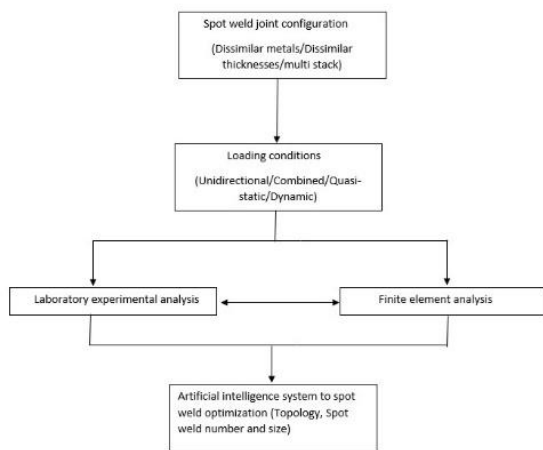


Figure 18. Spot welds and their stress components<sup>[121]</sup>

Hence, the practical spot weld failures may not be accurately analysed in the laboratory experimentation. Furthermore, Li and Feng[123], from their work have concluded that static performance of the BIW in typical working condition is impacted by static torsional stiffness and static bending stiffness. The spot weld failure due to torsional loading have not been extensively analysed in any work. Also experiments on combined loading was attempted by Song.et.al[59] and Dorribo et.al[114], but the joints were only made from similar steels. Therefore, a test sample similar to that used in Wang et al.'s work [113] could be used to conduct analyses on spot weld failure due to torsion. Furthermore, spot weld failure in dissimilar steels with different thickness under combined loading need to be further investigated to address the current automotive design. This may involve requirement for specially designed jigs and fixtures to experimentally impose combined loading on spot welds.

The review also showed that weld bonded joints have better fatigue life compared to spot welded joints. Hence more investigations need to be carried out to explore this joint type. Current work seems to have only concentrated on similar joints. Dissimilar metal weld bonded joints with more than 2 stacks of sheets with different thicknesses need further concentration as this will allow automotive industries to achieve the MML design. In the case of FEA of spot weld failures, in general limited work was found in multi spot weld analysis and spot weld failure due to fatigue loading. Analysing failures involving multiple spot welds subjected to dynamic loading and fatigue loading will be more suitable to be carried out using FEA rather than laboratory experimentation due to the cost and complexity in experimental setup. Ryberg et.al[124] reported that topology optimization and spot weld density optimization are the approaches that have best potential to solve spot weld reduction problem for automotive structures. Both these approaches were evaluated using FEA. Therefore, taking into account these approaches, analyses of multi spot weld failures using combined loading is worth investigating considering the benefits to spot weld reductions. The review have only seen one work on this area; Wang et al.'s work[113] which in fact used quasi static loading.

The FEA of fatigue loading to spot weld failure in dissimilar metal joints and hybrid joints are potential areas for future research. The reviewed work on FEA of hybrid joint used only steel joints subjected to quasi static loading. The ability of hybrid joints to extend fatigue life of spot welds is an important information obtained from this review and further FEA investigation on this type of joint will be beneficial to the automotive industry. Automotive manufacturers are already looking to the potential use of adhesives in automotive manufacturing. However as reported by Kang et al.[120], a separate failure criterion for adhesive is required apart from the failure criterion for the sheets to accurately calculate the fatigue life in FEA. Furthermore, considering the existing limitations in experimental analysis and finite element analyses, development of a hybrid system as in Figure 19, incorporating experimental and numerical analyses to accurately characterise spot weld failure based on the loading conditions and the use of artificial intelligence (AI) systems for spot weld optimization is an area which has a very promising future.



**Figure 19.** Proposed hybrid system for spot weld failure analysis and optimization

## 8. Conclusion

The paper had critically reviewed the analyses of spot weld failures both experimentally and numerically using finite element analysis. The intention of the review is to give comprehensive information on the current practices and research interest related to RSW weld failure analysis. The review has concentrated on the spot weld failures on the current automotive metals, such as Advanced High Strength Steel (AHSS), aluminium and magnesium. Spot weld failure mainly depends on the strength of the spot weld joints which in turn relates to the material weldability, sheet thickness, spot weld positions, welding parameters, material coating and loading types. Currently, due to the need for weight reduction of automotive and increased safety and structural integrity requirement of automotive, dissimilar metal joints; joints made from different metals and thickness are gaining importance in automotive design. Apart from this, automotive industries are also studying the use of adhesive to form hybrid spot weld joints with an

intention to achieve multi-materials lightweight (MML) design.

The required weld joint strength was found to be achieved with the correct combination of welding parameters and balanced heat generation in both metals that are being used to form the weld joint, especially in dissimilar joints. Achieving both conditions will lead to the development of a sound weld nugget to join the metals that being welded. The mechanics of the formation of weld nugget seems different for different metals due to the differences in the materials thermal, mechanical and electrical properties. The joining of AHSS steels involves joining at the sheets interface due to higher dynamic resistance leading to localised metal heating, melting and solidification at the interface creating a weld nugget to join both steels together. The joining of AHSS and aluminium involves formation of intermetallic compound (IMC) layer at the interface and weld nugget only formed on the steel side. Meanwhile for AHSS and magnesium joint, weld nugget is formed on the magnesium side while the metals interface was combined by brazing, soldering and solid state joining.

Weld pull-out failure (PF) is the preferred weld failure in the automotive industries and achieving this failure is attributed to the weld diameter and the types of loading. At present, the ability to achieve PF of weld is being analysed experimentally by using the lap-shear test, coach-peel test and cross-tension test. Each of this test however analyse weld failure on unidirectional loading. Lap shear test produced a greater failure load follow by cross tension test and lastly the coach-peel test. Spot welds are also subjected to quasi-static, dynamic and fatigue loading conditions. The joints subjected to dynamic loading showed higher strength than the joints subjected to static loading. The fatigue life of spot welds can be increased with decrease in amplitude of the load cycles and inclusion of adhesive layer between sheets. Spot weld numerical failure analyses used different failure criteria to simulate the load-displacement curves. Finally, based on the review, future projects were proposed in areas where further research and investigations are required.

## References

- [1] Ambroziak, A.; Korzeniowski, M., Using Resistance Spot Welding for Joining Aluminium Elements in Automotive Industry. *Archives of Civil and Mechanical Engineering* **2010**, *10* (1), 5-13. DOI 10.1016/S1644-9665(12)60126-5
- [2] Yuan, X.; Li, C.; Chen, J.; Li, X.; Liang, X.; Pan, X., Resistance spot welding of dissimilar DP600 and DC54D steels. *Journal of Materials Processing Technology* **2017**, *239*, 31-41. DOI: 10.1016/j.jmatprotec.2016.08.012
- [3] Wan, X.; Wang, Y.; Zhang, P., Effects of Welding Schedules on Resistance Spot Welding of DP600 Steel. *ISIJ International* **2014**, *54* (10), 2375-2379. DOI: 10.2355/isijinternational.54.2375
- [4] Cooke, K. O.; Khan, T. I., Resistance spot welding aluminium to magnesium using nanoparticle reinforced eutectic forming interlayers. *Science and Technology of Welding*

- and Joining **2018**, 23 (4), 271-278. DOI: 10.1080/13621718.2017.1373481
- [5] Pouranvari, M., Critical assessment 27: dissimilar resistance spot welding of aluminium/steel: challenges and opportunities. *Materials Science and Technology* **2017**, 33 (15), 1705-1712. DOI: 10.1080/02670836.2017.1334310
- [6] Winnicki, M.; Małachowska, A.; Korzeniowski, M.; Jasiorski, M.; Baszczuk, A., Aluminium to steel resistance spot welding with cold sprayed interlayer. *Surface Engineering* **2018**, 34 (3), 235-242. DOI: 10.1080/02670844.2016.1271579
- [7] Rajarajan, C.; Sivaraj, P.; Balasubramanian, V., Microstructural analysis of weld nugget properties on resistance spot-welded advance high strength dual phase ( $\alpha + \alpha'$ ) steel joints. *Materials Research Express* **2020**, 7 (1), 016555. DOI: 10.1088/2053-1591/ab654d
- [8] Florea, R. S.; Bammann, D. J.; Yeldell, A.; Solanki, K. N.; Hammi, Y., Welding parameters influence on fatigue life and microstructure in resistance spot welding of 6061-T6 aluminum alloy. *Materials and Design* **2013**, 45, 456-465. DOI: 10.1016/j.matdes.2012.08.053
- [9] Geslain, E.; Rogeon, P.; Pierre, T.; Pouvreau, C.; Cretteur, L., Coating effects on contact conditions in resistance spot weldability. *Journal of Materials Processing Technology* **2018**, 253, 160-167. DOI: 10.1016/j.jmatprotec.2017.11.009
- [10] Safari, M.; Mostaan, H.; Yadegari Kh, H.; Asgari, D., Effects of process parameters on tensile-shear strength and failure mode of resistance spot welds of AISI 201 stainless steel. *The International Journal of Advanced Manufacturing Technology* **2017**, 89 (5), 1853-1863. DOI: 10.1007/s00170-016-9222-z
- [11] Brozek, M.; Novakova, A.; Niedermeier, O., Resistance spot welding of steel sheets of the same and different thickness. *Acta universitatis agriculturae et silviculturae mendelianae brunensis* **2017**, 65 (3), 807-814. DOI: 10.1016/j.jmatprotec.2017.08.035
- [12] Lin, H. C.; Hsu, C. A.; Lee, C. S.; Kuo, T. Y.; Jeng, S. L., Effects of zinc layer thickness on resistance spot welding of galvanized mild steel. *Journal of Materials Processing Technology* **2018**, 251, 205-213. DOI: 10.1016/j.jmatprotec.2017.08.035
- [13] Söderberg, R.; Wärmefjord, K.; Lindkvist, L.; Berlin, R., The influence of spot weld position variation on geometrical quality. *CIRP Annals - Manufacturing Technology* **2012**, 61 (1), 13-16. DOI: 10.1016/j.cirp.2012.03.127
- [14] Ou, Y.; Yueping, L., Quality Evaluation and Automatic Classification in Resistance Spot Welding by Analyzing the Weld Image on Metal Bands by Computer Vision. *International Journal of Signal Processing, Image Processing and Pattern Recognition* **2015**, 8 (5), 301-314. DOI: 10.14257/ijsp.2015.8.5.31
- [15] Vignesh, K.; Elaya Perumal, A.; Velmurugan, P., Optimization of resistance spot welding process parameters and microstructural examination for dissimilar welding of AISI 316L austenitic stainless steel and 2205 duplex stainless steel. *The International Journal of Advanced Manufacturing Technology* **2017**, 93 (1), 455-465. DOI: 10.1007/s00170-017-0089-4
- [16] Mousavi Anijdan, S. H.; Sabzi, M.; Ghoheiti-Hasab, M.; Roshan-Ghiyas, A., Optimization of spot welding process parameters in dissimilar joint of dual phase steel DP600 and AISI 304 stainless steel to achieve the highest level of shear-tensile strength. *Materials Science & Engineering A* **2018**, 726, 120-125. DOI: 10.1016/j.msea.2018.04.072
- [17] Pouranvari, M., Effect of Welding Parameters on the Peak Load and Energy Absorption of Low-Carbon Steel Resistance Spot Welds. *ISRN Mechanical Engineering* **2011**, 1-7. DOI: 10.5402/2011/824149
- [18] Russo Spena, P.; Cortese, L.; De Maddis, M.; Lombardi, F., Effects of Process Parameters on Spot Welding of TRIP and Quenching and Partitioning Steels. *steel research international* **2016**, 87 (12), 1592-1600. DOI: 10.1002/srin.201600007
- [19] Kim, G.-C.; Hwang, I.; Kang, M.; Kim, D.; Park, H.; Kim, Y.-M., Effect of Welding Time on Resistance Spot Weldability of Aluminum 5052 Alloy. *Metals and Materials International* **2019**, 25 (1), 207-218. DOI: 10.1007/s12540-018-0179-3
- [20] Shawon, M.; Gulshan, F.; Kurny, A., Effect of Welding Current on the Structure and Properties of Resistance Spot Welded Dissimilar (Austenitic Stainless Steel and Low Carbon Steel) Metal Joints. *Metallurgical & Materials and Mining Engineering* **2015**, 96 (1), 29-36. DOI: 10.1007/s40033-014-0060-6
- [21] Dwivedi, S. S. S., Optimization of Resistance Spot Welding Process Parameters on Shear Tensile Strength of SAE 1010 steel sheets Joint using Box-Behnken Design. *Jordan Journal of Mechanical and Industrial Engineering* 2016, 10 (2), 115-122.
- [22] Muhammad, N.; Manurung, Y. H. P.; Hafidzi, M.; Abas, S. K.; Tham, G.; Haruman, E., Optimization and modeling of spot welding parameters with simultaneous multiple response consideration using multi-objective Taguchi method and RSM. *Journal of Mechanical Science and Technology* **2012**, 26 (8), 2365-2370. DOI: 10.1007/s12206-012-0618-x
- [23] Wan, X.; Wang, Y.; Zhao, D., Multiple Quality Characteristics Prediction and Parameter Optimization in Small-Scale Resistance Spot Welding. *Arabian Journal for*

- Science and Engineering* **2016**, 41 (5), 2011-2021. DOI: 10.1007/s13369-016-2061-2
- [24] Thakur, A.; Nandedkar, V., Optimization of the Resistance Spot Welding Process of Galvanized Steel Sheet Using the Taguchi Method. *Arabian Journal for Science and Engineering* **2014**, 39 (2), 1171-1176. DOI: 10.1007/s13369-013-0634-x
- [25] Feujofack, K.; Jahazi, M.; Osmani, D., Optimization of resistance spot welding process applied to A36 mild steel and hot dipped galvanized steel based on hardness and nugget geometry. *The International Journal of Advanced Manufacturing Technology* **2020**, 106 (5-6), 2477-2491. DOI: 10.1007/s00170-019-04707-w
- [26] Wan, X.; Wang, Y.; Fang, C., Welding Defects Occurrence and Their Effects on Weld Quality in Resistance Spot Welding of AHSS Steel. *ISIJ International* **2014**, 54 (8), 1883-1889. DOI: 10.2355/isijinternational.54.1883
- [27] Zhao, D.; Wang, Y.; Liang, D.; Zhang, P., An investigation into weld defects of spot-welded dual-phase steel. *The International Journal of Advanced Manufacturing Technology* **2017**, 92 (5), 3043-3050. DOI: 10.1007/s00170-017-0398-7
- [28] Zhou, K.; Yao, P., Overview of recent advances of process analysis and quality control in resistance spot welding. *Mechanical Systems and Signal Processing* **2019**, 124, 170-198. DOI: 10.1016/j.ymsp.2019.01.041
- [29] Zhou, K.; Cal, L., Study on effect of electrode force on resistance spot welding process *Journal of Applied Physics* **2014**, 116 (8). DOI: 10.1063/1.4893968
- [30] Zhang, Y.; Shen, J.; Lai, X., Influence of Electrode Force on Weld Expulsion in Resistance Spot Welding of Dual Phase Steel with Initial Gap Using Simulation and Experimental Method. *ISIJ International* **2012**, 52 (3), 493-498. DOI: 10.2355/isijinternational.52.493
- [31] Zhou, K.; Yao, P.; Cai, L., Constant current vs. constant power control in AC resistance spot welding. *Journal of Materials Processing Tech* **2015**, 223, 299-304. DOI: 10.1016/j.jmatprotec.2015.04.016
- [32] Kang, Z.; Lilong, C., A Nonlinear Current Control Method for Resistance Spot Welding. *IEEE/ASME Transactions on Mechatronics* **2014**, 19 (2), 559-569. DOI: 10.1109/TMECH.2013.2251351
- [33] Bin, N.; Yonglin, C.; Hui, Z., Dynamic electrode force control of resistance spot welding robot. 2009; pp 2421-2426. DOI: 10.1109/ROBIO.2009.5420728
- [34] Ikeda, R.; Okita, Y.; Ono, M.; Yasuda, K.; Terasaki, T., Development of advanced resistance spot welding process using control of electrode force and welding current during welding. *Welding International* **2014**, 28 (1), 13. DOI: 10.1080/09507116.2012.715880
- [35] Chang, H.; Choi, D., Effect of profile force on toughness of resistance spot weld joints for ultra high strength steel. *Welding in the World* **2018**, 62 (3), 481-496. DOI: 10.1080/09507116.2012.715880
- [36] Bondarenko, O. F.; Bondarenko, I. V.; Safronov, P. S.; Sydorets, V. M., Current and force control in micro resistance welding machines Review and development. 2013; pp 298-303. DOI: 10.1109/CPE.2013.6601173
- [37] Matsushita, M.; Ikeda, R.; Oi, K., Development of a new program control setting of welding current and electrode force for single-side resistance spot welding. *The International Journal of Materials Joining* **2015**, 59 (4), 533-543. DOI: 10.1007/s40194-015-0228-1
- [38] Arabi, S. H.; Pouranvari, M.; Movahedi, M., Pathways to improve the austenite-ferrite phase balance during resistance spot welding of duplex stainless steels. *Science and Technology of Welding and Joining* **2019**, 24 (1), 8-15. DOI: 10.1080/13621718.2018.1468949
- [39] Shome, M.; Chatterjee, S., Effect of Material Properties on Contact Resistance and Nugget Size during Spot Welding of Low Carbon Coated Steels. *ISIJ International* **2009**, 49 (9), 1384-1391. DOI: DOI: 10.2355/isijinternational.49.1384
- [40] Aktas, S.; Ozsarac, U.; Aslanlar, S., Effect of Spot Welding Parameters on Tensile Properties of DP 600 Steel Sheet Joints. *Materials and Manufacturing Processes* **2012**, 27 (7), 756-764. DOI: 10.1080/10426914.2011.647940
- [41] Aydin, H., The mechanical properties of dissimilar resistance spot-welded DP600–DP1000 steel joints for automotive applications. *Proc IMechE PartD: Journal of Automobile Engineering* **2014**, 1-12. DOI: 10.1177/0954407014547749
- [42] Kishore, K.; Kumar, P.; Mukhopadhyay, G., Resistance spot weldability of galvanized and bare DP600 steel. *Journal of Materials Processing Technology* **2019**, 271, 237-248. DOI: 10.1016/j.jmatprotec.2019.04.005
- [43] Wei, S. T.; Lv, D.; Liu, R. D.; Lin, L.; Xu, R. J.; Guo, J. Y.; Wang, K. Q., Similar and dissimilar resistance spot welding of advanced high strength steels: welding and heat treatment procedures, structure and mechanical properties. *Science and Technology of Welding and Joining* **2014**, 19 (5), 427-435. DOI: 10.1179/1362171814Y.0000000211
- [44] Liu, L.; Xiao, L.; Chen, D. L.; Feng, J. C.; Kim, S.; Zhou, Y., Microstructure and fatigue properties of Mg-to-steel dissimilar resistance spot welds. *Materials and Design* **2013**, 45, 336-342. DOI: 10.1016/j.matdes.2012.08.018
- [45] Manladan, S. M.; Zhang, Y.; Ramesh, S.; Cai, Y.; Luo, Z.; Ao, S.; Arslan, A., Resistance element weld-bonding and resistance spot weld-bonding of Mg alloy/austenitic stainless steel. *Journal of Manufacturing Processes* 2019, 48, 12-30. DOI: 10.1016/j.jmapro.2019.10.005
- [46] Miyamoto, K.; Nakagawa, S.; Sugi, C.; Ogura, T.; Hirose, A., Seal spot welding of steel and aluminium alloy by resistance spot welding: dissimilar metal joining of steel and aluminium alloy by Zn insertion. *Welding International* 2016, 30 (9), 675-687. DOI: 10.1080/09507116.2016.1142189
- [47] Sakiyama, T.; Naito, Y.; Miyazaki, Y.; Nose, T., Dissimilar Metal Joining Technologies for Steel Sheet and Aluminum Alloy Sheet in Auto Body. NIPPON STEEL TECHNICAL REPORT 2013, 103, 91-98.
- [48] Mat Din, N. A.; Zuhailawati, H.; Anasyida, A., Resistance Spot Welding of AA5052 Sheet Metal of Dissimilar Thickness. Anasyida, A., Ed. 2016; Vol. 114, pp 12126-12133. DOI: 10.1088/1757-899X/114/1/012126

- [49] Zhang, H.; Qiu, X.; Xing, F.; Bai, J.; Chen, J., Failure analysis of dissimilar thickness resistance spot welded joints in dual-phase steels during tensile shear test. *Materials and Design* 2014, 55, 366-372. DOI: 10.1016/j.matdes.2013.09.040
- [50] Pouranvari, M.; Mousavizadeh, S. M.; Marashi, S. P. H.; Goodarzi, M.; Ghorbani, M., Influence of fusion zone size and failure mode on mechanical performance of dissimilar resistance spot welds of AISI 1008 low carbon steel and DP600 advanced high strength steel. *Materials & Design* 2011, 32 (3), 1390-1398. DOI: 10.1016/j.matdes.2010.09.010
- [51] Jawaid, R., Failure Study of Two Dissimilar Steels Joined by Spot Welding Technique. *Key Engineering Materials* 2018, 778, 262-267. DOI: 10.4028/www.scientific.net/KEM.778.262
- [52] Huin, T.; Dancette, S.; Fabregue, D.; Dupuy, T., Investigation of the Failure of Advanced High Strength Steels Heterogeneous Spot Welds. *Metals* 2016, 6 (5), 1-19. DOI: 10.3390/met6050111
- [53] Pouranvari, M.; Marashi, S. P. H.; Safanama, D. S., Failure mode transition in AHSS resistance spot welds. Part II: Experimental investigation and model validation. *Materials Science & Engineering A* 2011, 528 (29-30), 8344-8352. DOI: 10.1016/j.msea.2011.08.016
- [54] Xu, F.; Sun, G.; Li, G.; Li, Q., Failure analysis for resistance spot welding in lap-shear specimens. *International Journal of Mechanical Sciences* 2014, 78, 154-166. DOI: 10.1016/j.ijmesci.2013.11.011
- [55] Chen, F.; Sun, S.; Ma, Z.; Tong, G.; Huang, X., Effect of weld nugget size on failure mode and mechanical properties of microscale resistance spot welds on Ti-1Al-1Mn ultrathin foils. *Advances in Mechanical Engineering* 2018, 10 (7), 1-10. DOI: 10.1177/1687814018785283
- [56] Pouranvari, M., On the Failure Mode of Resistance Spot Welded Hsla 420 Steel Archives of Metallurgy and Materials 2013, 58 (1), 67-72. DOI: 10.2478/v10172-012-0152-y
- [57] Abadi, M.; Pouranvari, M., Failure-mode transition in resistance spot welded DP780 advanced high-strength steel: Effect of loading conditions. *Materials and Technology*. 2014, 48 (1), 67-71.
- [58] Zhao, D.; Wang, Y.; Liang, D.; Zhang, P., Modeling and process analysis of resistance spot welded DP600 joints based on regression analysis. *Materials & Design* 2016, 110, 676-684. DOI:10.1016/j.matdes.2016.08.038
- [59] Song, J. H.; Huh, H., Influence of Tensile Speeds on the Failure Loads of the DP590 Spot Weld under Various Combined Loading Conditions. *Advances in Materials Science and Engineering* 2015, 2015. DOI: 10.1155/2015/297915
- [60] Pouranvari, M.; Marashi, S., Factors affecting mechanical properties of resistance spot welds. *Materials Science and Technology* 2010, 26 (9), 1137. DOI: 10.1179/174328409X459301
- [61] Liu, X. D.; Xu, Y. B.; Misra, R. D. K.; Peng, F.; Wang, Y.; Du, Y. B., Mechanical properties in double pulse resistance spot welding of Q&P 980 steel. *Journal of Materials Processing Technology* 2019, 263, 186-197. DOI: 10.1016/j.jmatprotec.2018.08.018
- [62] Aleksija, Đ.; Biljana, M., Failure mode and strength analyses of resistance spot weld joints of aluminium and austenitic stainless steel sheet. *Applied Engineering Letters* 2018, 3 (1), 6-12. DOI: 10.18485/aeletters.2018.3.1.2
- [63] Boriwal, L.; Sarviya, R. M.; Mahapatra, M. M., Failure modes of spot welds in quasi – static tensile – shear loading of coated steel sheets. *Materials Today: Proceedings* 2017, 4 (2), 3672-3677. DOI: 10.1016/j.matpr.2017.02.261
- [64] Chen, N.; Wang, H.-P.; Carlson, B. E.; Sigler, D. R.; Wang, M., Fracture mechanisms of Al/steel resistance spot welds in lap shear test. *Journal of Materials Processing Technology* 2017, 243, 347-354. DOI: 10.1016/j.jmatprotec.2016.12.015
- [65] Kong, J. P.; Han, T. K.; Chin, K. G.; Park, B. G.; Kang, C. Y., Effect of boron content and welding current on the mechanical properties of electrical resistance spot welds in complex-phase steels. *Materials and Design* 2014, 54, 598-609. DOI: 10.1016/j.matdes.2013.08.098
- [66] Kang, J.; Rao, H. M.; Sigler, D. R.; Carlson, B. E., Tensile and Fatigue Behaviour of AA6022-T4 to IF Steel Resistance Spot Welds. *Procedia Structural Integrity* 2017, 5, 1425-1432. DOI: 10.1016/j.prostr.2017.07.207
- [67] Tavasolizadeh, A.; Marashi, S. P. H.; Pouranvari, M., Mechanical performance of three thickness resistance spot welded low carbon steel. *Materials Science and Technology* 2011, 27 (1), 219-224. DOI: 10.1179/174328409X441265
- [68] Summerville, C.; Compston, P.; Doolan, M., A comparison of resistance spot weld quality assessment techniques. *Procedia Manufacturing* 2019, 29, 305-312. DOI: 10.1016/j.promfg.2019.02.142
- [69] Kyung Min Lee; Dong Woon Han; Kim, H. K., Fatigue strength evaluation of self-piercing riveted cold rolled steel joints under mixed mode loading conditions. *International Journal of Engineering and Technology* 2016, 8 (4), 1826-1831. DOI: 10.21817/ijet/2016/v8i4/160804166
- [70] Pouranvari M; P, M., Failure of resistance spot welds: Tensile shear versus coach peel loading conditions. *Ironmaking & Steelmaking* 2012, 39 (2), 104-111. DOI: 10.1179/1743281211Y.0000000066
- [71] Chen, N.; Wang, H.-P.; Carlson, B. E.; Sigler, D. R.; Wang, M., Fracture mechanisms of Al/steel resistance spot welds in coach peel and cross tension testing. *Journal of Materials Processing Tech.* 2018, 252, 348-361. DOI: 10.1016/j.jmatprotec.2017.09.035
- [72] Yang Li; He Shan; Yu Zhang; Luo, Z., Failure mode of spot welds under cross-tension and coach-peel loads. *Welding Journal* 2017, 96 (11), 413-420.
- [73] Han, L.; Thornton, M.; Boomer, D.; Shergold, M., A correlation study of mechanical strength of resistance spot welding of AA5754 aluminium alloy. *Journal of Materials Processing Technology* 2011, 211 (3), 513-521. DOI: 10.1016/j.jmatprotec.2010.11.004
- [74] Chen, C.; Kong, L.; Wang, M.; Haselhuhn, A. S.; Sigler, D. R.; Wang, H.-P.; Carlson, B. E., The robustness of Al-steel resistance spot welding process. *Journal of Manufacturing Processes* 2019, 43, 300-310. DOI: 10.1016/j.jmapro.2019.02.030

- [75] Pouranvari, M., Susceptibility to interfacial failure mode in similar and dissimilar resistance spot welds of DP600 dual phase steel and low carbon steel during cross-tension and tensile-shear loading conditions. *Materials Science & Engineering A* **2012**, *546*, 129-138. DOI: 10.1016/j.msea.2012.03.040
- [76] Aghajani, H.; Pouranvari, M., A pathway to produce strong and tough martensitic stainless steels resistance spot welds. *Science and Technology of Welding and Joining* **2019**, *24* (3), 185-192. DOI: 10.1007/s11661-019-05443-2
- [77] Chao, Y., Ultimate strength and failure mechanism of resistance spot weld subjected to tensile, shear, or combined tensile/shear loads. *Journal of Engineering Materials and Technology (Transactions of the ASME)* **2003**, *125* (2), 125-132. DOI: 10.1115/1.1555648
- [78] Pouranvari, M.; Marashi, S. P. H., Failure Mode Transition in AISI 304 Resistance Spot Welds. *Welding Journal* **2012**, *91* (11), 303-309.
- [79] Spina, P.; Maddis, M.; D'Antonio, G.; Lombardi, F., Weldability and Monitoring of Resistance Spot Welding of Q&P and TRIP Steels. *Metals* **2016**, *6* (11), 270. DOI: 10.3390/met6110270
- [80] Subramanian, A.; Senthil, P. V.; Jabaraj, D. B.; Devakumar, D., Improving mechanical performance of resistance spot welded joints of AISI 409M steel by double pulse current. *Materials Today: Proceedings* **2019**, *16*, 949-955. DOI: 10.1016/j.matpr.2019.05.181
- [81] Amirthalingam, M.; van Der Aa, E.; Kwakernaak, C.; Hermans, M.; Richardson, I., Elemental segregation during resistance spot welding of boron containing advanced high strength steels. *Weld. World* **2015**, *59* (5), 743-755. DOI: 10.1007/s40194-015-0250-3
- [82] Park, G.; Kim, K.; Uhm, S.; Lee, C., A comparison of cross-tension properties and fracture behavior between similar and dissimilar resistance spot-weldments in medium-Mn TRIP steel. *Materials Science and Engineering: A* **2019**, *752*, 206-216. DOI: 10.1016/j.msea.2019.03.023
- [83] Uijl, N.; Moolevliet, T.; Mennes, A.; Ellen, A.; Smith, S.; Veldt, T.; Okada, T.; Nishibata, H.; Uchihara, M.; Fukui, K., Performance of Resistance Spot-Welded Joints in Advanced High-Strength Steel in Static and Dynamic Tensile Tests. *Welding in the World* **2012**, *56* (7), 51-63. DOI: 10.1007/BF03321365
- [84] Pizzomi, M.; Lertora, E.; Mandolino, C.; Gambaro, C., Experimental investigation of the static and fatigue behavior of hybrid ductile adhesive-RSWelded joints in a DP 1000 steel. *International Journal of Adhesion and Adhesives* **2019**, *95*, 102400. DOI: 10.1016/j.ijadhadh.2019.102400
- [85] Xiao, Z.; Zeng, K.; He, X.; Zhang, L., Fatigue strength and failure analysis of weld-bonded joint of stainless steel. *The Journal of Adhesion* **2019**, *95* (3), 1-17. DOI: 10.1080/00218464.2017.1414605
- [86] Fujii, T.; Tohgo, K.; Suzuki, Y.; Yamamoto, T.; Shimamura, Y., Fatigue strength and fatigue fracture mechanism of three-sheet spot weld-bonded joints under tensile-shear loading. *International Journal of Fatigue* **2016**, *87*, 424-434. DOI: 10.1016/j.ijfatigue.2016.02.023
- [87] Rao, H. M.; Kang, J.; Shi, L.; Sigler, D. R.; Carlson, B. E., Effect of specimen configuration on fatigue properties of dissimilar aluminum to steel resistance spot welds. *International Journal of Fatigue* **2018**, *116*, 13-21. DOI: 10.1016/j.ijfatigue.2018.06.009
- [88] Tanegashima, R.; Akebono, H.; Sugeta, A., Fatigue life estimation based on fracture mechanics of single spot welded joints under different loading modes. *Engineering Fracture Mechanics* **2017**, *175*, 115-126. DOI: 10.1016/j.engfracmech.2017.01.031
- [89] Heewon, C.; Sangwoo, N.; Insung, H.; Je Hoon, O.; Munjin, K.; Young-Min, K., Fatigue Behaviors of Resistance Spot Welds for 980 MPa Grade TRIP Steel. *Metals* **2019**, *9* (10), 1086. DOI: 10.3390/met9101086
- [90] Vigneshkumar, M.; Varthanan, P. A.; Ambrose Raj, Y. M., Finite Element-Based Parametric Studies of Nugget Diameter and Temperature Distribution in the Resistance Spot Welding of AISI 304 and AISI 316L Sheets. *Transactions of the Indian Institute of Metals* **2019**, *72* (2), 429-438. DOI: 10.1007/s12666-018-1494-6
- [91] Baskoro, A. S.; Edyanto, A.; Amat, M. A.; Muzaki, H., Study on Nugget Growth in Resistance Spot Welding of Thin Aluminum A1100 Using Welding Simulation. *Materials Science Forum* **2018**, *929*, 191-199. DOI: 10.4028/www.scientific.net/MSF.929.191
- [92] Wan, X.; Wang, Y.; Zhang, P., Modelling the effect of welding current on resistance spot welding of DP600 steel. *Journal of Materials Processing Technology* **2014**, *214* (11), 2723-2729. DOI: 10.1016/j.jmatprotec.2014.06.009
- [93] Jagadeesha T, T.; Jothi, T., Studies on the influence of process parameters on the AISI 316L resistance spot-welded specimens. *The International Journal of Advanced Manufacturing Technology* **2017**, *93* (1), 73-88. DOI: 10.1007/s00170-015-7693-y
- [94] Lee, Y.; Jeong, H.; Park, K.; Kim, Y.; Cho, J., Development of numerical analysis model for resistance spot welding of automotive steel. *Journal of Mechanical Science and Technology* **2017**, *31* (7), 3455-3464. DOI: 10.1007/s12206-017-0634-y
- [95] Zhao, D.; Wang, Y.; Zhang, P.; Liang, D., Modeling and Experimental Research on Resistance Spot Welded Joints for Dual-Phase Steel. *Materials* **2019**, *12* (7), 1-16. DOI: 10.3390/ma12071108
- [96] Wan, X.; Wang, Y.; Zhang, P., Numerical simulation on deformation and stress variation in resistance spot welding of dual-phase steel. *The International Journal of Advanced Manufacturing Technology* **2017**, *92* (5), 2619-2629. DOI: 10.1007/s00170-017-0191-7
- [97] Zhao, Y.; Zhang, Y.; Lai, X., Effect of Epoxy Adhesive on Nugget Formation in Resistance Welding of SAE1004/DP600/DP780 Steel Sheets. *Materials* **2018**, *11* (10). DOI: 10.3390/ma11101828
- [98] Tanco, J. S.; Nielsen, C. V.; Chergui, A.; Zhang, W.; Bay, N., Weld nugget formation in resistance spot welding of new lightweight sandwich material. *The International Journal of Advanced Manufacturing Technology* **2015**, *80* (5-8), 1137-1147. DOI: 10.1007/s00170-015-7108-0.

- [99] Wang, J.; Wang, H. P.; Lu, F.; Carlson, B. E.; Sigler, D. R., Analysis of Al-steel resistance spot welding process by developing a fully coupled multi-physics simulation model. *International Journal of Heat and Mass Transfer* **2015**, *89*, 1061-1072. DOI: 10.1016/j.ijheatmasstransfer.2015.05.086
- [100] Wan, Z.; Wang, H.-P.; Wang, M.; Carlson, B. E.; Sigler, D. R., Numerical simulation of resistance spot welding of Al to zinc-coated steel with improved representation of contact interactions. *International Journal of Heat and Mass Transfer* **2016**, *101*, 749-763. DOI: 10.1016/j.ijheatmasstransfer.2016.05.023
- [101] Du, H.; Bi, J.; Zhang, Y.; Wu, Y.; Li, Y.; Luo, Z., The role of the partial melting zone in the nugget growth process of unequal-thickness dissimilar aluminum alloy 2219/5A06 resistance spot welding. *Journal of Manufacturing Processes* **2019**, *45*, 304-311. DOI: 10.1016/j.jmapro.2019.06.026
- [102] Sedighi, M.; Afshari, D.; Nazari, F., Investigation of the effect of sheet thickness on residual stresses in resistance spot welding of aluminum sheets. *Proc IMechE Part C: J Mechanical Engineering Science* **2018**, *232* (4), 621-628. DOI: 10.1177/0954406216685124
- [103] Moharrami, R.; Hemmati, B., Numerical stress analysis in resistance spot-welded nugget due to post-weld shear loading. *Journal of Manufacturing Processes* **2017**, *27*, 284-290. DOI: 10.1016/j.jmapro.2017.05.007
- [104] Wang, B.; Hua, L.; Wang, X.; Song, Y.; Liu, Y., Effects of electrode tip morphology on resistance spot welding quality of DP590 dual-phase steel. *The International Journal of Advanced Manufacturing Technology* **2016**, *83* (9), 1917-1926. DOI: 10.1007/s00170-015-7703-0
- [105] Bi, J.; Song, J.; Wei, Q.; Zhang, Y.; Li, Y.; Luo, Z., Characteristics of shunting in resistance spot welding for dissimilar unequal-thickness aluminum alloys under large thickness ratio. *Materials & Design* **2016**, *101*, 226-235. DOI: 10.1016/j.matdes.2016.04.023
- [106] Yang, L.; Bi, J.; Zhang, Y.; Luo, Z.; Liu, W., Shunting characteristics in triangular arranged resistance spot welding of dissimilar unequal-thickness aluminum alloys. *The International Journal of Advanced Manufacturing Technology* **2017**, *91* (5-8), 2447-2454. DOI: 10.1007/s00170-016-9926-0
- [107] Podržaj, P.; Jerman, B.; Simončič, S., Poor fit-up condition in resistance spot welding. *Journal of Materials Processing Technology* **2016**, *230*, 21-25. DOI: 10.1016/j.jmatprotec.2015.11.009
- [108] Chung, K.; Noh, W.; Yang, X.; Han, H. N.; Lee, M.-G., Practical failure analysis of resistance spot welded advanced high-strength steel sheets. *International Journal of Plasticity* **2017**, *94*, 122-147. DOI: 10.1016/j.ijplas.2016.10.010
- [109] Noh, W.; Kim, W.; Yang, X.; Kang, M.; Lee, M.-G.; Chung, K., Simple and effective failure analysis of dissimilar resistance spot welded advanced high strength steel sheets. *International Journal of Mechanical Sciences* **2017**, *121*, 76-89. DOI: 10.1016/j.ijmecsci.2016.12.006
- [110] Paveebunvipak, K.; Uthaisangsuk, V., Microstructure based modeling of deformation and failure of spot-welded advanced high strength steels sheets. *Materials & Design* **2018**, *160*, 731-751. DOI: 10.1016/j.matdes.2018.09.052
- [111] Chen, J.; Feng, Z.; Wang, H.-P.; Carlson, B. E.; Brown, T.; Sigler, D., Multi-scale mechanical modeling of Al-steel resistance spot welds. *Materials Science and Engineering: A* **2018**, *735*, 145-153. DOI: 10.1016/j.msea.2018.08.039
- [112] Nguyen, N.; Kim, D.; Song, J.; Kim, K.; Lee, I.; Kim, H., Numerical prediction of various failure modes in spotwelded metals. *International Journal of Automotive Technology* **2012**, *13* (3), 459-467. DOI: 10.1007/s12239-012-0043-2
- [113] Wang, W.; Zhu, Q.; Liu, C.; Wei, X., An investigation on the resultant-based failure criterion for resistance spot welding joint in crush test. *International Journal of Crashworthiness* **2019**, *24* (2), 152-162. DOI: 10.1080/13588265.2017.1421012
- [114] Dorribo, D.; Greve, L.; Díez, P.; Arias, I.; Larráyoz-Izcara, X., Numerical estimation of the bearing capacity of resistance spot welds in martensitic boron steels using a J-integral fracture criterion. *Theoretical and Applied Fracture Mechanics* **2018**, *96*, 497-508. DOI: 10.1016/j.tafmec.2018.06.006
- [115] Weiland, J.; Debruyne, S.; Vandepitte, D.; Pulm, M.; Schiebahn, A.; Reisinger, U., Stiffness and strength analysis of hybrid adhesive bonded - resistance spot welded sandwich samples by means of virtual FE testing. *The Journal of Adhesion* **2019**, *95* (5-7), 543-557. DOI: 10.1080/00218464.2018.1553713
- [116] Souza, J. P. B.; Aguiar, R. A. A.; Costa, H. R. M.; Reis, J. M. L.; Pacheco, P. M. C. L., Numerical modelling of the mechanical behavior of hybrid joint obtained by spot welding and bonding. *Composite Structures* **2018**, *202*, 216-221. DOI: 10.1016/j.compstruct.2018.01.066
- [117] Long, H.; Hu, Y.; Jin, X., Stress intensity factor solutions and fatigue estimation for dual phase and low-carbon steel spot weld. *Theoretical and Applied Fracture Mechanics* **2018**, *96*, 408. DOI: 10.1016/j.tafmec.2018.06.003
- [118] Noh, W.; Koh, Y.; Chung, K.; Song, J.-H.; Lee, M.-G., Influence of dynamic loading on failure behavior of spot welded automotive steel sheets. *International Journal of Mechanical Sciences* **2018**, *144*, 407-426. DOI: 10.1016/j.ijmecsci.2018.06.009
- [119] Wu, G.; Li, D.; Su, X.; Peng, Y.; Shi, Y.; Huang, L.; Huang, S.; Tang, W., Experiment and modeling on fatigue of the DP780GI spot welded joint. *International Journal of Fatigue* **2017**, *103*, 73-85. DOI: 10.1016/j.ijfatigue.2017.05.017
- [120] Kang, H.; Li, Z.; Khosrovaneh, A. K.; Kang, B.; Li, Z., Fatigue Life Predictions of Adhesive Joint of Sheet Steels. *Procedia Engineering* **2015**, *133* (C), 518-527. DOI: 10.1016/j.proeng.2015.12.623
- [121] Patil, S. A.; Baratzadeh, F.; Lankarani, H., Modeling of the Weld Strength in Spot Weld Using Regression Analysis of the Stress Parameters based on the Simulation Study. *Journal of Materials Science Research* **2016**, *6* (1), 51. DOI: 10.5539/jmsr.v6n1p51
- [122] Rösch, P.; Schmidt, H.; Bruder, T., A novel approach to simulate the stiffness behaviour of spot welded vehicle

- structures under multi axial variable amplitude loading. *MATEC Web of Conferences* **2018**, 165. DOI: 10.1051/mateconf/201816517005
- [123] Li, S.; Feng, X., Study of structural optimization design on a certain vehicle body-in-white based on static performance and modal analysis. *Mechanical Systems and Signal Processing* **2020**, 135. DOI: 10.1016/j.ymssp.2019.106405
- [124] Ryberg, A. B.; Nilsson, L., Spot weld reduction methods for automotive structures. *Structural and Multidisciplinary Optimization* **2016**, 53 (4), 923-934. DOI: 10.1007/s00158-015-1355-4



# Experimental and Numerical Study of Heat Transfer and Tensile Strength of Engineered Porous Fins to Estimate the Best Porosity

Ali Heydari<sup>a\*</sup>, Mehrdad Mesgarpour<sup>b</sup>, Mohammad Reza Gharib<sup>a</sup>

<sup>a</sup> Department of Mechanical Engineering, University of Torbat Heydarieh, Torbat Heydarieh, Khorasan Razavi, Iran

<sup>b</sup> Fluid Mechanics, Thermal Engineering and Multiphase Flow Research Lab. (FUTURE), Department of Mechanical Engineering, King Mongkut's University of Technology Thonburi, Bangmod, Bangkok 10140, Thailand

Received May 22 2020

Accepted September 20 2020

## Abstract

In porous media, increasing porosity improves heat transfer rate and pressure drop across the fluid flow while decreasing strength of the body. Therefore, determining the optimum porosity is a serious challenge in balancing these two functional components of porous environments. In this research, an experimental study and numerical modeling of heat transfer and mechanical strength of engineered porous fin have been performed. In this regard, the model to create the porous medium is selected as a network of connected spheres. In order to estimate the best porosity, the effect of the porosity variation in the allowed range is investigated to achieve the best heat transfer and tensile strength simultaneously for three different materials of copper, aluminum and brass. The results show that the tensile strength and heat transfer optimized simultaneously for a specific porosity for each material.

© 2020 Jordan Journal of Mechanical and Industrial Engineering. All rights reserved

Keywords: Fins; heat transfer; porous media; tensile strength; porosity;

## 1. Introduction

Heat transfer has always attracted the attention of engineers and researchers from various perspectives. Several studies have been conducted in the field of extended surfaces as the first candidate for increasing heat transfer. Porous medium can be considered as an excellent solution for heat transfer augmentation due to the high surface area. By changing the structure and engineering the porous medium, engineered porous medium (EPM) has been presented. In this concept, instead of random distribution of porosity and irregularity in the shape of cavities, we encounter a completely united structure with an accurate porosity designation and a regular shape of cavities in each of the three directions. However, in a typical porous medium constructed by casting, spray forming or gas injection processes, all physical properties, such as porosity are distributed arbitrarily.

In the pre-engineered process of porous body, after designing the medium, which is based on the requirements, it is possible to manufacture a piece by manufacturing technologies according to the pre-plan. In fact, the basic difference between a typical porous medium and an engineered porous medium is the pre-design process and precise arrangement that would lead to the highest possible effectiveness. In engineering applications, effectiveness and manufacturing prospects should be considered simultaneously. In addition, the life of the manufactured

part, with respect to cost, is an important factor. So, the enhancement in thermal efficiency should not be along with the reduction in strength and the life of the piece. In general, metal foams are widely used as a porous medium to increase heat transfer. The advantage of using foams or fins that are designed as a network of connected spheres is that their porosity can be purposefully changed into different functions. For example, where conduction is essential, the spheres should be more compact, and the foam has less porosity. Where convection heat transfer is important, less spherical compaction and more porosity should be considered. On the other hand, the strength of these engineered fins must be considered. These fins can be a good alternative to solid (uniform) fins or heat sinks in the industry as less material is needed for construction while having higher heat transfer rates.

Numerous numerical, experimental and analytical investigations have been carried out on the topic of heat transfer in porous media such as [1-3]. Among the studies for developing the theoretical topics, the work of Hatami et al. [4] can be mentioned. They proposed a numerical solution method for solving the heat transfer equations in the porous fins which showed that the perturbation and repeating variable methods are the effective for solving nonlinear equations of convection and radiation.

Bejan and Morega [5] investigated the effect of thermal resistance on the porous fin. They revealed that the fins' arrangement and porosity percentage have a great influence on the flow regime, and consequently, the temperature

\* Corresponding author e-mail: a.Heydari@torbath.ac.ir

distribution of the porous fins. Jeng and Tzeng performed a numerical analysis of heat transfer in the porous fins [6]. They showed that in the lower Reynolds numbers, the highest Nusselt number occurs at the stagnation point, which moves downstream due to the Reynolds number rises. In 2008, Kiwan and Zeitoun [7], performed a research on heat transfer in the porous fin and reported 75% enhancement in heat transfer by the use of porous fins in two concentric cylinders. In addition, they declared the decreasing trend of heat transfer by increasing the attachment angle, unlike solid fins. Furthermore, they showed that the presence of fin on the inner cylinder would change the flow regime in the region between two cylinders. Foams have another advantage regarding fluid availability everywhere due to the continuous and attached flow paths which leads to reduce the size and weight of heat exchangers [8]. According to the obtained results by Liu et al. [9], the lower pressure drop in the foam matrix compared to the crystalline matrix in the same Reynolds number can be concluded. Hoseinzadeh et al. [10] numerically and analytically validated heat transfer in a rectangular cross-section porous fins. It was assumed that the fin is one-dimensional and homogenous, the flow is laminar, and the generated heat is a linear function of temperature. Their results agreed well with other numerical methods. Further, they used the same methods to simulate heat transfer of porous fins in an enclosure [11]. Three different analytical methods are applied to obtain the temperature distribution after deriving the heat transfer equation. The effects of various parameters of natural convection, porosity, Rayleigh numbers are examined in their research. Duwairi et al. [12] considered the MHD mixed convection flow about an isothermal cone embedded in a saturated porous medium. Their results showed that the increasing magnetic strength reduced the heat transfer rates, while increasing the cone angle enhanced the heat transfer rates.

Metal foams are made up of thin metal strings that form a continuum area. Due to the complex shape, different geometries and presence of random surfaces in these bodies along with the lack of knowledge about the actual surface, modeling these objects in the software has always been a problematic issue. Al-azmi and Vafai [13] and [14], simulated a model of open cell foam based on repetition of a unit in eight rows and modeled the fluid flow between these rows with different boundary conditions. Their results indicated the effect of the base metal including its density and other properties, such as the size of the cavities and the strings, etc., on reduction of pressure drop and heat resistance. They also showed that the elasticity of the foam is related to the size of the cavities characterized by the inner diameter of the cavity which is in the range of 0.3 to 4 millimeters. Jiang and Lu [15] studied the heat transfer on a series of sintered spheres in a channel, numerically. They observed that heat transfer would increase with decreasing the size of spheres. In another study [16], they examined the effects of boundary conditions on the natural convection of a sintered plate in a channel to evaluate the heat transfer and pressure drop. Shaik Dawood and Mohamed Nazirudeen [17] developed the technology for making porous gray iron metal foams castings. Box-Behnken Design was applied and density, percentage porosity was

found out. Also, radiography, microstructure, SEM analysis, compression and hardness tests were done.

It was found that in a sintered porous medium, the sintered layer amplifies heat transfer due to the change in the conduction coefficient. In 2002, Cao et al. [18] performed an experimental investigation on the evaporative heat transfer of a sintered copper layer by considering two different sizes of the particles and found optimal porosity for the maximum heat transfer. They also showed that the highest heat transfer rate occurs in the highest porosity percentage. In 2007, Kang et al. [19] experimentally studied the effect of nanofluids with different volume fractions on thermal efficiency of a tube with porous sintered layer. They used silver nanoparticles with diameter of 10 and 35 nanometers and reported the enhancement in thermal performance of the porous heat pipe. Mesgarpour et al. [20-23] examined the effect of contact type, fin shape, sphere diameter, boundary conditions, and variation of Reynolds number on fluid flow and heat transfer in the forced convection around an engineered porous fin with spherical connections in a channel. They showed that using the porous fins with diagonal connections, besides increasing pressure drop, improves thermal performance and increases heat transfer rates compared to parallel connections. They also conducted the use of aluminium and copper with constant heat flux and constant temperature as the boundary conditions in the base of the fin, respectively. Furthermore, they investigated the forced convection flow around a bundle of tapered porous fin in a channel and declared that in lower Reynolds numbers, the use of porous fin is preferred. While in higher Reynolds, solid fins have higher heat transfer and lower pressure drop. They investigated natural convection around the porous fins at different angle of positioning and showed that the best Nusselt number and efficiency will be achieved at 45-degree angle of positioning.

As described in this section, the porous medium offered an effective solution in order to increase heat transfer performance. However, the mechanical strength of the porous fin is another important factor that should be considered carefully for the use of porous medium. According to the literature review, few researches have been conducted about the strength of the porous materials. In 2011, Bouzid et al [24] examined the strength of a porous medium during the drying process and showed that the strength of the porous material in the porous medium is a function of cavity size, material and drying rate. Ito [25] studied the effect of the pressure gradient on the strength and failure of the porous medium. The results showed a logical relationship between the properties of the porous medium and the strength. In 2015, Maurath et al [26] examined the effect of the connection method, the size of cavities and the physical properties on the strength of the sintered fiberglass medium. They also declared the influence of environmental conditions on the quality of sintering process. Hoseinzadeh and Heyns [27] numerically investigated thermo-structural fatigue and lifetime of a heat exchanger as a feed water heater in power plant. They showed that the highest equivalent thermal stresses under these extreme load conditions occur at the joints of the tubes and tubes sheet.

So far, only the issue of heat transfer has been addressed in the discussion of metal foams. Reducing the porosity to

increase heat transfer also reduces the strength of the metal foam. Therefore, the innovation of the present work is the simultaneous study of these two categories and obtaining porosity that satisfies heat transfer and strength simultaneously. In this research, we aim to improve the heat transfer performance and the mechanical strength simultaneously by variation in porosity in an engineered porous medium which has been described in Ref. [22]. The experimental investigation, numerical validation and mesh analysis of heat transfer have been evaluated in this reference. The present work focused on the mechanical strength of the porous copper fin experimentally and numerically. Then, the results of numerical simulation have been obtained for copper, aluminum and brass porous fins to reach the best porosity. Numerical simulation of free convection heat transfer is carried out using STARCCM+ software and numerical analysis of mechanical strength is performed using ANSYS 18.2.

## 2. Governing equations

In this research, various relationships have been utilized for heat transfer analysis of experimental and numerical results of engineered porous fins. The dimensionless equations of mass, momentum, and energy for incompressible flow by neglecting pressure gradients are expressed as follows [28]:

$$\frac{\partial U_i^*}{\partial x_i^*} = 0, \quad (1)$$

$$\frac{\partial U_i^*}{\partial t^*} + U_i^* \frac{\partial U_i^*}{\partial x_i^*} = \frac{Gr}{Re} \theta + \frac{1}{Re} \frac{\partial^2 U_i^*}{\partial x_j^* \partial x_j^*}$$

$$\frac{\partial \theta}{\partial t^*} + U_i^* \frac{\partial \theta}{\partial x_i^*} = \frac{1}{Re \times Pr} \frac{\partial^2 \theta}{\partial x_i^* \partial x_i^*} + \frac{Ec}{Re} \phi^*$$

In the above equations,  $U_i^*$  and  $\theta$  are the dimensionless velocity components and temperature and respectively. Accordingly, the quantities of the dimensionless parameters are:

$$x^* = \frac{x}{L}, t^* = \frac{t U_\infty}{L}, U^* = \frac{U}{U_\infty}, \theta = \frac{T - T_\infty}{T_b - T_\infty}, \phi^* = \tau_{ij}^* \frac{\partial U_i^*}{\partial x_j^*}, \tau_{ij}^* = \frac{\tau_{ij}}{\frac{1}{2} \rho U_\infty^2} \quad (2)$$

$$Re = \frac{U_\infty L}{\nu}, Pr = \frac{\nu}{\alpha}, Gr = \frac{g \beta (T_s - T_\infty) L_c^3}{\nu^2}, Ec = \frac{U_\infty^2}{C_p (T_s - T_\infty)}$$

In the above equations  $Re$ ,  $Gr$  and  $Ec$  are Reynolds, Grashof and Eckert numbers respectively. Since low temperatures are analyzed in this paper, the radiation heat transfer mechanism can be ignored in the fin analysis [29]. Therefore, according to the energy balance in a control volume of fin, neglecting radiation heat transfer, we have:

$$\dot{Q}_{total} = \dot{Q}_{cond} + \dot{Q}_{conv} \quad (3)$$

In the above expression,  $\dot{Q}_{cond}$  is the heat transferred through conduction and  $\dot{Q}_{conv}$  is the heat transferred through convection. For the conductive and convective heat transfer, we also have:

$$\dot{Q}_{cond} = K_{fin} A_c \frac{\partial T}{\partial x} \quad (4)$$

$$\dot{Q}_{conv} = h A_s (T_s - T_\infty)$$

In the above relations,  $h$  is the free convective heat transfer coefficient of the flow,  $T_s$  and  $T_\infty$  are the of surface and far stream flow temperatures respectively.  $A_c$  and  $A_s$  are the area of solid cross section and solid surrounding surface respectively and  $K_{fin}$  is the thermal conductivity coefficient of the fin. One of the main goals of each experiment and numerical analysis on the convective heat transfer is to find the convective heat transfer coefficients. For this purpose, the average value of this coefficient can be calculated by the following equation:

$$h = \left( \frac{Q_{ave}}{A_s (T_{s,ave} - T_\infty)} \right) \quad (5)$$

In order to model the turbulence in the numerical solution of the heat transfer equations and fluid mechanics, the  $k-\varepsilon$  turbulence model is used in this study. The equations of kinetic energy ( $k$ ) and dissipations ( $\varepsilon$ ) are considered as follows [30]:

$$\frac{\partial}{\partial x_i} (\rho k u_i) + \frac{\partial}{\partial t} (\rho k) \quad (12)$$

$$= \frac{\partial}{\partial x_j} \left( \left( \mu + \frac{\mu_t}{\sigma_k} \right) \frac{\partial k}{\partial x_j} \right) + G_K + G_b - \rho \varepsilon - Y_M + S_K$$

$$\frac{\partial}{\partial x_i} (\rho \varepsilon u_i) + \frac{\partial}{\partial t} (\rho \varepsilon) \quad (13)$$

$$= \frac{\partial}{\partial x_j} \left( \left( \mu + \frac{\mu_t}{\sigma_\varepsilon} \right) \frac{\partial \varepsilon}{\partial x_j} \right) + C_{1\varepsilon} \frac{\varepsilon}{K} (G_K + C_{3\varepsilon} G_b) + C_{2\varepsilon} \rho \frac{\varepsilon^2}{K} + S_\varepsilon$$

In the above-mentioned relationships,  $G_K$  represents the production of turbulence kinetic energy in terms of velocity gradient,  $G_b$  is turbulence kinetic energy production due to buoyancy forces and  $Y_M$  represents the oscillation share in the turbulence density to the total loss; this term is also

known as the turbulence density.  $C_{1\varepsilon}$ ,  $C_{2\varepsilon}$  and  $C_{3\varepsilon}$  are the constant coefficients and  $\sigma_\varepsilon$  and  $\sigma_k$  are the Prandtl coefficients for turbulence.  $S_K$  and  $S_\varepsilon$  are also source terms [30].

For the above equations, it is assumed that flow is three dimensional, incompressible, fully turbulent, and steady. According to the physical nature of the problem, the boundary conditions for different parts of the problem can be defined. These conditions are automatically detected and applied by the STARCCM+ software during solution.

1. Constant temperature and constant heat flux as boundary condition of the fin base.
2. Conduction heat transfer in the Fin
3. The conduction/convection boundary condition on the Fin surface
4. The convection boundary condition in the air around the body

### 3. Experiments explanation

#### 3.1 Test sample

In order to study the effect of porosity on heat transfer and fin performance, as well as evaluating fin strength, an engineered copper porous fin is manufactured by casting method as shown in Figure 1. As can be concluded from Table 1, by comparing engineered porous fin with spherical connections and a rigid fin with identical dimensions, 42% reduction in fin volume and mass would be achieved. This reduction is accompanied with 21.72% increase in surface area. Therefore, besides the improving of heat transfer performance, the amount of material needed to produce the fin has decreased.

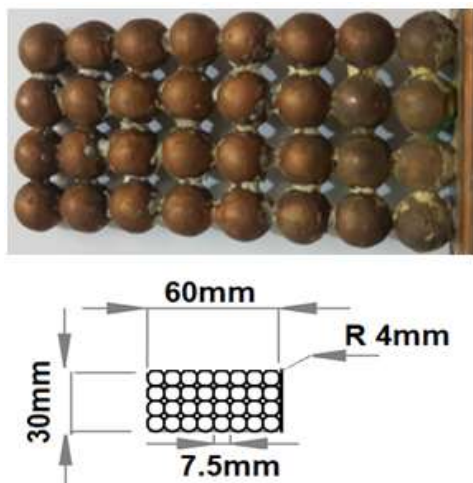


Figure 1: Manufactured engineered porous fin and its dimensions

#### 3-2 Tensile strength test

To evaluate the tensile strength of a porous fin, as described in Section 3.1, tensile test has been carried out at the Razi Reference Laboratory in Tehran, with reference standards. The results have been extracted in the form of strain-stress diagrams. The apparatus used for tensile test is INSTRON 8502 model with the power of 25 tons, which is composed of two jaws; an upper moving jaw and a lower fixed jaw. The stress is applied to the sample by the moving jaw with a frequency of 100 times per second, so the sample has been stretched up to its fracture point. Then the engineering stress-strain curve has been obtained by recording the applied force and the corresponding strain. The system can also provide complete information, such as yield stress and strain, necking, fracture, plastic strain of fracture, energy up to the yield and fracture strengths, as well as Young's modulus. The specification of the tensile testing apparatus is presented in Table 2. This apparatus includes the following sub-sections: force gauge, micrometers and laser distance meter. The accuracy and uncertainty of equipment are provided in Table 3.

Table 2: Specification of the tensile testing apparatus

Characteristic	Value
capacity (kgf)	2000
distance between columns (mm)	400
Jaw velocity (mm/min)	500
Maximum distance (mm) between two jaws	700
accuracy of measuring (mm) displacement	0.01
Force measurement resolution	1/20000
Force measurement accuracy	0.5%

Table 3: Accuracy and uncertainty of tensile test measurement devices

device	Accuracy	Uncertainty
Load cell	C4 class	
Micrometer	5 $\mu$ m	0.0028
Laser rangefinder	0.02mm	0.011

Table 1: Geometry and mass comparison of rigid and porous fin with identical dimension constructed in the present study

parameter	rigid fin	porous fin	percent of variation in porous fin relative to rigid one (%)
volume ( $mm^3$ )	21888/00	12729/54	-41/84
surrounding surface ( $mm^2$ )	7232/00	8803/43	21/72
mass (gr)	194/8	113/29	-41/84

### 3-2 Tensile strength test

To evaluate the tensile strength of a porous fin, as described in Section 3.1, tensile test has been carried out at the Razi Reference Laboratory in Tehran, with reference standards. The results have been extracted in the form of strain-stress diagrams. The apparatus used for tensile test is INSTRON 8502 model with the power of 25 tons, which is composed of two jaws; an upper moving jaw and a lower fixed jaw. The stress is applied to the sample by the moving jaw with a frequency of 100 times per second, so the sample has been stretched up to its fracture point. Then the engineering stress-strain curve has been obtained by recording the applied force and the corresponding strain. The system can also provide complete information, such as yield stress and strain, necking, fracture, plastic strain of fracture, energy up to the yield and fracture strengths, as well as Young's modulus. The specification of the tensile testing apparatus is presented in Table 2. This apparatus includes the following sub-sections: force gauge, micrometers and laser distance meter. The accuracy and uncertainty of equipment are provided in Table 3.

**Table 2:** Specification of the tensile testing apparatus

Characteristic	Value
capacity (kgf)	2000
distance between columns (mm)	400
Jaw velocity (mm/min)	500
Maximum distance between two (mm) jaws	700
accuracy of measuring (mm) displacement	0.01
Force measurement resolution	1/20000
Force measurement accuracy	0.5%

**Table 3:** Accuracy and uncertainty of tensile test measurement devices

device	Accuracy	Uncertainty
Load cell	C4 class	
Micrometer	5 $\mu$ m	0.0028
Laser rangefinder	0.02mm	0.011

## 4. Numerical modeling method

### 4-1- Modeling of heat transfer

All Numerical modeling methods for heat transfer simulation, such as software, solution method, assumptions,

viscosity model, boundary conditions, convergence criterion and discretization method have been described in ref. [22].

### 4-2- Modeling the strength

The tensile strength has been evaluated numerically with ANSYS workbench software. In static structure mode, after meshing, the model of the fin is subjected to fixed base and axial force boundary conditions. Generally, in solid analysis techniques and finite element methods, analysis of the grid is not of great importance. However, in this research, the accuracy of the grid is also investigated. In order to determine yield and fracture limit of the piece, yield strength is considered as a criterion according to the material properties references and imported to the software. In numerical analysis, it is possible to study the fatigue phenomenon based on the working cycle. As no results are available for fatigue validation, only a tensile stress analysis is performed. The calculation time of the numerical analysis is about 124 minutes.

## 5. Results and discussion

The validity of the numerical results for heat transfer analysis have been performed in previous work [22]. For experimental validation, the comparison of temperature distribution with analytical results reveals a maximum error of 1.5%. For Nusselt number 6 percent difference was reported. For validation of numerical results, the maximum error value is about 3.1% in numerical calculations of temperature distribution along the fin length in three different angles. According to this reference, the mesh independency has been checked, and a grid with 455,789 nodes has been selected.

### 5-1- Investigating the tensile strength test

The main difference between porous and rigid fins subjected to tensile forces and corresponding stresses is the cross-section area. In other words, the cross-section area of the porous fins varies as a periodic function, while it is constant for the rigid fin. The results of stress and strain for porous copper fins extracted from the tensile test apparatus and the final fractured fin are depicted in Figure 2. According to this diagram, although the copper fin requires higher force for deformation, the deformation in fracture zone is low, while it has a wide area of plastics deformation.

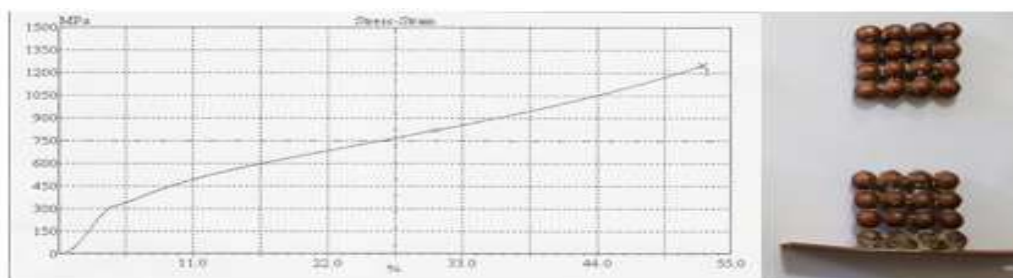


**Figure 2:** Stress-strain diagram for porous copper fin and its final fracture

5-2- Numerical Analysis:

Figure 3 shows the mesh independency and generated grid on the porous copper fin. The uniform and coherent grid is of great importance in stress-strain analysis. The mesh number is selected 4000 due to mesh independency and it is unstructured.

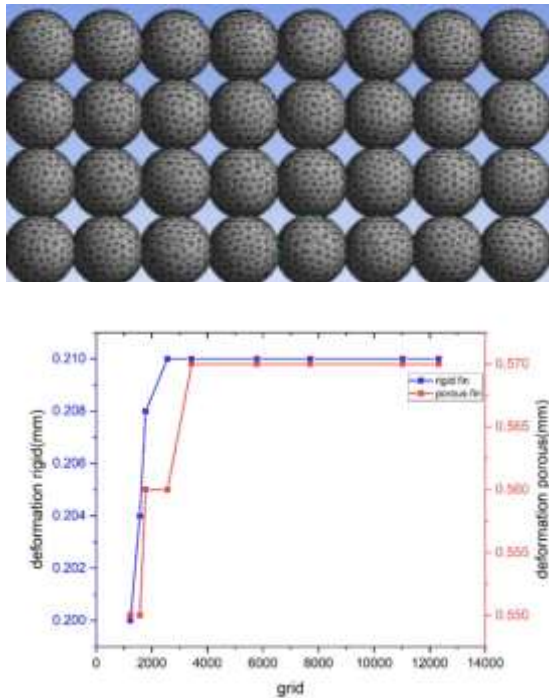


Figure 3: Mesh independency and generated grid on a porous copper fin

Figure 4 shows the deformation versus the applied force for numerical and experimental results. As can be seen, the numerical results provide an accurate estimation of the stress-strain relationship for a porous fin sample especially for higher forces.

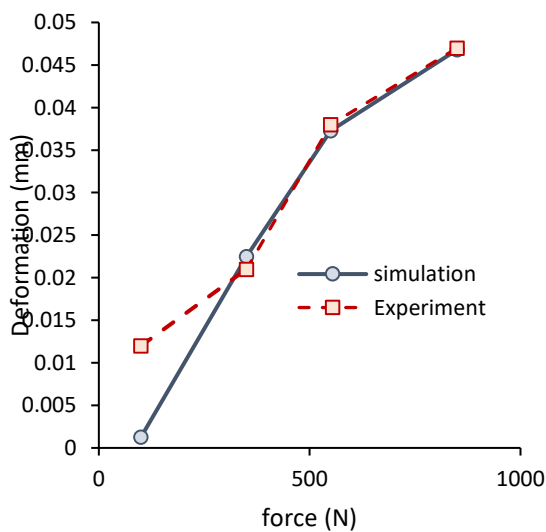


Figure 4: Comparing deformation versus applied force for numerical and experimental results

To compare the tensile strength of the porous and rigid fins with the same dimensions, it can be referred to the numerical results of Figure 5. As expected, the deformation

according to the maximum force is almost twice for the porous fin relative to rigid one. The deformation of the rigid fin at the maximum force of 10,000 N is 0.04 millimeters, while this value is equal to 0.777 millimeter for the porous fin. So, it can be concluded that the deformation of the porous fin is higher, and consequently, the strength of the porous fin is lower compared to the rigid one. The reason for this is due to the reduction of the fin cross section at the points where the spheres connect to each other. By reducing the cross section for a constant force, the applied stress and the consequently resulting strain increase. Furthermore, the location of the lowest thickness is the most suitable candidate for fracture (see figure 2).

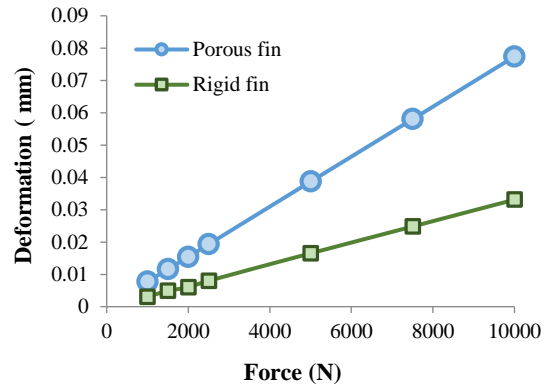


Figure 5: Deformation versus Force for the porous and rigid fins with the same dimensions

5-3- Estimation of the best porosity

The results of the strength analysis indicate less strength of the porous fin due to the presence of areas with low thickness. On the other hand, the results of heat transfer analysis, showed the superior performance of the porous fin. The most important issue is the selection of the middle condition for the fin porosity, in which the best possible strength and thermal performance are achieved simultaneously.

According to Figure 6, four fin models are plotted by considering the distance of the spheres' centers as a variable. The minimum and the maximum possible distances are selected considering the rigidity and integrity of the fin respectively. It can be seen that with increasing the distance of the spheres' center, the porosity percentage changes according to Table 4. This change in the porosity is associated with increasing the length and the width of the piece.

Table 4: Geometric specifications of porous fins with different porosity

distance between two balls	Surrounding surface area (mm <sup>2</sup> )	Volume (mm <sup>3</sup> )	Porosity percentage
6	5600.62	10821.44	27.11853
6.5	6653.56	11633.72	31.56635
7	7705.16	12234.09	36.59779
7.5	8754.97	12606.28	42.00276

The obtained results show that increasing the distance between two balls leads to enhancement in the porosity percentage, which would intensify the share of thermal convection in heat transfer consequently. On the other hand, increasing the porosity leads to a decrease in strength as can be concluded from Table 5. As well, the behavior of the thermal convective heat transfer coefficient for different porosity under the constant temperature and the constant thermal flux boundary conditions in the fin base is distinct.

**Table 5:** Tensile strength and heat transfer coefficient for different porosity percentage

Porosity percentage	Max. Tensile strength	Convective Heat transfer coefficient for constant heat flux in the base ( $W/m^2K$ )	Convective Heat transfer coefficient for constant temperature in the base ( $W/m^2K$ )
27.1	120.3369	7.163	33.464
31.6	102.459	8.633	33.765
36.6	82.23684	8.125	85.736
42	55.4939	7.578	47.321

In Figure 7, the variation of the convective coefficient and strength versus the porosity percentage is shown for the constant flux and the constant temperature boundary conditions at the base for three materials (copper, aluminum and brass). According to this diagram, it is clear that in all of these states, the heat transfer coefficient at a specific porosity is the maximum (36.6% for brass and aluminum fins and 31.6% for copper fin) and it is reduced with further increase in the porosity. The reason is due to reduction in cross section area of heat transfer and consequently decrease in the conductive heat transfer between the spheres. In this porosity, in fact, the sum of the conduction heat transfer between the spheres and the convective heat transfer from the spheres to the fluid reaches its highest value. As the percentage of porosity increases, decrease in conduction heat transfer is more sharply than increase in convective heat transfer. The highest tensile strength is achieved for the aluminum fin and the strength of the copper

and the brass fins are similar. This fact is related to the modulus of elasticity of these materials and because copper and brass have a higher modulus of elasticity than aluminum, they have less elastic deformation and fail sooner. By increasing the porosity the strength of the fin decreases for all materials because of reduction in cross section area in connection points.

The best conditions obtained with regard to the cross-point of two curves in this graph. This porosity for the porous fins of different material with different boundary conditions of the fin base are presented in Table 6.

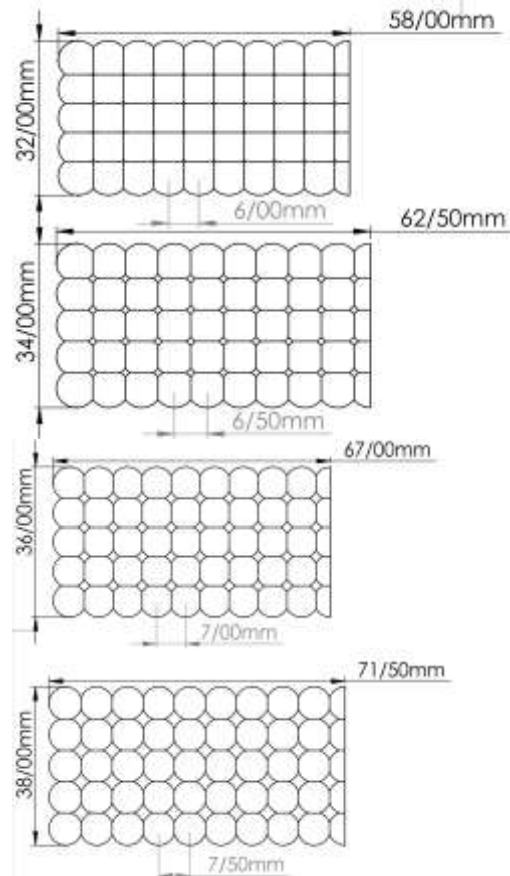


**Figure 6:** Geometric dimensions of porous fins with different porosity

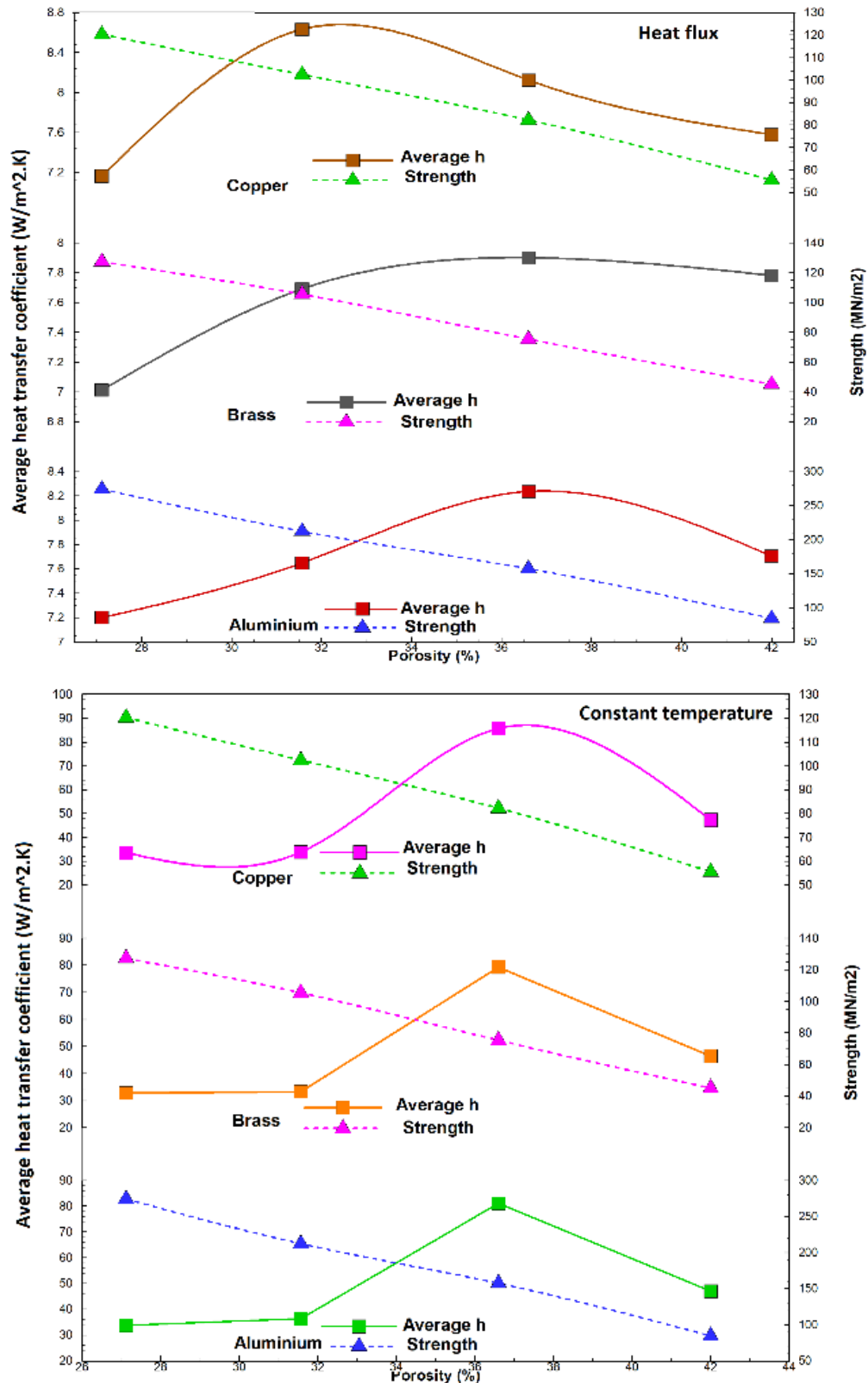


**Figure 7:** Variation of the convective heat transfer coefficient and strength versus the porosity percentage with different materials for (a) constant flux and (b) constant temperature boundary conditions at the base

Finding the optimum porosity for satisfying the best possible heat transfer and strength simultaneously is the most important innovation of this research. The main restriction for using these results is that:

- The Rayleigh number should be within the laminar free convection range.
- The manufacturing conditions have no effect on strength.
- The porosity percentage is constant in all directions.

**Table 6:** the optimal porosity for satisfying the best possible heat transfer and strength simultaneously for different materials and different boundary conditions at the base

material	constant flux at the base	constant temperature at the base
Copper	30.1%	34.2%
Aluminum	31.4%	34.5%
Brass	32.7%	34%

## 6. Conclusion

In this research, with experimental and numerical analysis of free convection heat transfer and strength in engineered porous fin, the best porosity satisfies the heat transfer and the strength simultaneously in different boundary conditions of the base and three different materials of the fin. The following consequences have been conducted:

- The results show that the strength decreases with increasing the porosity percentage.
- It has been found that for a specific porosity, the strength and the heat transfer are simultaneously satisfactory. This value of porosity varies from one material to another and it depends on the boundary condition of the base.
- If the boundary condition of the base is selected as a constant temperature, the best porosity is obtained around 34% for all materials which is higher than the best porosity for constant heat flux boundary condition (around 31%).
- For maximum heat transfer point of view for constant heat flux at the base, the best porosity among the studied porosity percentage is 36.6% for brass and aluminum fins and 31.6% for copper fin. However, it is calculated 36.6% for all materials for constant temperature at the base.

## References

- [1] I. J. J. Zahmatkesh, "Heatline visualization of buoyancy-driven flow inside a nanofluid-saturated porous enclosure," vol. 9, no. 2, 2015.
- [2] I. Zahmatkesh, S. A. J. J. J. o. M. Naghedifar, and I. Engineering, "Pulsating Nanofluid Jet Impingement onto a Partially Heated Surface Immersed in a Porous Layer," vol. 12, no. 2, 2018.
- [3] Z. Uddin, M. J. J. J. o. M. Kumar, and I. Engineering, "MHD Heat and Mass Transfer Free Convection Flow near The Lower Stagnation Point of an Isothermal Cylinder Imbedded in Porous Domain with the Presence of Radiation," vol. 5, no. 2, 2011.
- [4] M. Hatami and D. Ganji, "Thermal performance of circular convective-radiative porous fins with different section shapes and materials," *Energy Conversion and Management*, vol. 76, pp. 185-193, 2013.
- [5] A. M. Morega, A. J. I. J. o. H. Bejan, and M. Transfer, "Heatline visualization of forced convection laminar boundary layers," vol. 36, no. 16, pp. 3957-3966, 1993.
- [6] T.-M. Jeng, S.-C. J. I. J. o. H. Tzeng, and M. Transfer, "Numerical study of confined slot jet impinging on porous metallic foam heat sink," vol. 48, no. 23-24, pp. 4685-4694, 2005.
- [7] S. Kiwan and O. Zeitoun, "Natural convection in a horizontal cylindrical annulus using porous fins," *International Journal of Numerical Methods for Heat & Fluid Flow*, vol. 18, no. 5, pp. 618-634, 2008.
- [8] S. Mahjoob and K. Vafai, "A synthesis of fluid and thermal transport models for metal foam heat exchangers," *International Journal of Heat and Mass Transfer*, vol. 51, no. 15, pp. 3701-3711, 2008.
- [9] J. Liu, W. Wu, W. Chiu, and W. Hsieh, "Measurement and correlation of friction characteristic of flow through foam matrixes," *Experimental thermal and fluid science*, vol. 30, no. 4, pp. 329-336, 2006.
- [10] S. Hoseinzadeh, A. Moafi, A. Shirkhani, A. J. J. J. o. T. Chamkha, and H. Transfer, "Numerical validation heat transfer of rectangular cross-section porous fins," vol. 33, no. 3, pp. 698-704, 2019.
- [11] S. Hoseinzadeh, P. S. Heyns, A. J. Chamkha, and A. Shirkhani, "Thermal analysis of porous fins enclosure with the comparison of analytical and numerical methods," *Journal of Thermal Analysis and Calorimetry*, vol. 138, no. 1, pp. 727-735, 2019/10/01 2019.
- [12] H. Duwairi, O. Abu-Zeid, A. D. J. J. J. o. M. Rebhi, and I. Engineering, "Viscous and Joule heating effects over an isothermal cone in saturated porous media," vol. 1, no. 2, pp. 113-118, 2007.
- [13] K. Vafai, "Analysis of variable porosity, thermal dispersion, and local thermal nonequilibrium on free surface flows through porous media," 2004.
- [14] B. S. Al-azmi and K. Vafai, "Analysis of variants within the porous media transport models," Ohio State University, 2000.
- [15] P.-X. Jiang, X.-C. J. I. J. o. H. Lu, and M. Transfer, "Numerical simulation of fluid flow and convection heat transfer in sintered porous plate channels," vol. 49, no. 9-10, pp. 1685-1695, 2006.
- [16] P.-X. Jiang, M. Li, Y.-C. Ma, Z.-P. J. I. J. o. H. Ren, and M. Transfer, "Boundary conditions and wall effect for forced convection heat transfer in sintered porous plate channels," vol. 47, no. 10-11, pp. 2073-2083, 2004.
- [17] S. J. M. I. E. Nazirudeen, "A Development of Technology for Making Porous Metal Foams Castings," *Jordan Journal of Mechanical and Industrial Engineering*, vol. 4, pp. 292-299, 2010.
- [18] X. Cao, P. Cheng, T. J. J. o. t. Zhao, and h. transfer, "Experimental study of evaporative heat transfer in sintered copper bidispersed wick structures," vol. 16, no. 4, pp. 547-552, 2002.
- [19] S.-W. Kang, W.-C. Wei, S.-H. Tsai, and C.-C. J. A. T. E. Huang, "Experimental investigation of nanofluids on sintered heat pipe thermal performance," vol. 29, no. 5-6, pp. 973-979, 2009.
- [20] M. Mesgarpour, A. Heydari, and S. Soddodin, "Investigating the effect of connection type of a sintered porous fin through a channel on heat transfer and fluid flow," *Journal of Thermal Analysis and Calorimetry*, pp. 1-14.
- [21] M. Mesgarpour, A. Heydari, and S. Saedodin, "Numerical analysis of heat transfer and fluid flow in the bundle of porous tapered fins," *International Journal of Thermal Sciences*, vol. 135, pp. 398-409, 2019.
- [22] M. Mesgarpour, A. Heydari, and S. Saedodin, "Comparison of free convection flow around an engineered porous fin with spherical connections and rigid fin under different positioning angles—An experimental and numerical analysis," *Physics of Fluids*, vol. 31, no. 3, p. 037110, 2019.
- [23] M. Mesgarpour and A. Heydari, "Numerical investigation of heat transfer in a sintered porous fin in a channel flow with the aim of material determination," *Journal of Heat and Mass Transfer Research*, vol. 6, no. 1, pp. 63-74, 2019.
- [24] M. Bouzid, L. Mercury, A. Lassin, J. M. Matray, and M. Azaroual, "In-pore tensile stress by drying-induced capillary bridges inside porous materials," *J Colloid Interface Sci*, vol. 355, no. 2, pp. 494-502, Mar 15 2011.

- [25] T. J. E. F. M. Ito, "Effect of pore pressure gradient on fracture initiation in fluid saturated porous media: Rock," vol. 75, no. 7, pp. 1753-1762, 2008.
- [26] J. Maurath, J. Dittmann, N. Schultz, N. J. S. Willenbacher, and P. Technology, "Fabrication of highly porous glass filters using capillary suspension processing," vol. 149, pp. 470-478, 2015.
- [27] S. Hoseinzadeh and P. S. Heyns, "Thermo-structural fatigue and lifetime analysis of a heat exchanger as a feedwater heater in power plant," *Engineering Failure Analysis*, vol. 113, p. 104548, 2020/07/01/ 2020.
- [28] L. Leal, *Advanced Transport Phenomena: Fluid Mechanics and Convective Transport Processes*. Cambridge University Press, 2007.
- [29] R. S. R. Gorla and A. Y. Bakier, "Thermal analysis of natural convection and radiation in porous fins," *International Communications in Heat and Mass Transfer*, vol. 38, no. 5, pp. 638-645, 2011/05/01/ 2011.
- [30] H. K. Versteeg and W. Malalasekera, *An introduction to computational fluid dynamics: the finite volume method*. Pearson education, 2007.

# Potential Utilization of Iraqi Associated Petroleum Gas as Fuel for SI Engines

Jehad A. A. Yamin<sup>a</sup>, Eiman Ali Eh Sheet<sup>b</sup>

<sup>a</sup>Mechanical Engineering Department, School of Engineering, The University of Jordan, Amman 11942, Jordan

<sup>b</sup>Energy and Renewable Energies Technology Center, University of Technology-Iraq, Baghdad 10066, Alsenaa Street, Iraq

Received October 19 2019

Accepted August 31 2020

## Abstract

An engine modelling study was conducted to investigate the relative change in performance and emissions of a 4-stroke, spark-ignition engine using Iraqi Associated Petroleum Gas as fuel. The research was done using a well-verified simulation software Diesel-RK. The data available for Ricardo E6/T variable compression ratio spark-ignition engine was used to conduct this study. The performance of the engine using associated petroleum gas was compared with those for gasoline, natural gas, and the average properties of the natural gas in Europe. The performance parameters studied were engine power, thermal efficiency, oxides of nitrogen, unburned hydrocarbon, and carbon monoxide levels. The study showed that the Iraqi associated petroleum gas could not be used "as is" if the aim is to cut down pollution. The main advantage is the absence of sulfur in the gas, which is present in the gasoline used in Iraq. There is a significant rise in NO<sub>x</sub> levels, a reduction in UHC, and also a rise in CO levels when using APG fuel. Further, there is an average reduction in engine power of about 10% with the associated gas compared with gasoline. At the same time, the only gain is the reduction in SFC and improvement in thermal efficiency with the new fuel.

© 2020 Jordan Journal of Mechanical and Industrial Engineering. All rights reserved

Keywords: Associated gas, SI engine, Methane gas, Engine emissions, Natural gas;

## 1. Introduction

Gaseous deposits that often exist in petroleum are usually called Associated Petroleum Gas (APG) or Flare gas (FG). These gaseous deposits usually consist of methane and other short-chain hydrocarbons which are considered as by-product of oil production. They are, in many cases, either flared or vented.

With reference to the data collected from satellites, the quantity of this gas that gets flared and vented annually in the world is estimated to be 140-170 billion cubic meters (BCM) (Elvidge et al., 2009, and 2013, <https://visibleearth.nasa.gov/view.php?id=83178>, Vorobev and Shchesnyak, 2019). Iraq burned approximately 30 BCM of APG in 2018 (<https://www.iea.org/reports/iraq-energy-outlook-2019>), and it is estimated according to the report that this quantity will rise to around 50 BCM.

Flaring is preferable to venting from a global warming point of view. Though this process produces Carbon Dioxide (CO<sub>2</sub>), it, however, reduces the overall potential for global warming caused by methane and other hydrocarbons. Methane that is present as deposits in petroleum is considered to be (on a 100 years time-scale) more potent than CO<sub>2</sub> (Holmes et al., 2013; Myhre et al., 2013; Boucher et al., 2009).

Though flaring helps reduce global warming gases that are flammable in nature, it, on the other hand, produces some other pollutants, such as Oxides of Nitrogen (NO<sub>x</sub>), Carbon Monoxide (CO), and Black Carbon (BC). One of the by-products of APG flaring is BC. This by-product causes climate warming, speeds up ice melting and blackens its surface, and affects the dynamism of the clouds. (Myhre et al., 2013).

It was estimated that 4% of the global BC emissions are produced by APG flaring. With an estimated amount of 230 Gg/yr, this is considered more than three times higher than spark ignition engines' vehicles global BC emissions of about 80 Gg/yr (Boucher et al., 2009, Bond et al., 2013, Stohl et al., 2013). APG can be utilized in so many ways provided they are processed in certain ways. Some ways of the utilization of APG include power generation which is sold out for certain chemical and petrochemical industries, injected in petroleum well to improve oil recovery.

Upon reviewing the literature, limited or no research is found on the use of this gas as a fuel for Spark Ignition (SI) engines. Zyryanova et al. (2013) showed a faster payback of the capital investment achieved for the power plants that used fuel made catalytic reforming of APG into Methane-hydrogen mixture compared with direct burning of APG only. They attributed this to the extended service life, extended durations of overhaul, and low rated power losses.

\* Corresponding author e-mail: yamin@ju.edu.jo

AI Gur'yanov et al. (2015) conducted a computational analysis on the effect of converting Natural Gas (NG) powered gas turbine combustion chamber to be fueled with APG. They took into their consideration the change in power density, thermal and combustion efficiencies as well as engine-out emissions. One of the significant conclusions they reported was the need to redesign the air distribution system as well as the method of fuel introduction due to the variable composition of the APG from field to field compared with methane gas.

Vazim et al. (2015) conducted an economic study on the use of APG as fuel in a small power generation unit in Tomsk Oblast. They showed increase in profitability and reduced payback period when using this type of fuel.

Using APG as fuel for SI engines resulted in a new concept of the fuel's tendency to resist knocking rises. Methane Number (MN) (Roy et al., 2019), is a new term used to indicate the fuel's ability to resist knocking (similar to Octan Number (ON) in conventional fuels).

Methane is usually given an arbitrary number of 100 (being strong resistant to knocking) while hydrogen is given the scale of zero due to its relative fast burning compared with methane. MN can be determined by the percentage of methane in the mixture of methane and hydrogen that will give the same knocking characteristics of the test fuel. Thus, a fuel with MN=90 means that this fuel has knock resistance equivalent to a mixture of 90% methane and 10% hydrogen.

APG flaring in Iraq has increased in mid-1970s. This situation continued till the Gulf War in 1992 where it reduced significantly and then rose again in 2011 to a level of 9.4 BCM of natural gas. Some known agencies estimated that around 70% of APG in Iraq is being wasted by flaring. (<https://visibleearth.nasa.gov/view.php?id=83178>).

Significant amount of research and efforts have been directed towards improving utilization of APG in Iraq and Arab countries to be used in fertilizers, power generations and other applications.

It was estimated that in 2013, 21.8 BCM of APG (out of a total of 24 Million Barrel per Day (MBD)) was flared. This amount increased in 2017, to about 25.5 BCM (out of a total of 26 MBD of crude oil produced). These figures indicate that the amount of APG being lost by flaring has increased, thus, increasing the loss in a potential source of energy. (<https://www.ecomena.org/gas-flaring-in-iraq/>).

More recently and with the energy crisis due to unrest in the region, the value of gas as a source of energy and its environmental benefits were gradually realized, and some regulations were introduced to limit gas flaring to the minimum.

Based on the above introduction, it becomes clear that APG represents a potential source of energy that must be investigated in the automobile sector. This paper discusses the relative change in spark-ignition engine emissions and performance when using Iraqi APG as fuel compared with gasoline, natural gas (NG), and pure methane.

## 2. The Study

### Mathematical modeling

This model treats the combustion chamber in a way that it consists of two distinct zones (e.g. burned and unburned) separated by the flame front. The main equations applied to

analyse those zones are the first law of thermodynamics and the continuity equation. These equations are derived with respect to crank angle ( $\theta$ ) to yield several coupled first order differential equations for pressure, volume, temperature (burned and unburned), mass, heat flux ...etc. that are applied for both zones. As for the cylinder pressure, it is usually assumed to be in uniform all through the cylinder charge. The model is also assumed to have no chemical reaction between cylinder constituents prior to combustion, and that the mixing inside the cylinder between its constituents is a perfect one.

Derivation of the equation of state with respect to  $\theta$  gives (Yamin et al., 2003):

$$\frac{dP}{d\theta} = \frac{\left[-\left(1+\frac{R}{C_v}\right)P\frac{dV}{d\theta} - \frac{R}{C_v}\frac{dQ_{cr}}{d\theta} + \frac{R}{C_v}\frac{dQ_{hl}}{d\theta}\right]}{V} \quad (1)$$

$$\frac{dT}{d\theta} = T \cdot \left(\frac{1}{P}\frac{dP}{d\theta} + \frac{1}{V}\frac{dV}{d\theta}\right) \quad (2)$$

Where; "P" is the cylinder pressure (kPa), "T" is the cylinder temperature (K), " $\theta$ " is the crank angle (degree), "V" is the cylinder volume ( $m^3$ ) which is a function of crank angle rotation, "R" is the gas constant (kJ/kg-K), "C<sub>v</sub>" is the specific heat at constant volume (kJ/kg-K), "Q<sub>cr</sub>" is the total heat flux lost to crevice (or with blow-by) and "Q<sub>hl</sub>" is the total heat flux lost to coolant (kJ).

The instantaneous cylinder volume "V( $\theta$ )" measured from bottom dead center (BDC) position can be expressed using cylinder mechanism (slider crank mechanism) with certain modifications as :

$$V(\theta) = V_s \left[ \left(\frac{CR}{CR-1}\right) - \left(\frac{1-\cos(\theta)}{2}\right) + \left(\frac{CRL}{S}\right) - \frac{1}{2} \sqrt{\left(\frac{2 \cdot CRL}{S}\right)^2 - \sin^2(\theta)} \right] \quad (3)$$

Where; "CR" is the compression ratio, "CRL" is the connecting rod length (m), "S" is the stroke length (m), and "V<sub>s</sub>" is the stroke volume ( $m^3$ ).

Derivation of equation (3) with respect to  $\theta$  gives the rate of change of cylinder volume with crank angle as follows :

$$\frac{dV}{d\theta} = \frac{1}{2} V_s \sin \theta \left( \frac{\cos \theta}{\sqrt{\left(\frac{2 \cdot CRL}{S}\right)^2 - \sin^2 \theta}} - 1 \right) \quad (4)$$

This is helpful in calculating the rate of change of indicated work "W" with crank angle :

$$\frac{dW}{d\theta} = P \frac{dV}{d\theta} \quad (5)$$

Also; the heat lost during the cycle (Q<sub>hl</sub>) is used as follows :

$$\frac{dQ_{hl}}{d\theta} = \frac{h_w}{\omega} A_w(\theta) [(T - T_w)] \quad (6)$$

Where; "A<sub>w</sub>" is the cylinder wall surface area ( $m^2$ ), "T<sub>w</sub>" is the cylinder wall temperature (K) and " $\omega$ " is the angular velocity ( $s^{-1}$ ).

Woschni's (1968) formula is used for the calculation of the heat transfer coefficient (h<sub>w</sub>) from cylinder contents to walls. This is shown below in equation (7).

$$h_w = \frac{P^{0.8} v^{0.8}}{T^{0.53} D^{0.2}} \quad (7)$$

where; the value of the gas velocity v is taken to be equal to 6.18\*v<sub>m</sub> during scavenging and intake stroke (m/s); and during compression stroke it takes the value equal to



**CO Formation:**

Carbon monoxide values usually lie between the maximum and the exhaust values. For this purpose, certain multiplication factor  $CO_{FAC}$  is used in the model to obtain the most correct value. This is shown below in equation (13).

$$X_{CO} = X_{CO_{eq}} + CO_{FAC} * (X_{CO_{max}} - X_{CO_{eq}}) \quad (13)$$

Where;

$X_{CO}$  = Corrected concentration of CO.

$X_{CO_{eq}}$  = Concentration of CO at equilibrium.

$X_{CO_{max}}$  = Maximum value of CO concentration at equilibrium condition.

The fuel used for this study was the APG produced in Al-Basrah (south of Iraq) oil fields. The constituents of the fuel compared with other fuels used in this study are presented below in Table (1)

([https://www.naesb.org/pdf2/wgq\\_bps100605w2.pdf](https://www.naesb.org/pdf2/wgq_bps100605w2.pdf), <https://www.iasj.net/iasj?func=fulltext&aId=28281>)

The engine used for the study is the Ricardo E6/T variable compression ratio engine. The engine design parameters are shown below in Table (2).

The study concentrated on simulating the engine performance and emission characteristics when running the engine on the lean side to avoid excess fuel consumption, achieve the best thermal efficiency and minimum fuel consumption, and also least pollution.

The equivalence ratio was varied in the range of 0.8 to 0.95; the engine speed range was covered 1000 to 3000 rpm, ignition timing at 15° bTDC, which is nearly best for all fuels tested.

The performance of the Iraqi Associated Gas was compared with gasoline, methane, and average data gathered for the Natural gas elsewhere. This is done for the sake of comparison. The results of the study were divided into emissions and performance comparison.

**3. Results and Discussion**

First, model verification results for gasoline are shown below in Figures (1-A and B). These figures clearly show that the model was able to follow the engine behavior trends to a reasonable degree of accuracy. The model was further tested using other types of fuels as in (Yamin et al., 2000, 2002, and 2003; Hackan et al., 2008; Yamin, 2006).

Those two figures show a comparison between the experimental results as supplied by the manufacturer in the user manual and the mathematical model. The first figure (1-A) shows the comparison with the power parameters (indicated power (IP), indicated mean effective pressure (IMEP), brake power (BP), and Brake mean effective pressure (BMEP)). The second figure shows the cylinder pressure for both cases (model and simulation). The purpose of those graphs is to check the validity of the model to predict the engine behavior. As stated above, the model was verified for different types of fuels.

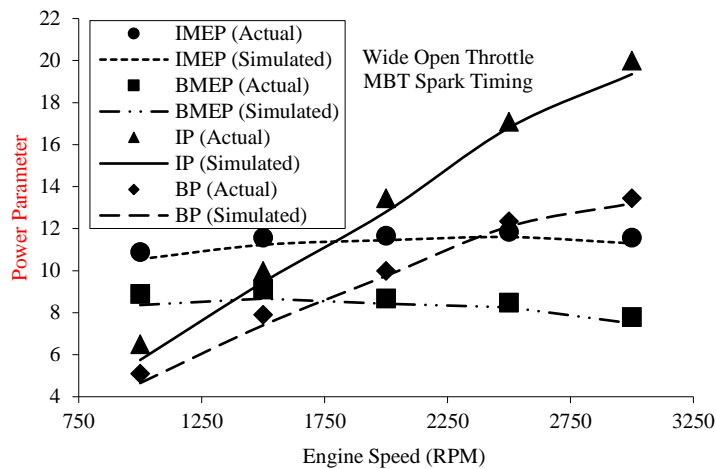


**Figure (1-A):** Comparison between experimental and model results (performance parameters)

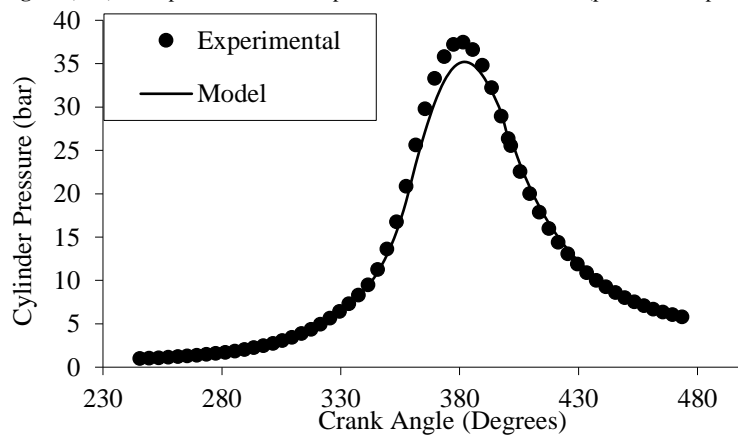


**Figure (1-B):** Comparison between experimental and model results (cylinder pressure)

**Table (1):** Fuel composition on a volume basis.

	Iraqi APG	Natural Gas	Methane	Gasoline
C1	79.5%	94.9%	100%	
C2	0.14%	2.5%		
C3	0%	0.2%		
nC4	9.24%	0.03%		
iC4	5.56%	0.03%		
nC5	0.89%	0.01%		
iC5	2.22%	0.01%		
C6	0.72%	0.01%		
H2O	0%	0%		
CO2	0%	0.7%		
N2	0%	1.6%		
O2	0%	0.02%		
H2	0%	Traces		
H2S	0%	0%		
Chemical Formula	C1.4H4.4O0.0028	C0.98H3.98	CH4	C8H18
Calorific Value (MJ/kg)	47.8	46	50	44

**Table (2):** Engine design parameters

Engine Speed (rpm)	1000-3000
Compression Ratio Range [ND]	4.5-20 (8 for this study)
Bore / Stroke (mm)	76.2/111.1
Connecting Rod Length (mm)	231.7
Crank Radius (mm)	55.5
Swept Volume (cm <sup>3</sup> )	507
Inlet Valve Open/Close (deg)	10° bTDC/36° aBDC
Exhaust Valve Open/Close (deg)	43° bBDC/8° aTDC
Maximum Valve lift Inlet/Exhaust (mm)	10.6/10.48
Tappet Clearance Inlet/Exhaust (mm)	0.152/0.203

*Engine Emissions*

The engine emissions studied were the carbon monoxide (CO), unburned hydrocarbon (HC), and oxides of nitrogen (NOx).

Before starting the discussion, let us point out the following essential points:

1. Hydrocarbon fuel burns, ideally, in two steps. First the HC molecules gets disintegrated to Hydrogen (H) and Carbon (C). Then, if the process is ideal, The C atom gets burned to CO<sub>2</sub> and that for H atom to H<sub>2</sub>O. molecules, respectively..
2. This real burning process deviates considerably from the ideal one if the fuel used is a complex (mixture of different hydrocarbons) than simple (single hydrocarbon component).
3. The more complex the combustion process is, the less effective the utilization of the fuel becomes.

In this study, the fuel used, e.g., Iraqi APG is a mixture of components that are different in nature and properties. For example, the ignition temperature in air (°C) for methane is 595, ethane 510; propane is 470, butane is 460, while gasoline has 220. Therefore, the engine needs to be modified for the new gas. Further, Octan Number (ON) of Methane, propane, and butane are higher than 100; we find that n-butane is 91, n-pentane 62, and n-hexane 25. This causes the overall mixture to behave differently during the combustion process compared with methane and other natural gas fuels.

Figure (2) shows the variation of CO with engine speeds for different equivalence ratios. It is estimated that 60% of the annual globally emitted CO gas (which is estimated to be around 2600 million tonnes) comes from industrial or human activities. The rest are from natural sources.

Those 60% emitted from human-related activities are primarily due to the incomplete combustion of the carbon atoms in the fuels. They get emitted from the exhaust system of the internal combustion engines. The most significant quantities of these type of emissions are produced as exhausts of internal or external combustion systems (e.g. engines, powerplants, incinerators ...etc.). These systems have undergone significant modifications to enhance their performance in the past few decades. ([http://www.euro.who.int/\\_\\_data/assets/pdf\\_file/0020/123059/AQG2ndEd\\_5\\_carbonmonoxide.PDF](http://www.euro.who.int/__data/assets/pdf_file/0020/123059/AQG2ndEd_5_carbonmonoxide.PDF)).

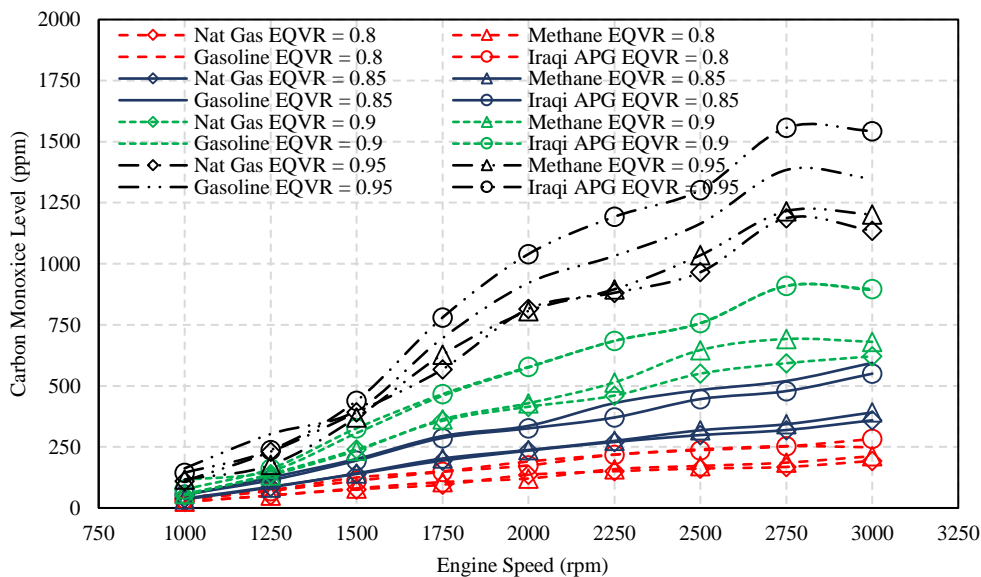


**Figure (2):** Carbon monoxide variation with engine speeds at different equivalence ratios

Generally, it is understood that the existence of CO in the exhaust of any combustion system is related to oxygen deficiency inside the combustion chamber of that system (Springer, 2012). There may be another reason for the CO to exist in the exhaust products which is the dissociation of CO<sub>2</sub> to CO and O<sub>2</sub>.

The chemical equilibrium equation for the formation of CO represented by the water gas equation as shown below :

$$\text{CO} + \text{H}_2\text{O} \rightarrow \text{H}_2 + \text{CO}_2$$

At the peak value of flame temperatures, this equilibrium produces greater amounts of CO compared to CO<sub>2</sub>. This situation occurs even if the Air/Fuel ratio used is lean. This scenario is completely altered as the products of combustion temperature falls below the peak value. This is the reason behind the less quantities of CO appearing in the exhaust when using lean or stoichiometric Air/Fuel mixtures.

For rich Air/Fuel mixtures, oxygen deficiency is the prime cause for the appearance of CO in the relatively cooler exhaust products.

As shown in Figure (3), the lower exhaust product temperature for methane and natural gas can be the reason for their lower CO levels. Further, this also explains the lower CO levels for APG at lower speeds and lower equivalence ratios.

Further, CO emissions increase with an engine speed for all fuels. This is expected to be the result of a reduction in the amount of air induced as the engine speed increases.

For all fuels, CO levels increase with the equivalence ratio. This is (as stated earlier) due to the incomplete combustion of the fuel carbonaceous contents which, due to oxygen deficiency) are partially burned.

Further, the performance of the Iraqi APG was better than gasoline for low equivalence ratios (0.8 and 0.85) for low and medium speeds. There was a maximum reduction of 20% at low speed, and the least reduction was 1.6% at 2000 rpm. At higher speeds, the performance got worsened compared with all other fuels. The increment in CO reached 13% at 3000 rpm. This is compared with other gaseous fuels, has the highest C/H ratio. Hence, higher number of carbon atoms is burned. Further, the amount of air admitted at higher gets reduced with engine speed. Therefore, the performance worsened with higher equivalence ratios and engine speeds.

Another trend shown in the figure is the advantage of using methane as fuel. For all engine speeds and

equivalence ratios, methane and natural gas produced the least CO emissions. This is due to the less carbon content of either fuels (or C/H ratio) compared with gasoline and APG. Further, those two types of fuels require less amount of air compared with gasoline and APH for complete combustion, which is already available. Similar results are shown in this review study by Singh et al. (2019).

Figure (4) shows the variation of HC with engine speeds for different equivalence ratios. Generally, HC molecules that are emitted in the exhaust are mainly unburned fuel that were deprived from getting burnt due to "flame quenching" phenomenon.

UHC can be formed due to several sources. Some of these sources are listed below :

1. Flame quenching near the cold surfaces.
2. The inability of the flame to reach certain crevices where some fuel-air mixture might exist.
3. Quenching within the bulk gas-phase due to extreme Air/Fuel conditions.
4. Fuel that gets absorbed by the lubricant during compression and later on it gets desorped as the cylinder pressure drops during exhaust process. This is known to be one of the significant phenomena.

Another theory describing the formation of HC is the crevice theory. It assumes that, especially during compression and combustion strokes, the fuel can penetrate through certain areas in the engine cylinder where the flame cannot reach (quenching distance). This part of the fuel is then gets released when the pressure drops during the expansion stroke. Some of them get burned during the after-burn process while the majority are expelled with the exhaust.

Several researchers (Lakshminarayanan et al., 2010) reported that quenching layers do exist inside the cylinder. They also showed that UHC emissions are propotional to these layers. Others reported these quench masses of the mixture are mixed with the burned mass and then get oxidized inside the cylinder during the expansion and exhaust strokes. It was estimated that less than 10% of the emitted HC was due to the wall quenching. Others attributed the HC emission due to the unburned fuel adsorption/desorption processes by lubricating oil films.

As shown in the figure below, the accelerated decrease in HC emission will be due to the reduced engine cycle time. This allows for lower absorption and desorption to occur.

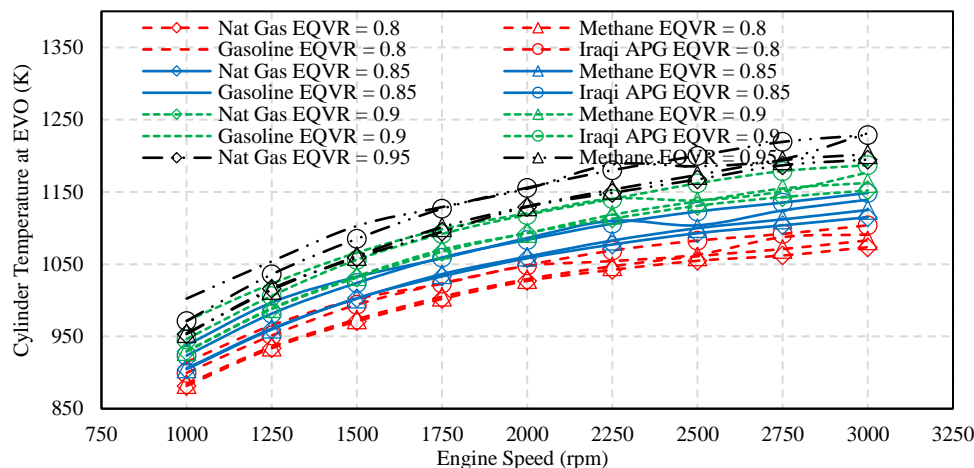


Figure (3): Exhaust temperature variation with engine speed at different equivalence ratios

With the increase in cylinder temperature at higher engine speeds, the thickness of the oil film at the wall decreases (due to reduced viscosity). This results in less amount of the unburned fuel to be absorbed by the oil film.

Henry (Lakshminarayanan et al., 2010) defined a new constant by dividing the partial pressure of the fuel vapor ( $P_{fs}$ ) in the gas phase just at the surface of the oil film to the mole fraction of the fuel dissolved in the oil film ( $n_{fl}$ ). This constant was found to increase with engine speeds and cylinder temperatures.

Another reason for the reduction of HC with engine speed is the higher exhaust temperature. This decreases the desorbed HC mass fraction (ppm) emitted due to increased wall temperature and the increased post desorption oxidation due to higher burned gas temperatures with increasing engine speed.

Further, increasing equivalence ratio ( $\Phi$ ) increases the concentration of fuel vapor in the cylinder. This will make

more of the fuel vapor to be absorbed and later on desorbed by the oil film. This phenomenon will also increase with cylinder pressure. Higher cylinder pressure will also increase the amount of mixture that will enter the crevices e.g. between rings, piston and cylinder clearance, valve and head ...etc. These places are considered as quenching distances for the flame where it cannot penetrate, hence, UHC levels will increase. This situation will be further aggravated if both the cylinder pressure and the mixture strength are increased.

Based on this, the Iraqi APG performs better than other gaseous fuels since it produces higher cylinder temperature and pressure during the cycle.

Figure (5) shows the variation of NOx emissions with engine speeds for different equivalence ratios.

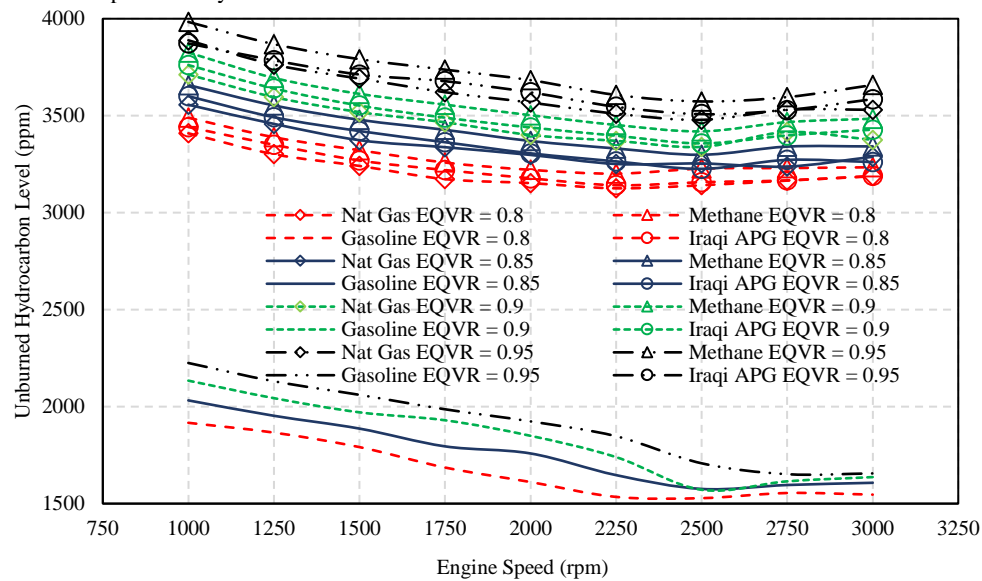


Figure (4): Hydrocarbon variation with engine speed at different equivalence ratios

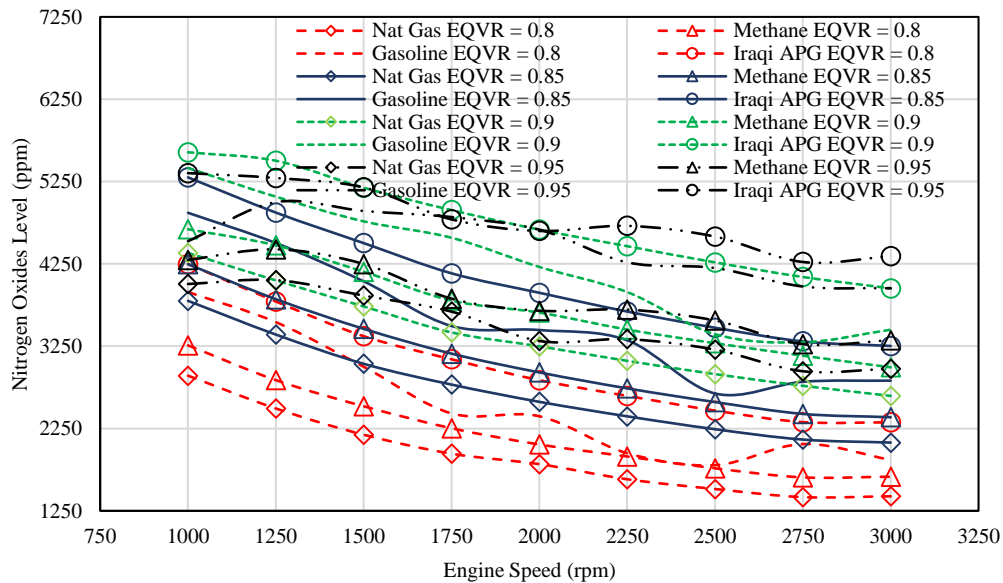


Figure (5): Oxides of nitrogen variation with engine speed at different equivalence ratios

NOx molecules in the exhaust are products of a high cylinder temperature that causes some secondary reactions that results from the disassociation of the nitrogen that enters the cylinder with atmospheric air. Some of this nitrogen also gets burned to form nitric oxide (NO), this NO is later converted to other nitrogen oxides, such as nitrogen dioxide (NO2). NOx formation depends on several factors, including cylinder temperature, oxygen availability, residence time (combustion duration), and A/F ratio.

Contrary to the behavior of CO, NOx emissions decrease with engine speed. This is clear for all fuels. The reduction in oxygen concentration and combustion duration are the primary reasons for this behavior. It is also noticed that NOx emissions are maximum for an equivalence ratio of 0.9.

As for the APG, NOx emissions are higher than others due to higher calorific value, which results in higher cylinder temperature and pressure, as shown in Figure (6).

Therefore, to conclude this section, based on the above discussion, the Iraqi association gas cannot be used "as is" if the aim is to cut down pollution. The main advantage is the absence of sulfur in the gas, which is present in the gasoline used in Iraq.

Further gas processing is needed to reduce the constituent and make it more uniform. The higher carbon components must be reduced to the least. Some studies (Lakshminarayanan et al., 2010 and Porpatham et al., 2012, Ayandotun et al., 2012) showed that the presence of CO2 in the mixture up to a certain level is helpful to cut down the NOx emissions.

On the other hand, the the higher the concentration of CO2 in the fuel mixture, the lower the heating value of this fuel mixture. This reduction in the heating value and the increase in its specific heat capacity as well reduces the flame velocity of the burned mixture and thus adversely affects the engine performance (Porpatham et al., 2012).

Engine Performance

From the engine performance point of view, brake power (Figure (7)), brake thermal efficiency (Figure (8)), volumetric efficiency (Figure (9)), and brake specific fuel consumption (BSFC) (Figure (10)).

These figures show that the power developed by the associated gas is 12% less than that for gasoline. Other fuels showed a reduction of 15% or more compared with gasoline. This is clear for all equivalence ratios studied.

Heywood (1989) developed an equation correlating engine performance parameters to power as shown below :

$$Power = \rho_{ai} A_p S \eta_{th} \eta_{vol} Q_{HV} \left(\frac{F}{A}\right) \left(\frac{N}{60}\right) \left(\frac{n_c}{n_r}\right) \quad (16)$$

where, "ρ<sub>ai</sub>" is the air density at inlet conditions, "A<sub>p</sub>" is the piston area (m<sup>2</sup>), "S" is the stroke length (m), "η<sub>th</sub>" is the indicated thermal efficiency, "η<sub>vol</sub>" is the volumetric efficiency, "Q<sub>HV</sub>" is the fuel's heating value (kJ/kg), "(F/A)" is the fuel-air ratio, "N" is the engine speed (rev/min), "n<sub>c</sub>" is the number of cylinders, "n<sub>r</sub>" is the number of stroke rotations needed to complete one cycle.

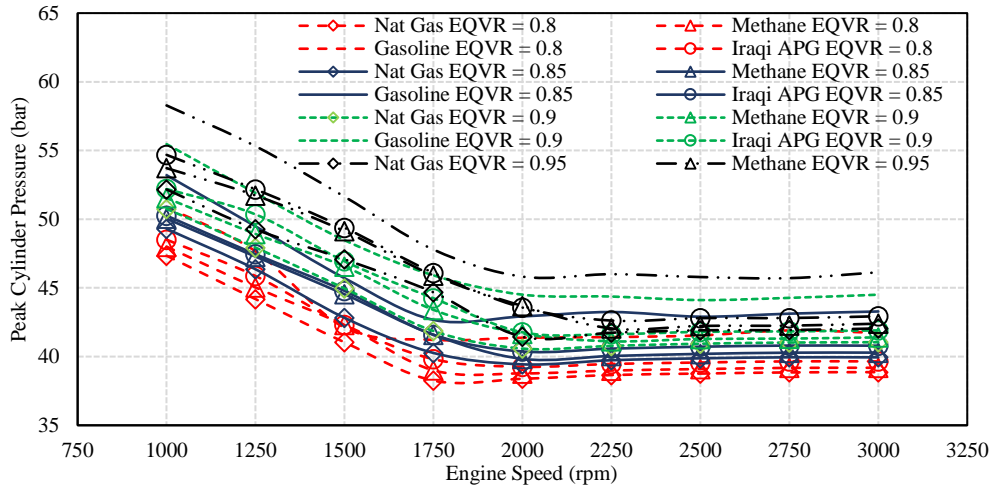


Figure (6): Peak cylinder pressure variation with engine speed at different equivalence ratios

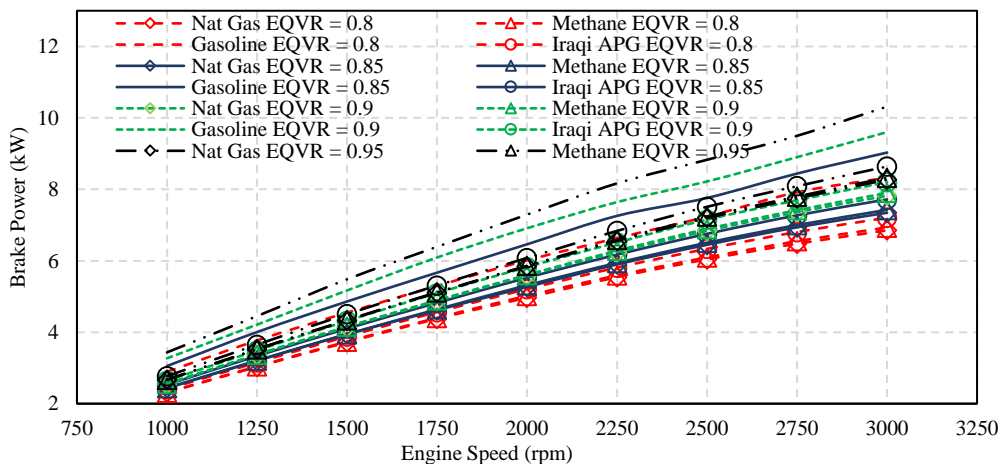


Figure (7): Brake power variation with engine speed at different equivalence ratios

As the above equations suggest, higher power can be achieved by increasing the engine displacement, engine speed, thermal efficiency, volumetric efficiency, or using fuel with higher calorific value keeping other parameters the same.

In this study, the engine dimensions were kept constant (i.e.  $\rho_{a_i} A_p S$  and  $\left(\frac{n_c}{n}\right)$ ). For each engine speed (N), the fuel equivalence ratio ( $\Phi$ ) was varied between 0.8 and 0.95. The other controlling parameters for the power (based on equation 16) will be volumetric and thermal efficiencies and calorific values.

Figure (8) shows the brake thermal efficiency for all fuels at the test conditions. It is clearly shown that the engine's thermal efficiency increases linearly for all values of  $\Phi$  from leanest till near stoichiometric. This is thought to be the result of lower cylinder temperature (compared with near stoichiometric to 10% rich mixtures) and less amount of complex components like  $CO_2$  and  $H_2O$  that are formed in the cylinder which increase the thermal capacity of the products of combustion. This, in turn, increases the amount of sensible heat resulting from converting of the fuel's chemical energy to thermal energy near top dead center. Subsequently, larger fraction of the fuel's energy is utilized to develop work inside the cylinder during expansion, and hence, less will be the amount wasted with exhaust.

This figure also shows that for all equivalence ratios, gasoline showed best results followed by APG. Thermal efficiency is also linked to the calorific value of the fuel as shown in equation (17) (Heywood, 1989):

$$\eta_{th} = \frac{Power}{\dot{m}_f Q_{cv} \eta_c} \quad (17)$$

Referring to Table (1), the calorific value of methane is the highest with 20% higher than that for gasoline. APG has

a higher calorific value than other fuels (10% greater than gasoline). However, the oxygen availability with gasoline fuel (shown in figure (9)) helped improve the combustion efficiency ( $\eta_c$ ) and hence improve thermal efficiency. This availability is also higher for APG compared with methane and natural gas. Therefore, the thermal efficiency of APG is higher than methane and natural gas. The reduction in the thermal efficiency for the methane and natural gas is of the order of 8-9%, while that for APG is 6-7% compared with gasoline.

One reason can be thought of is the latent heat of evaporation of gasoline. During evaporation, gasoline tends to cool down the engine and inlet manifold, hence increase the amount of air admitted to the engine (represented by volumetric efficiency) and, therefore, better combustion compared with gaseous fuels. Figure (9) suggests a 12-13% reduction in volumetric efficiency for methane and natural gas fuels compared with gasoline against a 9-10% reduction for APG.

The higher amount of air that the engine admits to the engine due to the cooling effect of liquid fuel being evaporated provides more oxygen for combustion and hence better combustion. Figure (9) shows the clear advantage of liquid fuel over gaseous fuel (unless the engine design is altered).

Therefore, there is quite a direct correlation between the change in thermal and volumetric efficiencies with engine power (keeping other parameters constant).

From a specific fuel consumption point of view, there is an apparent 2-3% reduction when using associated gas compared with other gaseous fuels. This is shown in Figure (10). Two factors affecting such behavior, i.e., the power developed and calorific value of the fuel.

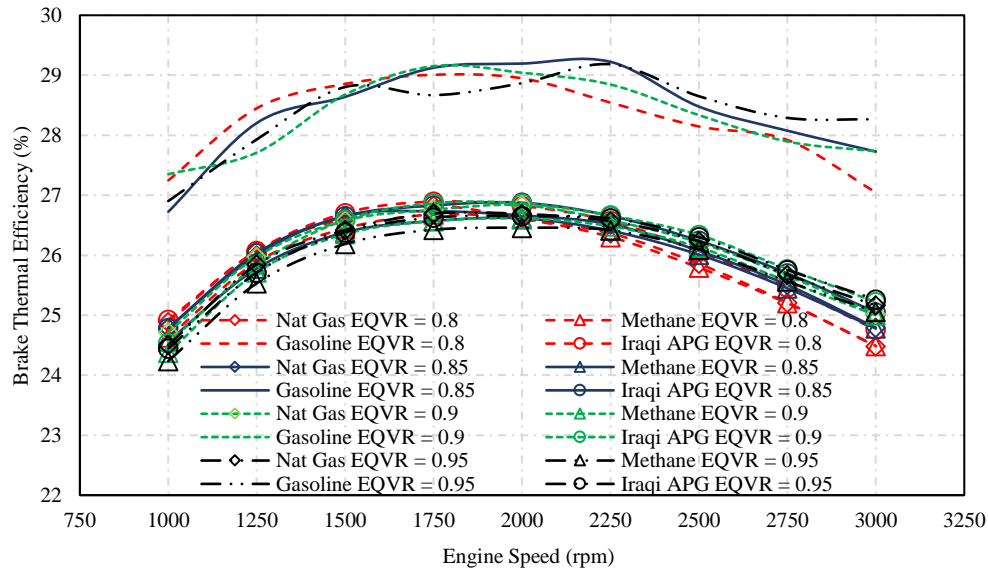


Figure (8): Brake thermal efficiency variation with engine speed at different equivalence ratios

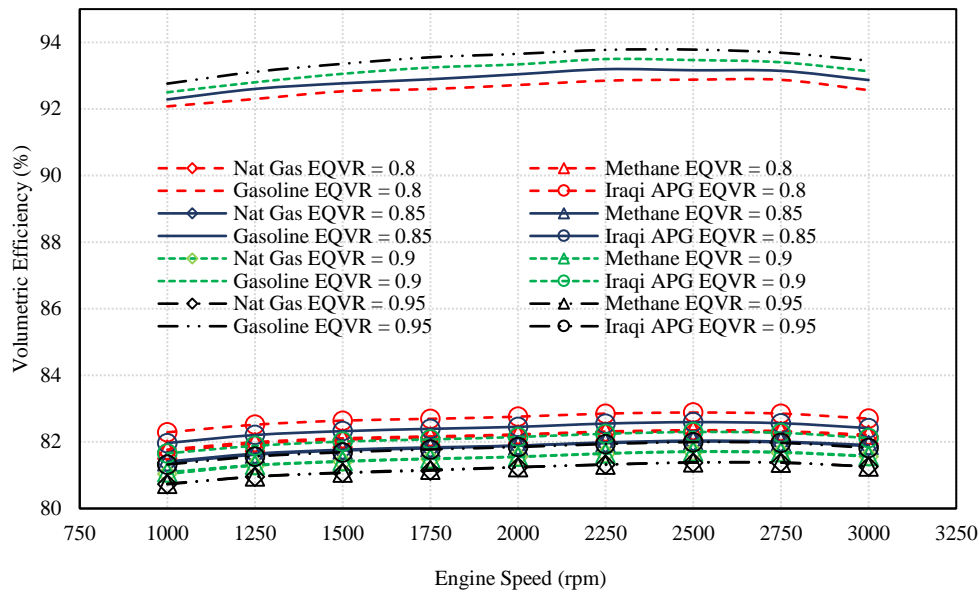


Figure (9): Volumetric efficiency variation with engine speed at different equivalence ratios

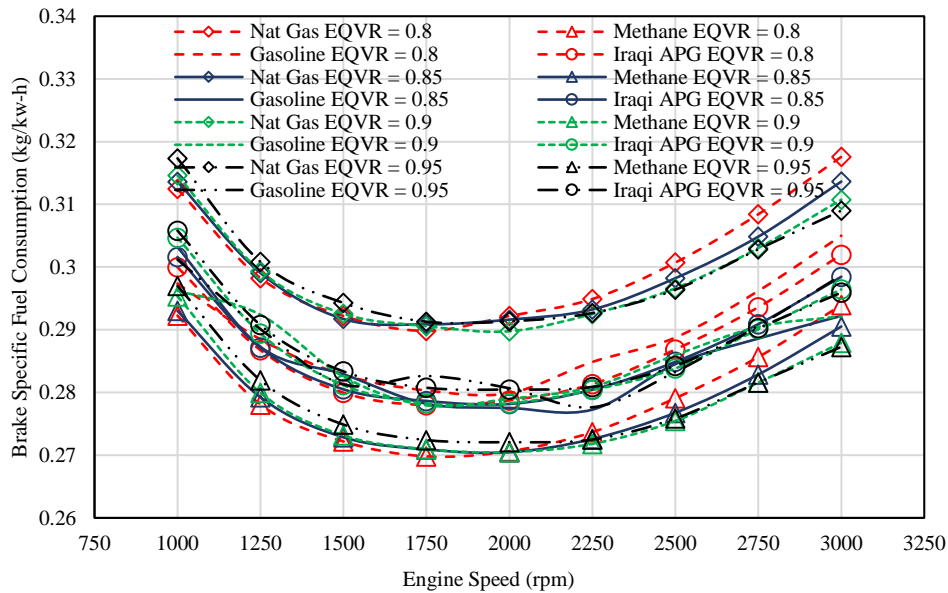


Figure (10): Brake SFC variation with engine speed for different equivalence ratios

To conclude this part, there is an average reduction in engine power of about 10% with the associated gas compared with gasoline, while the only gain is the reduction in SFC of the fuel.

4. Conclusion

A simulation study was conducted to study the performance of the SI engine using Iraqi associated gas. The study showed that the Iraqi APG needs processing before use as fuel for Si engines if the aim is to cut down pollution. The main advantage is the absence of sulfur in the gas, which is present in the gasoline used in Iraq. Further, there is an average reduction in engine power of about 10% with APG compared with gasoline, while the only gain is the reduction in SFC of the fuel.

References

- [1] Annand, W.J.D., 1974. First Paper: Effects of Simplifying Kinetic Assumptions in Calculating Nitric Oxide Formation in Spark-Ignition Engines. *Proceedings of the Institution of Mechanical Engineers*, 188(1), pp.431-436. [https://doi.org/10.1243/PIME\\_PROC\\_1974\\_188\\_049\\_02](https://doi.org/10.1243/PIME_PROC_1974_188_049_02)
- [2] Ayandotun B. Wasii, Abd. Rashid Abd. Aziz and Morgan R. Heikal, 2012. The Effect of Carbon Dioxide Content-natural Gas on the Performance Characteristics of Engines: A Review. *Journal of Applied Sciences*, 12: 2346-2350. DOI: 10.3923/jas.2012.2346.2350
- [3] Bond, T.C., Doherty, S.J., Fahey, D.W., Forster, P.M., Bernsten, T., DeAngelo, B.J., Flanner, M.G., Ghan, S., Kärcher, B., Koch, D. and Kinne, S., 2013. Bounding the role of black carbon in the climate system: A scientific assessment. *Journal of Geophysical Research: Atmospheres*, 118(11), pp.5380-5552. DOI:10.1002/jgrd.50171.
- [4] Boucher, O., Friedlingstein, P., Collins, B. and Shine, K.P., 2009. The indirect global warming potential and global temperature change potential due to methane oxidation.

- Environmental Research Letters*, 4(4), p.044007. <https://doi.org/10.1088/1748-9326/4/4/044007>
- [5] Daneshyar, H., and Watfa, M., 1974. Second Paper: Predicting Nitric Oxide and Carbon Monoxide Concentrations in Spark-Ignition Engines. *Proceedings of the Institution of Mechanical Engineers*, 188(1), pp.437-445. [https://doi.org/10.1243/PIME\\_PROC\\_1974\\_188\\_050\\_02](https://doi.org/10.1243/PIME_PROC_1974_188_050_02)
- [6] Elvidge, C., Zhizhin, M., Hsu, F.C., and Baugh, K., 2013. VIIRS Nightfire: Satellite pyrometry at night. *Remote Sensing*, 5(9), pp.4423-4449. <https://doi.org/10.3390/rs5094423>
- [7] Elvidge, C., Ziskin, D., Baugh, K., Tuttle, B., Ghosh, T., Pack, D., Erwin, E., and Zhizhin, M., 2009. A fifteen-year record of global natural gas flaring derived from satellite data. *Energies*, 2(3), pp.595-622. <https://doi.org/10.3390/en20300595>
- [8] Gatowski, J.A., Balles, E.N., Chun, K.M., Nelson, F.E., Ekchian, J.A. and Heywood, J.B., 1984. Heat release analysis of engine pressure data. SAE transactions, pp.961-977.
- [9] Gur'yanov, A.I., Evdokimov, O.A., Piralishvili, S.A., Veretennikov, S.V., Kirichenko, R.E., and Ievlev, D.G., 2015. Analysis of the gas turbine engine combustion chamber conversion to associated petroleum gas and oil. *Russian Aeronautics (Iz VUZ)*, 58(2), pp.205-209.
- [10] Heywood, J. B., 1989, *Internal Combustion Engine Fundamentals*. McGraw Hill, New York.
- [11] Holmes, C.D., Prather, M.J., Søvde, O.A., and Myhre, G., 2013. Future methane, hydroxyl, and their uncertainties: key climate and emission parameters for future predictions. *Atmospheric Chemistry and Physics*, 13(1), pp.285-302. DOI:10.5194/acp-13-285-2013
- [12] [http://www.euro.who.int/\\_data/assets/pdf\\_file/0020/123059/AQG2ndEd\\_5\\_carbonmonoxide.PDF](http://www.euro.who.int/_data/assets/pdf_file/0020/123059/AQG2ndEd_5_carbonmonoxide.PDF)
- [13] <https://visibleearth.nasa.gov/view.php?id=83178>
- [14] <https://www.iasj.net/iasj?func=fulltext&aId=28281>
- [15] [https://www.naesb.org/pdf2/wgq\\_bps100605w2.pdf](https://www.naesb.org/pdf2/wgq_bps100605w2.pdf)
- [16] Lakshminarayanan, P. A., and Yoghesh V. Aghav. Modelling diesel combustion. Springer Science & Business Media, 2010.
- [17] Myhre, G.; Shindell, D.; Brèon, F.; Collins, W.; Fuglestedt, J.; Huang, J.; Koch, D.; Lamarque, J.; Lee, D.; Mendoza, B.; Nakajima, T.; Robock, A.; Stephens, G.; Takemura, T.; Zhang, H., 2013, Anthropogenic and Natural Radiative Forcing. In: *Climate Change 2013: The Physical Science Basis. Contribution of Working Group I to the Fifth Assessment Report of the Intergovernmental Panel on Climate Change*. Cambridge University Press, Cambridge, United Kingdom and New York, NY, USA.
- [18] Porpatham, E., Ramesh, A., and Nagalingam, B., 2012. Effect of compression ratio on the performance and combustion of a biogas fuelled spark ignition engine. *Fuel*, 95, pp.247-256. <https://doi.org/10.1016/j.fuel.2011.10.059>
- [19] Roy, P.S., Ryu, C., Dong, S.K. and Park, C.S., 2019. Development of a natural gas Methane Number prediction model. *Fuel*, 246, pp.204-211.
- [20] Singh, A.P., Sharma, Y.C., Mustafi, N.N. and Agarwal, A.K., 2019. *Alternative Fuels and Their Utilization Strategies in Internal Combustion Engines*. Springer.
- [21] Springer, G. ed., 2012. *Engine emissions: pollutant formation and measurement*. Springer Science & Business Media.
- [22] Stohl, A., Klimont, Z., Eckhardt, S., Kupiainen, K., Shevchenko, V.P., Kopeikin, V.M. and Novigatsky, A.N., 2013. Black carbon in the Arctic: the underestimated role of gas flaring and residential combustion emissions. *Atmospheric Chemistry and Physics*, 13(17), pp.8833-8855. <https://doi.org/10.5194/acp-13-8833-2013>
- [23] Vazim, A., Romanyuk, V., Ahmadeev, K., and Matveenko, I., 2015. Associated petroleum gas utilization in Tomsk Oblast: energy efficiency and tax advantages. In *IOP Conference Series: Earth and Environmental Science (Vol. 27, No. 1, p. 012078)*. IOP Publishing.
- [24] Vorobev, A. and Shchesnyak, E., 2019, September. Associated Petroleum Gas Flaring: The Problem and Possible Solution. In *International Congress on Applied Mineralogy (pp. 227-230)*. Springer, Cham.
- [25] Winterbone, D., and Turan, A., 2015. *Advanced thermodynamics for engineers*. Butterworth-Heinemann.
- [26] Woschni, G., 1968. A universally applicable equation for the instantaneous heat transfer coefficient in the internal combustion engine. SAE transactions, pp.3065-3083.
- [27] Yamin, J.A., Gupta, H.N., Bansal, B.B. and Srivastava, O.N., 2000. Effect of combustion duration on the performance and emission characteristics of a spark-ignition engine using hydrogen as a fuel. *International Journal of Hydrogen Energy*, 25(6), pp.581-589.
- [28] Yamin, J.A., and Badran, O.O., 2002. Analytical study to minimise the heat losses from a propane-powered 4-stroke spark-ignition engine. *Renewable energy*, 27(3), pp.463-478.
- [29] Yamin, J.A., Gupta, H.N., and Bansal, B.B., 2003. The effect of combustion duration on the performance and emission characteristics of propane-fueled 4-stroke si engines. *Emirates Journal for Engineering Research*, 8(1), pp.1-14.
- [30] Yamin, J.A., 2006. Comparative study using hydrogen and gasoline as fuels: Combustion duration effect. *International journal of energy research*, 30(14), pp.1175-1187.
- [31] Zyryanova, M.M., Snytnikov, P.V., Amosov, Y.I., Belyaev, V.D., Kireenkov, V.V., Kuzin, N.A., Vernikovskaya, M.V., Kirillov, V.A. and Sobyenin, V.A., 2013. Upgrading of associated petroleum gas into methane-rich gas for power plant feeding applications. Technological and economic benefits. *Fuel*, 108, pp.282-291.





الجامعة الهاشمية



المملكة الأردنية الهاشمية

المجلة الأردنية  
للمهندسة الميكانيكية والصناعية

JJMIE

مجلة علمية عالمية محكمة  
تصدر بدعم من صندوق البحث العلمي

<http://jjmie.hu.edu.jo/>

ISSN 1995-6665

# المجلة الأردنية للهندسة الميكانيكية والصناعية

المجلة الأردنية للهندسة الميكانيكية والصناعية: مجلة علمية عالمية محكمة تصدر عن الجامعة الهاشمية بالتعاون مع صندوق دعم البحث العلمي والابتكار - وزارة التعليم العالي والبحث العلمي في الأردن.

## هيئة التحرير

### رئيس التحرير

الأستاذ الدكتور محمد سامي الأشهب

### مساعد رئيس التحرير

الدكتور احمد المقدادي

الدكتور مهند جريسات

## الأعضاء

الأستاذ الدكتور طارق العزب

جامعة البلقاء التطبيقية

الأستاذ الدكتور محمد الوديان

جامعة العلوم والتكنولوجيا الاردنية

الأستاذ الدكتور جمال جابر

جامعة البلقاء التطبيقية

الأستاذ الدكتور محمد تيسير هياجنه

جامعة العلوم والتكنولوجيا الاردنية

الأستاذ الدكتور محمد الطاهات

الجامعة الاردنية

الأستاذ الدكتور علي جوارنه

الجامعة الهاشمية

## فريق الدعم

### المحرر اللغوي

الدكتور بكر محمد بني خير

### تنفيذ وإخراج

م . علي أبو سليمة

ترسل البحوث إلى العنوان التالي

رئيس تحرير المجلة الأردنية للهندسة الميكانيكية والصناعية

الجامعة الهاشمية

كلية الهندسة

قسم الهندسة الميكانيكية

الزرقاء - الأردن

هاتف : 00962 5 3903333 فرعي 4147

Email: [jjmie@hu.edu.jo](mailto:jjmie@hu.edu.jo)

Website: [www.jjmie.hu.edu.jo](http://www.jjmie.hu.edu.jo)